UNIVERSITÀ DEGLI STUDI DI ROMA "ROMATRE"
DIPARTIMENTO DI INGEGNERIA

Mechanical and Optical Behaviour of Coated and Non-coated Al-1%Si Tethers for the Electric Solar Wind Sail Technology

PhD student: Giuditta Montesanti

Tutor: Prof. Edoardo Bemporad

Doctorate Dissertation

2017

ROMA TRE
UNIVERSITÀ DEGLI STUDI

INGEGNERIA MECCANICA E INDUSTRIALE

SCUOLA DOTTORALE / DOTTORATO DI RICERCA IN

XXVIII

CICLO DEL CORSO DI DOTTORATO

MECHANICAL AND OPTICAL BEHAVIOUR OF COATED AND NON-COATED AL-1%Si TETHERS FOR THE ELECTRIC SOLAR WIND SAIL TECHNOLOGY

Titolo della tesi

GIUDITTA MONTESANTI

Nome e Cognome del dottorando

G Montesanti

firma

EDOARDO BEMPORAD

Docente Guida/Tutor: Prof.

firma

EDOARDO BEMPORAD

Coordinatore: Prof.

firma

2

1 INDEX

ABSTRACT

The tether is a device used in space technology to perform attitude manoeuvres, re-entry operations, to create propulsion or to generate energy. In practice, the tether is a conducting wire that interacts with the surrounding plasma, thanks to its electric field. The tether taken into consideration in this study is the heytether developed in the frame of the electric solar sail (E-sail) technology. The peculiar feature of this technology is to use a number of km-long wires, electrically charged at a 20-40 kV positive potential, which gain momentum from the electrons of the interplanetary plasma in order to generate a low and continuous thrust in space. The heytether is a multi-wire structure composed by four wires bonded ultrasonically. The tether material currently considered is Al-1%Si alloy.

In the literature, Al-1%Si mechanical properties at the micron scale have not been extensively studied at variable temperatures and for this particular application. Moreover, due to the fact that the tether diameter is in the order of micrometres, its mechanical properties may not be directly derived from the ones of bulk aluminium. This is because of scale effects, such as the dimension of the grains with respect to the tether's diameter.

The optical properties of the surface, moreover, strongly affect the equilibrium temperature of the tether in space. It is therefore crucial, after having estimated the effects of the temperature on the bare material – which has both a structural and an electrical function – to assess to which extent coatings are capable of modifying the equilibrium temperature in space. In the past, the emissivity of the E-sail tether has been measured by heating the wire in vacuum while measuring the voltage drop across the wire. However, no measure was performed for the absorbance, so it was not possible to determine whether the optical properties of the coating (α/ε ratio) were fitting the requirements or not.

This research includes an in-depth analysis of the properties of this material thanks to a mechanical test campaign carried out at different temperature conditions (from -40 °C up to 250 °C) and an optical test campaign aiming at measuring the tether emissivity ε in the infrared region and the absorbance α in the optical region. To this scope, four coatings (Al_2O_3, TiO_2, ZnO and $TiZnO$) have been deposited on aluminium samples (both on tether samples and on flat aluminium plates) and their optical properties studied.

Mechanical tests have been performed using a Dynamic Mechanical Analyser (DMA Q800) from TA Instruments. The objective of the tests was to assess the mechanical properties of the bare tether by performing tensile tests at several temperatures above ambient temperature and at low temperatures using the DMA liquid nitrogen cooling system.

The mechanical test campaign provided a detailed view of the trend of breaking load with temperature. The breaking load decreases at a rate of about 0.5 mN/ °C. Such information is essential to estimate the performance of the E-sail technology, since its thrust may be linked to the tensile strength.

While the data obtained for the breaking load provided good reliability and reproducibility, the data related to the elongation to failure presented a higher variability. Possible sources of error have been extensively discussed and the Digital Image Correlation (DIC) method has been used to confirm the measurement of the displacement at ambient temperature. The viscoelastic properties observed for the Al-1%Si material, mainly through the creep test and strain rate sensitivity test, are also discussed.

The optical measurements provided the α/ε parameter, crucial to estimate the equilibrium temperature in space. All coatings seem to increase the operating temperature and the highest values of α/ε ratio were obtained for ZnO e TiZnO. For these reasons, such coatings are believed to improve the thermal conditions of the tether for space missions to the outer solar system, where temperatures are lower.

ACKNOWLEDGEMENTS

LIST OF FIGURES

LIST OF TABLES

1. INTRODUCTION

The tether is a device used in space technology to perform attitude manoeuvres, re-entry operations, to create propulsion or to generate energy. In practice, the tether is a conducting wire that interacts with the surrounding plasma. When a potential difference is applied, the tether generates an electric field that is used to provide propulsion.

Depending on the specific application, several configurations of tethers have been proposed and studied. The tether taken into consideration in this study is the heytether developed in the frame of the electric solar sail (E-sail) technology. The peculiar feature of this technology is to use a number of km-long wires, electrically charged at a 20-40 kV positive potential, which gain momentum from the electrons of the interplanetary plasma in order to generate a low and continuous thrust in space.

The tether material selected in the frame of the ESAIL FP7 project was Al-1%Si alloy. This choice was mainly driven by the formability capabilities of this material. In fact, the tether is not a single wire but a multi-wire structure composed by four wires bonded ultrasonically.

The microstructural aspects of the tether's material were not specifically addressed in the frame of the ESAIL FP7 project, even if the tensile strength of the tether is one of the main design drivers and has a significant impact also on the thrust performances of the system. Moreover, the optical properties of the tether's surface (namely the absorbance α/emissivity ε ratio), which have a dramatic impact on the equilibrium temperature of the tether, were not extensively studied. A specific study aiming at linking the surface properties and the mechanical performances of the material at different temperatures was missing in the engineering design of the E-sail tether in space.

In this work, the properties of this material have been studied in depth, both relying on the literature and by means of direct observations of the microstructure. Furthermore, a mechanical test campaign has been carried out to study the response of the bare tether material to different temperature conditions (from -40 °C up to 250 °C).

The research also aims at improving the material properties of the tethers by applying specific coatings. The coating of the tether should be selected carefully, since its optical properties – the emissivity ε in the infrared region and the absorbance α in the optical region – strongly affect the equilibrium temperature of the tether in space. More precisely, the equilibrium temperature scales linearly with the parameter $\sqrt[4]{\alpha/\varepsilon}$. When moving in the Solar system, the equilibrium temperature of a black body may vary dramatically, ranging from 180 °C near Mercury to -200 °C near Pluto. It is therefore crucial, after having estimated the working temperature of the tether – which has both a structural and an electrical function – to assess whether coatings capable of modifying the optical properties of the surface could be employed.

Coatings may also have other functions, such as preventing the cold welding of the metallic tethers during the launch phases. In the frame of the ESAIL FP7 project, Rauhala *et al.* (2013) demonstrated that an Atomic Layer Deposition (ALD) coating could reduce the risk of cold welding due to launch vibrations. However, the main parameter contributing to the thermal equilibrium of the tether material in space – the α/ε ratio – had not been measured yet.

This study aims at analysing the mechanical and optical properties of the E-sail tethers, with the objective to identify potential coatings. In the frame of this PhD activity, four coatings (Al_2O_3, TiO_2, ZnO and $TiZnO$) have been deposited on aluminium samples (both on tether samples and on flat aluminium plates) in order to study their optical properties. To this scope, the absorbance and the emissivity have been measured for a broad range of temperatures.

The work has been carried out mainly at the LIME laboratory (*Laboratorio Interdipartimentale di Microscopia Elettronica*) of University of Roma Tre and in cooperation with the inventor of the ESAIL technology and the Project Manager of the ESAIL FP7 project Dr. Pekka Janhunen (Finnish Meteorological Institute). The coatings have been produced by University of Brescia with funding from the region Lombardia (MALDIT project). Mechanical tests have been carried at the laboratory *Materiali Multifunzionali* of the University of Roma Tre, while the optical tests have been carried out by Sapienza University of Rome. Tether samples have been provided by Dr. Pekka Janhunen.

After a description of the state of the art of the E-sail technology, this study describes the requirements for the tether material. Afterwards, the E-sail tether characteristics are described, focusing both on the bare aluminium material and the coating. Furthermore, the mechanical and optical test campaigns are described and discussed. Finally, conclusions are drawn from this work.

2. THE ESAIL TECHNOLOGY – STATE OF THE ART

2.1. SUMMARY

E-sail is a propellantless propulsion technology invented by Dr Pekka Janhunen in 2004. The concept of the E-sail, that makes use of the solar wind particles to generate thrust, is firstly explained. Then, the theory underpinning the functioning of this concept is discussed, making reference to the physics of a charged probe in a plasma. In the following section, the different components of the E-sail system are described. In the last part of the chapter, possible innovative applications of the E-sail technology are presented and the current and planned projects further developing the technology are illustrated.

2.2. CONCEPT

The E-sail is a propellantless propulsion technology that was invented by Dr Pekka Janhunen in 2004 (Janhunen (2004)). Differently from the solar sail concept, which exploits the motion of the photons coming from the Sun, the E-sail makes use of the solar wind particles to generate thrust. In space, a conductive tether charged at a certain voltage, either positive or negative, generates an electric field. The ions and electrons present in the low density plasma of the solar wind interact with this electric field, generating momentum.

Propellantless propulsion systems produce a very low but continuous thrust. Therefore, they are continuously accelerating. Over a period of months, a solar sail accelerates a spacecraft to incredibly high velocities (100-150 km/s or 20-30 au/year) (Wiegmann (2015)).

The idea of using tethers in space for different purposes has been firstly proposed by Mario Grossi to the Italian Space Agency and NASA in the early 1970s (Cosmo *et al.* (1997)). A first mission, the TSS-1, was then developed in 1985 and launched in 1992. The mission demonstrated the feasibility of the concept.

Apart from long-distance missions, tethers may also be used to de-orbit a small satellite at the end of its life (Cosmo *et al.* (1997), Janhunen (2010)). An example of this function is the Japanese "Kounotori Integrated Tether Experiment", where the satellite Kounotori 6, launched in December 2016, carried a scientific payload aiming at testing an electrodynamic tether (*Phys.org* (2016)).

Since the 1970s, such electrodynamic tethers have been considered for applications limited to the Earth's magnetosphere, using the Lorentz force generated thanks to the current flowing in the conducting wire. On the contrary, the E-sail is based on a different concept – the interaction of the conducting wire with the solar wind plasma – and therefore only applies outside a planet's magnetosphere.

Zubrin *et al.* (1991) were the first to propose to make use of solar wind momentum, creating an artificial magnetosphere around the spacecraft to deflect the solar wind and thus extract momentum from it. Pekka Janhunen (2004), building on this magnetic sail concept, proposed to use a number of tethers, km-long, attached to the spacecraft on one side and stretched out as sunburst, as shown in Figure 1.
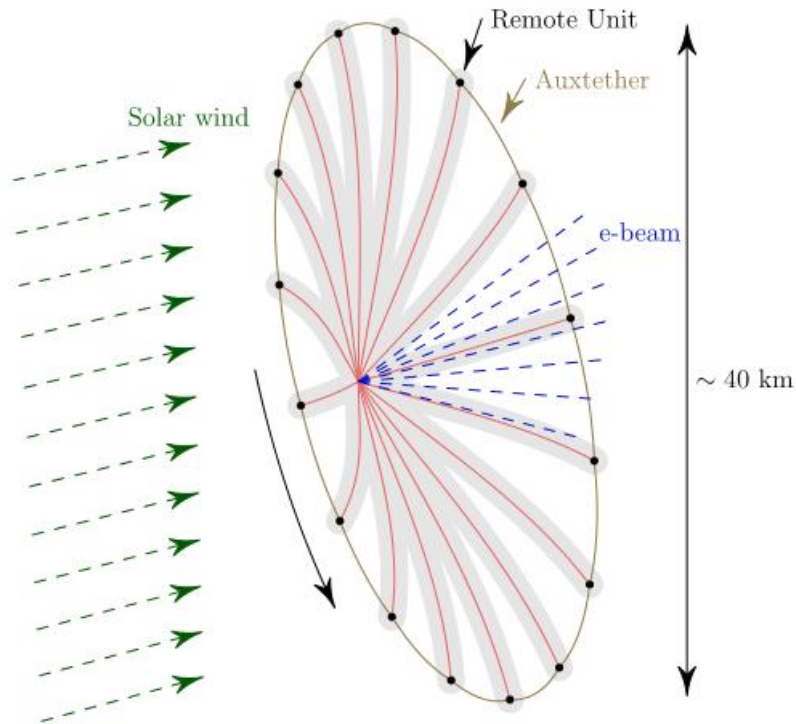
Figure 1: Schematic view of a spinning E-Sail. Janhunen et al. *(2015).*

In order to stretch out the tethers, the spacecraft should be put in rotation. Thanks to a small mass placed at the other tip of the tether, the centrifugal force generated by the spacecraft rotation puts the tether in tension. The tether is then charged at a voltage in the order of kV. The voltage should be preferably positive, even if other solutions have also been studied (Janhunen (2009)). The tether would then generate an electric field and behave in space as an electron collector, following the Langmuir principle (Janhunen *et al.* (2007)). An electric current would then flow in the tether. To be closed, the electric circuit would need an electron gun, which is responsible for expelling the electrons back to space. The solar wind dynamic pressure is on average about 2 nPa at 1 au distance from the Sun (Janhunen *et al.* (2007)).

The E-sail principle relies on the presence of a plasma, even if with very low density. For this reason, it cannot be used inside a planet's magnetosphere. In the case of the Earth, this means that the E-sail works above on average 10 times the Earth's radius. This limitation is even more stringent in the Earth shadow, due to the elongated shape of the magnetosphere (Janhunen *et al.* (2014)).

The E-sail system can be scaled depending on the payload mass and tethers configuration. The performances vary accordingly and are therefore not trivial to estimate. The thrust generated by the E-sail, when going away from the Sun, is inversely correlated with the distance from the Sun. The correlation can be approximated to an inversely proportional one. This feature represents a big advantage compared to the solar sails, for which the thrust decay is proportional to the square root of the distance from the Sun. The relation between the thrust and the distance from the Sun may be also influenced by other factors, such as the decay of the solar wind density, the increase in the effective sail area and the reduction of the solar panel power (Toivanen *et al.* (2009)). The $1/r$ relationship is based on the assumption that the solar wind density goes as $1/r^2$ and that the effective electric width of the

tethers scales with density in the same way as the plasma Debye length. The solar illumination of the solar panels also scales exactly as $1/r^2$, while the solar panel power might scale somewhat differently depending on technical properties of the panels.

As a reference, we can consider that at 1 au solar distance the E-sail propulsive system generates 1 N of thrust. For payloads up to a few hundred kilograms of mass the characteristic acceleration would be 1 mm/s^2, corresponding to ~30 km/s of Δv capability per year (Janhunen *et al.* (2014)). The characteristic acceleration is defined as the acceleration achieved when the E-Sail spacecraft is pointed directly at the Sun (i.e., the sail plane is normal to the Sun vector) at 1 au.

The whole propulsion system includes not only the tethers and the remote units, but also the power generation unit and the electron guns. The mass budget modes have been studied in Janhunen *et al.* (2013). For example, for a spacecraft of 1290 kg, the resulting mass of an E-sail with specific acceleration of 0.1 mm/s^2 is 74 Kg.

It is possible to tilt the E-sail thrust up to $\pm 30°$ with respect to the direction of the solar wind (Janhunen *et al.* (2014)). A 30° tilting can be used to spiral inwards or outwards the solar system. In the first case, however, the absolute speed of the satellite will decrease during the travel. Manoeuvring the E-sail is not trivial when flying towards the Sun, when passing through the shadow of a planet (Janhunen *et al.* (2015)) or when tilting at angles close to 30° with respect to the solar wind direction.

The development of the E-sail technology has been partially funded by the European Union in the frame of the FP7 project called "ESAIL".

In 2015, NASA included the E-sail technology in the in the list of the advanced propulsion technologies (TRL < 3) in the *In-Space Propulsion Systems Roadmap* (NASA (2015)), showing a considerable interest in this technology. The main challenges identified were the quantification of thrust magnitudes with on-orbit data, the demonstration of noninterfering centrifugal deployment of multiple wires from a single spacecraft and the development of long-life, extremely long bare wires.

2.3. THEORY

In vacuum, the electric potential around a charged wire is:

$$V(r) = V_0 \frac{\ln(r_0/r)}{\ln(r_0/r_w)}$$

Where r_0 is the distance at which the potential becomes zero and r_w is the tether's radius.

In the plasma, however, the potential vanishes at a lower distance from the wire, compared to the vacuum case, becoming:

$$V(r) = V_0 \frac{\ln\left[1 + (r_0/r)^2\right]}{\ln\left[1 + (r_0/r_w)^2\right]}$$

$$r_0 = 2\lambda_{De} = 2\sqrt{\frac{\epsilon_0 T_e}{n_0 e^2}}$$

Eq. a

16

where λ_{De} is the Debye length.

The spatial scale size of the electric field is related to the Debye length of the plasma. The sheath radius delimitates the area where the space charge separation between ions and electrons in the plasma takes place. Outside that space, the plasma in considered to be overall electrically neutral. The electron sheath width is estimated to be ≈100 m at 1 au (Janhunen *et al.* (2010)). For high voltages – much higher than electron temperature, as in our case – the sheath radius can be more than 10 times larger than the Debye length (8 m). The sheath size remains proportional to the Debye length, with about one order of magnitude difference between the two values. A schematic of the tether's sheet is shown in Figure 2.
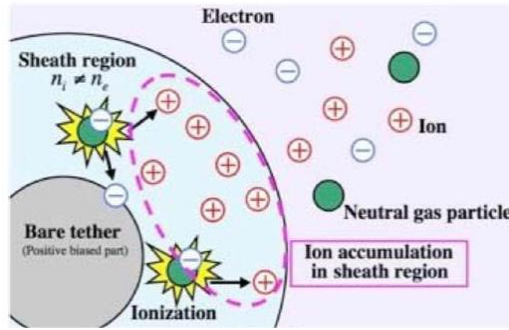
Figure 2: Schematic of the tether's electron sheath. Kashihara et al. *(2008)*

Janhunen (2004) made the hypothesis that the incoming solar wind protons see the tether as an impenetrable barrier over the Debye length if the voltage is higher than the kinetic energy of the solar wind protons (about 1 keV). Therefore, he made a simple calculation for the maximum force acting on a rectangular mesh of tethers (Figure 3), under the hypothesis of a mesh perpendicular to the solar wind direction:

$$F = p_{dyn} \cdot A$$

where p_{dyn} is the dynamic pressure of the solar wind and A is the area of the mesh of tethers.
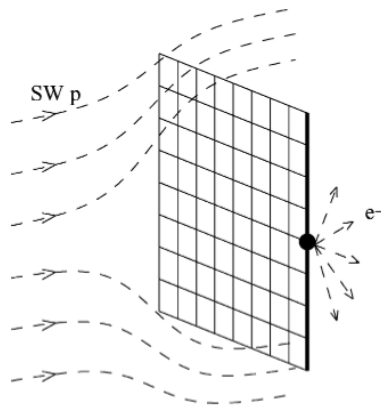
Figure 3: Schematic of a two-dimensional mesh of tethers. Janhunen (2004).

In the case of a single tether, the area A is calculated as the length of the tether multiplied by the effective width of the tether. The effective width is proportional to the "proton stopping distance" r_s and was calculated numerically by Janhunen (2007), obtaining:

$$r_s = \frac{\frac{1}{2}m_p v^2}{eV}. \qquad \text{Eq. b}$$

The dynamic pressure is:

$$p_{dyn} = \rho_{SW} \cdot v^2$$

where ρ_{SW} is the solar wind mass density and v is the flow velocity.

$$\rho_{SW} = n \cdot m_p$$

where n is the plasma density and m_p the proton mass. Janhunen (2004) assumes that at 1 au n=7.3 cm^{-3}, v = 400 km/s and p_{dyn} = 2 nPa.

The force per unit length then becomes:

$$\frac{dF}{dz} = K m_p n_0 v^2 r_s \qquad \text{Eq. c}$$

where the value of K ≈ 3.09 was determined numerically by Janhunen (2007).

While the protons are repelled, electrons are attracted by the tether due to their positive potential. Electrons will therefore "bombard" the tether and will be captured in the form of an electric current flowing in the wire. If the electrons would not be expelled from the tether (and the satellite) structure, the overall charge would increase indefinitely. For this reason, an electron gun should be used to expel electrons back to space. As already mentioned, the tether behaves like a Langmuir probe in space and the orbital motion limited (OML) theory can describe such behaviour (Sanmartín *et al.* (1999)). As explained by Chen (2015), "due to the enormous disparity between tether thickness and collecting length, each point on the anodic segment would collect current as if it were a cylindrical Langmuir probe, uniformly polarised at the tether-to-plasma bias".

In Figure 4, a bare tether in space is displayed. In the anodic segment (from point A to point B) the current increases and the voltage difference between the tether and the surrounding plasma (ΔV) decreases (becoming zero in point B). Between points B and C, the voltage is lower than the plasma voltage V_{pl}. This section is however shorter than the anodic segment and it is considered not to lower significantly the total current reaching the cathode used to expel electrons. In this configuration, a current is therefore established.
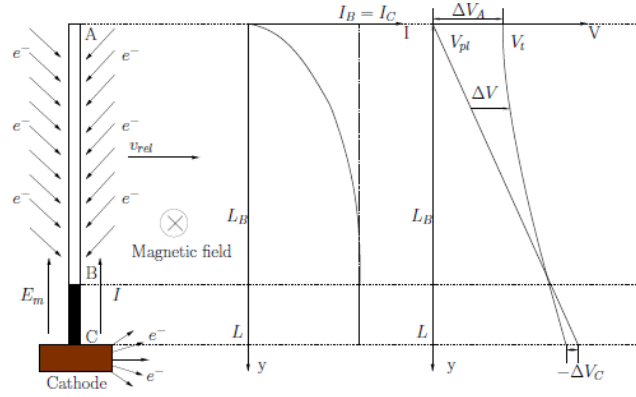
Figure 4: Schematic of current and potential variation in the tether frame for a bare tether. Only tether resistance and a very small hollow-cathode impedance are considered. V_{pl} is the plasma voltage, V_t is the tether voltage. Chen (2015).

Using equation a) and equation b), we obtain the following expression for the proton stopping distance r_s:

$$r_s = \frac{r_0}{\sqrt{\exp\left[\frac{m_p v^2}{e V_0}\ln(r_0/r_w)\right] - 1}}$$

Substituting the previous equation in equation c), we obtain the expression of the force per unit length:

$$\frac{dF}{dz} = \frac{K m_p n_0 v^2 r_0}{\sqrt{\exp\left[\frac{m_p v^2}{e V_0}\ln(r_0/r_w)\right] - 1}}$$

The force per unit length results to be proportional to the square root of the electron temperature. Higher electron temperature yields wider electron sheath and larger propulsive effect (Janhunen (2007)). Figure 5 provides the force per unit length as function of the tether's voltage V_0. A 20 kV charged tether, considering average solar wind conditions, produces $\approx$ 580 nN/m thrust per unit length at 1 au (Janhunen *et al.* (2013)). Therefore, 100 tethers, each of them 20 km long, produce $\approx$ 1.1 N of thrust.

Force per unit length
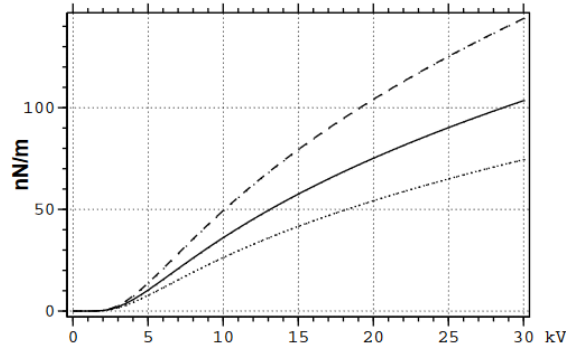
Figure 5: Force per unit length as function of voltage V0. Solid curve is for baseline electron temperature 12 eV, dotted for 6 eV and dashed for 24 eV. The wire radius is 10 μm. Janhunen (2007).

For what concerns the relation between the force and the distance from the Sun, we can consider that the solar wind density goes with $1/r^2$, the solar wind speed remains nearly constant and the solar wind temperature goes as $1/r^{1/3}$. Therefore, we obtain:

$$F \sim n_0 r_0 \sim \sqrt{n_0 T_e} \sim \sqrt{\frac{1}{r^2} \frac{1}{r^{1/3}}} = \left(\frac{1}{r}\right)^{7/6}$$

More recent derivations provided even a dependence from the distance to the Sun of 1/r (Janhunen *et al.* (2010)).

The force decay is slower than for the solar sail case, which is proportional to $1/r^2$, thus making the E-sail technology more interesting for missions to the outer solar system.

According to Janhunen (2010) and Janhunen *et al.* (2013), under the assumption of a distance from the Sun of about 1 au and the current known solar wind parameter, the force per unit length can be simplified as a function of the tether's voltage V_0:

$$f = f_V V_0 - f_0,$$

Where f_0 = 24.16 nN/m and f_V = 24.16 nN/mkV (Janhunen *et al.* (2013)).

The main parameters describing the performance of a space propulsion system are the thrust and the characteristic acceleration. Depending on whether we have a high power propulsion system, such as a chemical rocket, or a low power propulsion system, such an ion engine, either the thrust or the characteristic acceleration becomes the main parameter of interest for the technology. In our case, being the E-sail a low-power and continuous thrust propulsion system, the characteristic acceleration is to be considered. The characteristic acceleration of the E-sail is (Janhunen *et al.* (2013)):

$$a = \frac{fNL}{m},$$

where f is the force per unit length of the tether, N is the number of tethers, L is the length of the tethers and m the spacecraft mass.

Quarta *et al.* (2010) present mission design results for a range of characteristic accelerations from 0 to 2 mm/sec^2. By contrast, 0.5 mm/sec^2 is considered a high level of performance for a solar sail (Wiegmann (2015)).

2.4. E-SAIL SYSTEM

We may subdivide the components of the E-sail propulsion system as follows:

1. <u>High voltage subsystem</u>. The electron guns are part of this subsystem. The electric power varies with the distance from the Sun. Generally, three electron guns are considered in the design, for redundancy reasons. In order to distribute high voltage and grounding plan, a frequently used method consists in having a relatively low energy (e.g. 1 kV) electron gun connected to a common internal bus that maintains the electron gun at its voltage. Each tether can then have its own small, high voltage source, thus allowing an arbitrary differential modulation of tether voltages (Janhunen *et al.* (2013)).

2. <u>Main tethers</u>. The main tethers are the core of the E-sail technology, since their interaction with the solar wind generates the thrust. They connect the spacecraft with the remote units and are stretched thanks to the centrifugal rotation of the spacecraft, as shown in Figure 6. A typical spin period is some tens of minutes (Janhunen *et al.* (2013)). Since the main tethers should withstand micrometeoroids bombardment, Janhunen *et al.* (2013) propose to use a base wire to which three wires with smaller diameter are bonded (Figure 6). Heytether is roughly equivalent to the criss-crossed four-wire hoytether proposed by Hoyt *et al.* (2000), but is considered to be easier to manufacture by the ESAIL FP7 project method, thanks to the use of a single base wire. The heytether was invented by Henri Seppänen.

3. <u>Main tether reel assembly</u>. Before deployment, the tether is kept inside the reel thanks to a motorised mechanism. The system is also responsible for the release and deployment of tether in space.

4. <u>Auxiliary tether</u>. The auxiliary tether is used to connect the remote units in order to avoid collisions between adjacent tethers; its current design envisages the use of Kapton (Janhunen *et al.* (2010)).

5. <u>Remote units</u>. They are placed at the tip of each tether and are used to dynamically stabilise the tether rig reducing the need of active control (Janhunen *et al.* (2010)). Each remote unit hosts a propulsive system for controlling the tether rig's spin (Janhunen *et al.* (2013)).

6. <u>Tether cameras and controller</u>. The cameras are used to verify the actual position of each remote unit. An example of such a subsystem for the imagining of the tether and its end-mass is reported in Kuuste *et al.* (2014).

7. <u>Power generation subsystem</u>. This subsystem includes the solar panels, their deployment mechanism and a power processing unit.

8. <u>Telemetry, ACS, thermal and structure</u>. The requirements for this subsystem are primarily related to the payload characteristics, but they should also include functionalities related to the E-sail propulsion system. In fact, the spacecraft should be put in rotation in order to keep the tethers stretched and it should be tilted for the purpose of manoeuvring.
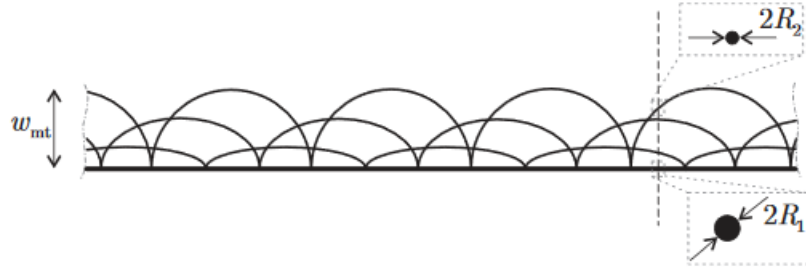
Figure 6: Configuration of the heytethers. Janhunen et al. (2013).

In an electric propulsion system, the power conditioning unit has a large mass impact on the satellite. In a similar way, the structure of the E-sail system has to be considered in the overall mass budget. Janhunen *et al.* (2013) developed a mass budget model for the entire spacecraft propelled with an E-sail system. In the paper, the authors assume to know the characteristic acceleration and the payload mass and power.

As an example, the mass budget for an E-sail system with characteristic acceleration of 1 mm/s is reported in Figure 7.

Payload m_{pay} (kg)	100	200	300
Number of tethers N	44	62	86
Tether length L (km)	15.3	19.4	20.0
E-sail thrust at 1 AU (N)	0.39	0.70	1.00
E-sail power $P_o + P_{eg}$ (W)	409	720	1026
Payload idle power (W)	12.5	25.0	37.5
Payload duty power (W)	125	250	375
Main tethers $N m_{mt}$ (kg)	7.79	13.9	19.8
Main tether reels $N m_{mr}$ (kg)	9.21	14.8	20.8
Electron guns $3 m_{eg}$ (kg)	1.20	2.13	3.05
HV source m_{vs} (kg)	7.98	14.2	20.3
Cameras and computer (kg)	1.48	1.48	1.48
Remote units $N m_{ru}$ (kg)	43.1	59.3	77.6
Auxtethers (kg)	26.1	32.9	34.0
Power system m_{sa} (kg)	32.0	61.6	91.3
Telemetry system (kg)	25.0	50.0	75.0
Thermal control (kg)	9.31	18.1	26.9
ACS (kg)	13.8	24.7	35.3
Structure (kg)	48.9	87.0	125
20% margin (kg)	65.2	116	166
Total without E-sail (kg)	248	490	732
E-sail effective (kg)	143	206	264
Total (kg)	391	696	996
E-sail mass fraction (%)	36.6	29.6	26.5
E-sail specific acc. $\mathrm{mm\,s^{-2}}$)	2.73	3.38	3.77

a) Schematic view of the ESAIL with remote units and auxiliary tethers	b) Spacecraft mass budget

Figure 7: Spacecraft mass budget for an E-sail system with characteristic acceleration of 1 mm/s. Janhunen et al. (2013).

2.5. POSSIBLE SPACE MISSIONS

In the first part of the PhD project, while studying the E-sail technology, the investigation of possible applications led to the contribution to the peer reviewed article published in the *Proceedings of the Estonian Academy of Science* (Janhunen *et al.* (2014)). We recall hereafter the main findings of the study.

The main limitation in the use of this technology is the need to operate outside a planet's magnetosphere. Moreover, the current E-sail design foresees a range of operations in the Solar system between 0.9 au and 4 au, but this range can be eventually extended in the future. According to the study carried out by NASA (Wiegmann (2015)), the system could even provide accelerations up to 30 au; therefore, one interesting potential application could be travelling to the heliopause.

In order to compare the E-sail with electric propulsion systems, different parameters are to be selected. As for electric propulsion, the mass of the system and the thrust generated are important parameters.

Possible E-sail space missions are:

- Terrestrial planets and asteroids (the estimation of the delta-V increases with respect to chemical propulsion missions is mentioned) such as Venus, Mars and Phobos, Mercury and the Asteroids;
- Maintaining non-Keplerian orbits (Figure 8), which could be used to perform helioseismology from a lifted orbit, remote sensing of the Earth and Earth's environment, observe the giant planet auroras and monitor of off-Lagrange point solar wind;
- Near-Sun missions;
- Boosting to the outer solar system;
- Impactors and Data Clippers;
- Asteroid resource utilisation.
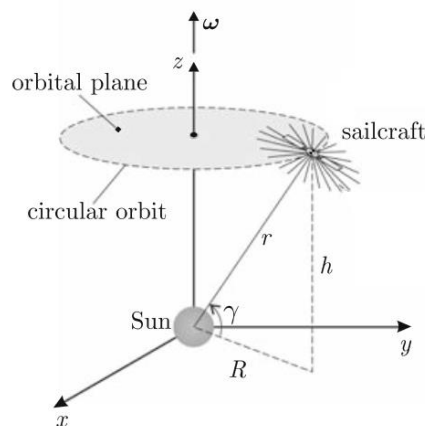
Figure 8: Layout of non-Keplerian orbits. Mengali et al. (2009).

A representation of a scientific mission to the giant planets (Jupiter, Saturn, Uranus, Neptune), which benefits from a single launch, is reported in Figure 9. For easier visualisation, the details on how the data from the atmospheric probe are relayed by the E-sail mother spacecraft flying by the giant planet are shown only in Saturn's case.
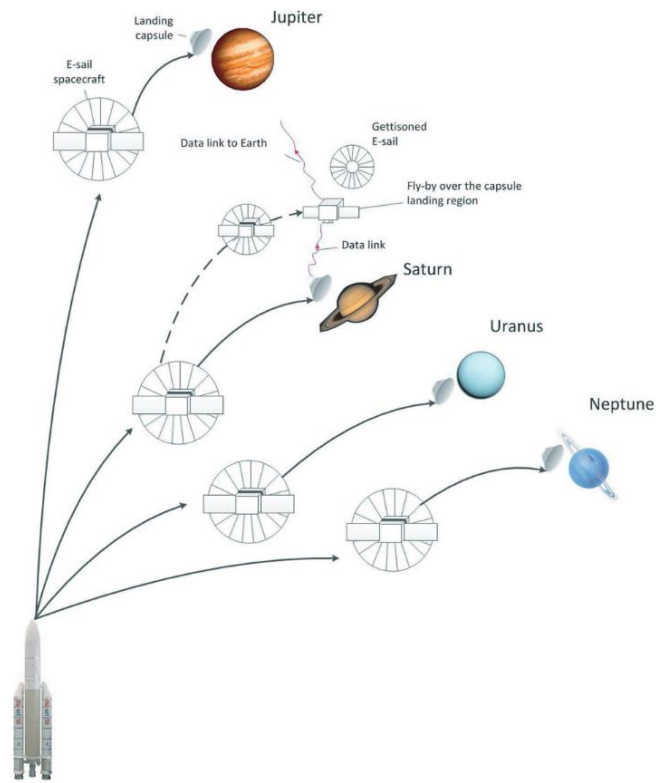
Figure 9: Scenario for four identical atmospheric probes to all four giant planets by a single launch. Illustrative photos courtesy by Arianespace, ESA, and NASA. Janhunen et al. (2014).

Resources such as water, other volatiles or metals could be in the future mined from asteroids and then transported by the E-sail. This could be used for lifting satellites to a higher orbit or for manned exploration missions to Mars, asteroids and other bodies. An example of such ideas is reported in Figure 10.
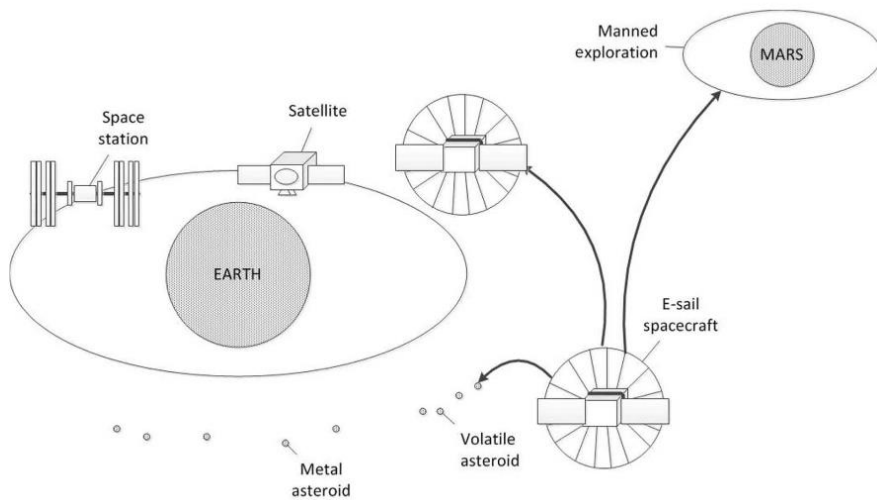
Figure 10: Asteroid resource utilisation. Janhunen et al. (2014).

2.6. CURRENT E-SAIL PROJECTS

Several activities have been undertaken by the international space community to further develop the E-sail concept.

At the European level, the Estonian satellite CubeSat[1] EstCube-1 (Figure 11) embedded the first E-sail concept test in space. This CubeSat was the result of the work of a team of students. It was launched as a piggy-back on board a Vega launch on 7 May 2013 from the European Spaceport in Kourou, French Guiana, to polar Sun-synchronous 667 km orbit. EstCube-1 is a CubeSat made of one single unit.

The main task of the E-sail payload was to measure the strength of the E-sail effect in low Earth orbit. There, the satellite has a different velocity from the ionospheric plasma, thus reproducing in a smaller scale the solar wind behaviour. The E-sail effect was supposed to be measured by monitoring the spin rate of the satellite, since if the tether is charged when moving in the opposite direction to the plasma stream, the spin rate would then decrease. To this end, the EstCube-1 satellite was provided with a 10 m long tether (Envall *et al.* (2014)). Unfortunately, the test could not be carried out, since the tether deployment was unsuccessful (Slavinskis *et al.* (2015)).
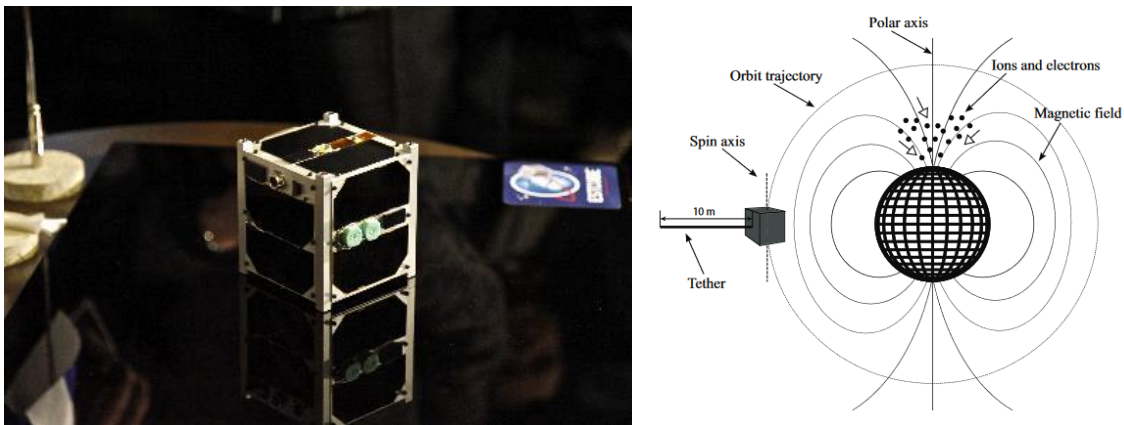
Figure 11: EstCube-1 satellite. Left image: https://www.electric-sailing.fi/projects.html; right: Lätt et al. (2014).

In Finland, another mission (Aalto-1) is currently being developed, with the aim to test a 100 m E-sail tether. The Aalto-1 is a CubeSat made by three units, with dimensions 30x10x10 cm (*eoPortalDirectory* (2017)).

In 2012 NASA decided to start a project related to the E-sail technology called Heliopause Electrostatic Rapid Transit System (HERTS) (Wiegmann (2015)). The project was funded by the NASA Innovative Advanced Concepts (NIAC) for six months and selected in the frame of the US National Academy of Science's 2012 Heliophysics Decadal Survey. The primary objective of the study was to assess the

---

[1] CubeSats are nanosatellites with the dimension of 10x10x10 cm and a maximum weight of 1 kg per unit. This type of technology has been widely used in recent years, mainly for training purposes and to create low-budget space missions with students all around the world. This technology was also used in the project QB50, which embeds 50 CubeSats built by different research centres, universities and companies. The QB50 project is led by the Von Karman Institute in Belgium.

feasibility of a mission to the hedges of the Solar System, the heliopause, in less than 10 years using the E-sail as the main thrust system. The cruising time would be significantly faster than for the Voyager 1, which travelled at a speed of 3.6 au/year. The results of the study were extremely positive and confirmed the feasibility of such space mission. In addition, the thrust at 1 au for an applied voltage of 6 kV was estimated as 2500 nN/m, about 3.5 times higher than what was foreseen by Janhunen *et al.* (2013)). Wiegmann (2015) concluded that the system could be "developed within a decade and provide meaningful heliophysics science and outer planetary science returns in the 2025-2035 timeframe". One of the main changes in the E-sail system design proposed by NASA was related to the deployment method. The author proposes to deploy a group of wires by using just two rockets to reduce forces applied on the tethers during deployment.

In 2015, the HERTS project has been selected for a two-year grant funded by the Phase II NIAC Fellow programme. The objective of the project was to perform the first experimental activity on-ground of the E-sail concept and to collect modelling data. The on-ground testing activity was started in 2016 and as of Spring 2017 the results of the testing activities have not been disclosed yet by NASA (*Nasa.gov* (2016)).

3. MOTIVATIONS

The E-sail material has been selected in the frame of the ESAIL FP7 project, Al-1%Si, mainly on the basis of the requirements related to the possibility (i) to create the complex structure of the heytether using ultrasonic bonding and (ii) to minimise the total weight, as will be discussed in the next chapter. The microstructural aspects of the tether's material, however, were not specifically addressed in the frame of the ESAIL FP7 project; they play nonetheless a crucial role in the determination of the mechanical performances of the tether due to its geometry.

Even if Al-1%Si wires can be produced in the form of very thin wires with micrometric dimension diameter and can be bonded ultrasonically quite easily, such material is mainly used in the electronics industry for packaging purposes. For the E-sail technology application, however, the tether should have a structural function, as it should be always kept under tension during operations. Moreover, the tensile strength is one of the main design drivers, since the thrust level is roughly proportional to the usable tensile strength per mass density of the tethers.

Since the tether diameter is in the order of micrometres, its mechanical properties cannot be directly derived from the ones of bulk aluminium. This is because of scale effects, such as the dimension of the grains and the ratio between the grain's diameter and the tether's diameter. For example, Engel *et al.* (2002) showed that the flow stress decreases with increasing miniaturisation, since free surface grains show less hardening compared to the inner volume grains. In practice, the strength of specimens containing only a small number of grains across the cross section decreases with the ratio between the wire diameter and the grain diameter. In this sense, mechanical properties of micrometric wires are strongly affected by their production process, Liu *et al.* (1999)), as it will be discussed in further detail in the next chapters.

In the literature, Al-1%Si mechanical properties at the micron scale have not been studied for this particular application. Even if publications exist on the mechanical properties of Al-1%Si wires (Liu *et al.* (2004), Danaher *et al.* (2011)), they focus on the applications for the electronics industry. Moreover, extensive studies on the breaking load of this specific material at variable temperatures were not found.

A second area of study was related to the optical properties of the tether's surface. Since the E-sail is a technology needed for travelling in the Solar System, it would face a variable operating temperature along its life. Depending on the optical properties of the surface of the tether, namely the ratio between the absorbance and the emissivity, and on the distance from the Sun, the range of temperature to which the tether's material would be exposed could very dramatically. In this context, the temperature may even affect the mechanical properties of the tether by processes such as creep.

Even though in the frame of the ESAIL FP7 project some preliminary studies on the optical properties of the surface and coatings have been conducted, the results were not conclusive. In fact, only the emissivity of the wire was measured, but no measure was performed for the absorbance. Therefore, it was not possible to determine whether the optical properties of the coating were fitting the requirements or not.

The motivation of the work was therefore twofold: (i) investigating the mechanical behaviour of the tether material, by relating it to its microstructure and production process, and (ii) studying the optical behaviour of its surface. Such an approach, aiming at linking the surface properties and the mechanical

performances of the material at different temperatures, was in practice missing in the engineering design of the E-sail tether in space.

In order to fill this knowledge gap, it was decided to perform mechanical tests on the bare tether using a Dynamic Mechanical Analyser. The objective of the tests was to assess the mechanical properties of the bare tether by performing tensile tests at several temperatures above and below the ambient temperature. The results of this activity will be published in a peer reviewed journal in the near future. Furthermore, a study of the Atomic Layer Deposition coatings properties was carried out together with the Università degli Studi di Brescia (MALDIT project) and Università degli Studi di Roma "La Sapienza".

4. REQUIREMENTS FOR THE TETHER MATERIAL

4.1. SUMMARY

First, the requirements for the tether material and coating are discussed, building on the results emerging from the ESAIL FP7 project. The requirements related to the tensile strength and the thermal equilibrium are the core of this work and are therefore analysed in more detail. Then, some material options for the bare tether are considered. Finally, the coating requirements, with particular regard to the capability to modify the optical properties of the tether surface, are discussed. Other options investigated so far, as well as production concerns, are also taken in consideration.

4.2. MAIN TETHER REQUIREMENTS

The main requirements for the E-sail tether have been identified within the ESAIL FP7 project (Koivisto *et al.* (2011)), Seppänen (2013), Rauhala *et al.* (2013)) and are recalled hereafter.

The selection of the tether's material is based on some requirements such as:

- Vacuum compatibility. The tether material should be vacuum compatible. The vacuum compatibility of metals is good, while polymer solutions or coatings should be space-qualified.
- Tensile strength. The tether has to withstand the static pull corresponding to weight of 5 g (also considering the crossing of an eclipse region). The tether material should have a high (> 10 MPa) and stable tensile strength in a wide range of temperatures, as discussed in the following paragraph.
- Mass density. The mass density of the tether should be minimised. The tether's subsystem weight has been estimated for different E-sail missions by Janhunen *et al.* (2013).
- Resistivity. The tether will collect electrons in the solar wind plasma and should have a high conductivity to minimise the power loss due to Joule effect. Considering a copper wire with conductivity at room temperature of 60 $(M\Omega m)^{-1}$, Janhunen (2004) estimated a heating power of 8 μW for a 30 km long wire. The resistivity of steel is considered sufficient.
- Resistance to electron bombardment. The tether material should sustain an electron bombardment of 20-40 keV without significant material degradation. Moreover, it should sustain sparks in case of failures.
- UV degradation. The material should have an excellent resistance to UV exposure.
- Operating temperature. The equilibrium temperature of the tether may affect the mechanical properties, such as the creep, of the tether material. The equilibrium temperature depends on the surface properties, which may be altered by the presence of a coating. The coating may even degrade due to a change in the temperature. The E-sail is preferably used outside eclipse regions in the solar system to avoid sudden temperature jumps. This topic has been studied in the solar distance range 0.9 - 4 au by Janhunen *et al.* (2015). The survival temperature of the electronics (-20 °C to +70 °C) could be considered as an indicative range of operation for the E-sail. Metals are good candidates for this purpose. For missions close to the Sun, the tether's surface should have a low absorbance in the optical range and a high emissivity in the infrared range. The exact

opposite is required when operating in the outer solar system. Metals are generally highly reflective. Coatings could be selected to tune these parameters.

- Micrometeoroid resistance: the tether should be designed to minimise the risks of failure due to micrometeoroid impact. Such requirement has been studied in the past by Sturmfels (2001). The response of a tether structure in space has been investigated in the frame of the MAST space tether experiment (Hoyt *et al.* (2007)) using a CubeSat. It was estimated that the lifetime of a multi-wire structure increases dramatically the survival probabilities (Figure 12).

- Workability of material. In order to create the structure needed against micrometeoroid impact, the production process of the multi-wire system (the heytether) should be affordable. In that sense, the tether material should have a high workability. In the case of metals, aluminium has a good workability while titanium poses more problems. If coatings are to be considered, the impact on the production process of the heytether should be taken into account.

- Deployment friction. During the assembly of the satellite, the launch and the early operations, the tether is stored in a reel. Especially during the launch, the reel is subject to high vibrational loads that may cause undesired bonds between the turns. Afterwards, these bonds could prevent the complete deployment.

- Cost. In order to estimate the final cost of the technology, not only the cost of the material itself is to be considered, but also the cost of the production process of the multi-wire system.

- Lifetime. The lifetime requirement of the tether is 5 years.

- Other requirements. The tether should not be magnetic in order not to interfere with the other subsystems of the satellite.
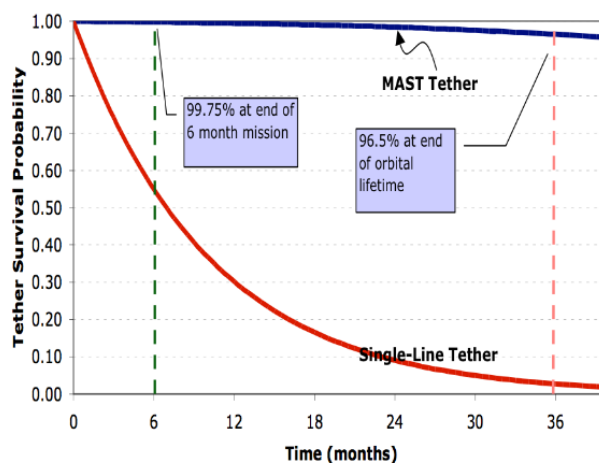
Figure 12: Survivability of the MAST multi-wire tether to the impact of micrometeoroids and orbital debris in space compared to a single-line tether of equal mass. Hoyt et al. *(2007).*

4.3. TENSILE STRENGTH

The E-sail tethers should be always kept under tension during operations. To this end, the satellite is put in rotation. Therefore, the tether's motion is controlled both by the thrust vector and the centrifugal force. The resulting force will have a coning angle with respect to the original tethers plane,

similarly to the case of the helicopter blades. The relation between the electric sail force and the centrifugal force is further explained by Toivanen *et al.* (2014).

The centrifugal force should be such that it overcomes the propulsive thrust by a factor of about 5. As a consequence, it is assumed that the tether should withstand a continuous tensile force corresponding to about 5 g in the Earth's gravity field (Janhunen *et al.* (2013)).

In Figure 13 the Coriolis force is the G vector, while the thrust is the F vector. The direction of the solar wind is also indicated (V_{SW}). Toivanen *et al.* (2017) showed that the resulting shape of the tether "is such that near the spacecraft, the roots of the main tethers form a cone, whereas towards the rim, this coning is flattened by the centrifugal force, and the sail is coplanar with the sail spin plane".
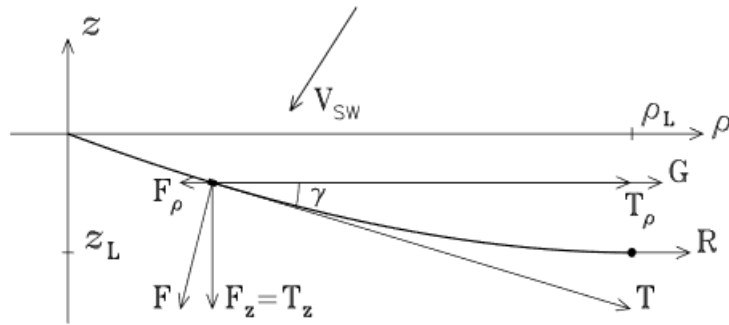
Figure 13: Forces applied on the tether. Electric sail tether (thick solid curve), remote unit (black dot). Toivanen et al. (2017).

Ashby (2010) identified the main performance index for a cylindrical shape material during tension as the ratio between the tensile strength and the material density. In fact, in order to minimise the weight, we need to maximise the tensile strength/density parameter. This can be clearly understood by noting that the stress σ on the wire is equal to the tensile load T divided by the cross sectional area A. The total weight of the tether w is the material's density ϱ multiplied by the length L and the cross sectional area A. By isolating the term A, we obtain:

$$w = \frac{\rho}{\sigma} \cdot T \cdot L.$$

This equation clearly shows that to minimise the total weight of the tether, the term σ/ϱ is to be maximised.

The tensile strength of the tether is therefore one of the main design drivers, since the thrust level is roughly proportional to the usable tensile strength per mass density of the tethers. The specific acceleration as a function of thrust at different tether's tensile strength has been estimated by Janhunen *et al.* (2010), as shown in Figure 14. The 10 MPa curve corresponds to ultrasonically bonded aluminium tether. 100 MPa has been selected as a representative value for carbon fibres and/or silicon carbide fibres, while 10 GPa for a hypothetical carbon nanotube tether. With a better material, having 100 MPa strength for instance, the available thrust would be ten times higher.
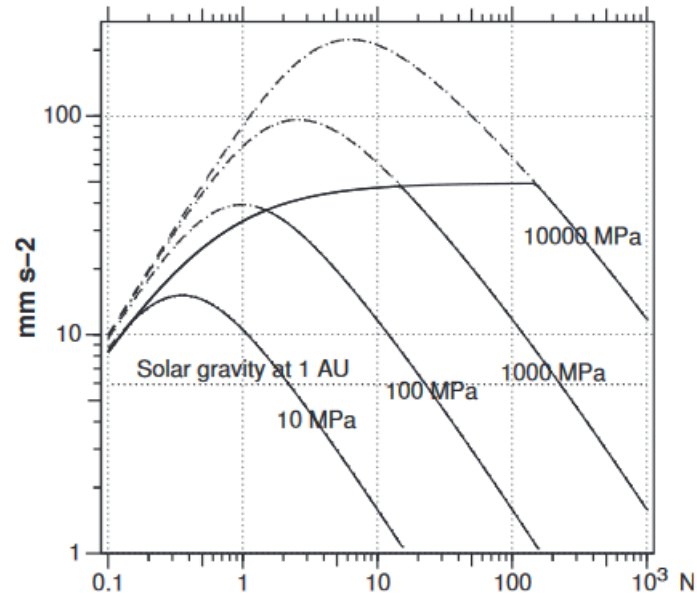
Figure 14: E-sail specific acceleration as function of thrust for four tether usable tensile strength values. Dashed lines are cases where the tether wire is thinner than 18 μm. A system base mass of 10 kg and a voltage of 30 kV are assumed. Dotted horizontal line gives the level of solar gravity at 1 au for reference (propulsion system reaching solar gravity acceleration are usually considered very good). Janhunen et al. (2010).

In the case of the Aalto-1 satellite, the tension of a 100 m long tether as a function of the angular velocity has been simulated, as shown in Figure 15 (Khurshid *et al.* (2012)). The maximum tension has been estimated at around 19 mN, for an angular velocity of almost 150°/s. The maximum tension point is estimated at 5.3 m length.
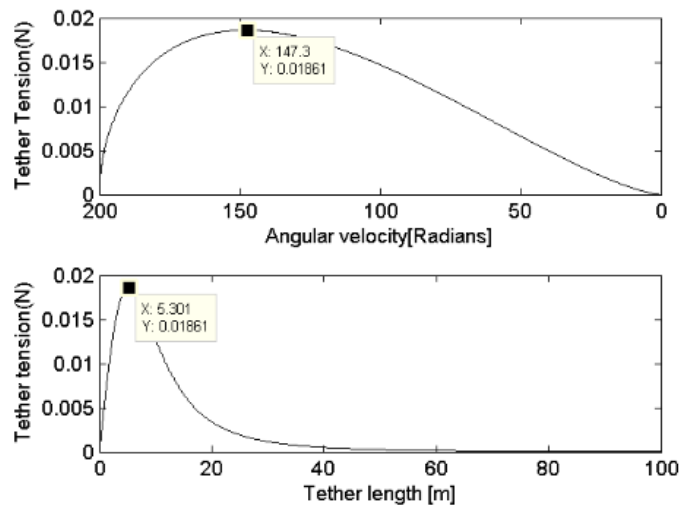
Figure 15: Tether tension as a function of the angular velocity and tether length for the Aalto-1 satellite. Khurshid et al. (2012).

As described by Toivanen *et al.* (2017), a tether voltage modulation is required for the maintenance of the sail attitude. For this reason, the tensile force is not constant over time, but it has a certain dynamic.

For instance, when flying through a planetary or moon eclipse, the tethers can undergo significant contraction and expansion due to temperature variation (Janhunen *et al.* (2015)). A maximum increase in tension of 0.7 g is foreseen during eclipse. The oscillations of the end-mass take place at a frequency lower than 0.1 Hz. An example of the dynamic behaviour of the tension is shown in Figure 16.
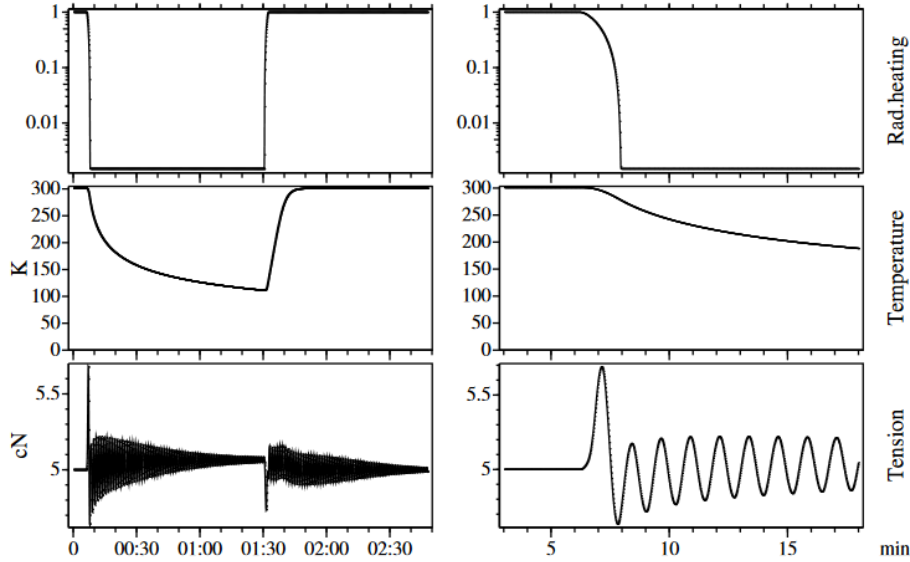
Figure 16: Relative radiative heating, tether temperature and tether tension as function of time in circular orbit round Mars and Deimos distance. The right panel shows details around the 10 minutes' mark from the even's start. Janhunen et al. (2015).

4.4. THERMAL EQUILIBRIUM AND THE A/E PARAMETER

In space, the only heat exchange mechanism is radiation. Depending on the distance from the Sun, the Earth and other planets and bodies, the thermal equilibrium of a spacecraft or component can be derived.

According to the Stefan-Boltzmann's law, the energy radiated from the surface of the Sun per unit area is equal to:

$$E_n = \sigma T^4 = 5.67 \cdot 10^{-8} \frac{W}{m^2 K^4} \cdot (5778\ K)^4 = 6.33 \cdot 10^7 W/m^2$$

where σ is the Stefan-Boltzmann constant (5.6696x10^{-8} W/(m²K⁴).

Since the surface of a sphere is 4πr², and the energy is conserved, the radiated flux per unit area at 1 au scales as r² and becomes 1367 W/m2 at 1 au (Figure 17):

$$S_0 = E_n^{Earth} = \frac{R_{Sun}^2}{R_{Earth}^2} \cdot E_n^{Sun} = \frac{(0.695 \times 10^9)^2}{(1.496 \times 10^{11})^2} \cdot 6.33 \times 10^7 = 1367 \frac{W}{m^2}$$

This calculation holds for the solar constant and a fixed distance of the Earth from the Sun. In reality, due to the Solar variations and the eccentricity of the orbit of the Earth, the solar irradiance changes with time at the Earth position.
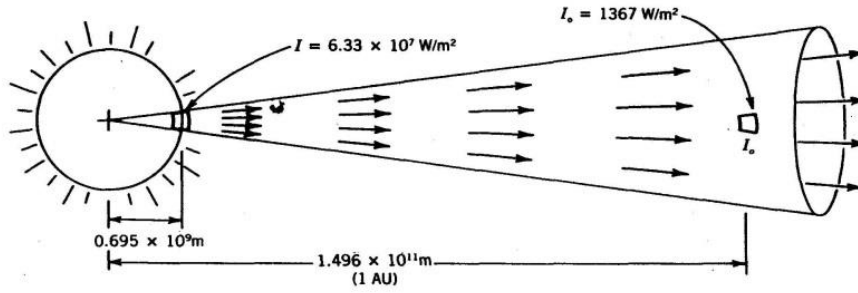
Figure 17: Radiated flux from the Sun (http://en.wikipedia.org/wiki/Solar_constant).

In thermal equilibrium, all the contributions to the energy balance are:

$$\dot{q}_{emitted} = \sum \dot{q}_{in} = \dot{q}_{solar} + \dot{q}_{internal} + \dot{q}_{aerodyn.} + \dot{q}_{albedo} + \dot{q}_{earth}$$

In thermal equilibrium, the power radiated by the tether is:

$$\dot{q}_{emitted} = \varepsilon \cdot \sigma \cdot A_{tether} \cdot (T_r^4 - T_0^4)$$

where

- ε is the emissivity; the hemispherical emissivity ε_H is generally considered, integrated in the range of frequencies 5-50 μm (corresponding to a black body with a temperature in the range -250 to 300 °C);
- A_{tether} is the radiating area of the surface, equal to the total surface area of the tether;
- T_0 is the temperature of background radiation (with radiating properties similar to a black-body radiating at 2.7 K).

For many applications, the temperature of the emitting body (in our case the tether) is much higher than 2.7 K, so we can discard the term T_0^4:

$$\dot{q}_{emitted} = \varepsilon \cdot \sigma \cdot A_{tether} \cdot (T_r^4)$$

The absorbed power from the Sun is:

$$\dot{q}_{solar} = S_0 \cdot A_a \cdot \alpha \cdot \cos \theta$$

where

- S_0 is the solar constant, 1367 W/m²;
- α is the absorbance; it is generally considered the solar absorbance, α_S, integrated in the range of frequencies 0.2-2.8 μm (covering 95% of solar spectrum);
- A_a is the area of the surface exposed to the Sun;
- θ is the angle of incidence (the angle between the surface normal and the direction of the Sun).

Considering the mass budget model produced by Janhunen *et al.* (2013) and reported in Figure 7, at 1 au the electron gun power is 720 W, the total tether length is 1.2 km and the total tether surface is

about 600 m^2. The resulting power per unit length in this case is 1.2 W/m^2. In general, $\dot{q}_{internal}$ is in the range of 1-2 W/m^2 and can be therefore discarded in this calculation.

In case the satellite is at a low altitude (e.g. in Low Earth Orbit, LEO), the thermal power generated due to aerodynamic drag $\dot{q}_{aerodyn.}$ shall be also considered.

$$\dot{q}_{aerodyn.} = 0.5 \cdot \rho \cdot A_{drag} \cdot \cos\gamma \cdot v_{drag}^3$$

where

- ρ is the atmosphere drag
- A$_{drag}$ is the area exposed to the air drag
- γ is the angle between the surface normal and the velocity vector
- v_{drag} is the speed of the satellite.

However, since the E-sail operates outside from the magnetosphere of the planets, this contribution is disregarded.

When the satellite is close to Earth, part of the solar irradiance is reflected back from the albedo of the Earth.

$$\dot{q}_{albedo} = (a) \cdot 1367 \frac{W}{m^2} \cdot \alpha \cdot A_{albedo} \cdot F \cdot \cos\beta$$

where

- a is the albedo of the Earth (this value ranges from 5 to 30 %)
- A_{albedo} is the area of the tether exposed to the albedo of the Earth
- F is the view factor from the Earth sphere to the tether (in LEO it is about 0.3)
- β is the angle between the position of the satellite with respect to the Earth and the position of the Sun (see Figure 18).
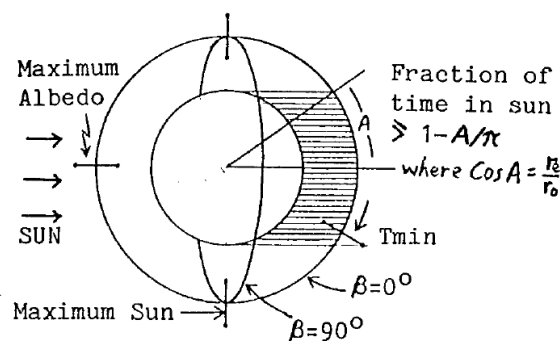
Inclination	β Range
0°	0–23.5^o
28.5^o	0–52°
>66.5^o	0–90°

(β = Sun out-of-plane angle)

Figure 18: Angle β for the tether. Cosmo et al. (1997).

The radiated flux from the Earth due to infrared radiation is:

$$\dot{q}_{earth} = \varepsilon_{earth} \cdot \sigma \cdot T_{Earth}^4 \cdot A_{Earth} \cdot F_{Earth-tether} = \varepsilon_{earth} \cdot \sigma \cdot T_{Earth}^4 \cdot A_{tether} \cdot F_{tether-Earth} =$$
$$\varepsilon_{Earth} \cdot 215 \frac{W}{m^2} \cdot A_{tether} \cdot F_{tether-Earth}$$

where

- ε_{earth} is the emissivity of the Earth
- A_{tether} is the area of the tether
- $F_{tether-Earth}$ is the view factor (0.5 in case of a flat surface, the Earth as seen from the spacecraft, and a sphere). In general, the following holds: $A_1 F_{1-2} = A_2 F_{2-1}$, where F_{1-2} is the view factor or the fraction of radiating energy which leaves the surface 1 and reaches the surface 2.
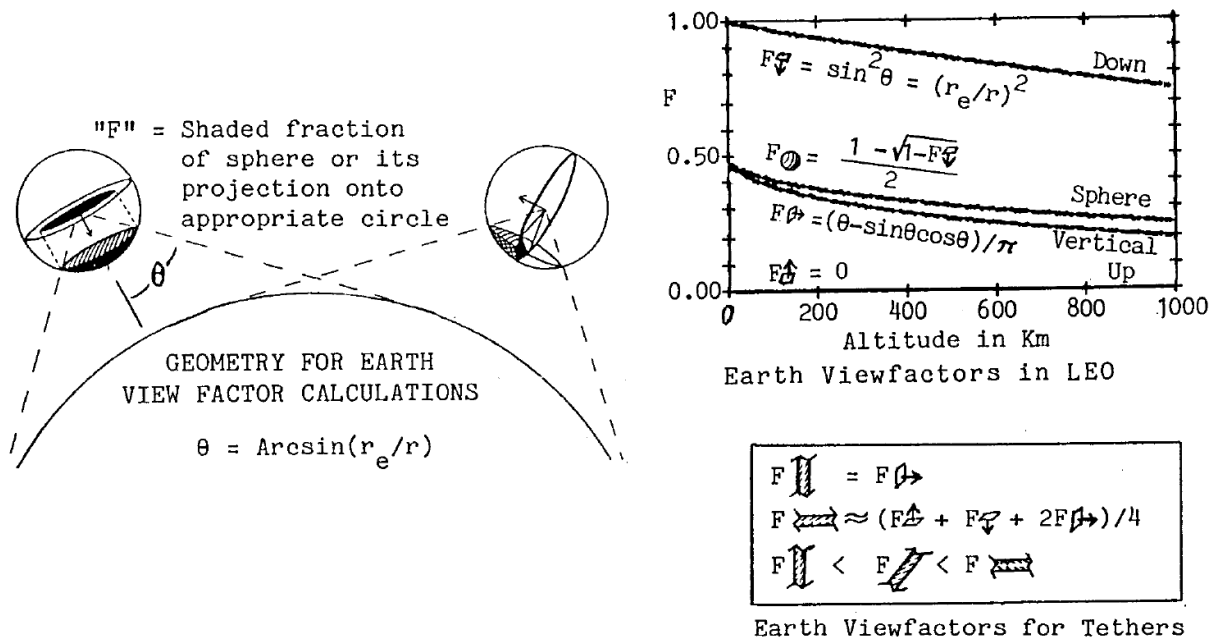
Figure 19: Tethers view factors. Cosmo et al. (1997).

We assume, discarding the other minor contributions, that:

$$\dot{q}_{emitted} = \dot{q}_{solar}$$

The equilibrium temperature in this case becomes:

$$T = \sqrt[4]{\frac{\alpha}{\varepsilon} \times \frac{A_\alpha \times cos\vartheta}{A_\varepsilon} \times \frac{S_0}{\sigma}} = \sqrt[4]{\frac{\alpha}{\varepsilon} \times \frac{1}{\pi} \times \frac{S_0}{\sigma}}$$

Based on the above equation, the final equilibrium temperature of the tether with a certain geometry depends on the term $\frac{\alpha}{\varepsilon}$, which is mainly dependent on the surface and/or the coating material. It is important to note also that generally the ratio $\frac{\alpha}{\varepsilon} = \frac{\alpha_S}{\varepsilon_H}$ is considered, where α_S is measured over the optical spectrum and ε_H over the infrared spectrum. Moreover, the above function is valid in the

36

simplified case of a cylinder-shape tether and with the angle between the tether wire direction and sun direction being 90°. We can refer to this as the worst case, providing the maximum equilibrium temperature, considering also that the loop wires are all in view of the Sun.

However, in the case of the E-sail heyether, $\frac{A_{tether}}{A_\varepsilon}$ is different. In order to calculate the area of the tether A_{tether}, we consider a portion of the tether of length L. Considering the simplified geometry shown in Figure 20, the external area is:

$$A = L \cdot \left(\pi \cdot 2 \cdot r_{base_{wire}}\right) + 3 \cdot \frac{\pi}{2} \cdot L \cdot \left(\pi \cdot 2 \cdot r_{loop_{wire}}\right) = L \cdot (\pi \cdot 50 \ \mu m) + 3 \cdot \frac{\pi}{2} \cdot L \cdot (\pi \cdot 25 \ um) = L \cdot 510 \ \mu m$$

So the final area of the tether is:

$$A_{tether} = L_{tether} \cdot 510 \ \mu m$$

where L_{tether} is the length of one tether.
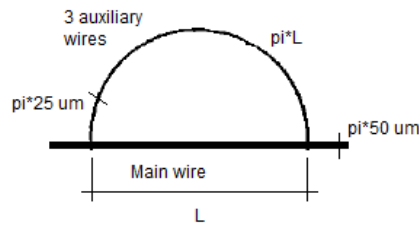
Figure 20: Schematic of a heytether single-loop.

The black body temperature as a function of the distance from the Sun is reported in Figure 21.
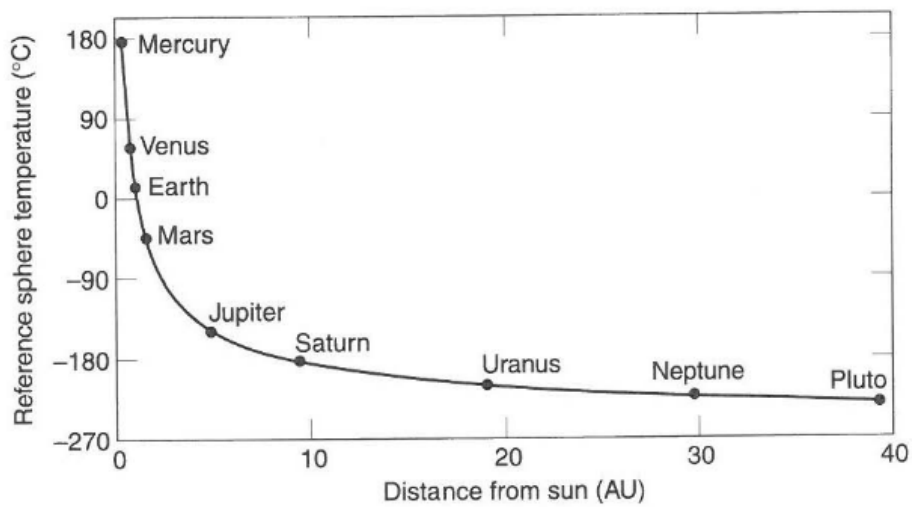
Figure 21: Black body temperature according to its distance from the Sun (ignoring planet albedo). Gilmore (2002).

The equilibrium temperature has been plotted as a function of the Sun distance and for different α/ε ratios, as shown in Figure 22. The influence of the planets is not considered in the plot. The tether's thermal equilibrium is reported in Janhunen *et al.* (2015).
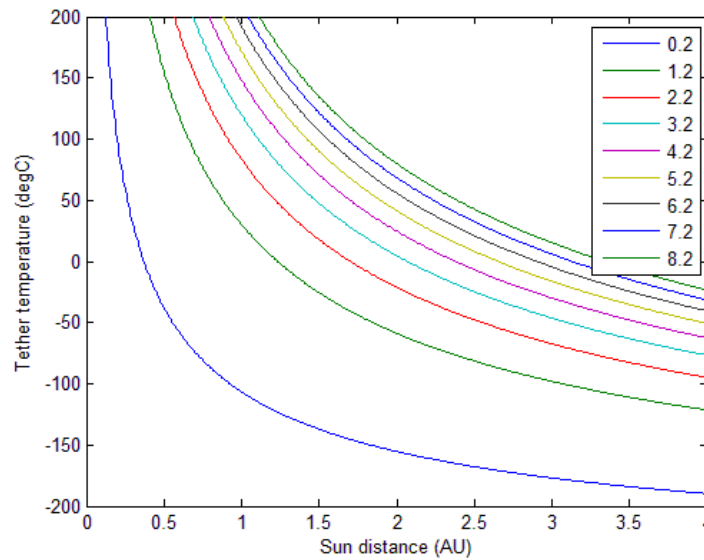
Figure 22: Equilibrium temperature plotted as a function of the Sun distance for different a/ε ratios.

4.5. TETHER MATERIAL OPTIONS

We can make a first down-selection of material options based on the UV radiation and electrical resistivity properties. To this end, a plot was produced using the software database *CES EduPack 2013 by Granta© Design Limited* with the Level 3 aerospace database.

In the graph below (Figure 23), we see a comparison between the properties of the fibres included in the Level 3 CES aerospace database and the properties of aluminium and stainless steel. Organic fibres are generally not vacuum compatible and are prone to degradation due to UV exposure. Therefore, they have been discarded from the plot. Other material options, not included in the CES database, are discussed afterwards.
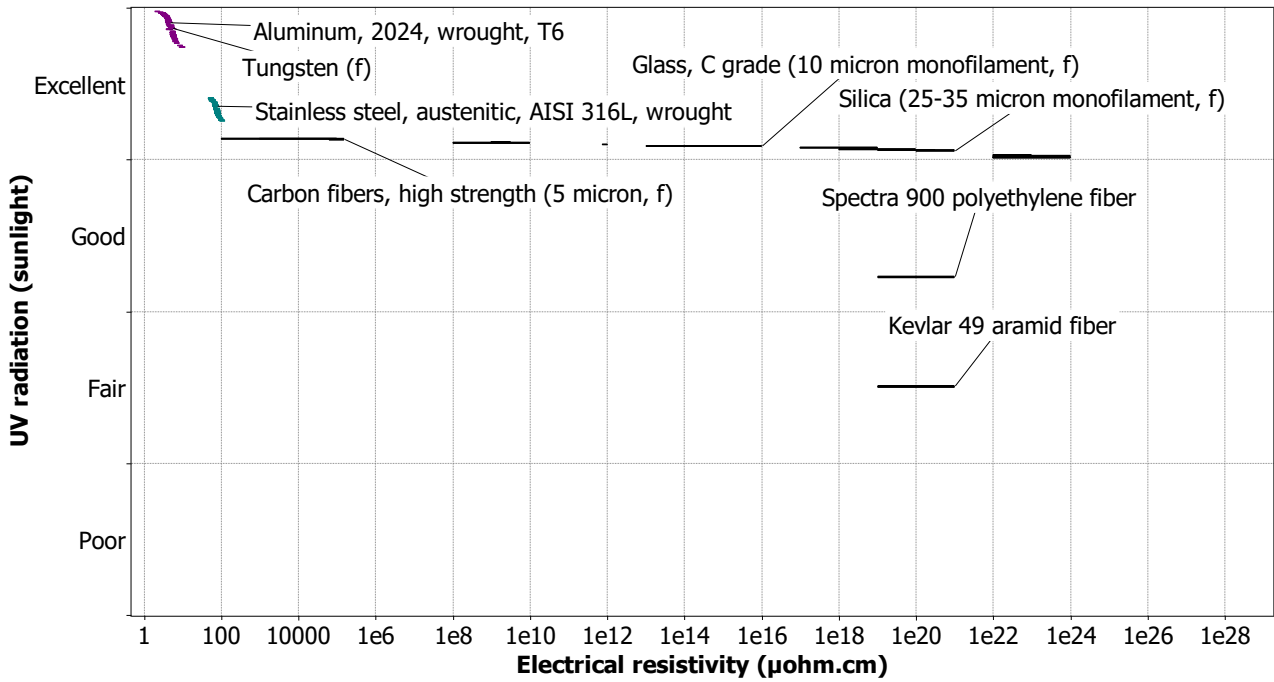
Figure 23: Comparison of the UV resistance and electrical resistivity of fibres includes in the Level 3 CES aerospace database with the aluminium and stainless steel.

At first sight, some synthetic fibres, such as Honeywell Spectra® polyethylene fibre (similar to the Dyneema fibre) and the Kevlar, have both UV radiation and electrical resistivity much lower than aluminium. For this reason, in space these materials are protected by UV radiation with coatings, as discussed in the following paragraph.

By using the parameter tensile strength/density, we made another comparison among materials. In Figure 24, we can see that all materials above the line have a better ratio of tensile strength over mass density compared to the materials below the line. Carbon fibres have the best performance in this respect. Other plots showed that aluminium with 99 % purity, even if not among the best materials, is clearly better than gold, platinum and silver with commercial purity.
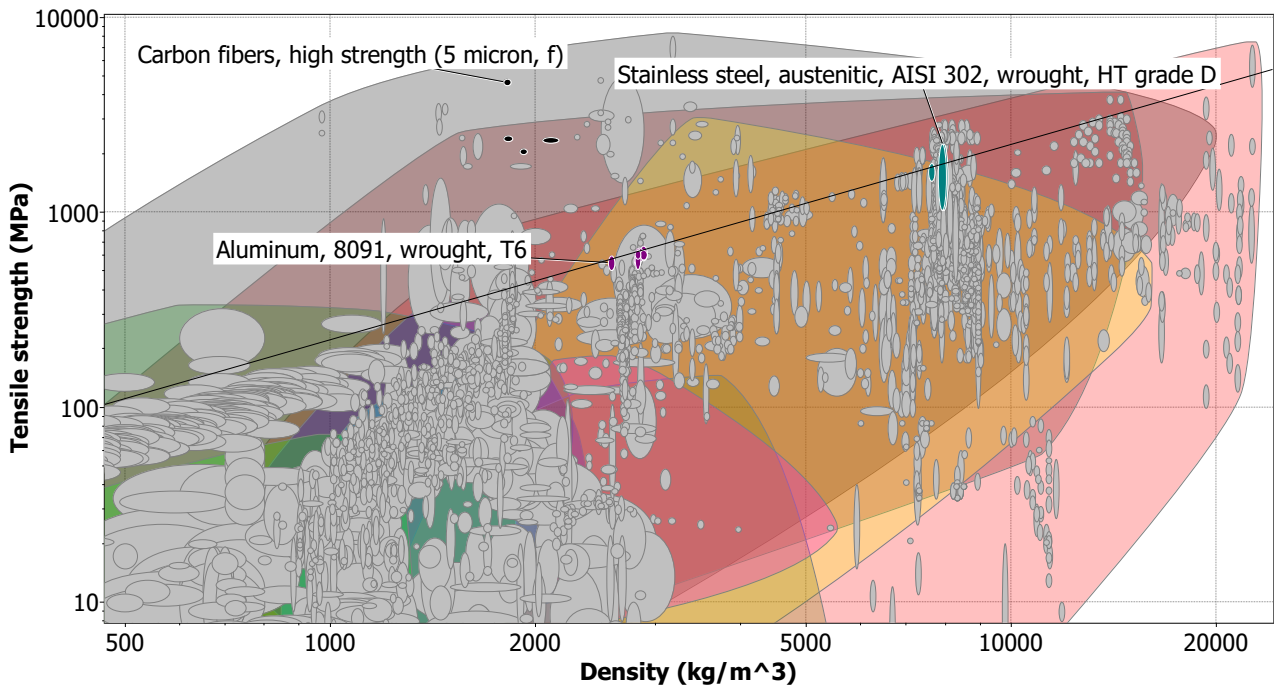
Figure 24: Tensile strength vs density for different materials.

If we limit our observation to only the carbon fibres and the best performing metals, we obtain the chart in Figure 25.
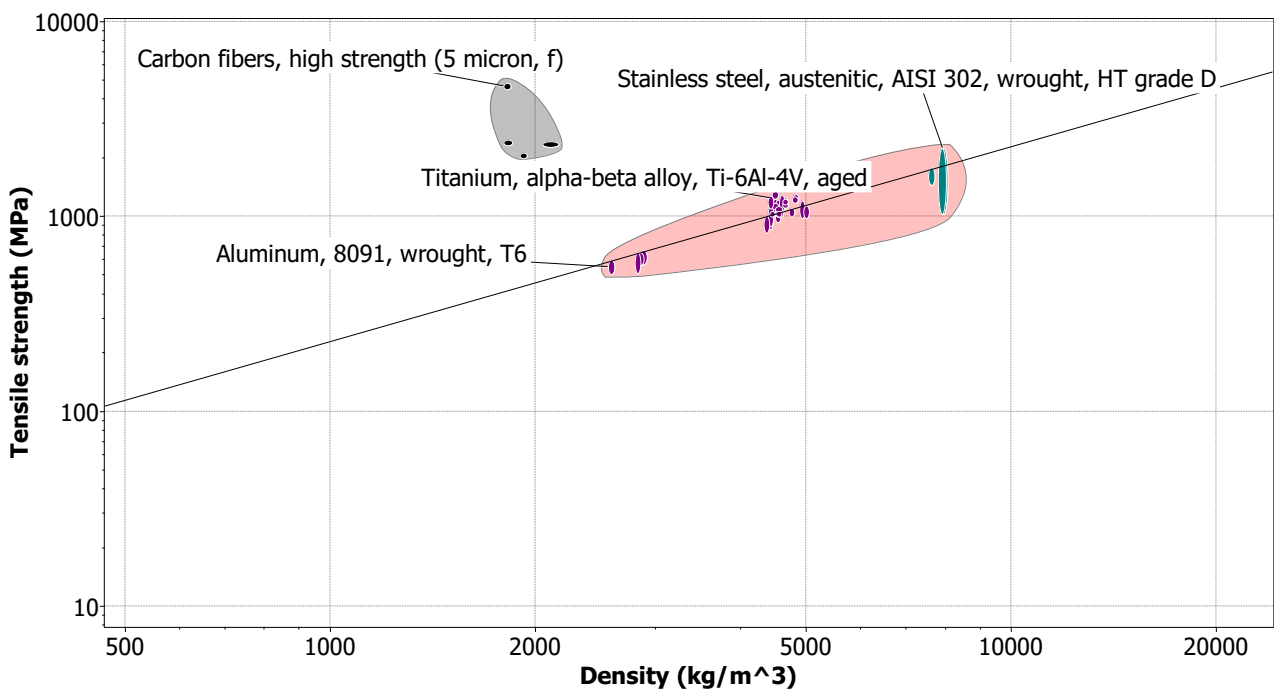
Figure 25: Tensile strength vs density for materials above the threshold line.

In our analysis, Titanium and steel are discarded because they are not bondable. Bonding is necessary to create multi-wire structure and to increase micrometeoroids resistance. Even if techniques are under study, these materials are considered at present to be not enough advanced to ensure bonding with both good mechanical and good electrical properties (Fischer *et al.* (2012)).

In general, metal wires can be good candidates since they are conductive, UV resistant and vacuum compatible. However, it is also important to assess the impact of thermal treatments on the metals (e.g. the dimension of the grains has an impact on the mechanical behaviour).

Synthetic fibres could be good candidates if electrical conductivity is not a requirement. Kapton has been selected in the ESAIL FP7 project for the auxiliary tethers in the form of sheets (Polkko (2012)). However, for conductive tethers, the use of Kapton has been excluded several years ago following some observations (wire damages and short circuits, arc-tracking/flashover) of in-orbit use by the NASA (Van Laak (1994)). NASA Head Quarter recommends not using any Kapton wire for any power circuit due to risks of arc tracking (transformation of plastic material from non-conductive to conductive through a process of surface degradation).

In the *Tethers in Space Handbook* (Cosmo *et al.* (1997)) aluminium is considered as the main choice for the material of the electrodynamic tether.

Interesting information related to the tether's material selection can be found in the frame of the MXER project (Sorensen (2001)). The MXER is a momentum exchange tether which has been studied to propel spacecraft from Low Earth Orbit (LEO) to Geostationary Transfer Orbit (GTO). Even if some of the requirements are not in common with those of the tether's material of the E-sail technology, we report here some considerations which could be of interest. The MXER project (Sorensen (2003)) identifies several organic and synthetic materials for the tether, such as Spectra 2000, Zylon and Kevlar. The report assumes that the core tether would need to be coated to protect the surface from Atomic Oxygen bombardment in LEO. Some portions of the tether could contain aluminium or another metal with the objective to establish a potential difference across the wire. The main figure of merit considered is once again the specific tensile strength (tensile strength/material density). Moreover, the tether would be configured in a multi-strand, cross-linking configuration to reduce the risk of failure due to micrometeoroids impacts. Figure 26 reports the properties for the materials selected in the study.

Material	Tensile Strength (GPa)	Material Density (kg/m³)	Characteristic velocity (m/s)	
			safety factor = 2	safety factor = 3
UHMWPE (Spectra 2000)	3.5	970	1900	1550
PBO (Zylon)	5.8	1540	1940	1580
current PIPD (M5)	5.3	1700	1770	1440
anticipated PIPD (M5)	9.5	1700	2360	1930
Kevlar	2.76	1440	1380	1130

Figure 26: Tensile strength and material density for the tether material selected in the MXER project. Sorensen (2003).

Steel is also used for space tethers, as it can be produced in very thin wires. For example, the Nitronic 50 (AK steel) by *Alloy Wire International Ltd*[2] can be produced in 25 μm diameter-wide wires. The Japanese project Kounotori, for instance, embeds 700 m long magnetic tether made of aluminium strands and steel wire developed thanks to the fishnet know-how (*BBC.com* (2016)). A thin coating was also used as lubricant (*Spaceflightnow.com* (2016)).

However, steel's density is about three times higher than aluminium's, which implies that the total weight of the tethers is three times higher as well. This could be reflected also in a heavier weight of the tether reels and auxiliary units, and therefore of the whole E-sail structure. Steel could also provide good stability at a broader range of temperatures (-200 °C to +300 °C). However, ultrasonic bonding capabilities are poor. Therefore, alternative solutions for multi-wires structures should be found to protect from micrometeoroid impact.

The NASA HERTS project made a down-selection of materials and decided to investigate two other options: Amberstrand wires and Miralon® yarns (Wiegmann (2015)). Their properties are compared to the ones of aluminium and copper in Figure 27.

	Amberstrand		CNT yarn		Aluminum	Copper
Filament count, or wire size	66	166	1	4	35 ga	35ga
Diameter (μm)	230	370			142	142
Linear mass (g/km)	56	140	10	24	43	142
Each Wire length (km)	5	5	5	5	5	5
Wire mass (g)	280	700	50	120	260	860
Wire Strength (N)	41	105	15.00	36.00	1.96	8.04
Estimated material cost ($/km)	1300	1704	10000	25000	600	800
Est. Packed Volume @ 10 wires (cc)	140	350	125	300	961	961
Resistivity (ohms/m)	9	3	160	70	1.77	1.08

Figure 27: Down-selection of tether materials by the HERTS project. Wiegmann (2015).

Miralon® yarns[3] are carbon nanotube (CNT) wires produced by *Nanocomp Technologies Inc*. It is composed of aligned bundles of CNTs with diameter of hundreds of microns and length in the order of millimetres. Miralon® is commercially sold as a single ply yarn with a dimeter of 130 μm (A-series) or as a 4-ply high strength yarn (C-series). As an example, CNT yarns are considered as reinforcement fibres for pressure vessels by Kim *et al.* (2016).

The AmberStrand® fibre, produced by *Syscom Advanced Materials*, has been also considered by NASA for the E-sail technology. It is made by an inner Zylon® fibre core, with high strength, and a conductive metal outside layer. The outer layer can be metallised with copper, nickel or silver. Two types are commercially available, depending on the number of filaments. The 166-filaments type has a diameter of 246 μm. and the tensile strength is 5.8 GPa.

From our calculations, Miralon® CNT (A-series) and Amberstrand 166 and have different tensile strength (0.318 and 5.8 GPa respectively) and linear density (0.01 and 0.159 g/m respectively).

However, their specific tensile strength is comparable – 31.8 GPa·m/g for Miralon® CNT (A-series) and 36.47 GPa·m/g for Amberstrand 166.

The baseline material for NASA is a 32 μm gauge wire, 16500 meter-long made by Amberstrand. However, NASA is also considering the use of graphene materials developed by Manchester University (*Nextbigfuture.com* (2016)).

Kashihara *et al.* (2008) recommended to choose synthetic fibres with high conductivity as reinforcing material, with no insulating coating on the surface. This would reduce the risks of arching at triple junctions.

A very long term option for the tethers material could be using superconducting wires. This option has been discussed in Cosmo *et al.* (1997). However, to achieve superconducting temperatures, the wire should be housed in a tube with flowing supercooled (2° K) helium. The tube should be insulated and capped at each end with a refrigeration system.

4.6. TETHER COATINGS

4.6.1. Coating requirements

The performance of E-sail tethers can be significantly improved by coating the bulk material, as discussed in our recently published paper (Hassan *et al.* (2017)). The main aims are to increase the absorbance and/or the emissivity depending on the mission, reducing the risk of cold welding during launch, increasing the diffusive reflectance for optical visibility purposes. Moreover, the resistance to the harsh environment of space, such as UV radiation and atomic oxygen bombardment, is a desired feature. Indeed, synergic or separate interactions in the harsh aerospace environment can provoke corrosion, erosion, structure modification and surface roughening, thus degrading the optical, thermal, electrical and mechanical properties of the tethers. An approach to mitigate these effects for different types of tethers and external spacecraft parts consists of applying thin film coatings.

Considering the state of the art of the heytether design and production process, the main requirements for the coating could be divided between requirements related to the coating properties and requirements related to production issues. The latter are described in the following paragraph.

The tether coating requirements, also studied in the frame of the ESAIL FP7 project, are listed below and briefly discussed.

- Space environment compatibility. The coating should be space compatible. Generally, this requirement of vacuum compatibility can be considered fulfilled for coatings produced with PVD, ALD, CVD and other processes involving the use of low pressure. In the Low Earth Orbit (LEO) there is a heavy presence of atomic oxygen particles (AO). This would quickly imply the copper or aluminium wire strands to oxidise if the wires were left bare, without any coating. Following this oxidation, the capability of the tether to interact with the surrounding plasma would decrease substantially (Johnson *et al.* (2003)). Several studies have been carried out also by NASA (Gittemeier *et al.* (2005)) to investigate the effects of AO bombardment and UV radiation on coated tether materials in LEO.
- Bombardment of tether by 20 - 40 keV electrons. The coating has to resist possible wearing and material degradation caused by the E-sail specific electron bombardment.

- Tailored α/ε ratio (depending on the space mission target). In space, the only heat exchange mechanism is radiation. Therefore, the main contributions to the thermal equilibrium of a tether are the absorbed power from the Sun, function of the absorbance α, and the radiated power by the tether, which is a function of the emissivity of the surface ε. Given the distance from the Sun, the Earth and other planets and bodies, the final equilibrium temperature of the tether with certain geometry depends on the term $\sqrt[4]{(α/ε)}$, which is associated with the coating material. For this purpose, α is generally measured over the visible spectrum and ε over the infrared spectrum. Assuming a constant value of the emissivity, higher absorbance coatings may be chosen for missions to the outer solar system, where the equilibrium temperature needs to be higher, while coatings with lower values of the α/ε coefficient are to be selected for missions closer to the Sun (Hassan *et al.* (2017)). According to Cooke et al. (1961), ideally the tether coating shall have low α/ε ratio in the vicinity of the Earth. The authors point out that pure aluminium oxide is transparent to radiation in the visible region and that polished aluminium is a good reflector. For these reasons, α should be 0.1 and ε 0.9, with a ratio of 0.11.

- Avoid cold welding. The coating shall minimise the risk of cold welding, e.g. by providing low surface roughness and low friction. Cold welding could happen among the spool wires due to vibrations during launch. This issue has been analysed in the frame of the ESAIL FP7 project and it is discussed in one of the project reports (Rauhala *et al.* (2013)). A test aimed at measuring the force needed to pull the wire was conducted using a load cell. Since the wire was coated, the strength of the adhesion between the spool turns varied as it was unspooled. The force was ranging between 2 mN and 14 mN. Depending on the type of material and the coating to be selected, such test should be repeated in order to verify that the adhesion between the wire loops does not exceed the breaking load of the tether's material. In general, prevention of cold welding (low roughness) and high IR emissivity (high roughness) are contrasting requirements (Wen *et al.* (2006)).

- Highly diffusive. In order to improve the visibility from the optical cameras, the coating shall preferably be highly diffusive in the optic frequencies.

- Low thickness. The thickness shall be big enough for the optical properties of bare Al to be modified but as little as possible in order to minimise the total weight. In case the coating is isolating, the maximum thickness which allows the collection of electrons from the solar wind shall be estimated and considered (1 μm is a first estimate by P. Janhunen). Such dimensional constraint has in turn an impact on the selection of the coating material, since the emissivity of a thin film changes below a critical thickness level, in the order of tens or hundreds of nanometres depending on the material (Hassan *et al.* (2017)).

- Preferably low resistivity. Electrical resistivity of the coating is also a parameter of great importance for E-sail tethers. In order to facilitate the collection of electrons from the solar wind and reduce the risk of sparks due to charge build-up, the electrical resistivity should be minimised (Hassan *et al.* (2017)). Moreover, an insulating coating should be applied to the first portion of the tether for safety reasons, namely to avoid high voltage close to other parts of the spacecraft. Therefore, the resistivity requirements for this coating are higher than for the remaining part of the tether.

- Good aluminium/coating compatibility. The coating shall have good adhesion with Aluminium and a thermal expansion similar to the one of bare Aluminium. Each coating should also sustain thermal cycling, especially in the case of eclipse crossing, and thermal variations due to differences in thermal expansion between the tether material and the coating material. Such assessments have not been carried out in the frame of this study, but are not to be disregarded.

To improve the optical characteristics of the material, the concept of the double surface is frequently used in space. For example, in the case of aluminium coated with aluminium oxide, the oxide coating, having a sufficient thickness, would be opaque in the infrared wavelengths, while the substrate would reflect the solar radiation. Therefore, this double surface would emit as gross aluminium oxide in the infrared region, while reflecting in the optical region as bare aluminium. This concept relies on the presence of a sufficiently thick oxide layer, which could be afforded in most situations and for simple flat surfaces. An example of a coating of this type can be found in Kiomarsipour *et al.* (2013). However, for the case of the E-sail tether, an oxide coating with thicknesses in the µm range would not be affordable. For a coating in the nanometre range, it is much harder to use double surface effects, since emissivity is strongly affected by the coating's thickness (Edalatpour *et al.* (2013)).

The dimension requirement represents a real challenge in the choice of a coating with double surface effect such as the one described above. Edalatpour *et al.* (2013) explain that "only a small portion of volume below the emitting surface contributes significantly to the emitted spectrum; this small portion is defined as the critical thickness. The emissivity of a film with a thickness equal or greater than the critical thickness is referred to as the bulk emissivity. If the emitting medium is thinner than the critical thickness, the concept of emissivity, as defined in the classical theory of thermal radiation, is not valid anymore". This direct model, based on Maxwell's equations and fluctuational electrodynamics, leads to a simple closed-form expression for computing the thickness-dependent emissivity of films. For each material, the variation of emissivity against film thickness is calculated and the critical thickness above which no size effect is observed is determined. An approximate expression is then proposed for determining the critical thickness without performing extensive computations.
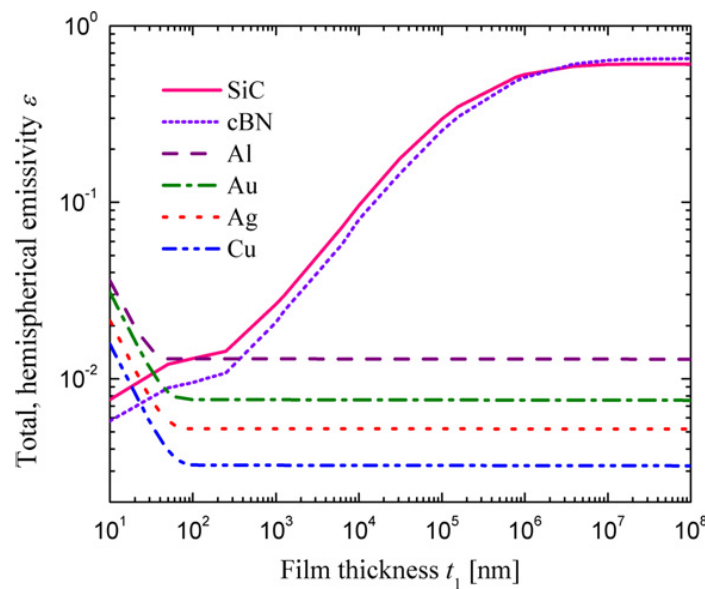
Figure 28: Total hemispherical emissivity of various materials as a function of the film thickness. Edalatpour et al. *(2013).*

In Figure 29 we can see why a thick film has a different impact compared to a thin film. For dielectric coatings, it is therefore recommended to increase the thickness of the coating in order to obtain a

higher emissivity. On the contrary, a very thin (few nm) metal layer could be used to obtain high emissivity.

The critical thickness can be approximated as

$$t_{cr}^* = -\ln(Ac)\, \delta_\lambda$$

where A_c is the desired accuracy and $\delta_\lambda = \bar{\lambda}/4\pi\kappa$.

The explanation of this phenomenon, provided by Edalatpour *et al.* (2013), is the following: "the emissivity of metals increases as the film thickness decreases because of the supplementary contribution of waves experiencing multiple reflections at the film interfaces." For dielectrics, the contribution from waves experiencing multiple reflections exists in both thin and thick films and is nearly unaffected by the size of the layer. Moreover, "the waves emitted by the extraneous source volume within a thicker film are not significantly attenuated in dielectrics, such that they have a strong effect on the emissivity. As a consequence, the emissivity of dielectric films is a pure volumetric phenomenon".
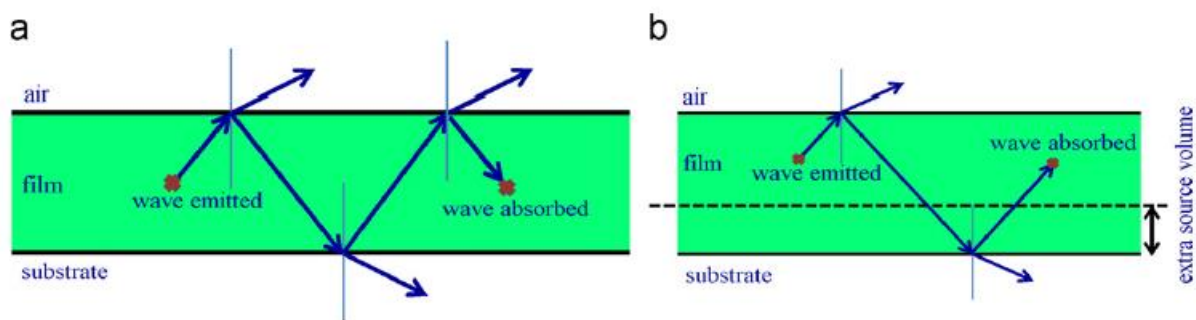
Figure 29: Wave propagation in a thin film (a) and in a thick film (b). Edalatpour et al. *(2013)*

4.6.2. Previous studies on tether coatings

A summary of the research carried out so far on tether coating is presented hereafter.

The final configuration of the MAST tether experiment, launched in 2007 (Hoyt *et al.* (2007)), was a Hoytether consisting of three lines coated with Triton Oxygen Resistant (TOR) polymer. The coating increased the tether mass by 2%.

Similar studies have been conducted by NASA in preparation to the Propulsive Small Expendable Deployer System (ProSEDS) mission. The mission is an on-orbit demonstration of the propulsion capabilities of electrodynamic tethers in space. The objective was to obtain a coating with a higher absorbance/emissivity ratio than bare aluminium, while preserving the ability of the tether to collect electrons. The Conductive-Colorless Oxygen Resistant (C-COR) polymer coating provided a ratio of 1.14 (Curtis *et al.* (2002)). This technology is covered by patent (Johnson *et al.* (2003)). The project also investigated the possibility to use an insulating AO resistant polymer coating, the TOR-BP (Vaughn *et al.* (2000)).

Lennhoff *et al.* (1999) report a characterisation of the COR polymer (Figure 30). A coating with thickness 25.4 μm presented a solar absorbance of 0.3 and a thermal emittance of 0.8, providing an

overall value of α/ɛ of 0.375. The coating thickness, however, is too high for the E-sail technology, as it would be in the same order of magnitude of the wire diameter.

Tensile strength	12 ksi
Modulus	300 ksi
Elongation	90%
Density	1.35 g cm^3
Solar absorptance	0.086
Thermal emittance	0.63
Glass transition	226 °C
AO reactivity (cm^3 per AO)	0.3×10^{-24}
UV stability	Moderate

Figure 30: Properties of the COR polymer. Lennhoff et al. (1999).

Other tether coating options were investigated by McCandless *et al.* (2005) in the frame of the MXER project to improve the surface properties of Zylon PBO. The coating was composed by an Aluminium layer, providing the high reflectivity needed to decrease the α/ɛ ratio, and an Al_2O_3 top layer providing protection from AO and UV present in LEO.

Other coating materials, such as VO_2 (Chen *et al.* (2012)) and LCSMO (Perovskitemanganese oxides) (Fan *et al.* (2013)), are temperature sensitive and are used to tune the emissivity of spacecraft surfaces. A patent has been filed on this concept by the Boeing company in 2006 (Cumberland *et al.* (2006)).

Frequency selective surfaces can be also produced with lithographic processes (Paul *et al.* (2001)), but they are not addressed in this study as they are believed to have production costs too high for the E-sail technology.

Finally, studies have been carried out to assess the feasibility of the use of a low-work function coating material, e.g. calcium aluminate C12A7 electride, to be used in a portion of the tether with the objective to eliminate, or reduce, the need of a cathode (Williams *et al.* (2012), Chen (2015)).

4.6.3. E-sail coating production constraints

Assuming that a coating for the E-sail tether would make use of the "tether factory" developed in the frame of the ESAIL FP7 project, some additional requirements related to production constraints should also be considered.

- Process and coating not harmful. Danger for operators should be avoided.
- Process compatible with the ESAIL "tether factory". Since the good functionality of the tether factory is already proven, the coating process should complement the heytether production process. For this purpose, there are three options: (a) coating of the aluminium wires before integration in the tether factory (in this case the tether shall be compatible with the ultrasonic bonding process); (b) coating of the entire heytether in-line with the tether factory; (c) coating of an entire heytether reel after the production of the reel with the tether factory. After a first attempt of Al_2O_3 ALD coating deposition, a sticking problem was experienced during unreel (Rauhala *et al.* (2013)). For

this reason, a coating method performed in line with the tether production is preferable. Roll-to-roll processes would be the preferred option in this respect.

- Fast coating speed. The speed of the coating process is a key parameter, as the quantity of tether to be produced for a single spacecraft could be significant (20 km x 20 tethers = 400 km). Moreover, since the speed of the ESAIL tether factory is 5 m/h, the coating speed should preferably be higher than this value.
- Cheap process. The cost of the coating process should be an important element of consideration in the selection of the technology.
- Handling. Handling of the tether should be minimised in order to reduce the damage to the tether during the production process.
- Process temperature. Process temperature should be such that it does not damage the tether material. A temperature lower than 150 °C would be preferable.

Oxides such as alumina, titania, magnesium oxide, zirconium oxide and nitrides, such as AlN, deposited using Physical Vapour Deposition (PVD) processes or Atomic Layer Deposition (ALD) techniques, have good adhesion to aluminium and could be considered as options, depending on the desired α/ε ratio. However, PVD processes are highly directional and obtaining a homogeneous coating on the cylindrical surface of the tether is not trivial.

Roll-to-roll processes exist for PVD and for the ALD technology. One example of roll-to-roll ALD system is the Beneq WCS 500. Assuming a deposition speed of 2 m/min for Al_2O_3, producing 300 nm coating would require a speed of 10 m/h, which would be compliant with the speed requirement.

Ambient pressure Chemical Vapour Deposition (CVD) is suitable for Al2O3 and TiO2 but the production temperature is too high (> 400 °C) and it is therefore discarded.

Electrolytic processes such as anodisation could be also considered as an option (Diggle *et al.* (1969)). In this case, a barrier type anodisation layer could be produced, instead of the thick and porous anodisation layer more widely used. The film is thin and compact, and can be produced quickly. The thickness depends on the applied potential (about 14 Å/V). The bath solution is very weakly acidic of neutral. This coating can be produced with a reel to reel process, in line, for example, with the ESAIL tether factory. The tether would pass in the electrolyte bath where also the anode and the cathode are present. In general, 1 km tether weighs 11 g, therefore its weight could be too low to be completely immersed in a bath, since the material would tend to float on the electrolyte bath. In this case, reels would be required to hold the tether in place during the anodisation. Three options could be considered in this case (Figure 31). The martin black is a special proprietary type of anodisation process, widely used for space applications.

a) Tether floating on the electrolyte bath	b) Use of pump for liquid recirculation	c) Reel immersed in the bath to hold the tether
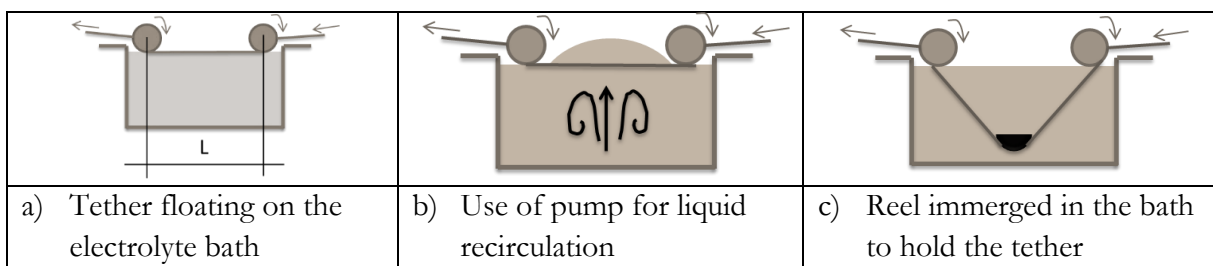
Figure 31: Options for a potential electrolyte bath for tether anodisation.

5. E-SAIL TETHER CHARACTERISTICS

5.1. SUMMARY

In this chapter, the E-sail features are analysed in depth. First, the material selected for the E-sail heytether (Al-1%Si) is presented. Then, we go through a literature review of the characteristics of the material. Furthermore, the results of an experimental activity aiming at studying the tether microstructure and its electrical resistivity are reported. Finally, the four coatings produced in the frame of this study (Al_2O_3, TiO_2, ZnO and TiZnO) are described and the results of scanning electron microscope observations are presented.

5.2. AL-1%SI WIRE SELECTED IN THE ESAIL PROJECT

Based on the above discussed requirements, the ESAIL FP7 project selected both the material of the tether and its structure. The selected configuration is named heytether. The heytether is a 4-wire tether made of aluminium (99% Al, 1% Si) wires with a diameter of 25 or 50 µm.

The 4-wire heytether is provided with a main wire (50 µm diameter) to which 3 wires are attached via ultrasonic bonding (25 µm diameter each) (Figure 32). The distance between single bonds is 10 mm, the loop length is 30 mm and the loop height is between 5 and 30 mm (Seppänen (2013)). The total thickness of the heytether should be higher than 2 cm, but should present the lowest surface area in order to minimise the collection of electrons from the solar wind.
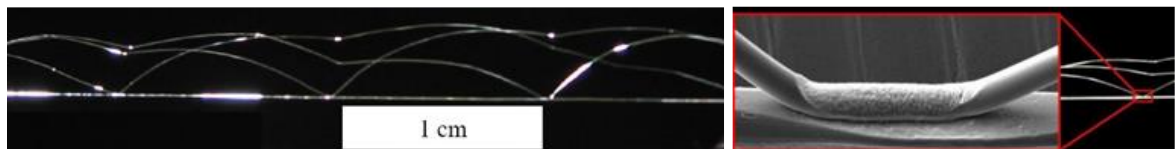
Figure 32: 4-wire tether (left) and bonding detail (right).

In reality, 50 mN are to be sustained by the base wire, since the loop wires are only for redundancy reasons and they are not stretched. Of course, should the base wire be broken by a micrometeoroid, the loop wires need to take over.

More precisely, the material selected for the tether in the frame of the ESAIL FP7 project was Al-1%Si TABN 32 µm produced by *TANAKA ELECTRONICS SINGAPORE Pte. Ltd.* A small amount of nickel was added to the alloy for better corrosion resistance. Without nickel doping, the material was scheduled for obsolescence. Al-1%Si is typically used for wire bonding in electronics, such as for radiofrequency power amplifiers. This material is therefore studies by electronic engineers. (Danaher *et al.* (2011)).

The production of the ESAIL heytether from the single Al wires is performed by a dedicated device, the "tether factory", shown in Figure 33, which is mainly responsible for the ultrasonic bonding process (Seppänen *et al.* (2011)). A 1 km wire has been produced (Seppänen *et al.* (2013)).
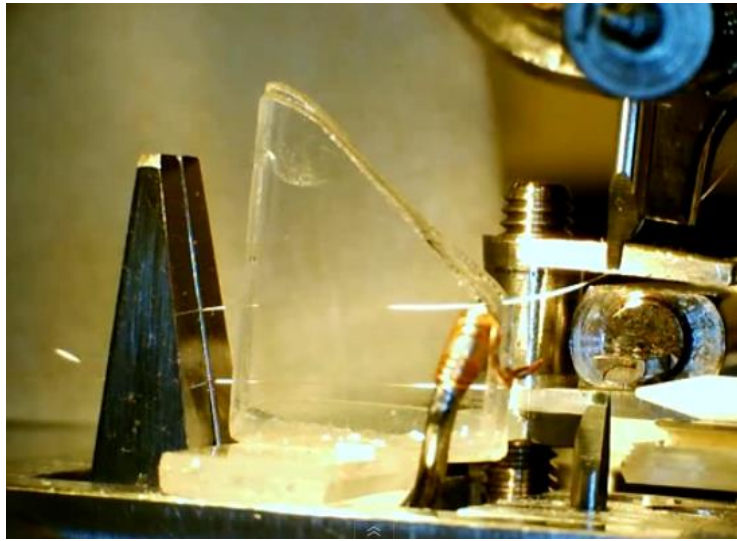
Figure 33: Image of the "tether factory". Seppänen et al. (2013).

From the datasheet it results that the exact composition of the alloy is: Aluminium 98.995 wt% + Silicon 1 wt% + Nickel 0.005 wt% (*TANAKA* (2015)). The exact chemical formula is Al-1%Si-0.005%Ni. The CAS No.: 7429-90-5 (Al), 7440-21-3 (Si), 7440-02-0 (Ni). Melting points: 660.4 °C (Al), 1410 °C (Si), 1453 °C (Ni).

The production process of the alloy is described in Figure 34. The raw material, after fine drawing, undergoes annealing at an unknown temperature (proprietary information of the manufacturer). The product is then winded to the individual spools, inspected and packaged before shipping to the customers.

Raw material
Comes directly from Tanaka Denshi kogyo K.K (Japan) in coil form.

Fine drawing
To draw intermediate wire continuously to required size.

Annealing
To heat-treat wire to acquire customers' required mechanical properties (BL, EL).

Packing & Shipping
To pack and ship out quality products

Inspection
Wire undergo visual inspection and checking of mechanical properties.

Winding
To wind wire on individual spool according to customers' specification

* **All Activities shown here are conducted in Tanaka Singapore**

Figure 34: Aluminium Silicon Bonding Wire Manufacturing Process, courtesy of TANAKA Electronics Singapore.

5.3. STATE OF THE ART

5.3.1. Al-Si systems

In order to understand the properties of Al-1%Si, it is necessary to begin by analysing the phase diagram of the Al-Si system (see Figure 35). It is a binary eutectic type phase diagram with limited aluminium and silicon solubility (Zolotorevsky *et al.* (2007)). The melting temperature of pure Al is 660 °C. The maximum solubility of silicon in aluminium is 1.65%, which is achieved at the eutectic temperature of about 577 °C, while the second phase is almost pure aluminium. The eutectic composition has been largely debated in the literature and it is considered to be 12.6 % in weight of silicon (Lasagni *et al.* (2008), Zhao *et al.* (2013)).

51
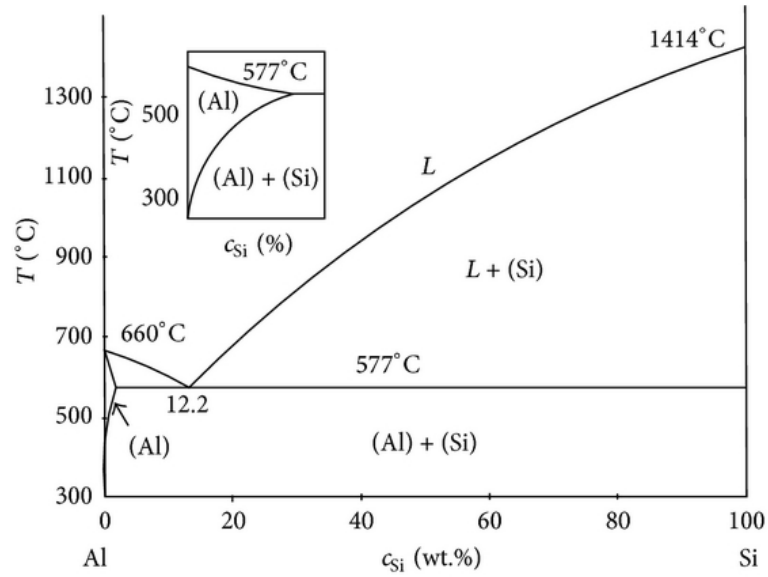
Figure 35: Al-Si phase diagram. Zolotorevsky et al. *(2007).*

Concerning the microstructure, Saini *et al.* (2015) report three reference micrographs for hypoeutectic (1.65-12.6 wt% Si), eutectic (12.6 wt% Si) and hypereutectic (> 12.6 wt% Si) Al-Si systems (Figure 36).
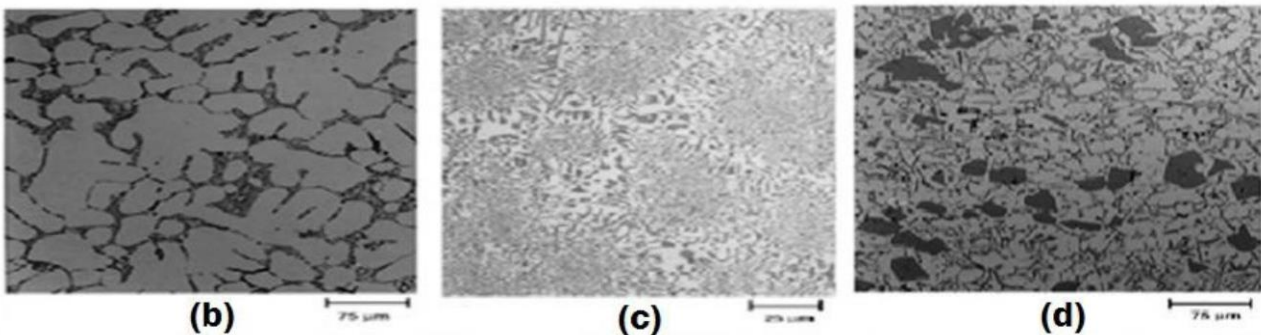
Figure 36: Al-Si microstructure for hypoeutectic (left) eutectic (centre), hypereutectic (right). Saini et al. *(2015).*

As for the case of lead-tin with hypoeutectic composition, when cooling from the liquid phase, the Al-1%Si alloy forms grains of the Al-reach α-phase at first. Then, precipitates of the β-phase, pure silicon in this case, are formed, since silicon largely exceeds the solubility in aluminium at ambient temperature.

Another example of microstructure for different types of hypoeutectic Al-Si systems is reported by Kim *et al.* (2017). In that particular case, even an undesired β-phase containing Fe was present. It can be observed (Figure 37) that for the lower composition of Si (0.8 wt%) only small precipitates of Si were present. Precipitation-free zones (PFZ) are present for 3 wt% Si composition around the eutectic silicon. At 9.5 wt% silicon, the amount of eutectic silicon is further increased. Moreover, Kim *et al.* (2017) observed that the PFZ is evidence of the dissolved silicon having contact with pre-formed silicon particle.
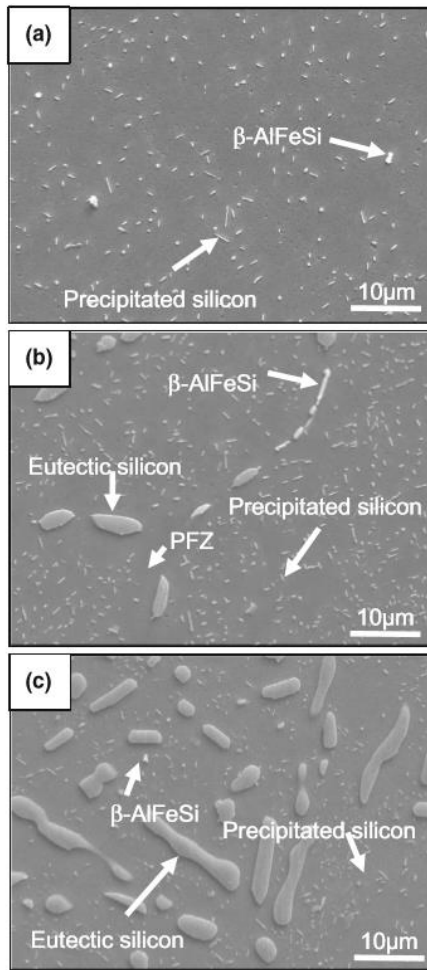
Figure 37: Precipitated silicon particles after aging for 4 h at 573 K for (a) Al-0.8Si, (b) Al-3.0Si and (c) Al-9,5Si. Precipitation-free zones (PFZ) are present for 3 wt% Si composition. Kim et al. (2017).

It was found that the Si precipitates have the usual diamond structure with atomic volume 21.4% higher than in solid solution FCC (Van Mourik *et al.* (1987)). Therefore, large stresses may develop on ageing. An example is represented by the lattice parameter of the α-phase, Al-reach, as a function of ageing time in Figure 38.
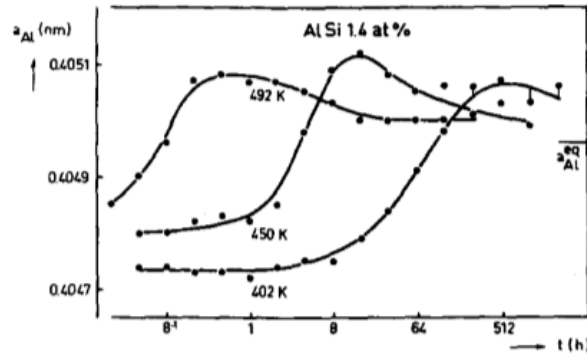
Figure 38: The Al-rich phase lattice parameter a_{Al} as a function of ageing time t for the solid quenched Al-1.4%Si. The ageing temperature applied is indicated. Van Mourik et al. (1987).

The microstructure has a significant impact on the mechanical behaviour of the alloy, as shown in Figure 39.

a) Young's modulus of Al-Si vs. Si content at room temperature: (1) results in the article and (2) results for conventional casting into a mould.	b) Young's modulus of Al-Si alloys vs temperature for various Si contents: (1) 11.5 wt%, (2) 20 wt%, (3) 30 wt%, (4) 35 wt% Si, (5) Al-11.5wt%Si-0.01wt%Sr.
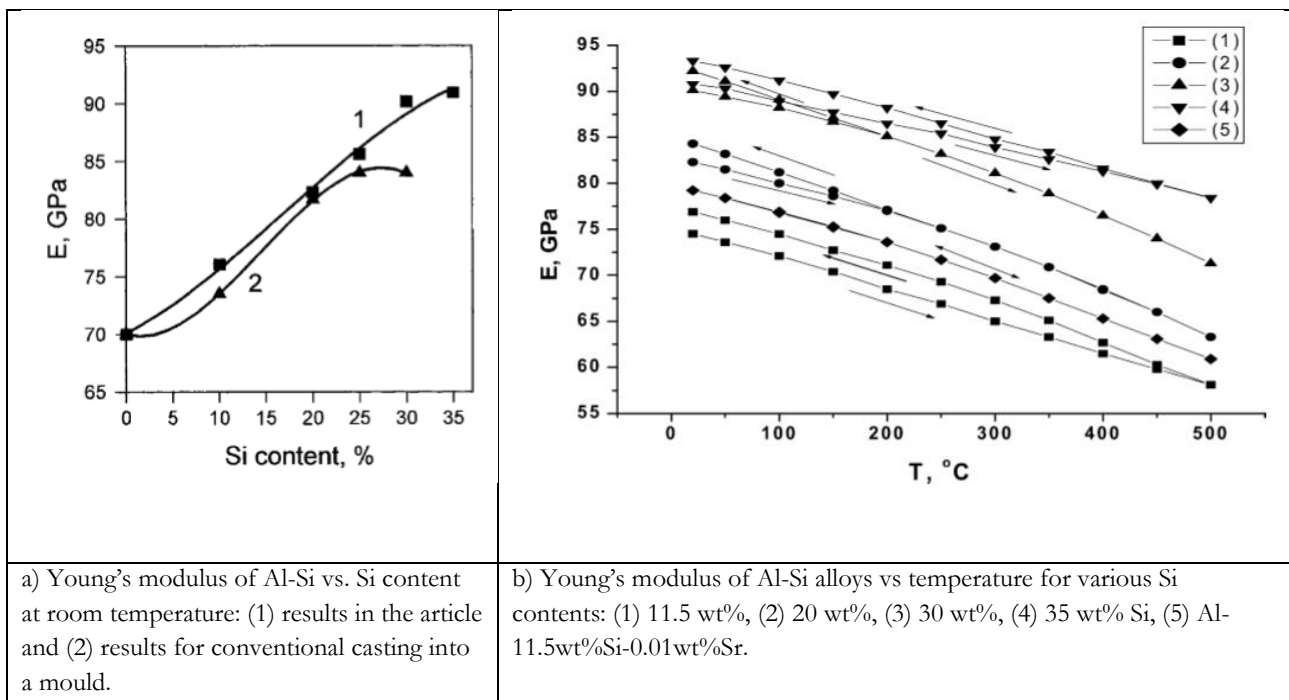
Figure 39: Al-Si Young modulus in various conditions. Nikanorov et al. (2005).

Examples of Guinier-Preston zones in the Al-Si systems were identified in hypereutectic Al-20%Si matrix reinforced with 35% SiC particles (Ma *et al.* (2013)). According to the authors, "after natural aging, spherical GP zones with a diamond crystal structure form in the supersaturated α-Al matrix produced by high pressure solidification. The lattice parameter of the GP zones is 1.62 nm and their structure consists of Si_3 atomic clusters".

5.3.2. Al-1%Si system

Aluminium with 1% content of silicon as alloying element is one of the most widely used materials for bonding wires for packaging in the electronics industry. Pure aluminium, easily formable in small diameter wires, is however very soft and alloying elements are used to increase its strength. 1%Si improves the mechanical properties of Al while maintaining its electrical conductivity and bondability via ultrasonic bonding. Previous studies on this include Harman *et al.* (1977), Krzanowski *et al.* (1990), Fitzsimmons *et al.* (1991), Geibler *et al.* (2009), Agyakwa *et al.* (2016).

These features are crucial for the E-sail application, especially in order to create multi-wires, as explained in the previous sections (Lau (1994)). The Al-1%Si is therefore a hypoeutectic system, which contains a quantity of Si lower that the solubility limit.

ASTM standards are used for these materials, e.g. ASTM F487 – 13, Standard Specification for Fine Aluminium-1% Silicon Wire for Semiconductor Lead-Bonding. Previous research suggests that silicon particle size should be limited to 0.5 μm (Lau (1994)).

Typical specification values for Al-1%Si wire are shown in Figure 40.

Diameter, in. (micron)	Tensile Strength grams	Elongation %
0.001 (25)	15–18	1–3.5
0.00125 (32)	19–22	1–4
0.002 (51)	38–44	2–6

Figure 40: Typical specification values for Al-1%Si wire. Lau (1994).

Aluminium-magnesium wires are also used for the same objective. Al-0.5%Mg has even a better breaking strength than Al-1%Si wires. Al-1%Si and Al-Mg (Al-0.5%Mg and Al-1%Mg) alloys are both used for the bonding wires to strengthen the aluminium produced in very thin wires (Liu *et al.* (1999)). The authors study the break strength, yield strength, elongation and resistance to corrosion, arguing that the desired mechanical properties are obtained by an anneal or a stress relief at final wire diameter and that corrosion of wires due to moisture penetration can cause serious wire degradation and electrical open circuits. As also shown in Figure 41, the authors find that the yield strength decreases progressively in the range 100 °C to 300 °C and then remains essentially constant up to 400 °C. "Al-0.5%Mg has the highest break strength at lower and intermediate annealing temperatures, 125 °C-300 °C. Al-1%Si and Al-1%Mg have essentially the same break and yield strengths over the entire annealing temperature range". "The wire grain structure experiences recovery, recrystallization, and grain growth as annealing temperature increases. At the same time, silicon tends to reprecipitate and coarsen at the grain boundaries and in the matrix since its solubility in aluminium is about 0.16% at room temperature versus 0.25% at 400 °C. The probability for silicon to precipitate and coarsen will increase as the annealing temperature rises. It is postulated that this phenomenon has an embrittling effect. Below 200 °C, recovery and recrystallization predominate, and ductility and elongation increase as temperature increases. In the range 200 °C~250 °C, silicon precipitation and coarsening predominates, and causes elongation reduction. In the range 250 °C~300 °C, recrystallization and moderate grain growth

predominate again and elongation increases. Above 300 °C, both silicon precipitation and coarsening, and excessive grain growth induce elongation reduction".

While Al-0.5%Mg wires present a higher strength than Al-1%Si alloys (Liu *et al.* (1999)), they could be more subject to embrittlement for low and intermediate annealing temperatures – 125 °C - 300 °C – (low elongation to failure).

In the case analysed by the authors, the cross sectional area of the 76 μm diameter wire is 0.004534 μm². Therefore, at 100 gram breaking strength, the strain is about 216 MPa.
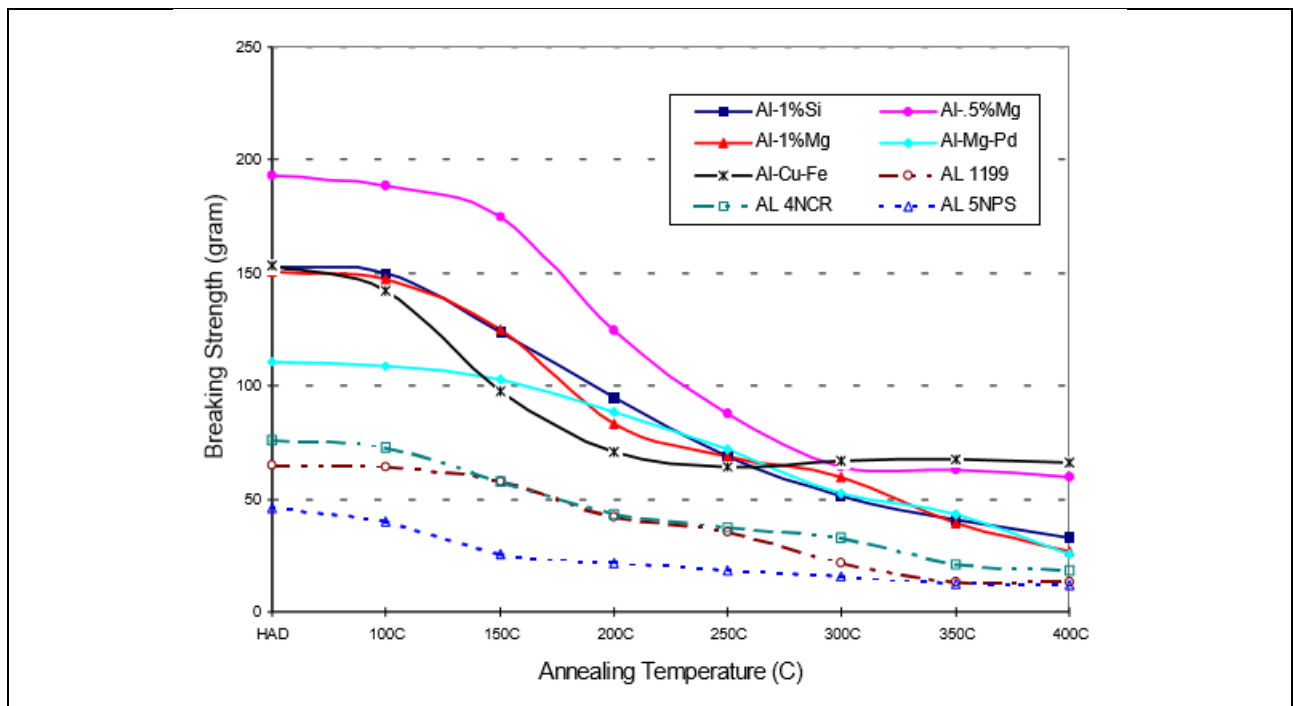
a) Breaking strength of 76 μm diameter wires annealed at various temperatures

b) Yield strength of 76 μm diameter wires annealed at various temperatures

c) Elongation of 76 μm diameter wires annealed at various temperatures
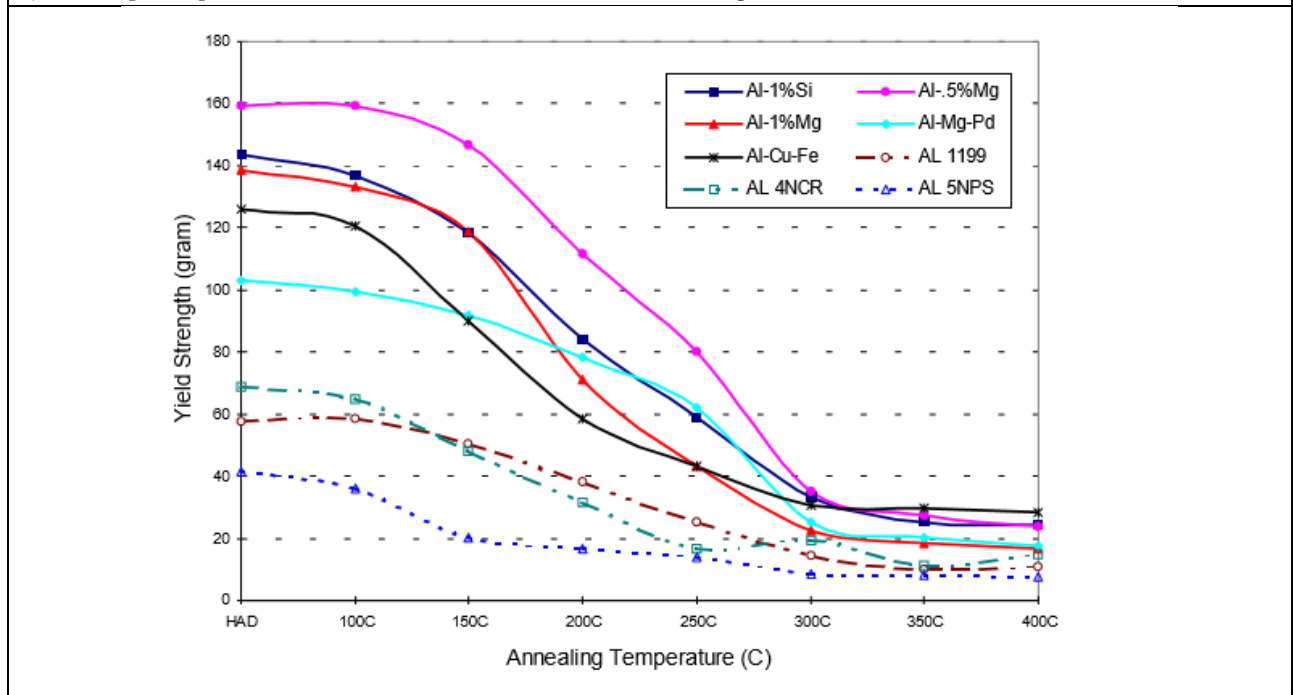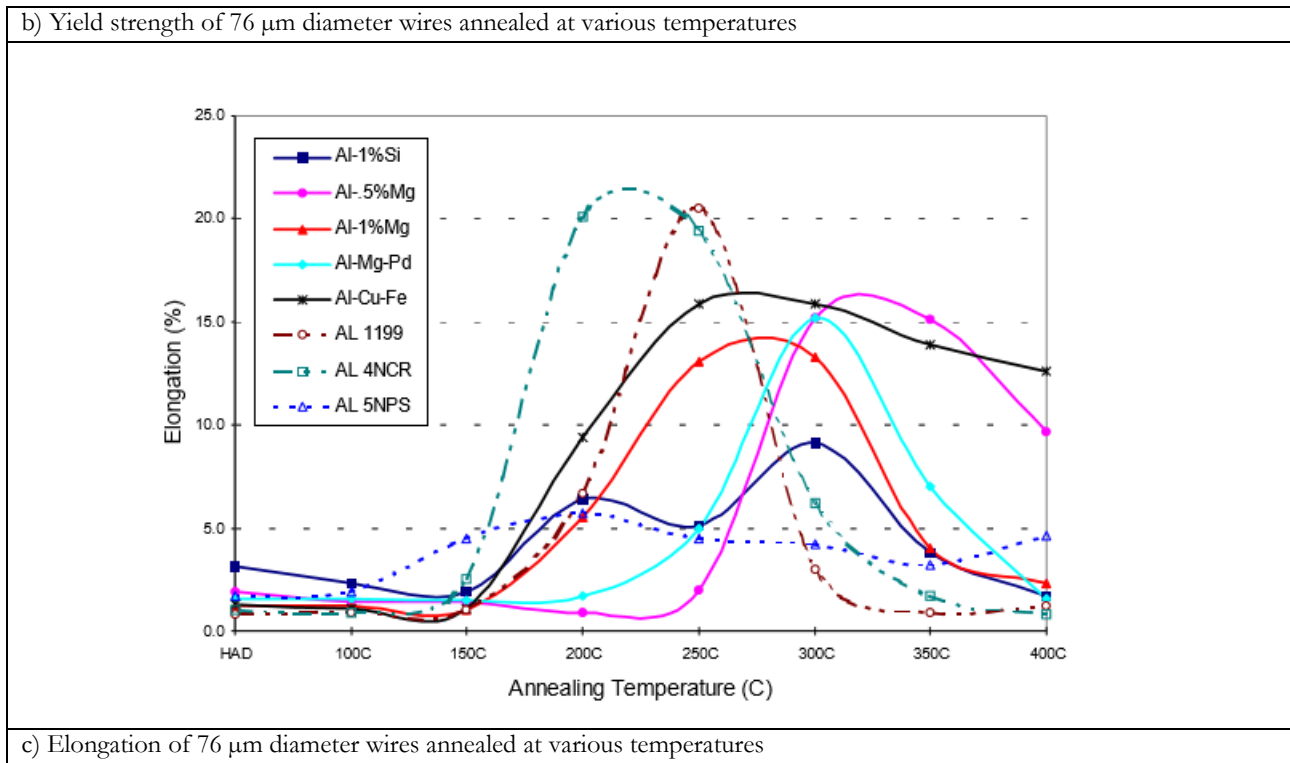
Figure 41: Mechanical properties of Al-1%Si wires. Liu et al. (1999).

A later study (Liu *et al.* (2004)) argues that over 480 °C, the grains grow rapidly to ultra-long grains and single slip occurs easily, resulting in lower strength and greater elongation (10–16%).

The annealing temperature has a strong effect on the silicon precipitates concentration and grains dimension. However, even the previous history has an effect on the final mechanical properties (Liu *et al.* (1999), Lasagni *et al.* (2008)). Zenou *et al.* (2006) also report that both coherent precipitates and dislocation loops are present and that the usual diamond crystallographic structure was observed for Si precipitates.

The effect of the annealing temperature on the dimension of the grains was also observed on Au wires (Takagi *et al.* (2016)).
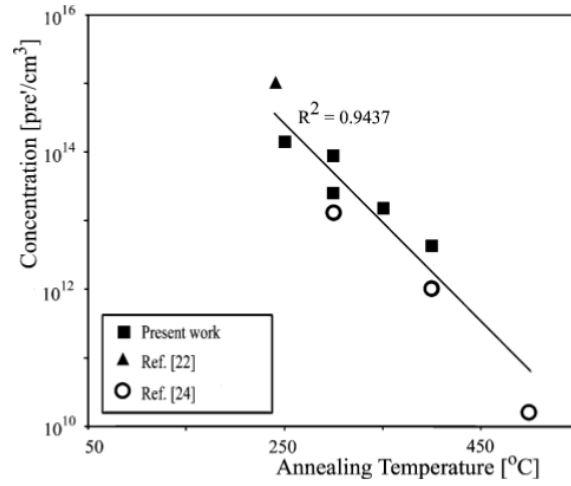
Figure 42: Experimental results for the concentration of Si precipitates as a function of annealing temperature. The annealing time was 16h. Zenou et al. (2006).

Moreover, the annealing time at a certain temperature has also a strong effect on the final mechanical properties (Liu *et al.* (2004)), as shown in Figure 43.
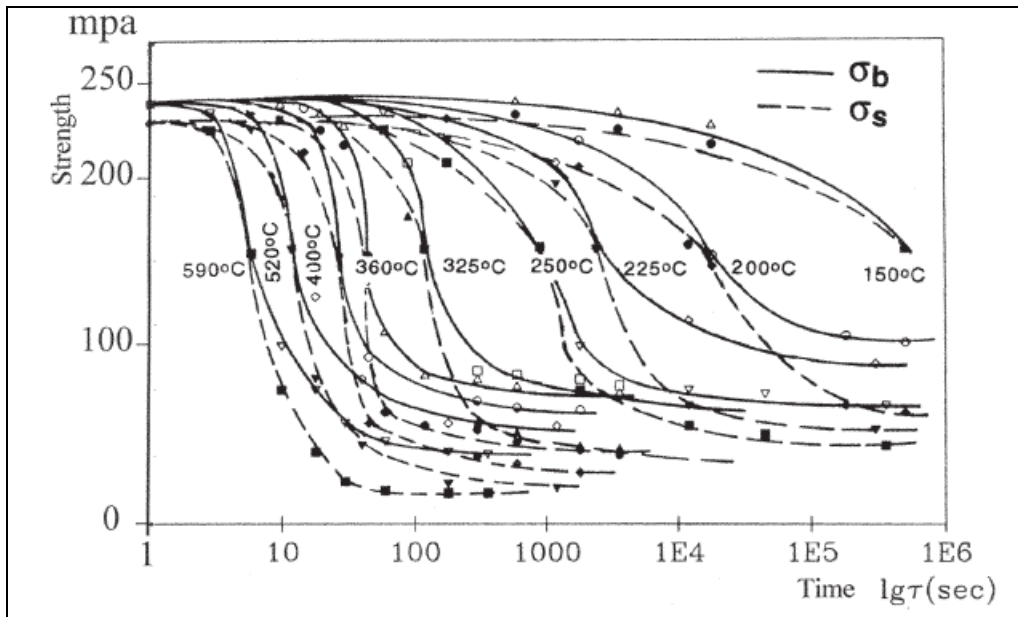
a) Strength at different annealing times
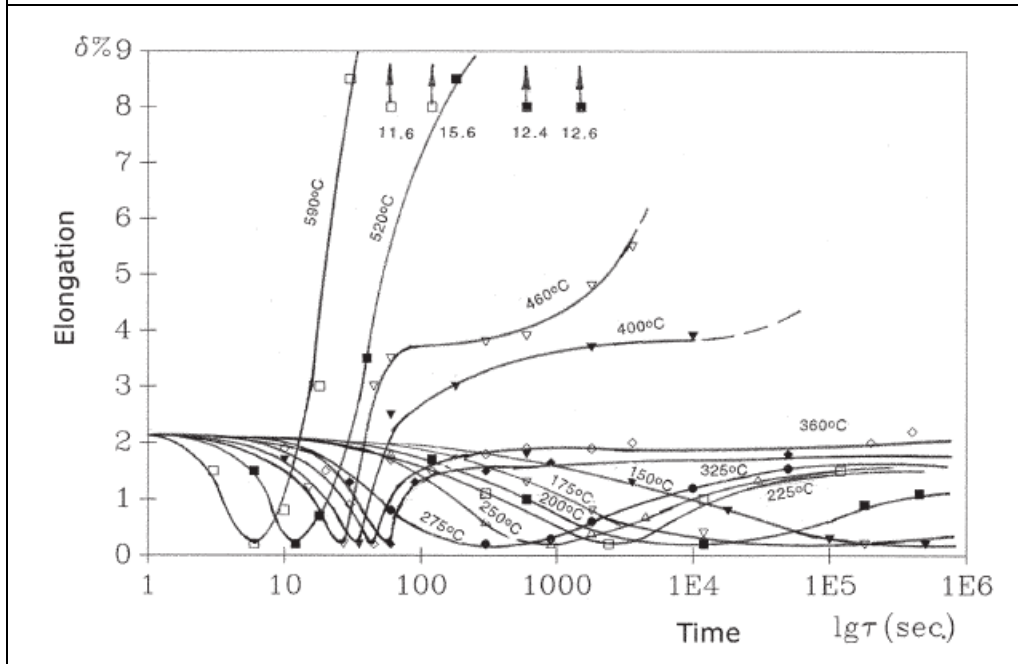
b) elongation at different annealing times.

Figure 43: Effect of the annealing time on the mechanical properties of Al-1%Si material. Liu et al. (2004).

Lasagni *et al.* (2008) show the TEM images of Si precipitates after water quenching at 540 °C and slow heating to different temperatures. In this case, the amount of Si (1.7%) is just above the maximum solubility of the state diagram.
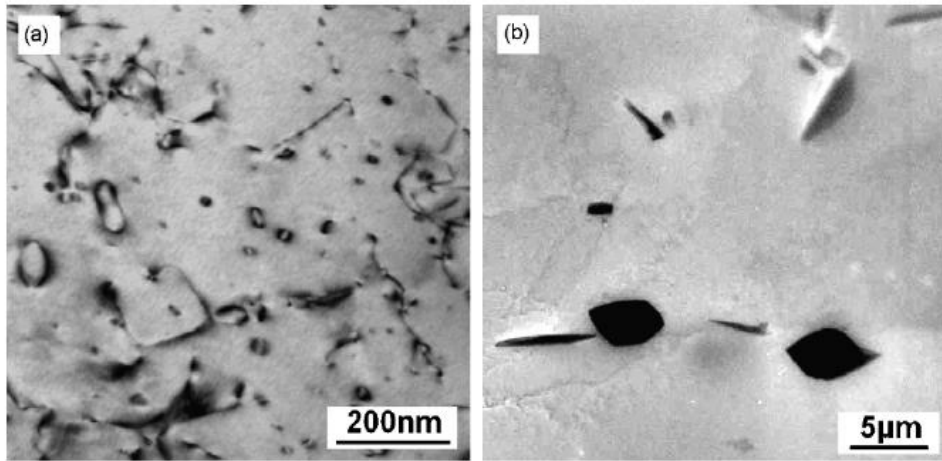
Figure 44: TEM micrograph of Al-1.7%Si showing dislocation and loops (left) and coarse Si inclusions along the grain boundaries (right). Lasagni et al. *(2008).*
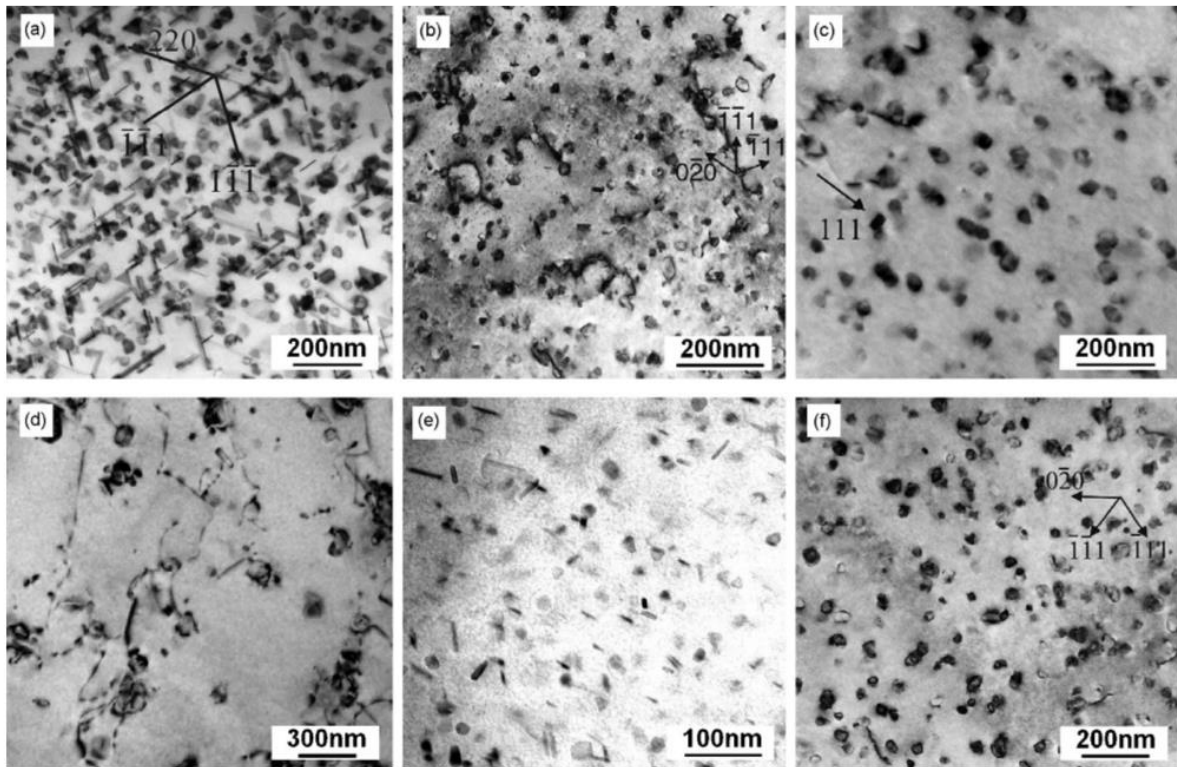
Figure 45: TEM micrographs of quenched Al-1.7%Si samples after heating at 3 K/min to (a) 270 °C, (b) 300 °C, (c) 370 °C, (d) 420 °C and isothermal holding at (e) 200 °C/10 h and (f) 300 °C/1 h. Lasagni et al. (2008).

Al-1%Si annealed bonding wire was observed with TEM in the literature, showing a fine and elongated structure, as shown in Figure 46. Al-1%Si grains were also observed by Kim *et al.* (2009).
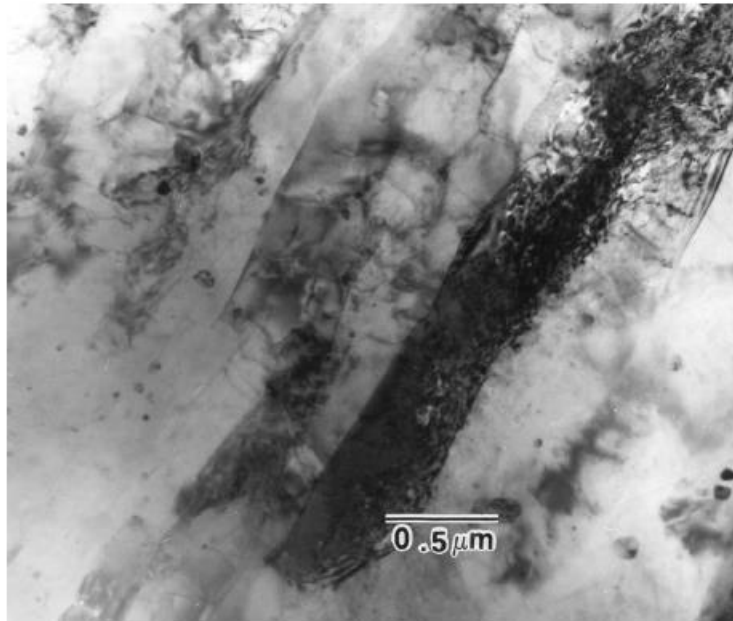
Figure 46: Microstructure of the as-received wire. Liu et al. (2004).

For what concerns corrosion, Liu *et al.* (1999) demonstrated that both Al-1%Si and Al-0.5%Mg displays severe intergranular corrosion. For this reason, other transition metals, such as Fe, Cu, In, Ni and their combinations, could be added to the system in order to provide effective corrosion resistance.

5.4. BARE TETHER: MICROSTRUCTURAL AND RESISTIVITY ANALYSIS

5.4.1. Microstructural properties

5.4.1.1. FIB/SEM images

A simplified version of the E-sail heytether has been observed for the purpose of this study with the Helios Nanolab 600 (DualBeam). This instrument embeds both the capabilities of Scanning Electron Microscope (SEM) and of the Focussed Ion Beam (FIB) systems, which allow performing both the tasks of milling and imaging of the material surface. An image of the instrument installed at the "Laboratorio Interdipartimentale di Microscopia Elettronica" (LIME) of University of Rome Tre is shown in Figure 47.

Figure 47: SEM-FIB Helios Nanolab 600 (Dualbeam) installed at LIME.

The observed heytether was composed by a base wire with 50 μm diameter and a single loop wire with 25 μm diameter.

The bonding point presented a rough surface resulting from the contact with the ultrasonic bonding tip (Figure 48 a) and b)). The different roughness could be considered as a positive element for what concerns the improved optical diffusive reflectance. In fact, such bonding point could be more easily identified by the optical camera responsible for monitoring the motion of the tether in space.

A cross section was then prepared to observe the bonding point at higher magnification. A platinum layer was first deposited in the middle of the bonding region with the objective to protect the material from the following milling. A first milling with large current was performed at 9 nA, followed by a cleaning milling at lower currents (0.9 nA) to improve the quality of the surface to be observed. The *in-situ* SEM with ionic source was used to take high-magnification images of the bonding cross section. Figure 48 c) shows the results of the cross-section preparation.

The high magnification image (25000x) showed that the bonding was not complete and that voids were present at the interface between the base wire and the loop wire (Figure 48 d).

| a) View of the bonding point of the heytether | b) Detail of the bonding point |
| c) Cross section at bonding point | d) Defect in the bonding section |
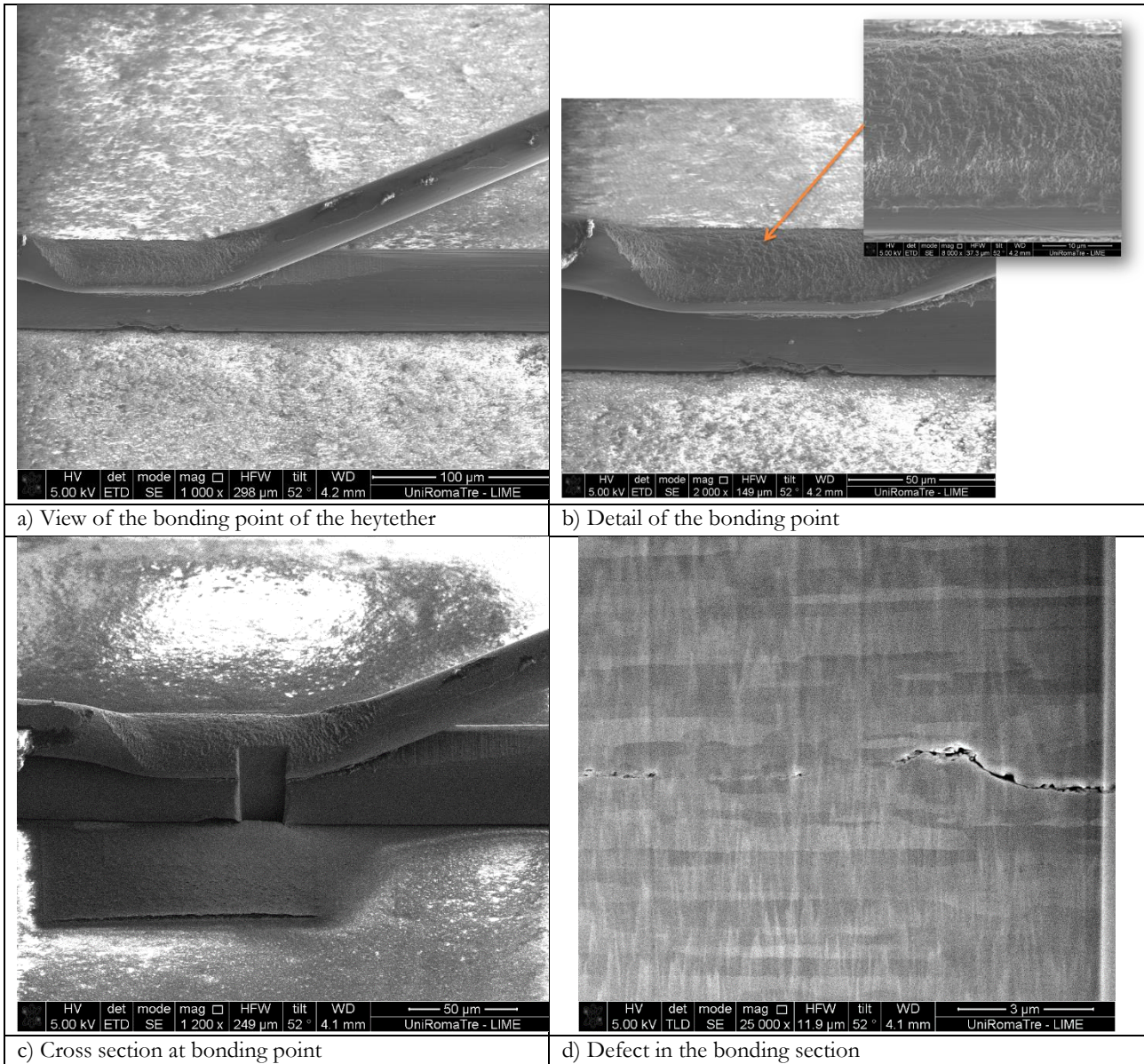
Figure 48: SEM/FIB images of the bonding point of the heytether.

5.4.1.2.   TEM images

TEM lamellas were prepared using the Helios Nanolab 600 (DualBeam). A metallic layer (Pt) has been deposited on the area of interest. Subsequent mills were then performed with gallium ions to reach a lamella thickness of about 1 μm. Then, the lamella was cut and removed from the milled trench using a micromanipulator and placed on a Cu grid. While on the grid, the lamella has been further thinned up to a thickness which is transparent to electrons (about 100 nm).

The lamella was then observed with the Transmission Electron Microscope (TEM) Philips CM120 Analytical. The instrument has a LaB6 filament, a CCD camera Olympus Megaview III and an Energy Dispersive X-ray Spectrometry (EDS) probe EDAX DX4.

An image of the TEM installed at the "Laboratorio Interdipartimentale di Microscopia Elettronica" (LIME) of University of Rome Tre is shown in Figure 49.

Figure 49: TEM (Philips CM120 Analytical) installed at LIME.

In Figure 50, the images illustrating the different stages of the lamella preparation for the sample are shown.

| a) Zone of TEM lamella extraction | b) TEM lamella before the extraction from the double cross section |

c) Top view of the lamella with the micromanipulator and the ion gun	d) TEM lamella ready for analysis
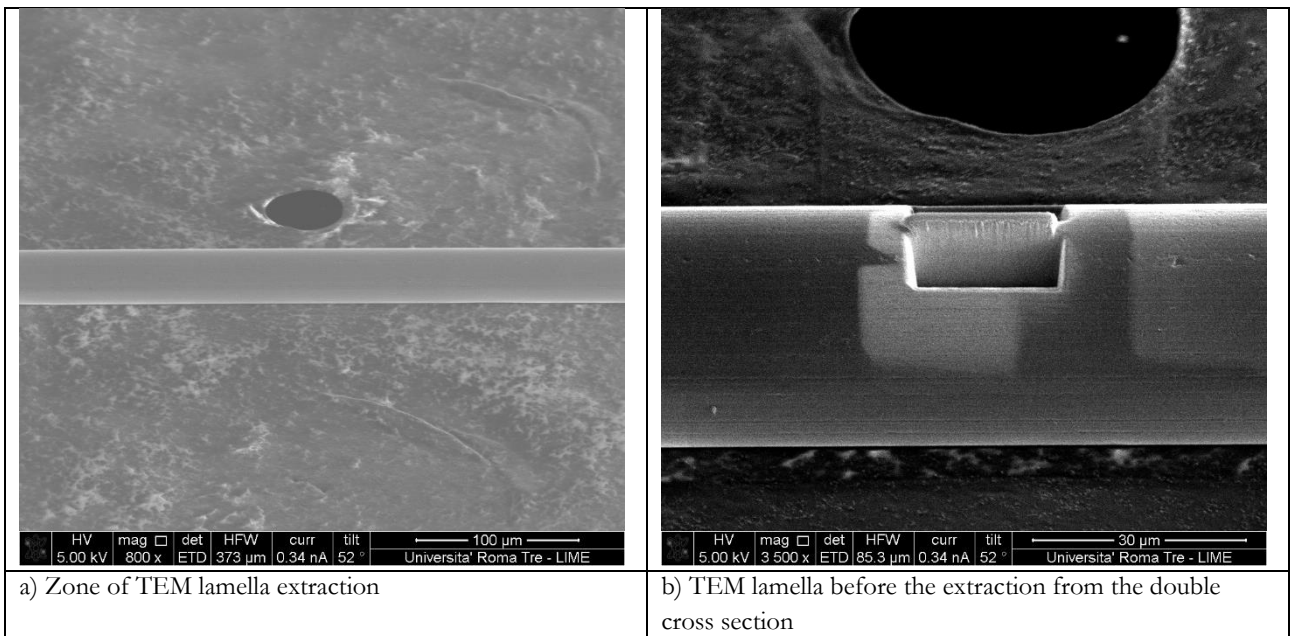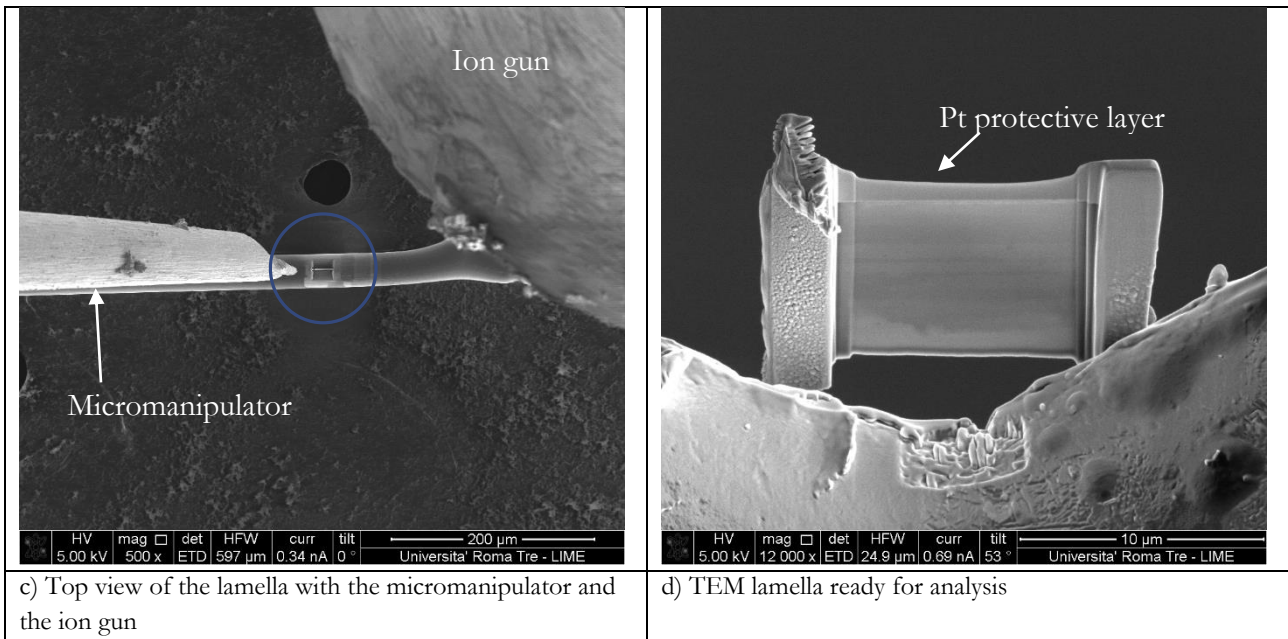
Figure 50: Stages of preparation of the TEM lamella using the SEM/FIB.

The lamella was observed at a voltage of 120 kV in bright field. We observe elongated bands with high contrast aligned with the direction of wire drawing (Figure 51). The bands may be single grains or dislocations cells/subgrains. The cells/grains are highly elongated and some of them present a high density of dislocations.
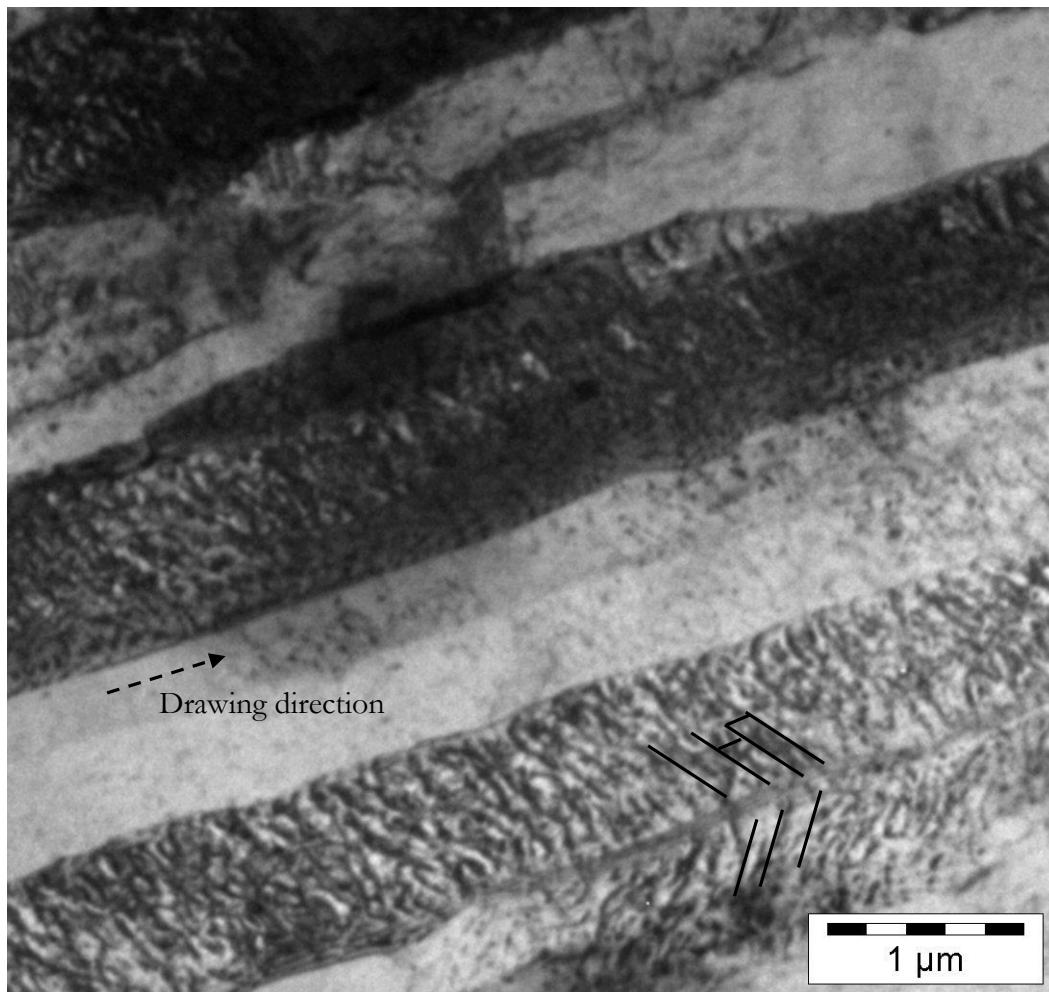
Figure 51: TEM lamella of the bare tether

Selected Area Electron Diffraction (SAED) analysis was performed to obtain diffraction patterns of the samples. A diaphragm allows selecting a spot size smaller of the entire surface. The area observed with this technique (up to 20 nm) is limited due to the spherical aberration of the objective lens. The spot was 500 nm.

The diffraction pattern produced by the three grains in figure below shows that the crystallographic directions of the different grains are very similar. This is in line with the hypothesis that they could be subgrains instead of grains. Amodeo *et al.* (1988) describe the subgrains as a "two dimensional honeycomb-like configuration in which there are regions of high dislocation density, the cell walls, and low dislocations density, the regions in between the walls".
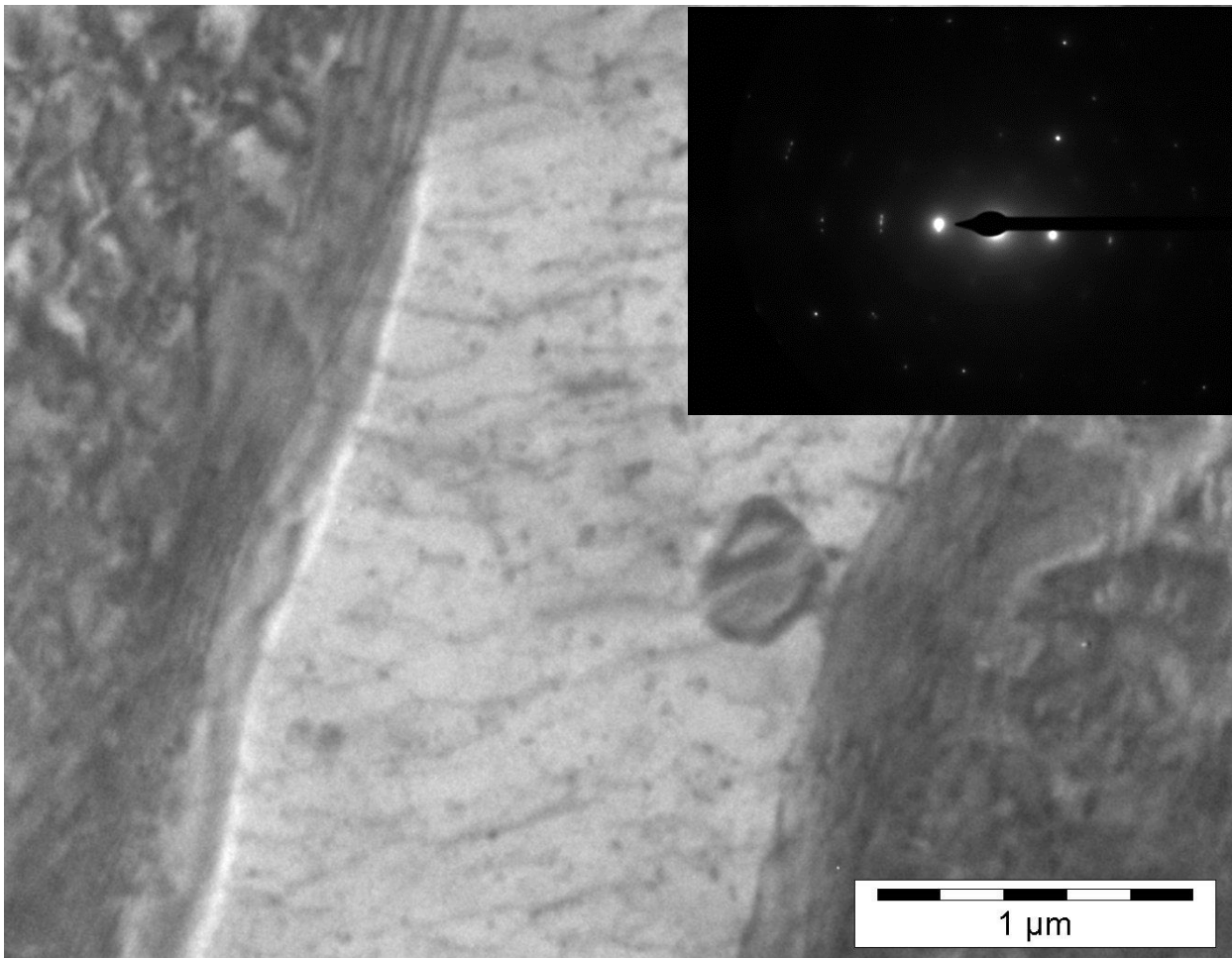
Figure 52: diffraction pattern of the TEM lamella details showing the similar crystallographic orientation of the three cells/subgrains.

Dense dislocation walls (DDWs) were identified inside the cells/subgrains, in line with what found by Bay *et al.* (1989) for aluminium and Ananthan *et al.* (1991) for copper. As described by Ananthan *et al.* (1991), the DDWs appear to have a macroscopically determined orientation. It is suggested that the DDWs separate regions of the crystal having different operating slip systems. This feature was also observed in the TEM micrographs obtained in our research. In our case, the DDWs seem to be aligned at 45° with respect to the drawing direction. These features are generally observed in cold rolled aluminium, especially when having a high purity, and other fcc metals. Microbands (MBs) were identified as well. The MBs are attached to the DDWs and are generally composed by multiple dislocations walls (Bay *et al.* (1989)), as shown in the figure below.

| a) Geometry of crossing DDW-MBs as they are often seen in thin foils from longitudinal sections in 30% cold rolled aluminium. | b) Idealised microstructure in a thin foil from a longitudinal section of a fcc metal such as aluminium after rolling. |
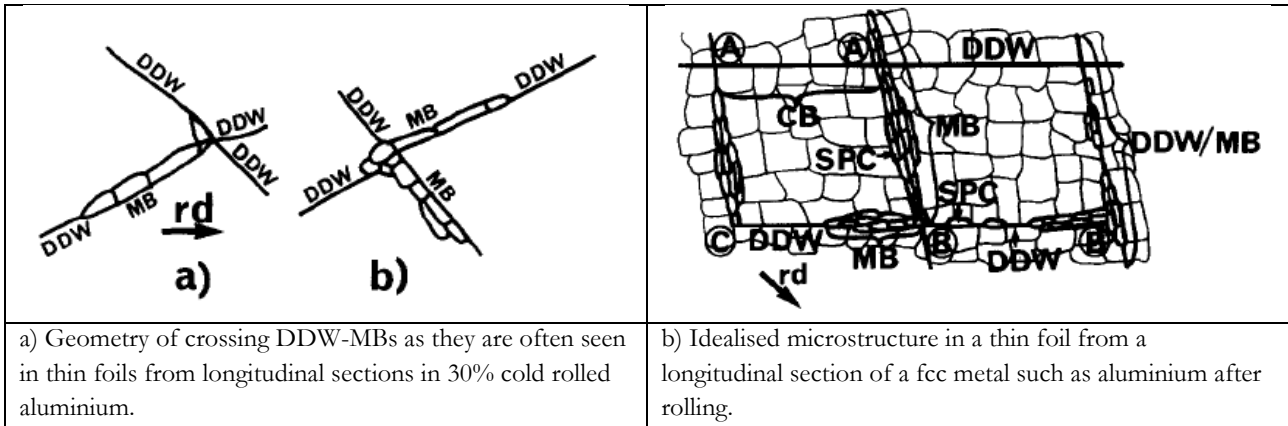
Figure 53: schematic of the DDWs and MBs. RD is the rolling direction. Bay et al. *(1989).*

First and second generation MBs exist. First generation MBs are aligned macroscopically to the specimen geometry (at angles of approximately 45° to the rolling direction and approximately parallel to the transverse section), but have no specific crystallographic orientation. Their function is to accomplish the subdivision of the grains into smaller, uniformly deforming volume elements. Second generation MBs are associated with concentrated shear (Ananthan *et al.* (1991)).

Moreover, Ananthan *et al.* (1991) explain that, depending on the strain induced during the cold working, a higher percentage of grains will present DDW/MBs. This is in line with the observation made in our study, since only some of the cells/subgrains present this dislocation structure (see Figure 54).
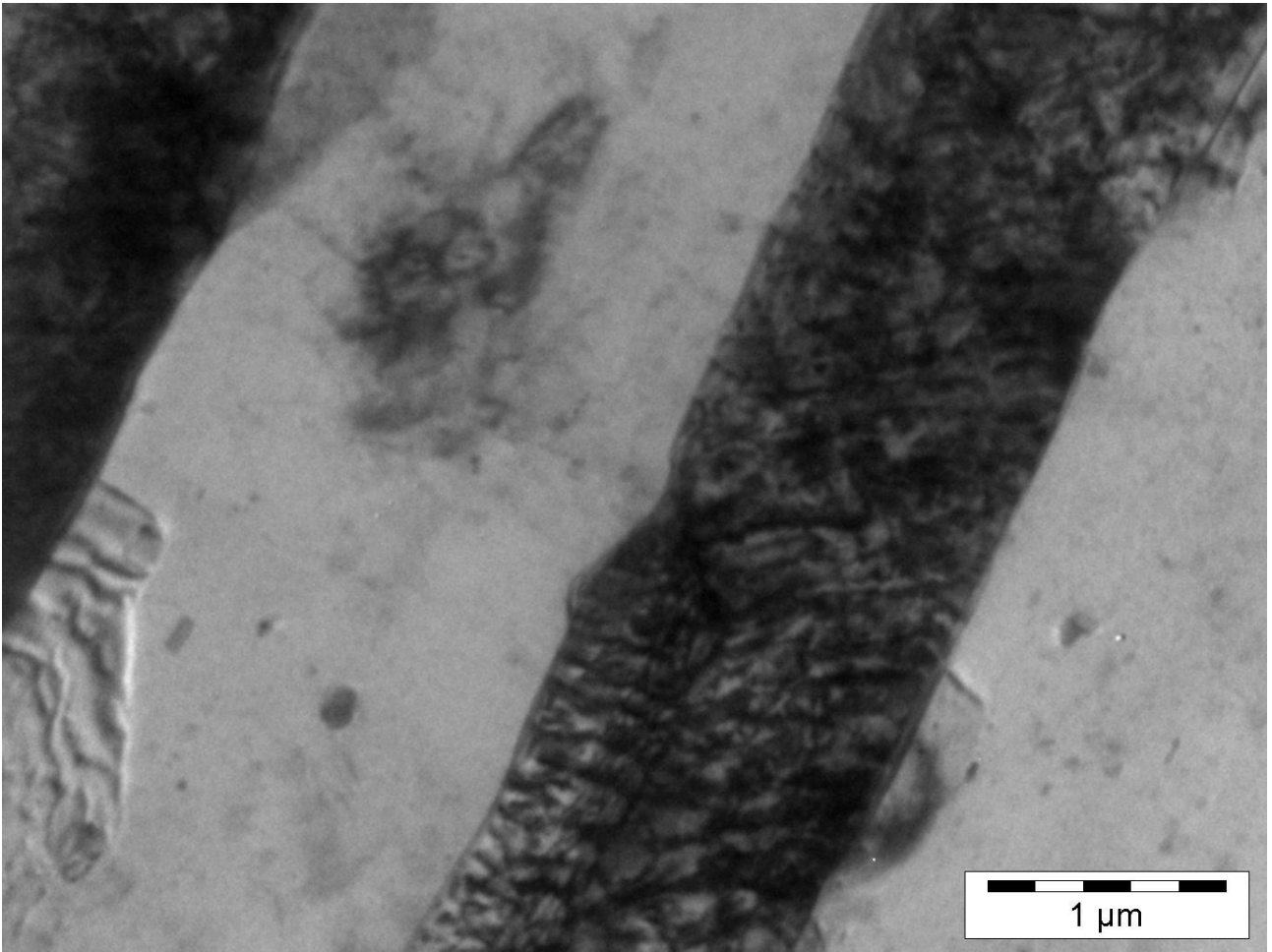
Figure 54: Details of the TEM lamella showing cell/subgrains with and without DDW/MBs.
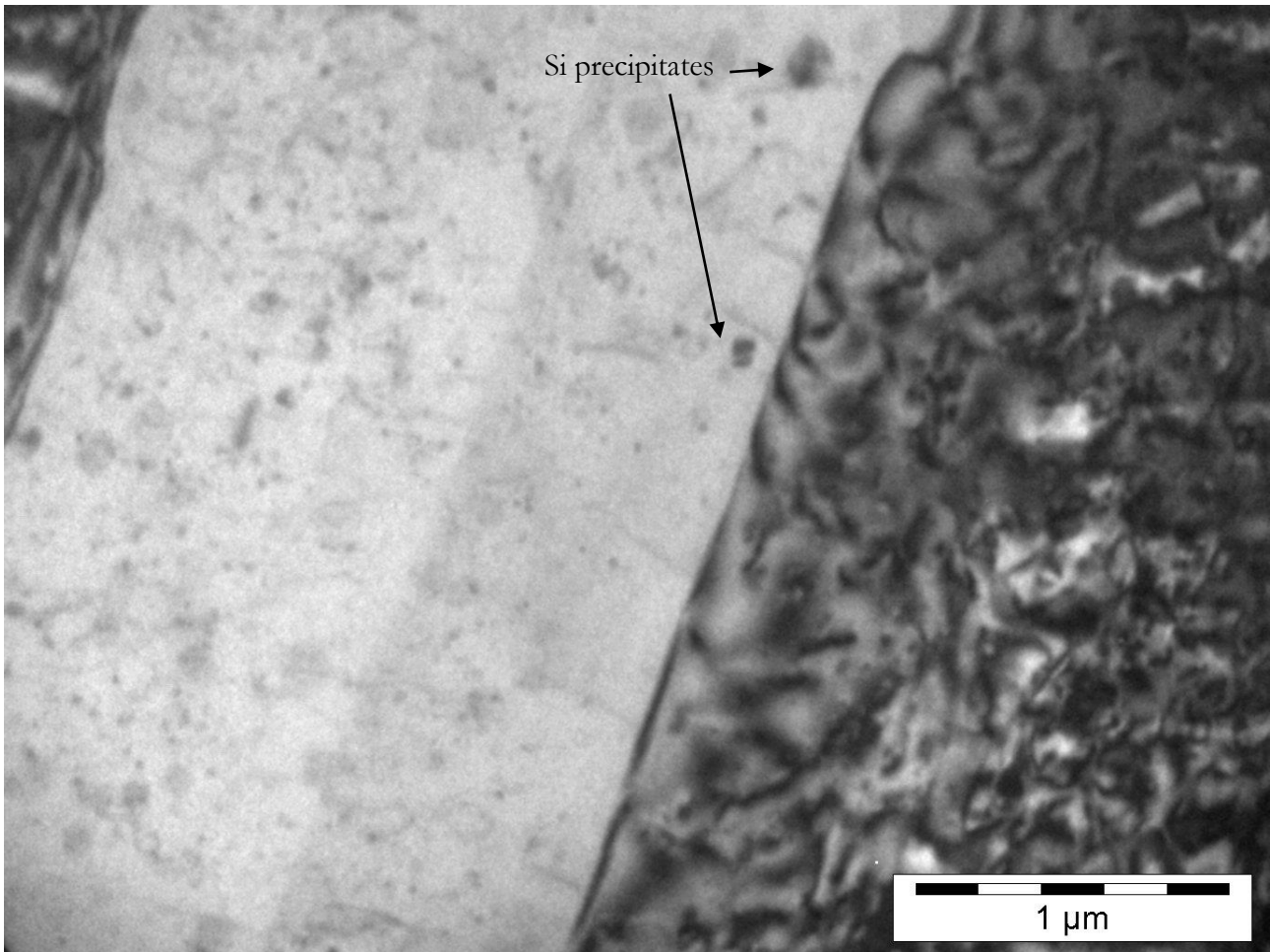
Figure 55: Details of the TEM lamella.

Energy-dispersive X-ray spectroscopy (EDS) was performed both inside a single cell/subgrain and in the precipitate (Figure 56). It was confirmed that the grain is pure Al.

In the precipitate the weight percentage of Al detected was 65%, while the one of Si was 35%. Cu and Ga were also detected but are considered not to be present in the metal observed. In the case of Cu, it is present in the TEM support, while the Ga was used in the process of preparing the lamella.

The quantities of the EDS are not in line with the expectations, since the phase beta should contain maximum 1.65 % of Si in the case of the eutectic. It is therefore concluded that the EDS system was not able to focus on one single Si particle, due to the limitations of the instrument, which also measured the Al surrounding the particle.

It was not possible to detect any nickel in the lamella due to its very low quantity.

a) EDS spectrum in the grain	b) EDS spectrum in the precipitate
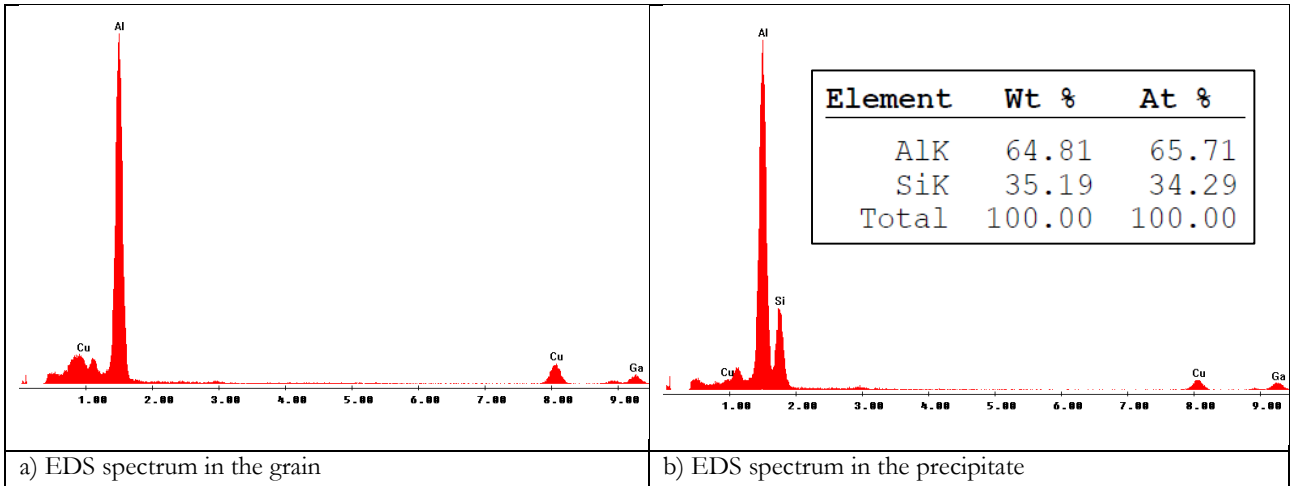
Figure 56: EDS spectrum of the ESAIL tether.

5.4.2. Resistivity tests of tether wire

Measuring the electrical resistivity of the wire is of particular interest as the electrical resistivity of pure aluminium and aluminium alloys is a function of the temperature, as shown in Figure 57. Therefore, the E-sail tether electrical properties may vary while travelling across the solar system and experiencing different equilibrium temperatures.
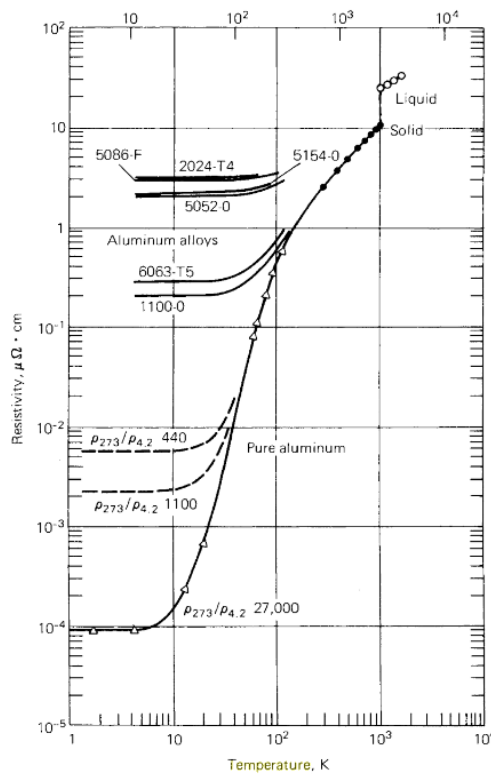
Figure 57: Electrical resistivity of pure aluminium and aluminium allows as a function of temperature. Hatch (1984).

Moreover, the electrical resistivity of wires can be affected by the mechanical treatment during the production process (Wei *et al.* (2011), Rosenbaum *et al.* (1958)). As an example, the plot of the fractional change in the electrical resistance during isothermal aging at 200 °C after various quenching treatments is presented in Figure 58 (Rosenbaum *et al.* (1958)).
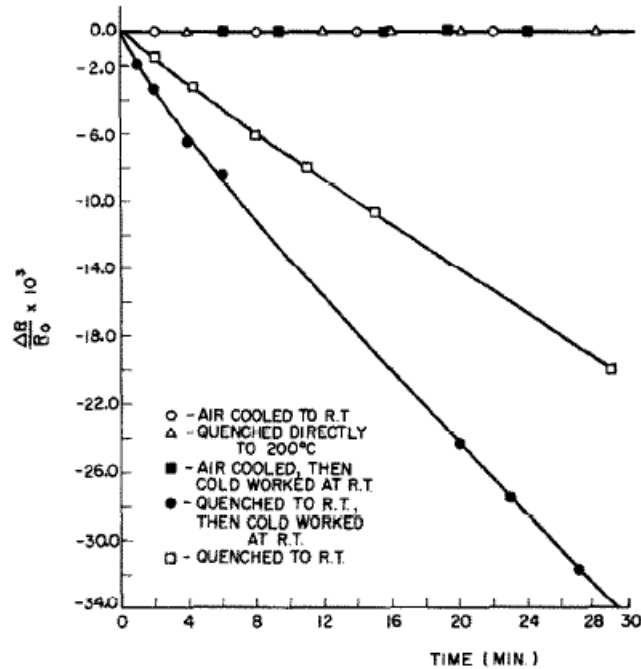
Figure 58: Plot of the fractional change in the electrical resistance during isothermal aging at 200 °C after various quenching treatments. Rosenbaum et al. (1958).

The electrical resistance of an Al-1%Si wire (*TANAKA* (2015)) with 32 µm diameter has been measured. The sample has been prepared by ultrasonically bonding the wire to a copper support.

The ultrasonic bonding of wires was made using a *Kulicke and Soffa Industries Inc.* ultrasonic bonding machine (model 4123) provided by the Institute for Photonics and Nanotechnologies of CNR.
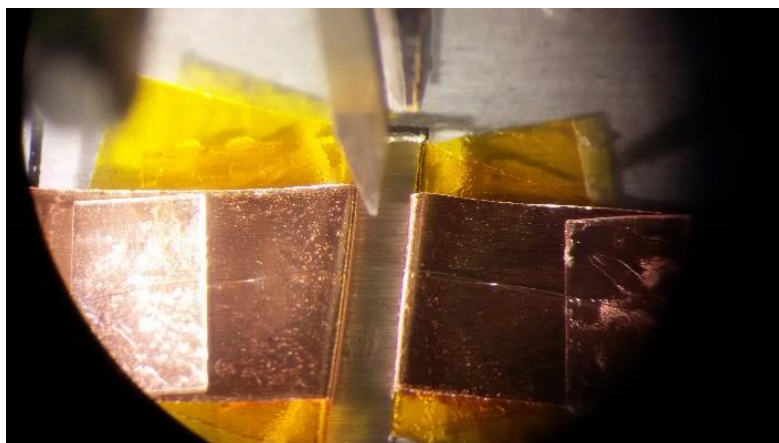
Figure 59: View from of the bonding tip.

After the bonding was made, the length of the sample was measured using optical images of the sample. Images were taken both of the front view and of the side-view using a Nikon DS-Fi1 video camera with Nikon Digital Sight controller. The objective used was HAMA OLYMUS 50 mm. The software used to analyse the images was NIS Elements F 2.30. The length of the sample was measured using the side image Figure 60 (b) and was 18.5 mm.

a) Sample U7 front view	b) Sample U7 side view
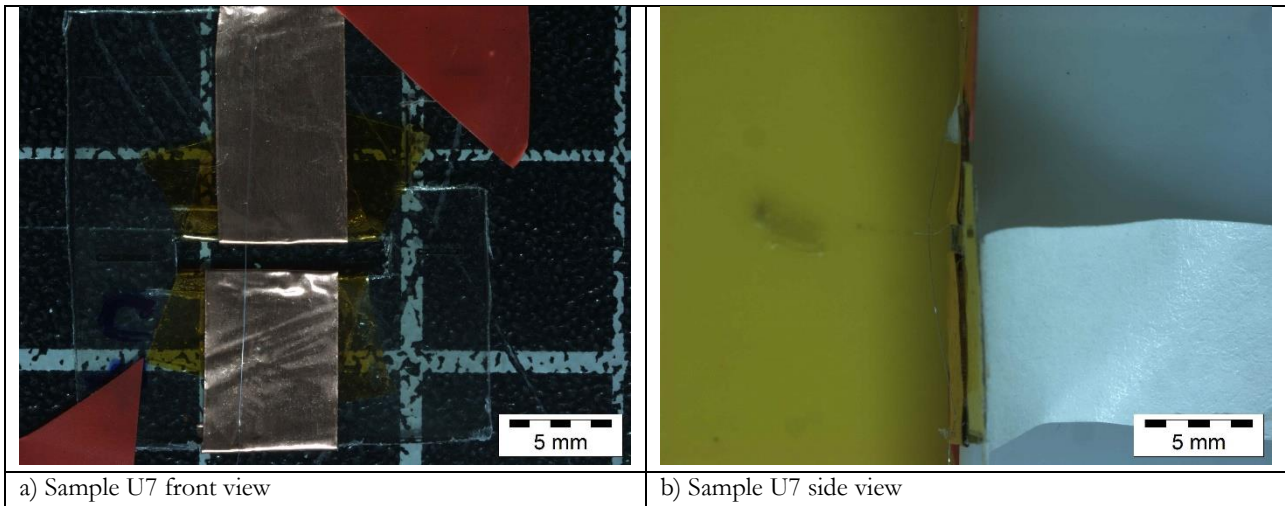
Figure 60: Sample used for the resistivity measurement.

The measurement of the electrical resistance has been done using a HP 34401A Digital Multimeter with 6½ digit resolution. The 4-wire configuration has been used to get a higher accuracy compared to the 2-wire set-up.

5 resistance measurements were taken. The mean value was 0.6610 Ω, with a standard deviation of 0,0007 Ω. The resultant resistivity was 2.87×10^{-8} Ωm. This value was close to the nominal resistivity of aluminium (2.82×10^{-8} Ωm).

5.5. TETHER COATING ACTIVITIES

5.5.1. ESAIL project coating

The state of the art of the E-sail coating is described in the ESAIL FP7 project technical document Project D22.1 (Rauhala *et al.* (2013)).

In the frame of the ESAIL FP7 project, the emissivity of the wire was measured by heating the wire in vacuum while measuring the voltage drop across the wire; in this way, a resistance value was obtained as a function of the wire temperature (Figure 61). The emissivity measured was 0.06 (double than the bulk material). However, no measure was performed for the absorbance, so it was not possible to determine whether the optical properties of the coating (α/ε ratio) were fitting the requirements or not.
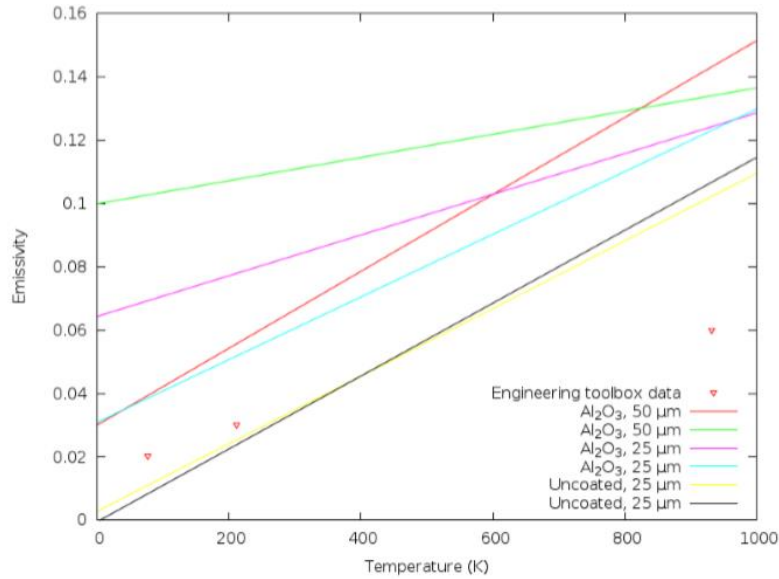
Figure 61: Measured emissivity of tether wire samples measured in the frame of the ESAIL project. Rauhala et al. *(2013).*

Moreover, after a first attempt of Al_2O_3 ALD coating deposition, a sticking problem was experienced during unreeling. This problem proved to be a major one, since during unreeling the pull force goes beyond the value of 6 g, the maximum load that can be sustained by the tether. For this reason, a different method could be preferred, to be performed in line with the tether production (*i.e.* using a reel to reel process).

Another feature required for the tethers would be to be able to prevent cold welding. Even if this could be obtained by using self-lubricating coatings, a properly designed oxide layer could be able to provide the required properties. In the ESAIL FP7 project, tests were conducted to simulate the cold welding response and it was demonstrated that a properly designed coating is able to prevent cold welding (Rauhala *et al.* (2013)).

The Al_2O_3 ALD coating produced in the frame of the ESAIL FP7 project has been observed with a SEM/FIB instrument and the images are reported in Figure 62. We can observe that the coating presents several cracks at the bonding point. Its thickness is regular along the loop wire, while it is highly variable at the rough bonding point. This was expected, since the ALD coatings are generally highly conformal to the substrate. However, it seems that the bending of the loop wire at the bonding point during the sample handling provoked several cracks.

Even though the failure of the coating at the bonding points is not desirable, it is not necessarily a show stopper for this technology since the main objective of the coating is to modify the overall optical properties of the tether. If the coating is lost at the bonding point, it would only constitute a low percentage of the overall tether's surface. However, it is a drawback when considering the prevention of short circuits in case of tether's failure.
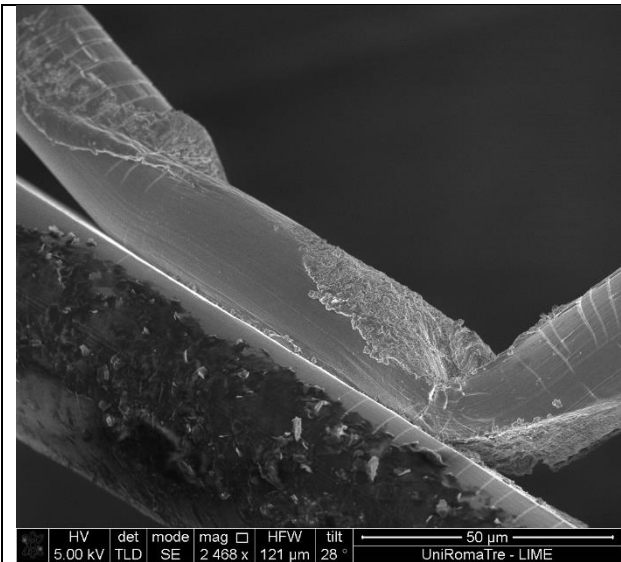
a) SEM view of the bonding point	b) Detail of the bonding point
c) Details of the bonding point	d) Measured thickness of the Al$_2$O$_3$ coating (97 nm).
e) View of the cross section in the loop wire	
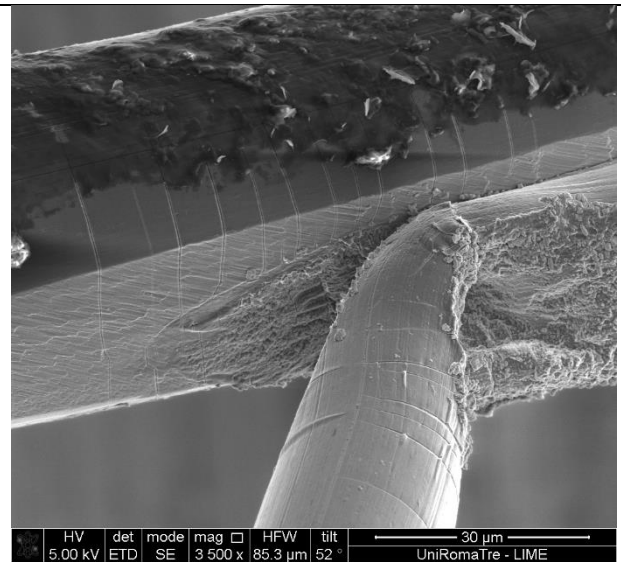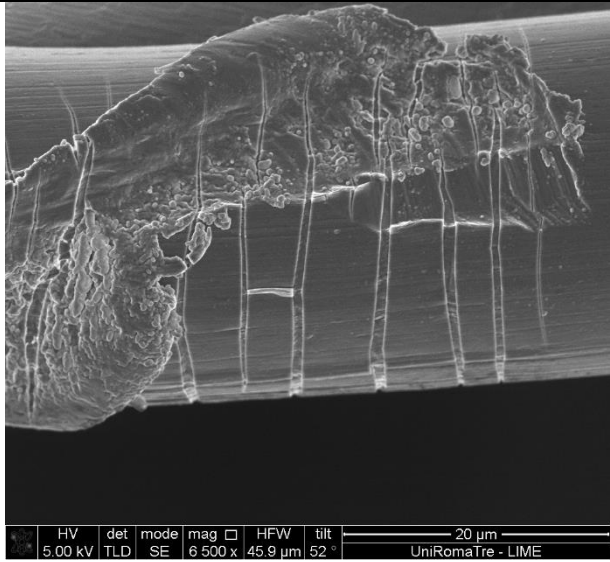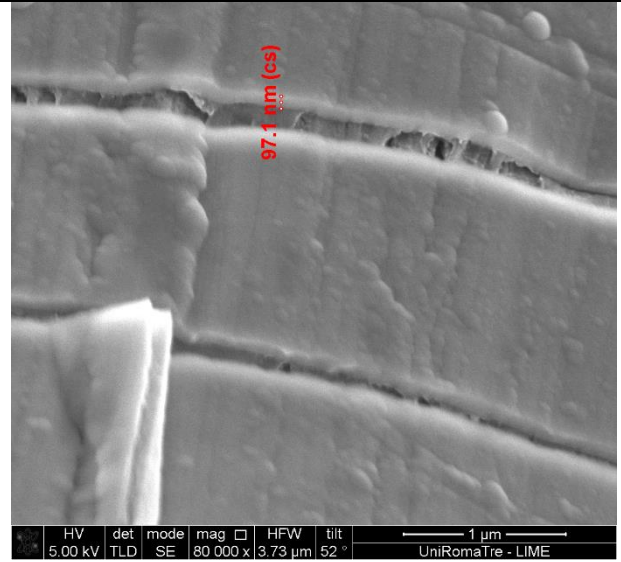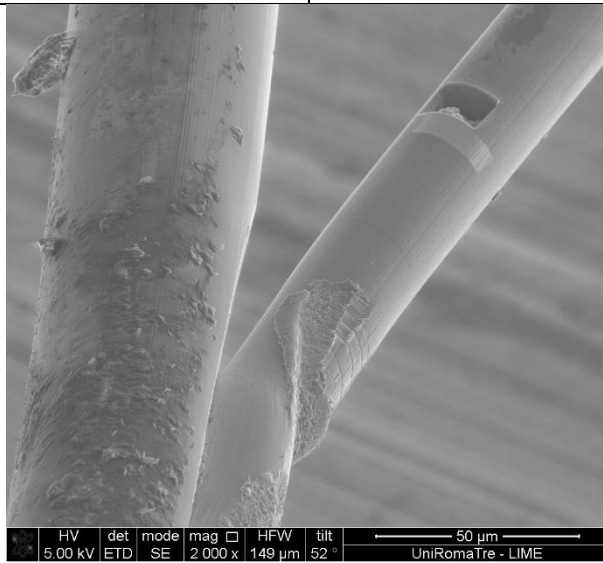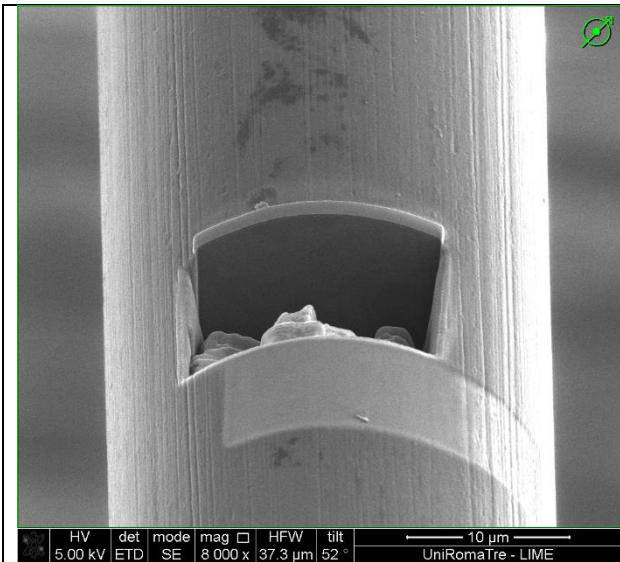
f) Closer image of the cross section in the loop wire
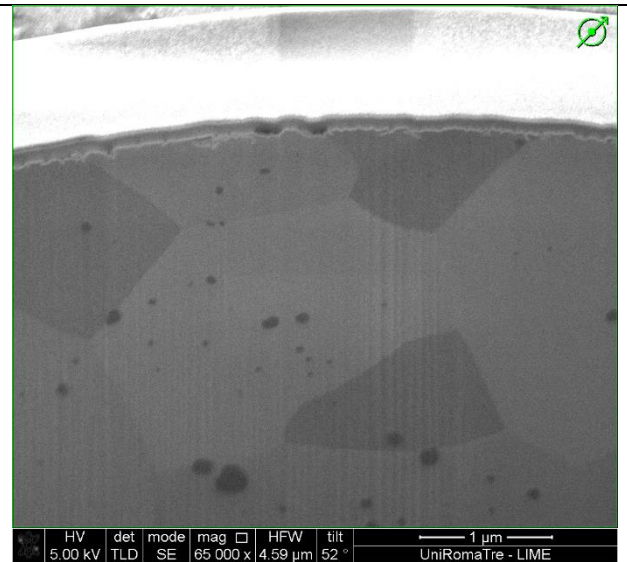
g) Cross section of the Al$_2$O$_3$ coating (100 nm thick).
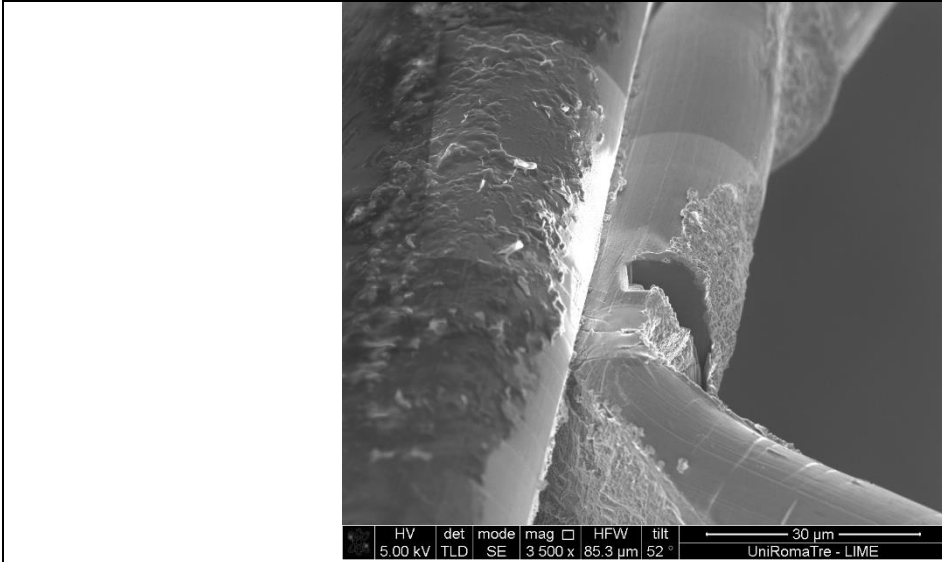
h) Cross section at the bonding point
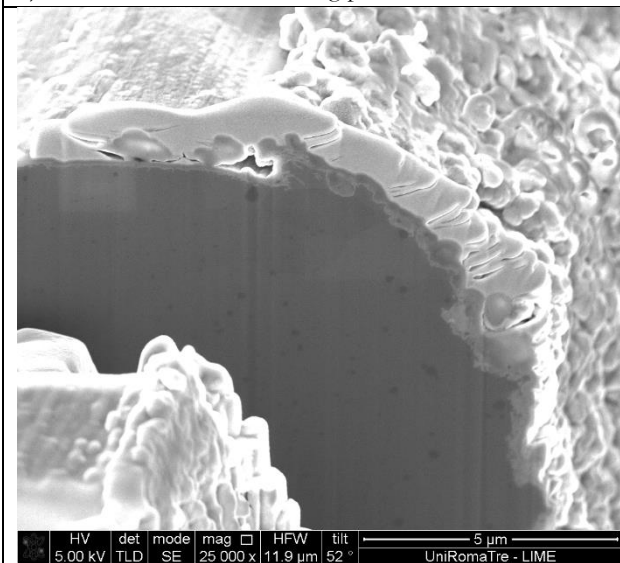
i) Cross section at the bonding point
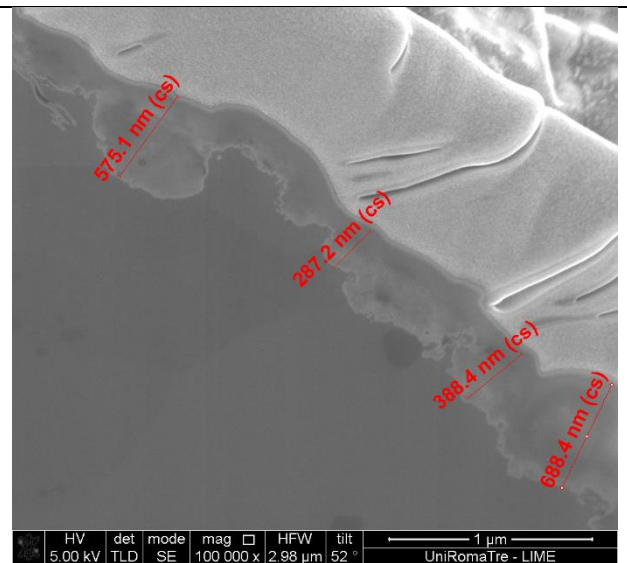
l) Al$_2$O$_3$ coating cross section at the bonding point

Figure 62: SEM/FIB images of the Al$_2$O$_3$ coated heytether (50 μm base wire + 25 μm loop) wire as produced in the ESAIL project.

5.5.2. Coatings produced in this work

In the frame of the PhD activity, a study of the ALD coatings properties was carried out together with the University of Brescia (project MALDIT). The University of Brescia made the ALD deposition of four coatings (Al_2O_3, TiO_2, ZnO and TiZnO) on aluminium samples (both on flat plates and on tether samples) in order to study their optical properties. The results of this work have been published in Hassan *et al.* (2017) and are reported below.

As we already discussed in Hassan *et al.* (2017), the ESAIL PF7 project demonstrated that ceramic coatings deposited by Atomic Layer Deposition (ALD), such as Al_2O_3, are beneficial in preventing cold welding of the tethers. ALD is a modified form of chemical vapour deposition technique which produces highly conformal coatings that are precisely controlled at Ångstrom level due to self-limiting surface reactions and separate introduction of material precursors in a cyclical manner. ALD coatings are without line of sight restrictions as in plasma enhanced vapour deposition, pinhole free and without defects. It is also possible to obtain different stoichiometries of Ti-Zn mixed oxides by tuning ALD parameters.

In this study, low thickness TiO_2, ZnO and Ti-Zn mixed oxide coatings were deposited on ESAIL tethers by ALD at low temperature. Morphological, optical, and electrochemical characterizations were performed to evaluate the coating performances with respect to the final application.

SiO_2, Al_2O_3 and Indium tin oxide (ITO) thin film coatings with thicknesses higher than 50 nm applied by sputtering or vapour deposition are widely used in aerospace applications as protective coating. SiO_2 coating was Magnetron sputtered on Kapton® H polyimide used for solar array of International Space Station. SiO_2 and polytetrafluoroethylene Teflon® coatings, when deposited by co-sputter deposition, are less prone to crack due to their ability to conform to flexure compression and expansion of substrate. Painted coatings based on ZnO and Zn_2TiO_4, considered for their UV stability, have proven to maintain their thermo-optical properties in space environments, compared to zirconia, alumina, and silica pigments. The reason for using TiO2 and ZnO is their high optical visibility, electrical conductivity and thermal stability compared to bare Al oxide.

The geometry of E-sail aluminium tethers is a complex one, due to the multiple wire bonding. For this reason, ALD is considered the best choice, as the only technique that ensures the complete conformality of the coating (Alessandri *et al.* (2009), Borgese *et al.* (2011), Hazra *et al.* (2012)).

It is well known that aluminium is a high reflecting metal in the whole visible and infrared range. As a consequence, it absorbs less than 10% of the solar energy. One way to increase such a value would be to grow a thin oxide layer. Roberto Li Voti has performed some numerical calculations for different oxide layers (Al_2O_3, ZnO and TiO_2) and different thicknesses by using the optical properties found in the literature (Devore (1951)). It was not possible to apply the same fitting procedure for the TiZnO coating due to the lack of information in the literature on the refractive index of the material.

In Figure 63 the absorbance, averaged over the solar spectrum (from 350 nm to 2 μm), is shown as a function of the thickness of the oxide layer for Al_2O_3, ZnO and TiO_2. Absorbance is calculated for normal incidence (dashed line) and over the whole solid angle of acceptance (continuous line).

By a first inspection of Figure 63, a maximum of absorbance can be obtained for thin films of about 50-100 nm for all the investigated oxides, giving a strong case for our experimental work. Thin films act in

this case as anti-reflecting coatings and maximise the absorbance. The other minor oscillations of the curves are due to interference effects (Li Voti (2012), Li Voti *et al.* (2012)).
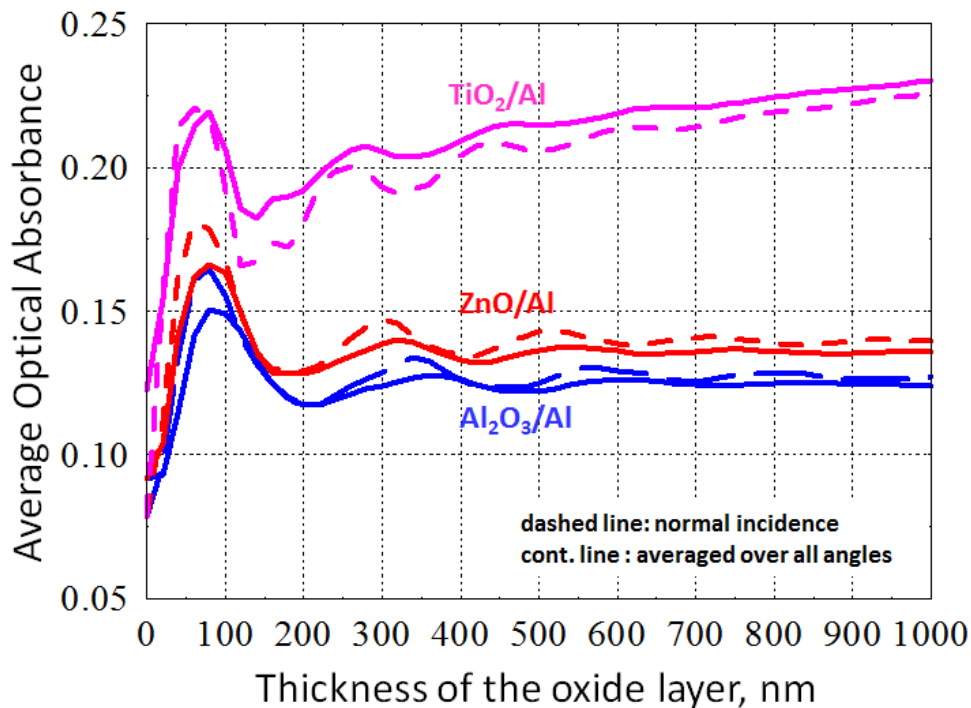
Figure 63: Average optical absorbance of Al_2O_3, ZnO and TiO_2 coated aluminium versus the thickness of the oxide layer. Hassan et al. (2017).

The mixed oxide contained Ti and Zn in mole ratio 1.75 (Borgese *et al.* (2011)), selected on the basis of the observed electrical resistivity (Hazra *et al.* (2012)). TiO_2 and Ti-Zn mixed oxide grown in the selected conditions are amorphous. It was also observed that ZnO is polycrystalline (Alessandri *et al.* (2009)). Table 1 resumes all the samples considered in the present study, specifying substrate, coating material and thicknesses, with nominal and experimental values obtained by FIB and optical measurements respectively.

The flat aluminium samples (series 4000, 4.4 % Si) were polished to obtain roughness average about 20 nm, comparable with the one of the bare tethers. The roughness average, Ra, of the tether was measured with a confocal profilometer (Leica DCM 3D) both on wires and flat samples (Hassan *et al.* (2017)). These samples can be considered smooth for what concerns the emissivity according to Wen *et al.* (2009). Their roughness should not affect the emissivity of the samples due to the fact that the infrared wavelengths are much higher than the dimension of peaks and valleys of the surface.

TiO_2, ZnO and TiZnO were deposited by ALD in the Savannah 100 flow reactor (Ultratech Cambridge Nanotech Inc.) at 90 °C. Titanium source was tetrakis(dimethylamido)titanium (TDMAT 99.999%; Sigma–Aldrich, Germany). Zinc source was diethylzinc (DEZ; 99.999%; Sigma–Aldrich, Germany). Oxygen source was ultrapure water (H2O Conductivity 0.054 μS/cm) produced directly from tap water with a Direct-Q system (Millipore, Italy). Detailed description of deposition parameters and processing cycles for the studied materials have been already reported (Hazra *et al.* (2012)).

Nominal thickness of 25, 50 and 100 nm were selected, and the processing cycles number was calculated on the basis of the growth curves of TiO_2, ZnO and mixed oxide on Si wafer substrate (Hassan *et al.* (2017)).

The optical absorbance and emissivity have also been measured on the flat samples. The experiments and results are discussed in chapter 6.

Table 1: Description of the studied samples. Substrate, coating material and nominal thickness are reported respectively in the 1st, 2nd and 3rd column. Thickness measured by coupled FIB-SEM measurements and estimated by fitting of reflectance spectra are reported in the 4th and 5th columns respectively.

	SAMPLE		THICKNESS (NM)	
N.	Substrate	Coating	Nominal	FIB-SEM
0	Al tether		_	_
1	Al tether	TiO_2	25	33.7 (2.3)
2	Al tether	TiO_2	50	51.9 (3.3)
3	Al tether	TiO_2	100	112.4 (5.2)
4	Al tether	ZnO	25	28.0 (2.4)
5	Al tether	ZnO	50	46.7 (3.7)
6	Al tether	ZnO	100	76.8 (9.6)
7	Al tether	Ti-Zn mixed oxide	25	26.0 (2.7)
8	Al tether	Ti-Zn mixed oxide	50	57.8 (4.1)
9	Al tether	Ti-Zn mixed oxide	100	97.2 (7.6)
10	Flat Al	TiO_2	100	102 (1)
11	Flat Al	ZnO	100	55 (7)
12	Flat Al	Ti-Zn mixed oxide	100	144 (3)

5.5.3. Microstructural properties of the coatings

The thickness of the ALD coatings was measured with a FEI Helios NanoLab600 FIB/SEM dual-beam instrument at University of Roma Tre (LIME laboratory). A cross-section of the coated tether was made using the ion beam; the coating was then observed using the *in-situ* SEM.

The tether was placed in the vacuum chamber of the FIB with its lateral surface in a position orthogonal to the ion gun, so that the non-flat surface seen from the gun was completely covered by the coating. Afterwards, platinum was preliminary deposited in order to protect the surface of the sample from the subsequent milling. This way, the artefacts created during the milling of the material were minimised. Then, the milling was performed using a relatively low value of ionic current (0.28 nA). The same current was used also to clean the surface at the end. Finally, the *in-situ* SEM with ionic source was used to take high-magnification images of the coating cross section. Using the ionic source

instead of the electron source allows to obtain higher contrast between the crystallographic grains and to better observe the sample microstructure.

FIB measurements are used to study the morphology and the thickness of the coating layers deposited on tethers and flat aluminium substrates. Figure 64 shows SEM images of FIB cross sections taken on sample n. 0, n. 3, n. 6, and n. 9 respectively. Different features can be highlighted in the pictures where coating thicker than 50 nm is shown. The surface is rough and presents grooving (Figure 64 c), with repetitive patterns in the longitudinal direction of the wire. This is probably related to the drawing process of wire production. This feature is still visible at the highest thicknesses, as expected due to the conformal features of ALD coatings. A layer is present on the uncoated tether surface (Figure 64 a) and underneath the coating (Figure 64 d). This layer is probably native Al_2O_3, naturally formed on the surface of aluminium.

The accuracy of thickness measurements by FIB cross section and following SEM image analysis may be affected by the removal of some coating from surface during the cross-section preparation. For this reason, two tests are performed on the same sample, protecting the cross section with different materials. Platinum and carbon are used as protective layers for measurements of sample n. 7, whose SEM images are reported in Figure 65 (a) and Figure 65 (b) respectively. The average calculated thickness, based on the measurements reported in Annex A, is not significantly different in the two cases, confirming that the measured thickness is comparable. Figure 65 (b) also shows that the ALD coating can effectively penetrate inside cracks. The calculated average thicknesses obtained from FIB measurements are reported in Table 1. Thickness comparison with nominal values highlights an overall agreement, considering the different substrate materials. Higher values can be due to the rounded geometry of tethers, and the high difficulty to create the cross section in perfect perpendicular conditions.
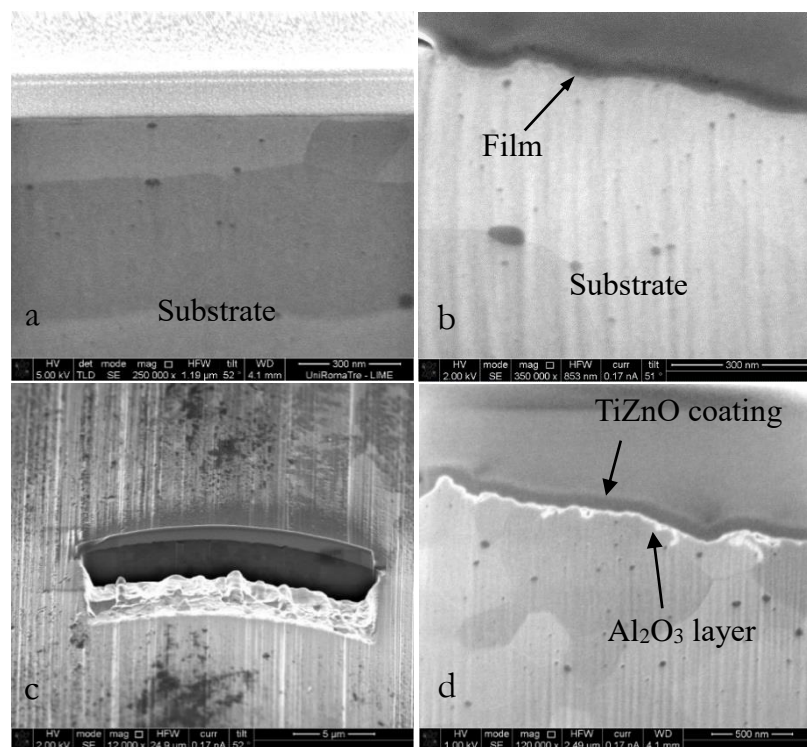
Figure 64: SEM images of FIB cross section of sample n. 0 (a), n. 3 (b), n. 6 (c), and n. 9 (d) respectively.
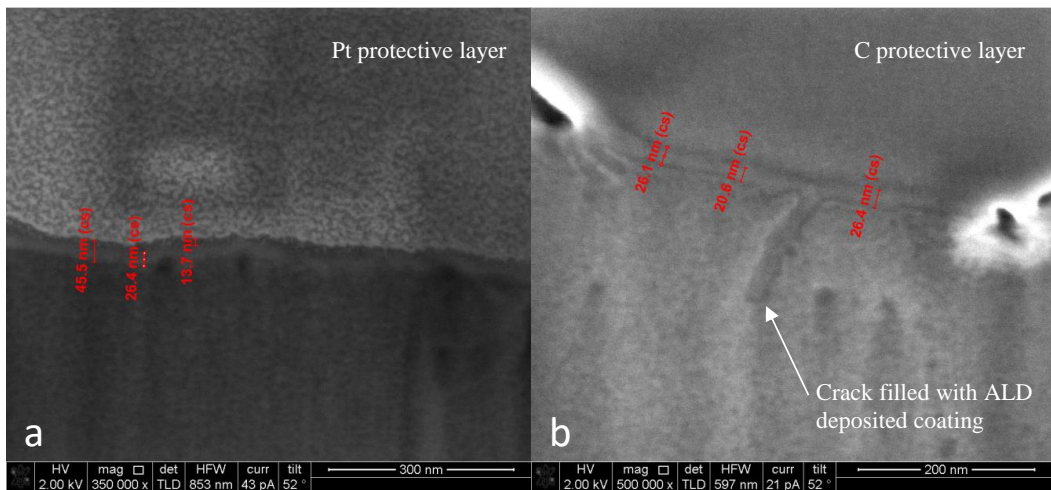
Figure 65: SEM image of FIB cross section of sample 7 protected with a layer of platinum (a) and carbon (b).

6. EXPERIMENTAL ACTIVITY: MECHANICAL TESTS ON THE BARE TETHER

6.1. SUMMARY

The experimental activities carried out on the bare tether to assess the mechanical properties at different temperatures (-40 °C up to 250 °C) are presented. A Dynamic Mechanical Analyser (DMA) has been used for this purpose. First, the mechanical test set-up is described. Then, the Digital Image Correlation (DIC) method used to verify the correct readout of the displacement of the specimen during testing is presented. The results of several test campaign are presented and discussed: tensile test to failure, load/unload test, creep test, strain rate sensitivity test and dynamic test. Finally, the results of FIB/SEM and TEM observations of the material microstructure close to the fracture section are reported and discussed.

6.2. INTRODUCTION

The objective of the experimental activity on the bare tether was to find the operating temperature range of the E-sail tether. Al-1%Si systems are mainly used in the electronics industry as a bonding device and they are not optimised for a structural application in a temperature range which may vary even of tens of degrees. This alloy has been selected by the ESAIL FP7 project team because it is considered to have the best forming performances (ultrasonic bonding for instance), on top of the usual aluminium properties. However, in the literature, Al-1%Si mechanical properties at the micron scale have not been extensively studied at variable temperatures, and we found that there is room for research in this direction.

It was therefore decided to perform mechanical tests using a Dynamic Mechanical Analyser (DMA Q800) from TA Instruments at the Faculty of Engineering of the University of Roma Tre. As shown in the previous paragraph, in order to derive the α/ϵ requirement for the coating of the tethers, it is necessary to estimate the operational temperature range of the material. The objective of the tests was to assess the mechanical properties of the bare tether by performing tensile tests at several temperatures above the ambient temperature. Similar tests have also been conducted at temperatures lower than ambient temperature using the DMA liquid nitrogen cooling system.

In the next paragraphs the test set-up, the test parameters and the test results are discussed.

6.3. MECHANICAL TESTS SET-UP

The DMA is capable of performing several types of mechanical tests (e.g. bending, torsion and tensile tests) controlling dynamically the applied force and displacement at a given temperature.

The instrument is provided with: (1) a clamp assembly, used to install the specimen; (2) a mechanical section enclosure, where the motion of the free clamp is mechanically controlled and the force and the

displacement are measured (3) a furnace assembly, which embeds the heaters and is used to create a stable environment temperature during the tests.

The instrument and its specifications are shown in Figure 66. The minimum force that the instrument can apply is 0.1 mN, while the maximum force is 18 N. The force resolution is 0.01 mN and the strain resolution is 1 nm. The DMA allows performing tests in the temperature range -150 °C to 600 °C.

The instrument is provided also with a tank for the LN2 distribution in the DMA temperature stabilised chamber. The tank has been used to perform the tests at temperatures lower than ambient temperature.
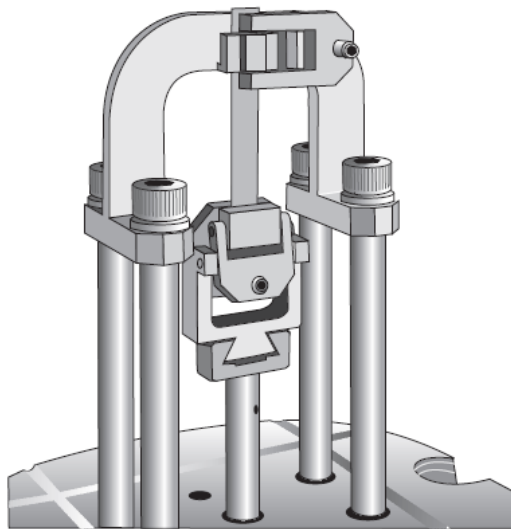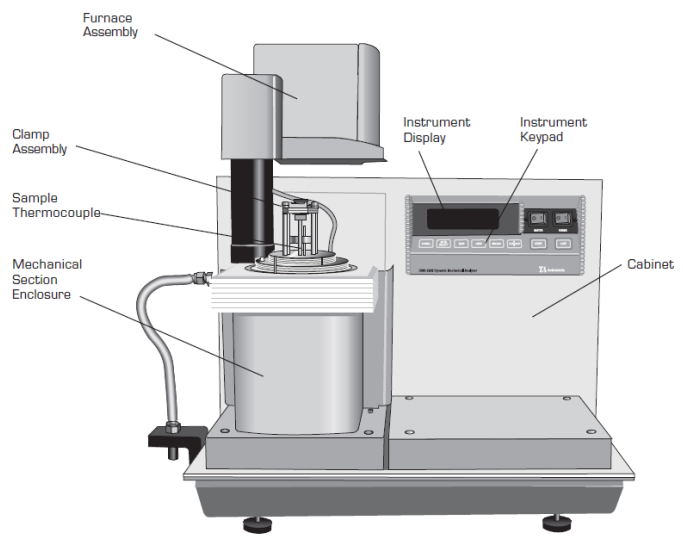
Maximum Force	18 N
Minimum Force	0.0001 N
Force Resolution	0.00001 N
Strain Resolution	1 nanometer
Modulus Range	10^3 to 3×10^{12} Pa
Modulus Precision	± 1%
Tan δ Sensitivity	0.0001
Tan δ Resolution	0.00001
Frequency Range	0.01 to 200 Hz
Dynamic Sample Deformation Range	± 0.5 to 10,000 μm
Temperature Range	-150 to 600 °C
Heating Rate	0.1 to 20 °C/min
Cooling Rate	0.1 to 10 °C/min
Isothermal Stability	± 0.1 °C
Time/Temperature Superposition	Yes
RH Control	Optional

Output Values		
Storage Modulus	Complex/Dynamic Viscosity	Time
Loss Modulus	Creep Compliance	Stress/Strain
Storage/Loss Compliance	Relaxation Modulus	Frequency
Tan Delta (δ)	Static/Dynamic Force	Sample Stiffness
Complex Modulus	Temperature	Displacement
Relative Humidity (Optional)		

Figure 66: DMA Q800, image (left) and specifications (right).

Details on the use of the DMA are provided in Menard (2008). The last chapter in particular provides indications on the right clamp to select and the test parameters (Figure 67). The author explains that the choice of the type of fixture is driven by the modulus of the material, its form and the type of stress the material experiences in use, suggests to select the fixture that allows an easy installation and

provides the most reproducible data. In our case, the best clamp and test type for the wire is the extension test using the film clamp. The fibre clamp was not selected due to the difficulty in the installation of the tether sample. The sample, in fact, was always cut close to one end due to the presence of sharp edges at the clamp.

Menard also warns about the difficulty of performing the extension tests since "the geometry is more sensitive to loading and positioning of the sample than most other geometries. Any damage or distress to the edges of the sample as well will cause inaccuracies in the measurements. A nick in the edge will also often cause early failure, as it acts as a stress concentrator. After loading a film or fibre in extension, it is important to adjust it so that there are not any twists, the sides are perpendicular to the bottom, and there are no crinkles".

Samples and Fixtures

Very Hard	3 pt. bending (large) 4 pt. bending (large)	Gooey	Various Parallel Plates Cone and Plates Torsion braid
Hard	3 pt. bending (large) Torsion bar	Fluid	Cone and Plate Parallel Plates Couette
Stiff and Flexible	3 pt bending (medium) Torsion bar	Film	Extension
Pliable	3 pt bending (medium) Dual cantilever Torsion bar	Fiber	Extension
Soft	3 pt bending (small) Dual cantilever Torsion bar	Suspension	Parallel Plate Cone and Plate Cup and Plate Couette
Very soft	Dual cantilever Axial Parallel Plates Torsion bar	Powder	Cup and Plate

Figure 67: Samples and fixtures of the DMA. Menard (2008).

The performance range of the DMA with the tension film/fibre clamp is identified by an envelope of specimen dimensions (based on the geometry factor) and material modulus, as shown in Figure 68. The geometry factor of the specimen is equal to the length of the specimen divided by the cross sectional area. In our case, considering a minimum length of the specimen of 4 mm and a wire having 32 μm diameter, we obtain a geometry factor of about 5×10^4 1/mm. The modulus is in the order of GPa. We can therefore identify that the DMA is operating inside its working envelope. More precisely, it is operating close to the upper boundary of its working envelope, due to the elongated shape of the sample.
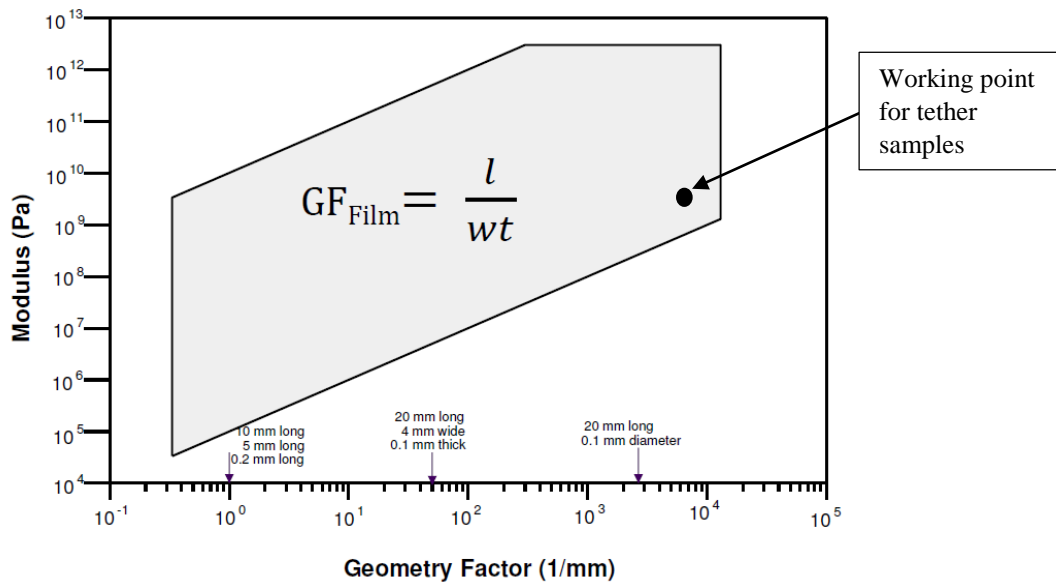
Figure 68: Working envelope of the DMA film/fibre clamp. Courtesy of TA Instruments.

The performance of mechanical tests on microscale wires using the extension clamp is not a trivial task. Challenges are not only related to the difficulty in handling the sample, but also to the geometric factors of the sample itself. While the geometry of standard bulk specimen in a tensile test is fixed (10 mm diameter and 100 mm length), this is not the case for the wires. This issue has been discussed, among others, by Liu *et al.* (2004). Moreover, the wire cannot be shaped in a way that would allow the control of the flow stress during the tests. In this sense, the clamping mechanism becomes a crucial step in the test set-up.

In order to install the tether in the clamp of the instrument without damaging the sample, a dedicated fixture needs to be developed. The fixture has been prepared making reference to the Springer Handbook of Materials Measurement Methods (Figure 69) and the ASTM-D3379 standard. Such standard foresees the use of a "mounting tab" to which the wire is attached, for example by means of glue. The "mounting tab" is then gripped to the DMA before cutting the support on the two sides and thus leaving the sample free to be stretched. However, the support is an additional element present in the set-up that could add uncertainties in the test results, as will be discussed later in the text.

A test was considered successful only when the fracture occurred in the middle of the sample. This confirmed that the stress was correctly transferred from the clamp to the specimen. On the contrary, tests were discarded when the final rupture was taking place at the clamping points, showing that there was a stress concentration due to the presence of a sharp edge. In practice, only less than one fourth of the tests could be considered successful, with related data being analysed. This shows the sensitivity of the results to the test set-up.
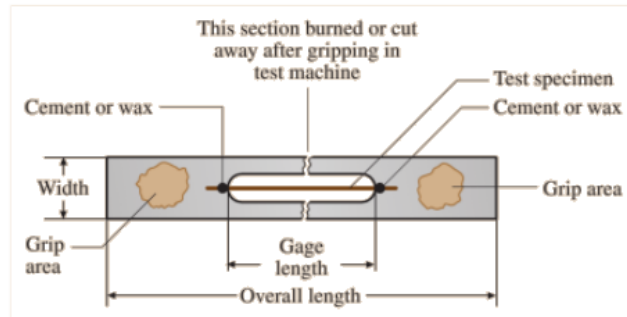
Figure 69: Springer Handbook of Materials Measurement Methods[4].

After a first test campaign, it was noticed that the optimal length of the sample was between 4 and 6 cm. It was then decided to design two different supports as interface with the DMA film tension clamp:

- Flexible support produced by cutting a thin transparent paper for printers or Kapton tape for testing at high temperature (Figure 70 a and c).
- Rigid support produced by latter cutter of a PMMA layer of 3 mm thickness. The laser cutter used was the 100 W RONCHINI MASSIMO SRL model RM-Lasermark 1613 (Figure 70 b and d).

In general, it was considered that the rigid support provided a better set-up due to the fact that less stress was induced to the sample during handling and installation on the DMA and due to a better alignment of the wire on the support itself. With the flexible support 167 tests have been conducted in total. Among them, only 20% has been considered successful. In Figure 70 c) the sample broken after the test in the middle of the support is shown.

a) Geometry of the flexible support	b) Geometry of the rigid support

---
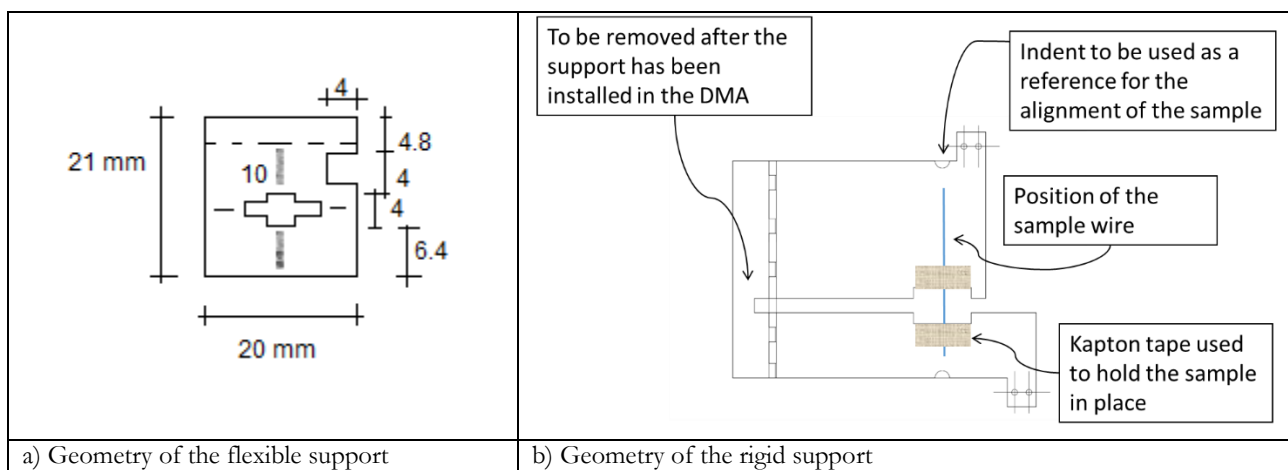
[4] ASTM D3379-75e1 Standard Test Method for Tensile Strength and Young's Modulus for High-Modulus Single-Filament Materials

| c) Image of the sample installed on the Kapton flexible support after the test. | d) Image of the sample installed on the rigid support (before testing). |
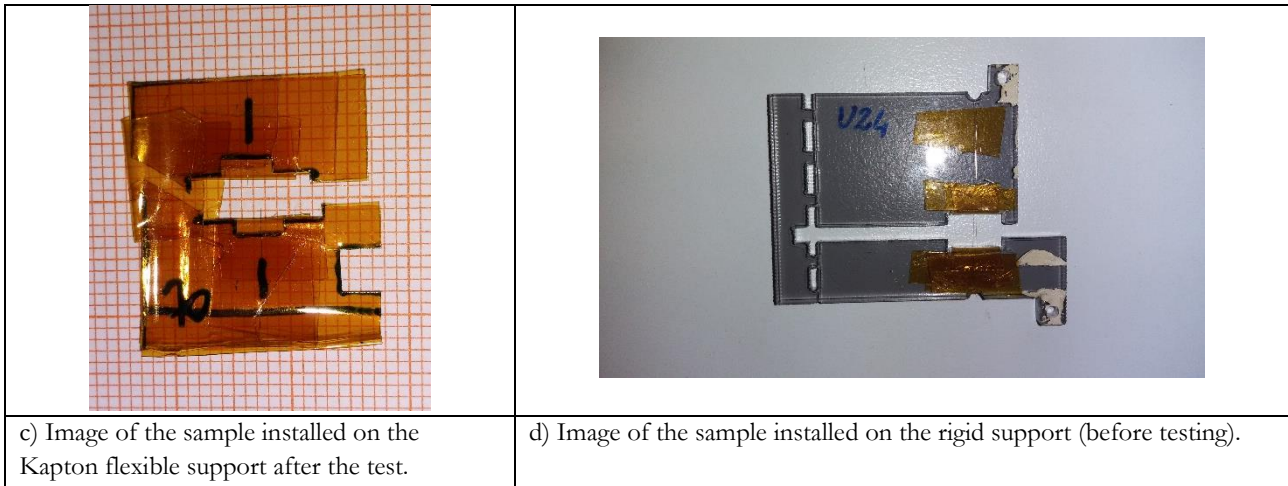
Figure 70: Interface for tether installation on the fibre clamp.

Kapton tape was used to fix the tether specimens to the support for easier handling before installing them on the DMA. Kapton tape adhesive is silicon, which has a working limit of about 300 °C. Generally, the adhesion on steel is 6 N per 25 mm tape width. The adhesion at higher temperature is generally quite stable, but it is not shared by the manufacturer. In our tests we did not exceed 250 °C, in order to avoid uncertainties due to the reduced adhesion of silicon.

Figure 71: Sample installed in the DMA before and after the tensile test.

Finally, the instrument is calibrated by means of several different calibrations. Four of them, the calibration of the electronics, the force, the dynamics calibration and the calibration of the temperature, are done once every few months. Each time the instrument is turned on, three other calibrations need to be performed: the calibration of the position, the calibration of the mass of the movable part and of the compliance (a measure of the stiffness of the DMA clamps).

6.3.1. Determination of the initial length of the sample

The optimal way to perform tensile tests is to use an extensimeter. Due to the little dimensions of the sample, such approach is not practical. It was then decided to verify the measure of the displacement using the Digital Image Correlation (DIC) method, at ambient temperature. A similar approach has been recently used in parallel and independently by other researchers to support the mechanical testing of Au bonding wires (Takagi *et al.* (2016)).

Since it is not possible to know precisely the length of the tether specimen during the DMA tests, it was decided to use markers applied on the wire at known positions using the FIB, which could be monitored with a video camera.

Small platinum markers were placed all along the wire. The separation length between the markers was 500 μm over a length of 15 mm centred in the middle of the tether. The precise geometry is shown in Figure 72. The platinum deposition was made with ions at 0.46 μA and 30 kV. The dimension of the platinum deposition geometry was 2 x 20 μm length and 0.5 μm width.

The platinum marks were placed on top of the tether's cross-section so that the video camera could record their position during the DMA test itself. The DIC method was then used to determine the strain during the test.

| a) Geometry of markers. | b) Side view of the tether and platinum deposition. |

c) Position of FIB markers.

| d) Sample installed on the FIB stub | e) Stub installed in the FIB chamber |
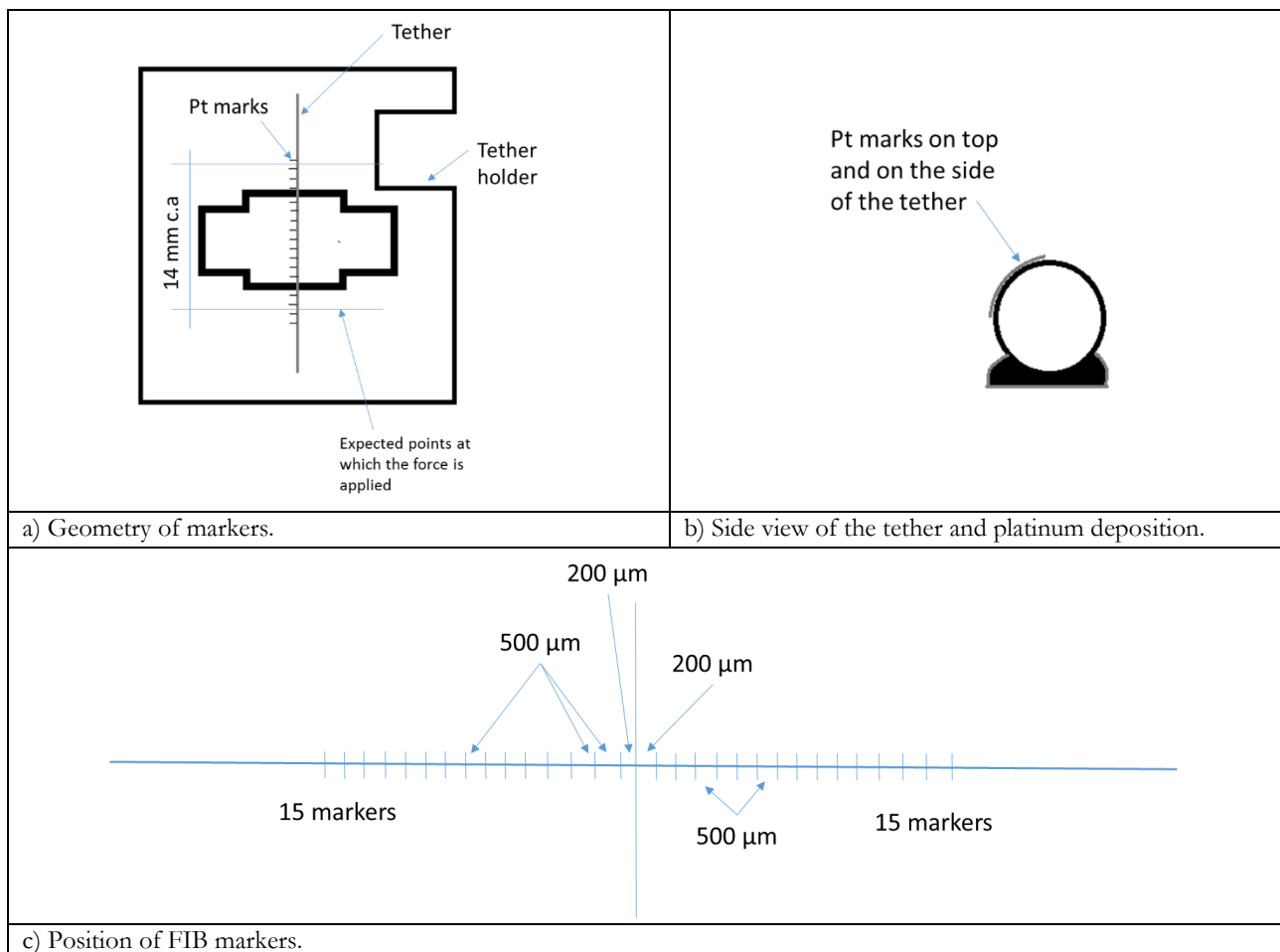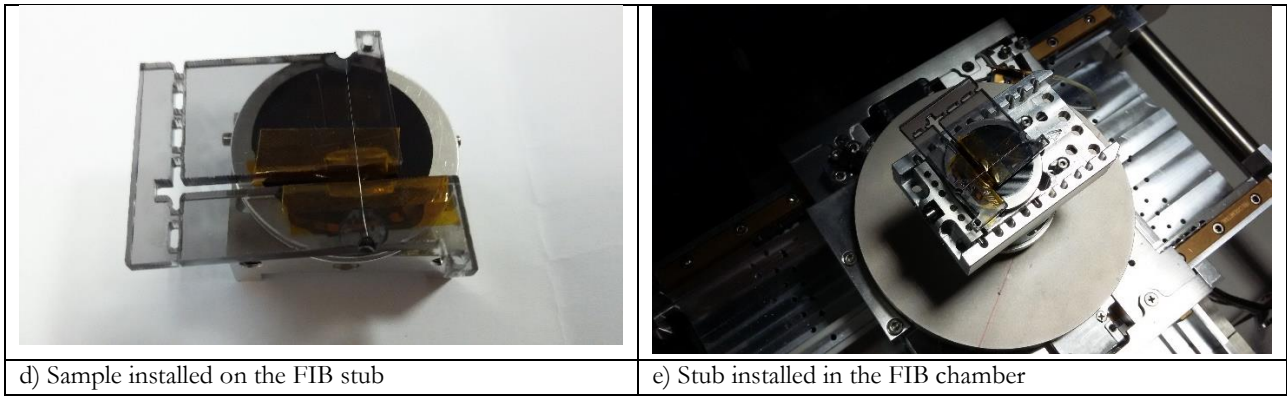
Figure 72: DIC analysis features

The video of the test was converted in TIFF images using the SW AVS Video Converter 9.4. The TIFF images were finally converted in BMP images using the SW Infraview. 367 images were analysed in total by the DMA (1 image per second). Three different images of the video taken during the test are shown in Figure 73.
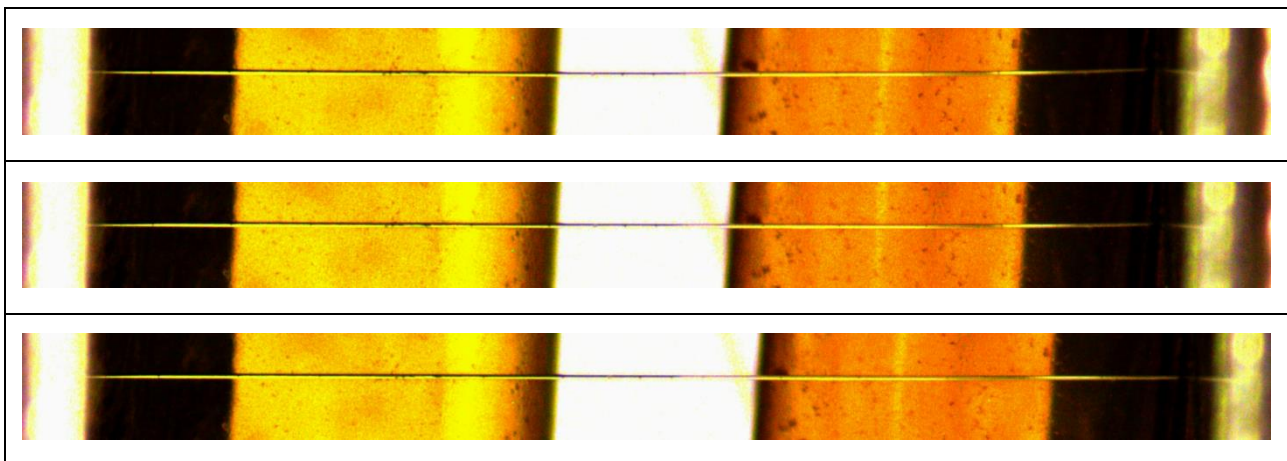
Figure 73: Screenshots during the tensile test.

The result of the markers deposition is shown in Figure 74:

a) FIB markers deposition before tensile test

b) Details off the markers

c) FIB markers deposition after the tensile test
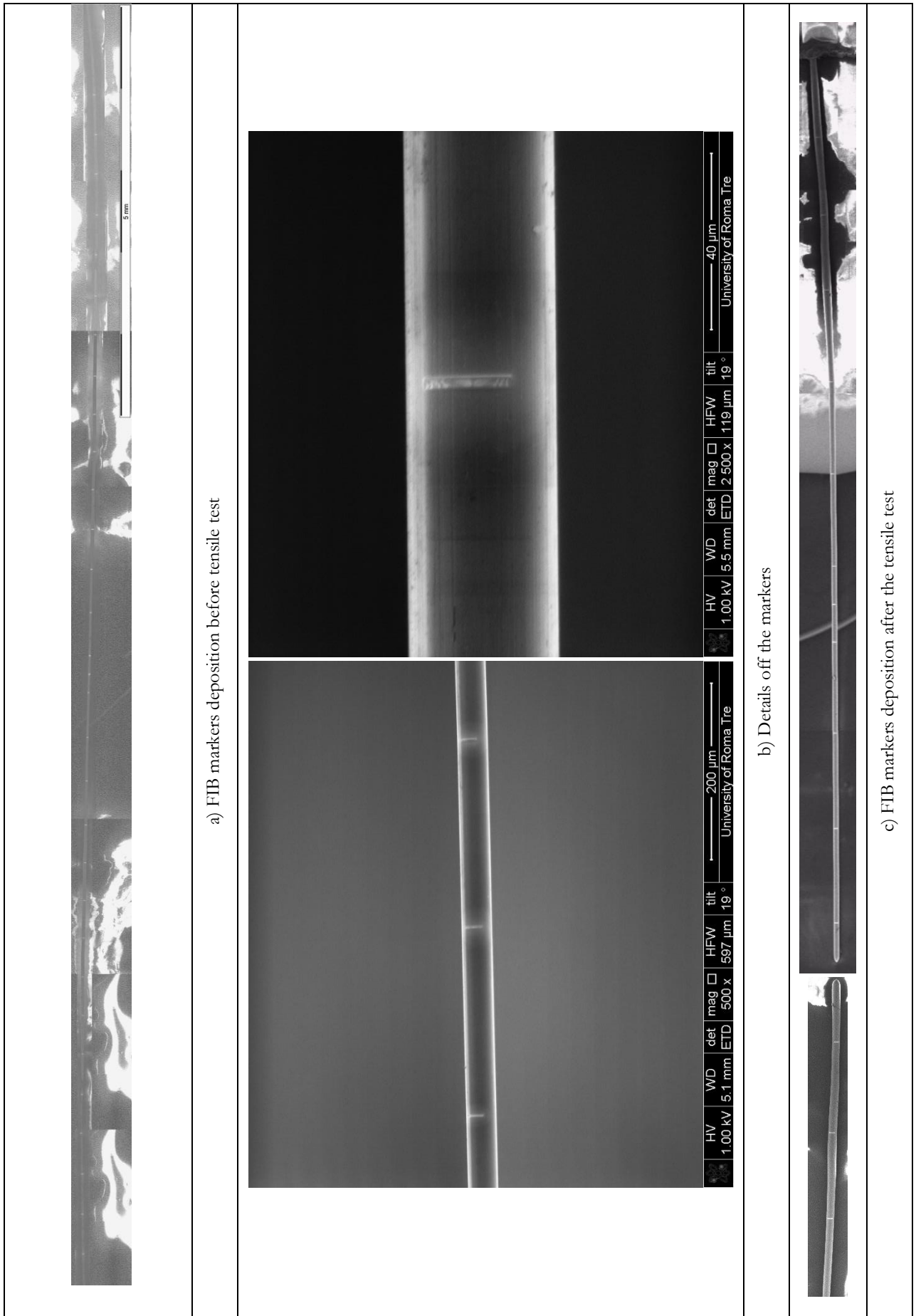
Figure 74: Images of the FIB markers on the sample.

The BMP images were then analysed by the DIC software under Matlab environment. The Matlab software Digital Image Correlation and Tracking, developed by Melanie Senn (Fraunhofer institute) in the frame of the FP7 iSTRESS project (Sebastiani *et al.* (2015)), was used. The software is capable of calculating the mean strain at each instant (each image) with respect of the original position (the first image).

The grid for the DIC was selected so that the position of each FIB marker was followed during the analysis. Alternative grids have also been used, such as markers linearly spaced along one line or an entire 2D area covered with markers. However, these alternative methods did not provide reliable results. In Figure 75 the green crosses are corresponding to the original position of the FIB markers and the red crosses represent the instantaneous position of the FIB markers.
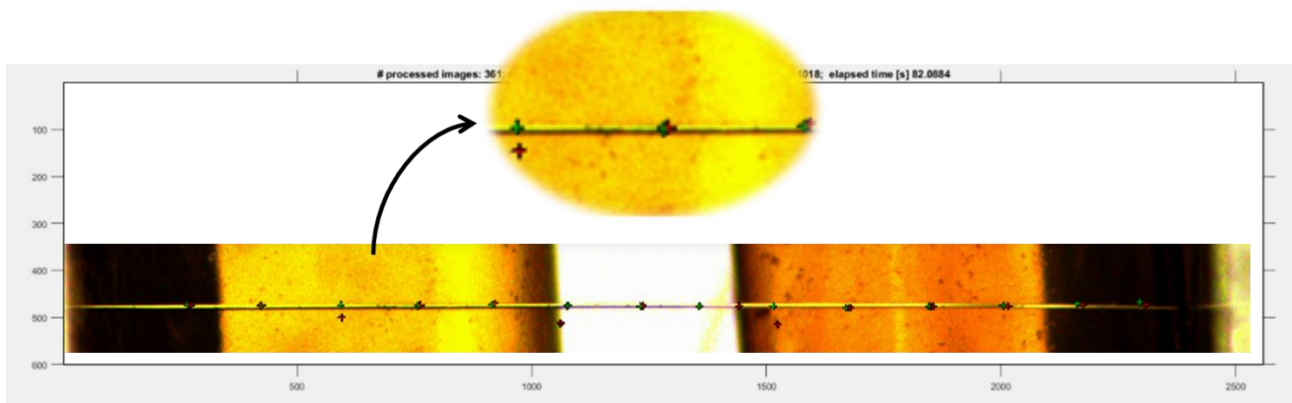
Figure 75: Screenshot taken during the DIC software analysis showing the instantaneous position of markers.

In Figure 76 a comparison between the strain recorded by the DMA and the one obtained with the DIC method are shown. The values measured by the DMA at the beginning of the test were not recorded for an error in the software set-up. The two measures are in good alignment and the maximum displacement differs by 13% with respect to the value measured by the DMA.

The stress/strain curves built using the DMA data and the DIC data are shown in the following plot (Figure 77). The Young modulus measured using the DIC data is 24 GPa.

91
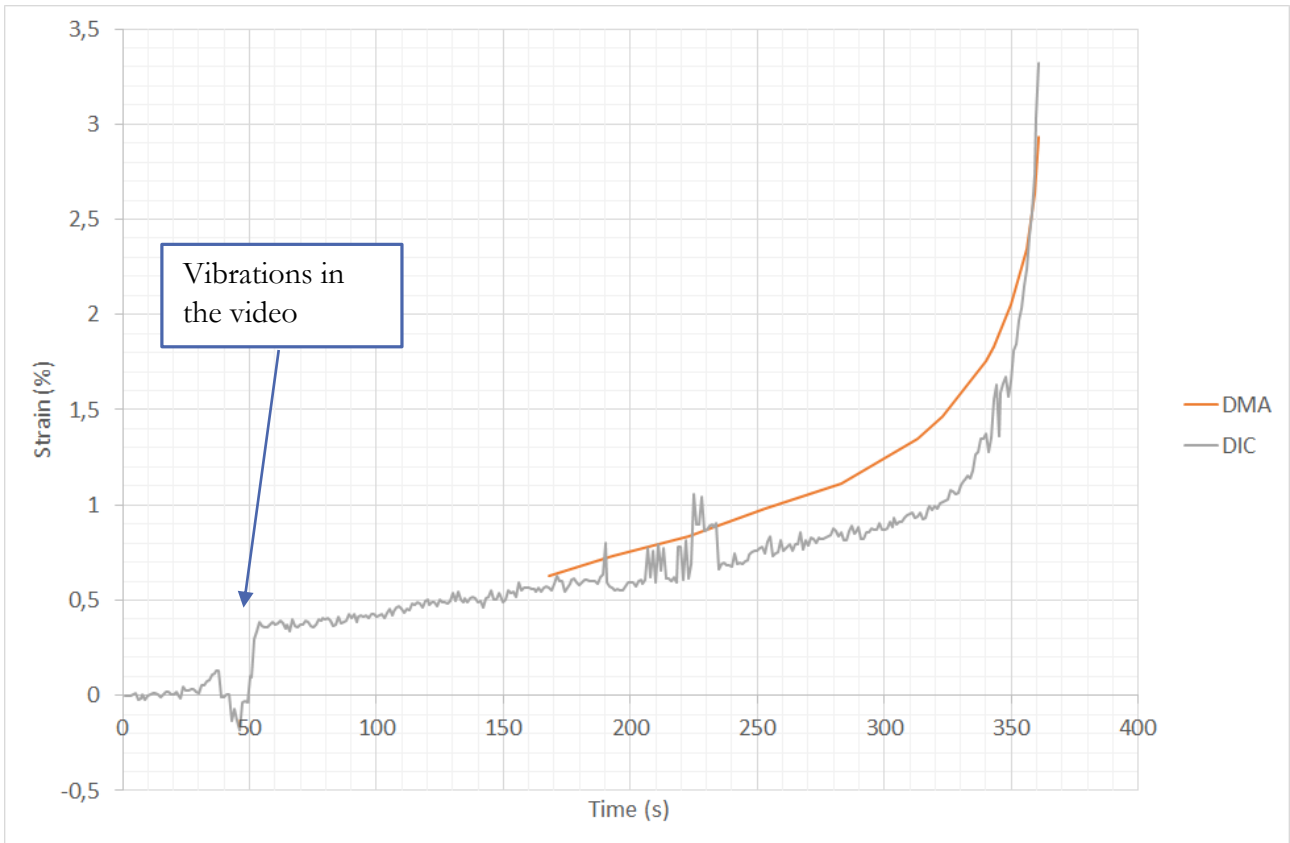
Figure 76: Strain evolution during the tensile test.
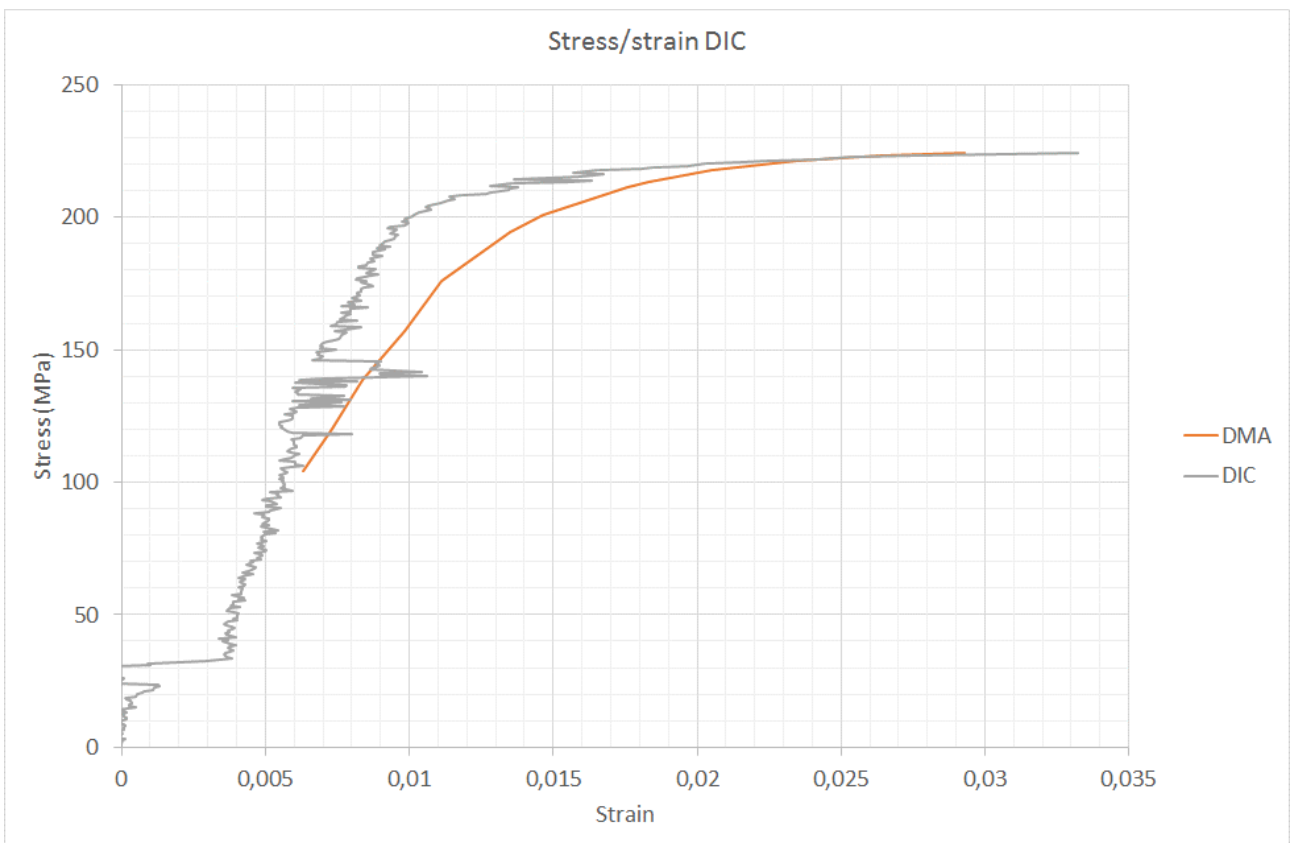
Figure 77: Stress-strain curve during the tensile stress.

It was concluded that the strain measurement of the DMA is relatively reliable, with an error in the order of 13%. No significant sliding of the sample has been observed during the test.

6.3.2. Verification of sliding for the tests at high temperature

The DIC method could be applied at ambient temperature, but not at higher temperatures due to the need to have the furnace closed and therefore preventing the optical observation of the specimen during the test itself.

It was therefore decided to coat one sample to be tested at temperatures higher than ambient with gold to verify if sliding occurred during the test. The gold coating was used to avoid polarisation of Kapton adhesive in order to observe how the wire was attached to the support.

The sample has then been observed with the Scanning Electron Microscope (Figure 78) after a test carried out at a temperature up to 115 °C. We could observe the effects of sliding at the Kapton/wire interface since some adhesive was visibly stretched. A sliding of about 50 μm was observed on one side and of about 100 μm on the other side (about 4% of the total sample length). For this reason, the test at higher temperatures should be considered having a higher error in the measurement of the displacement.

a) Detail of sample attached to the support (left).	b) Detail of sample attached to the support (right).
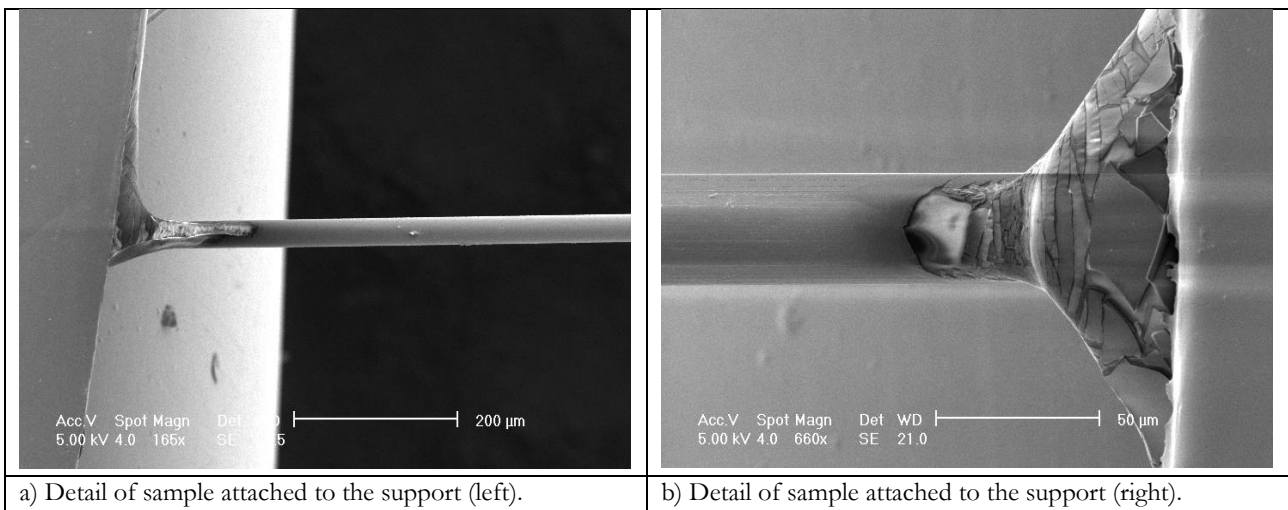
Figure 78: SEM image after the test.

6.4. TEST PARAMETERS

Different tests were conducted on the bare tether at different temperatures:

- Tensile tests until rupture (using DMA controlled force mode). Several tests have been conducted at different temperatures (-40 °C, -20 °C, 0 °C, 25 °C, 40 °C, 50 °C, 60 °C, 70 °C, 80 °C, 100 °C, 110 °C, 150 °C, 250 °C). The rates of application of the force were 20 mN/min, 30 mN/min and 60 mN/min. The tests have been executed using the flexible supports (made by plastic or Kapton at higher temperatures). In some cases, and at lower temperatures (< 70 °C), small pieces of graphite adhesive have been used to hold the tether in place during the test. For

each test, the target temperature has been reached by increasing the temperature at a rate of 3 °C per minute. The sample then was stabilised for about 1 hour and a half while maintaining it in tension at the preload (10 mN or 50 mN). This waiting time was needed to stabilise the displacement readout.

- <u>Creep test (using DMA creep mode)</u>. The test has been executed using the rigid support. One creep test has been conducted applying a load of 1 mN with a rate of 1 mN/min and maintaining the load for one hour at 35 °C. After the load was removed, the material has been left free to relax for 2 hours. The temperature was then increased to 50 °C and to 80 °C, repeating the same procedure. After the temperature was changed, at a rate of 3 °C/min, the sample was stabilised for three hours with no preload applied.

- <u>Load/unload test (using DMA controlled force mode)</u>. The test has been executed using the rigid support. Temperature stabilised at 32 °C. A ramp force was applied at a rate of 3 mN/min up to 15 mN. The load was then immediately removed at the same rate. The maximum load was selected in order to avoid the yield of the material.

- <u>Strain rate sensitivity test (using DMA strain rate mode)</u>. This test has been conducted at a constant temperature of 110 °C after two hours of stabilisation time. The test has been performed applying controlling the displacement at rates of 6 μm/min (1.73×10^{-3} s^{-1}) and 12 μm/min (3.48×10^{-3} s^{-1}).

- <u>Dynamic tests (using DMA multifrequency mode)</u>. Frequency scans were conducted at 1, 2, 5, 10, 20 and 50 Hz at different temperatures (35 °C, 45 °C, 55 °C, 65 °C, 75 °C, 85 °C, 95 °C, 105 °C, 115 °C). Each time the temperature was increased, the sample was left free to stabilise for 2 yours without any preload applied. The oscillation was of 5 μm with a preload force, or static force, of 1 mN. The manual of the DMA does not recommend to perform tests at amplitudes lower than 5 μm. Moreover, a "force track", or "autostrain", of 125% was applied by the DMA to automatically adjust the static force to be a specified percentage greater than the force required to apply the oscillatory amplitude. This is necessary to avoid the sample to be loaded in compression in an undesirable manner.

6.5. RESULTS

6.5.1. Tensile tests to failure

Below, a SEM image of a fractured wire is shown. As it can be seen, the fracture is highly ductile, as it is typically observed for pure aluminium. A similar type of fracture, by necking to a single point, has been observed also by Danaher *et al.* (2011).
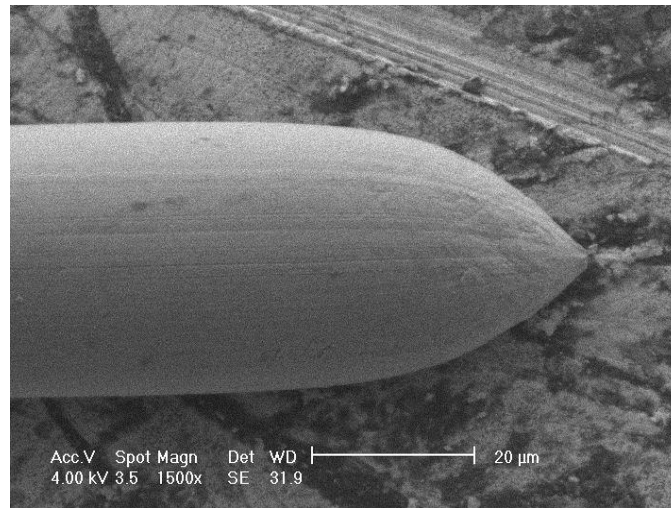
Figure 79: SEM image showing a detail of the fractured tether (fracture by necking to a single point).

The most significant result of this test campaign is the break load at different temperatures, both above and below the ambient temperature.

It can be clearly noticed from the following plots (Figure 80 and Figure 81) that there is a strong correlation between the temperature and the break load. At ambient temperature the mean value is 184 mN and the standard deviation is 5 mN. This value is in line with the product specifications provided by the manufacturer, TANAKA electronics, which is in the order of 186-206 mN[5].

The force rate did not seem to affect significantly the breaking load at the temperature observed, while the preload slightly decreased the breaking load.

The breaking load decreased with the increase of the temperature at a rate of about 0.5 mN/ °C. With an increase of 10 °C, the breaking load is reduced by almost 3%. This could be an important design parameter for the E-sail technology.

The test at 250 °C was not repeated because it resulted to be close to the working limit of the Kapton, the material used for the support of the specimen.

---

[5] TANAKA Bonding Wire Products Catalogue 2015.
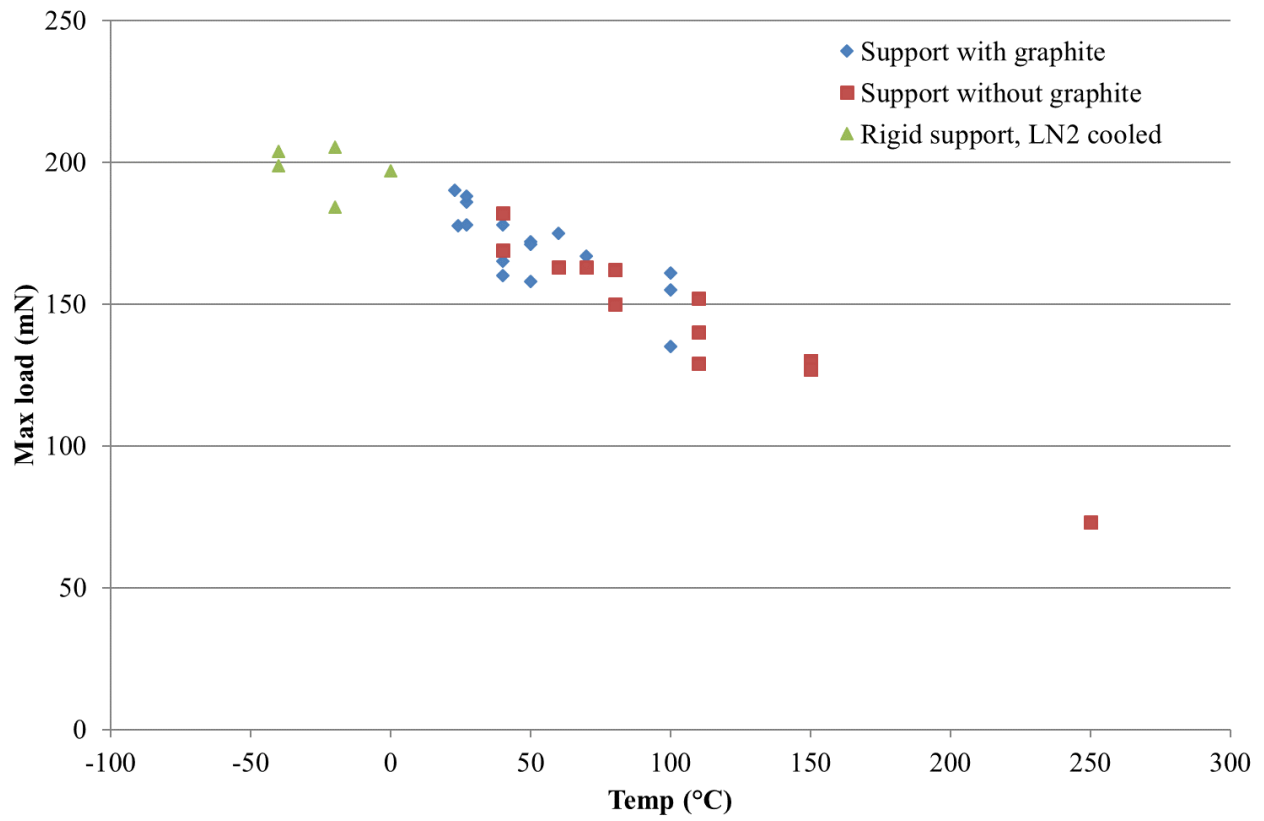
Figure 80: Breaking load versus temperature of the Al-1%Si wire.
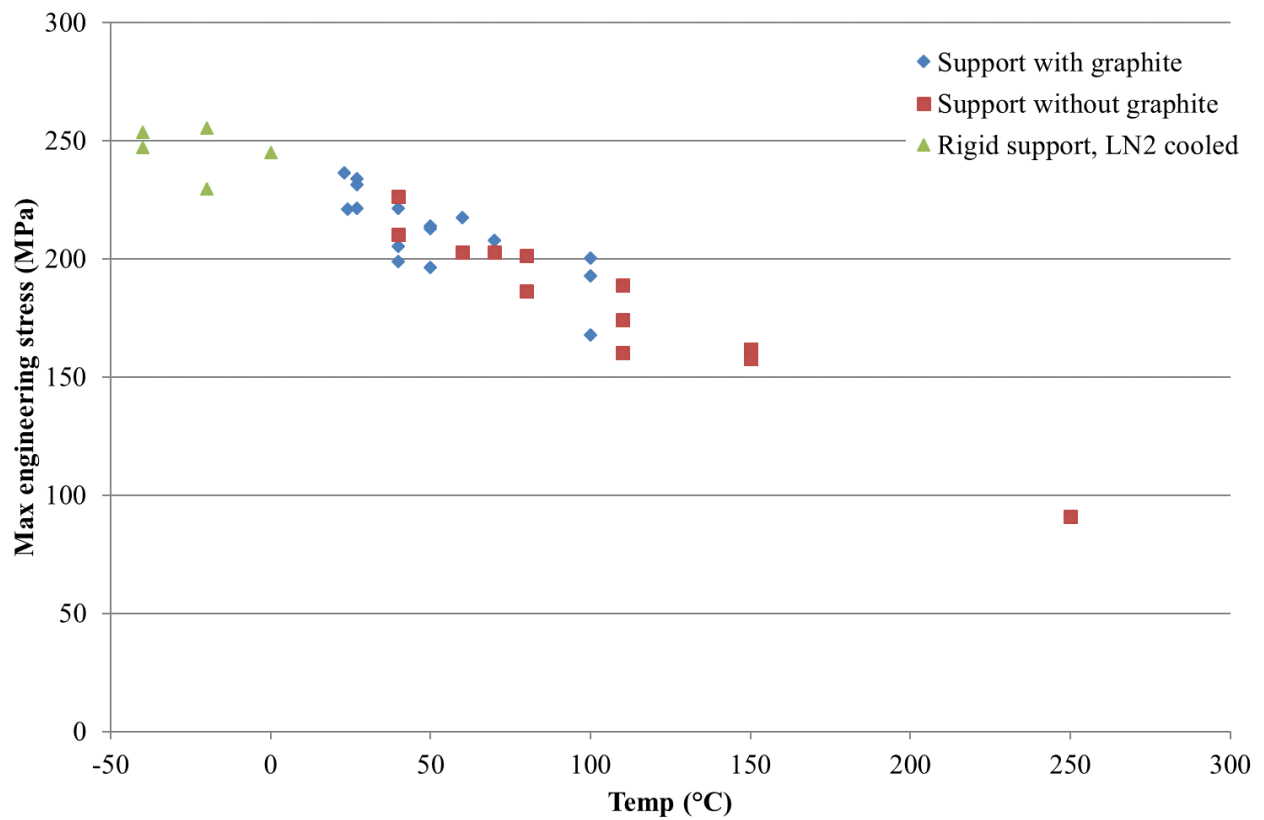
Figure 81: Engineering stress at failure versus temperature of the Al-1%Si wire.

96

The measure of the strain is affected by the errors related to the sliding of the sample inside the support, as explained in the previous paragraphs. Even if the silicon adhesive of the Kapton tape is supposed to degrade only at temperatures higher than 250 °C, the sliding prevented to have a significant value of strain, at least for temperatures above 100 °C. The graphite, used to hold the tether in place, seemed to degrade at high temperature and to slide on the Kapton underneath. Data related to the true strain at failure are reported in the following plot (Figure 82).
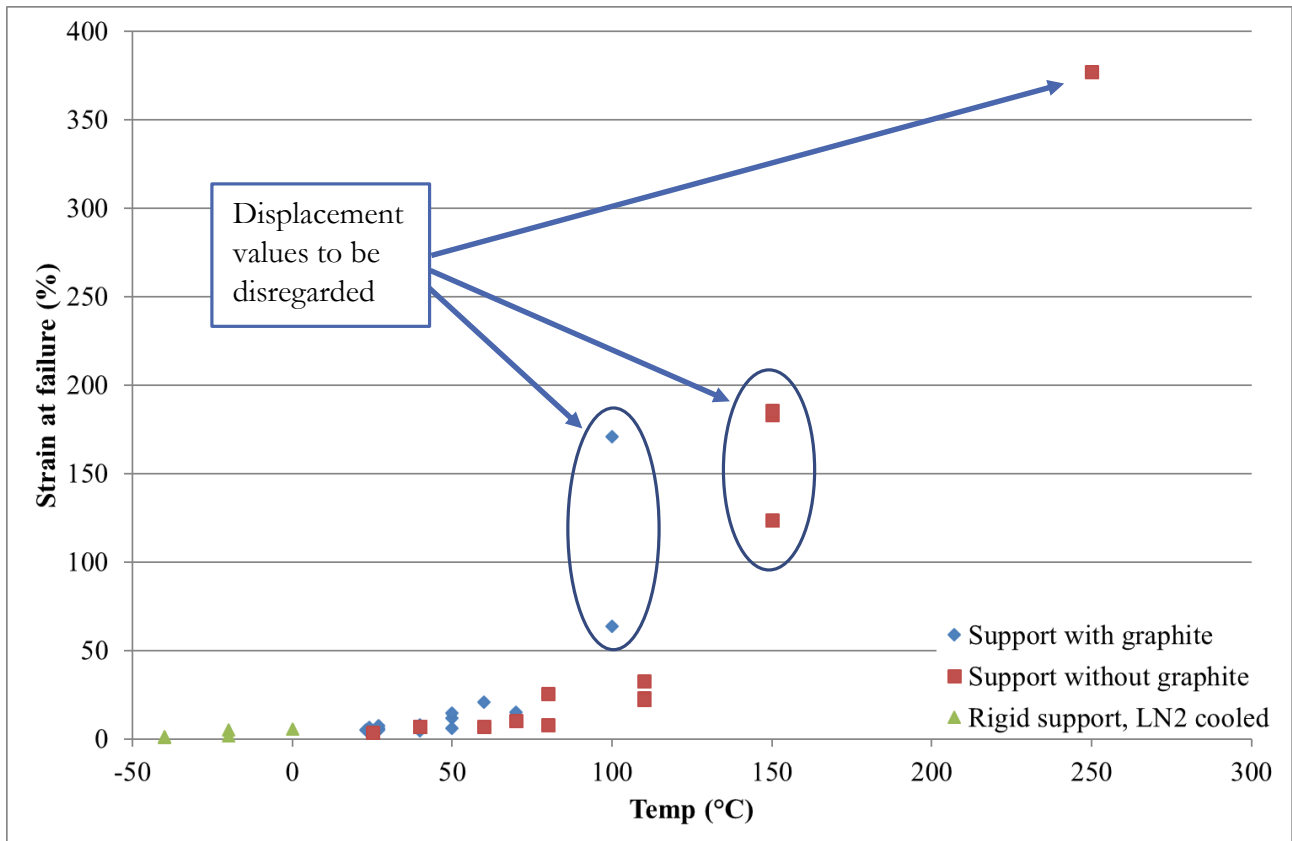
Figure 82: True strain at failure versus temperature of the Al-1%Si wire.

After having eliminated some data points related to the measure of the true strain, we concentrated our analysis on the following plot (Figure 83).

The maximum strain at ambient temperature resulted to be 5.7% with a standard deviation of 1.2%, slightly higher than the elongation to failure provided in the specifications by TANAKA Electronics (0.5% to 4.5%).

While at ambient temperature the value of the true strain is relatively repeatable, at higher temperature a high variability is observed. The general trend shows an increase in the displacement at failure when temperature increases. At 110 °C the mean strain to failure is 26%, with a standard deviation of 6 %.

We can also see the effect of the rate of the application of the force on the slope in Figure 84.

All tensile test data are reported in Appendix B.
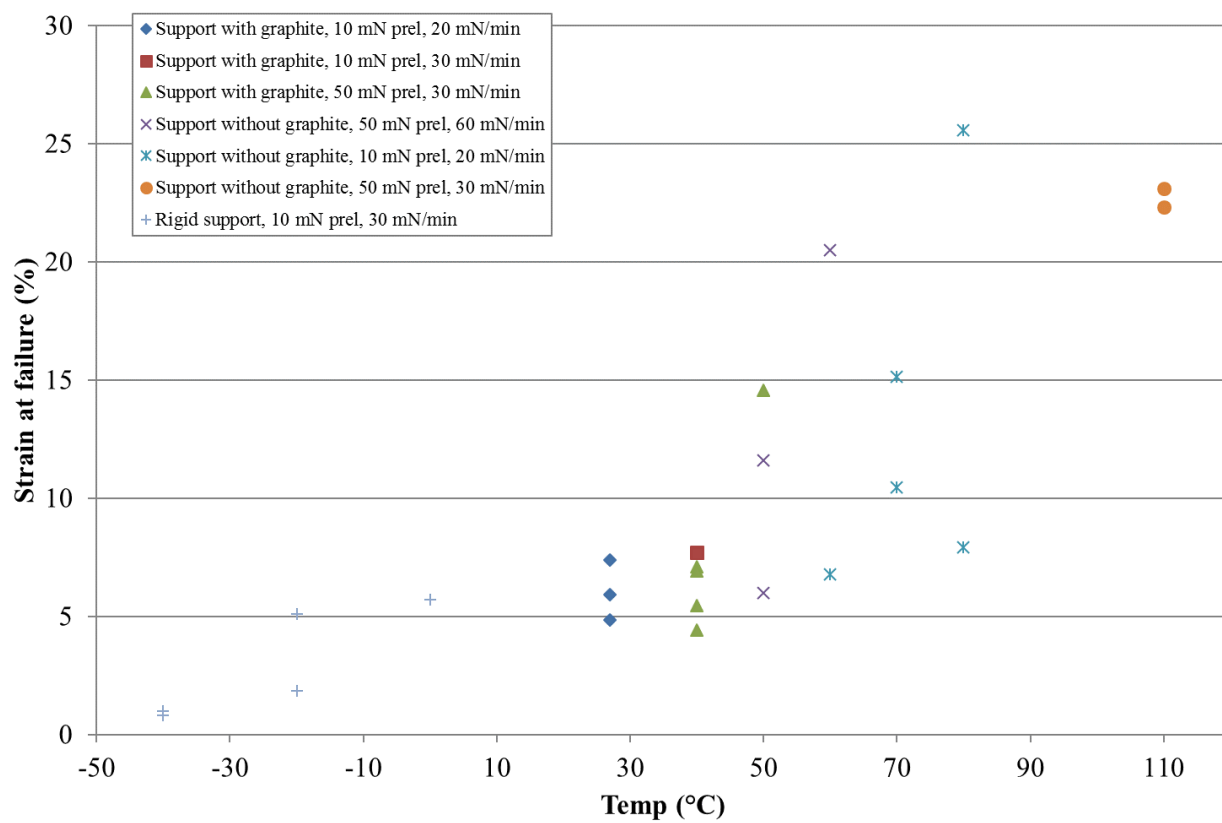
Figure 83: Strain at failure vs temperature.
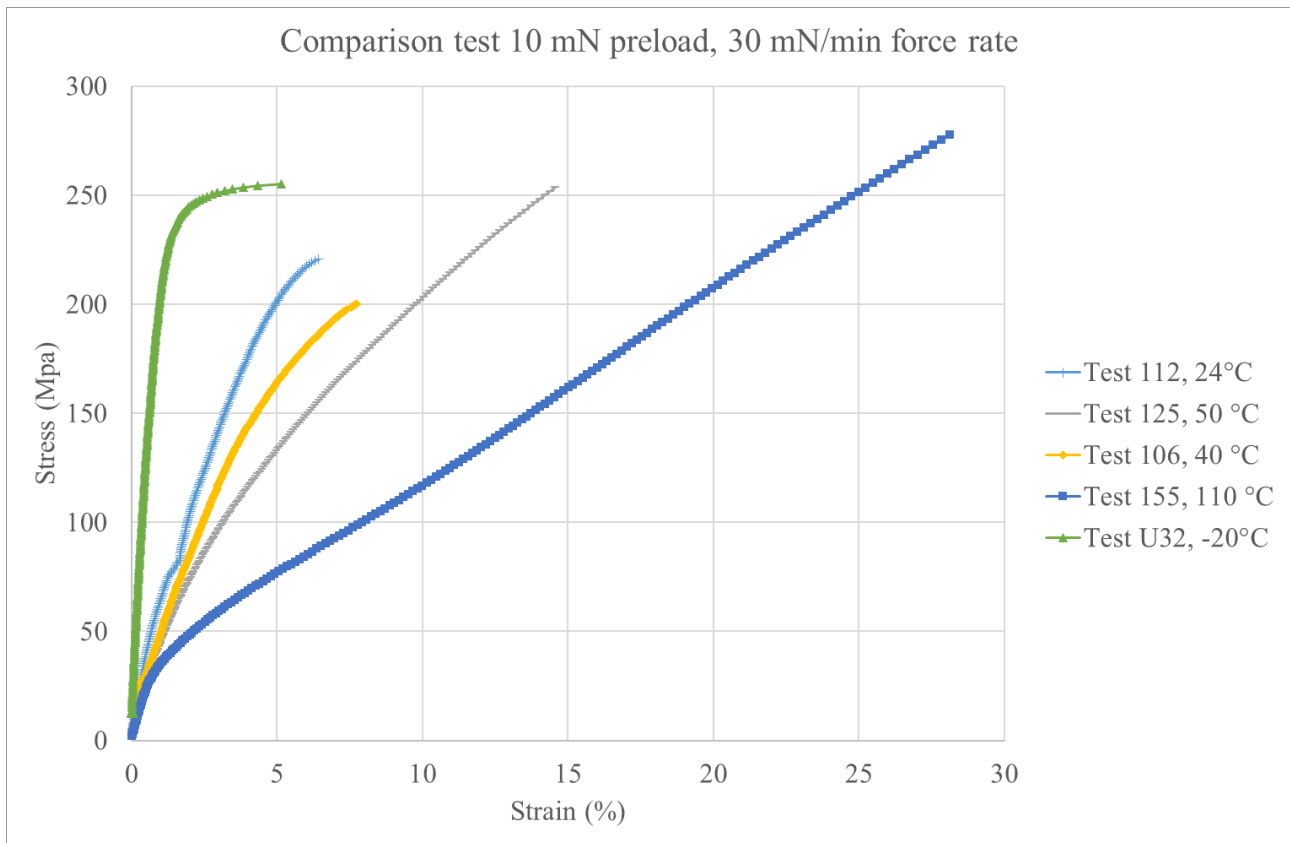
Figure 84: Stress/strain curves at different temperatures. The preload was 10 mN and the force rate was 30 mN/min.

6.5.2. Load/unload test

The test has been carried out to verify the response of the material in the elastic region.

In Figure 85 we can observe that the displacement returns to zero after the load is removed. In Figure 86, the stress/strain curve is reported. Once again the Young modulus was in the order of 27 GPa during loading.
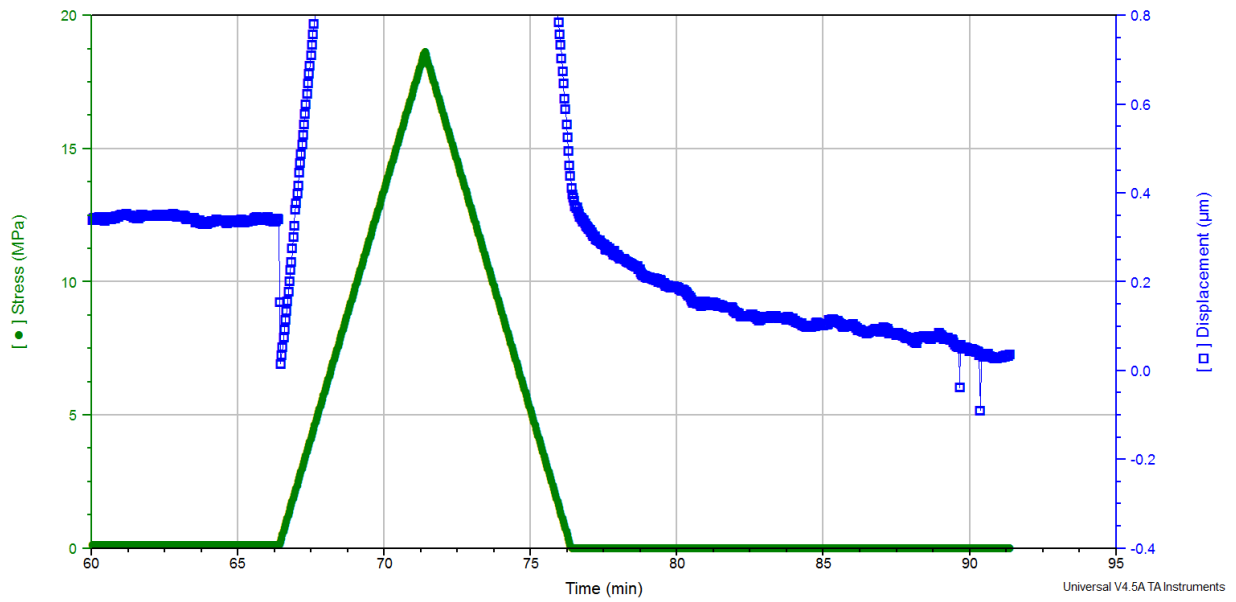
Figure 85: Stress and displacement over time during the load/unload test.
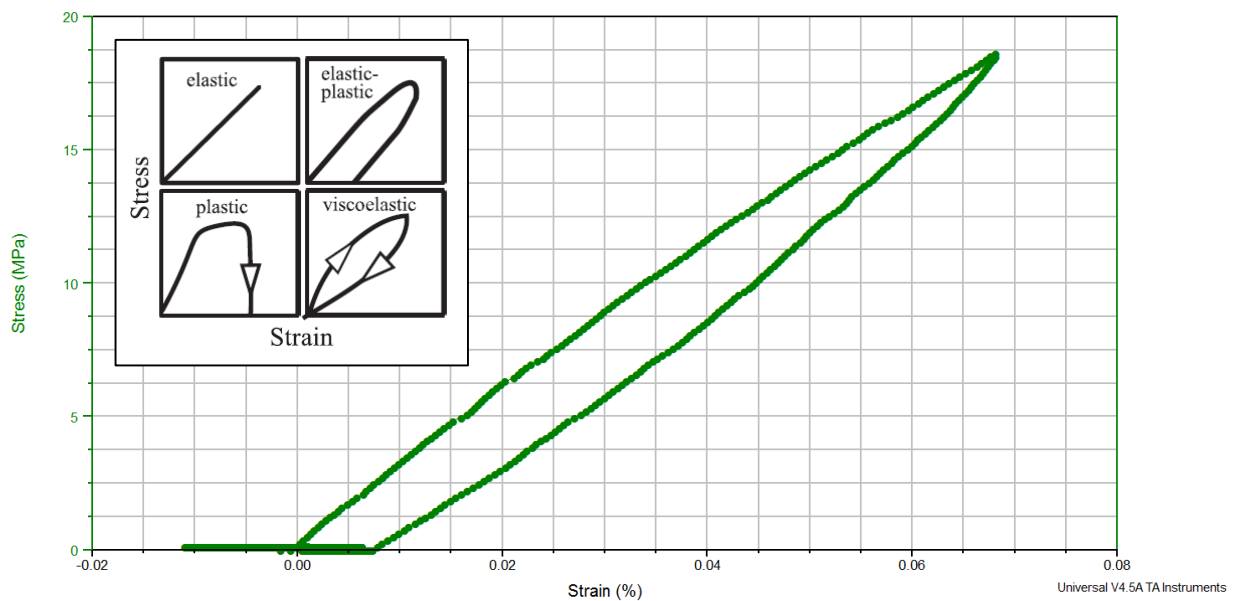
Figure 86: Stress/strain curve during the load/unload test. The schematic is by Vincent (2012).

6.5.3. Creep test

The result of the creep test is reported in Figure 87. A behaviour in line with the primary creep region for metals is observed. Then, the creep rate stabilises, as for the case of the secondary creep.

The steady state strain rate at 35 °C was 1.336 nm/min ($4x10^{-9}$ s^{-1}) and the one at 80 °C is 1.732 nm/min ($5x10^{-9}$ s^{-1}).

The value of the steady state creep has not been measured at 50 °C since the force readout presented sudden jumps and it was not possible to isolate the secondary creep region. These jumps could be explained with the occurrence of shocks and/or vibrations due to external sources.
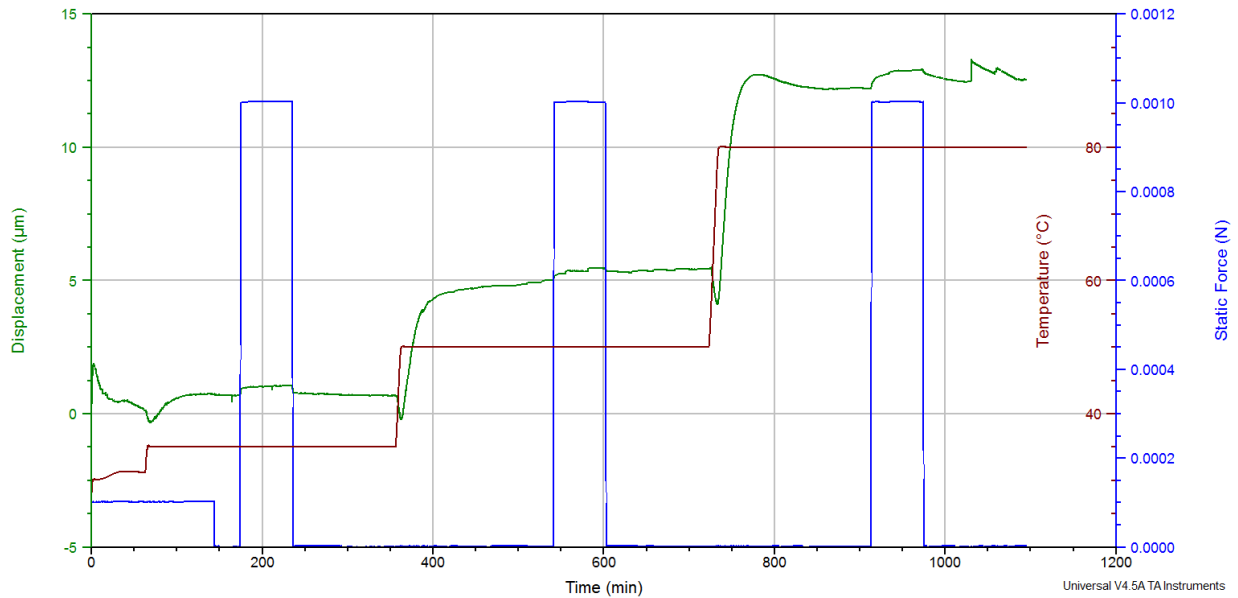
Figure 87: Creep test results.

When changing the temperature between the experiment set-points, the measured deformation decreased suddenly as soon as the temperature was changed and then rose again once the temperature was stabilised, as show in Figure 88. The rate of decrease of the displacement readout with the temperature was 0.075 µm/ °C when the temperature was increased from 35 °C up to 50 °C and 0.076 µm/ °C when the temperature was increased up to 80 °C. Then, the rate of increase of the displacement readout with time was about 0.2 µm/min at 50 °C and 0.45 µm/min at 80 °C.
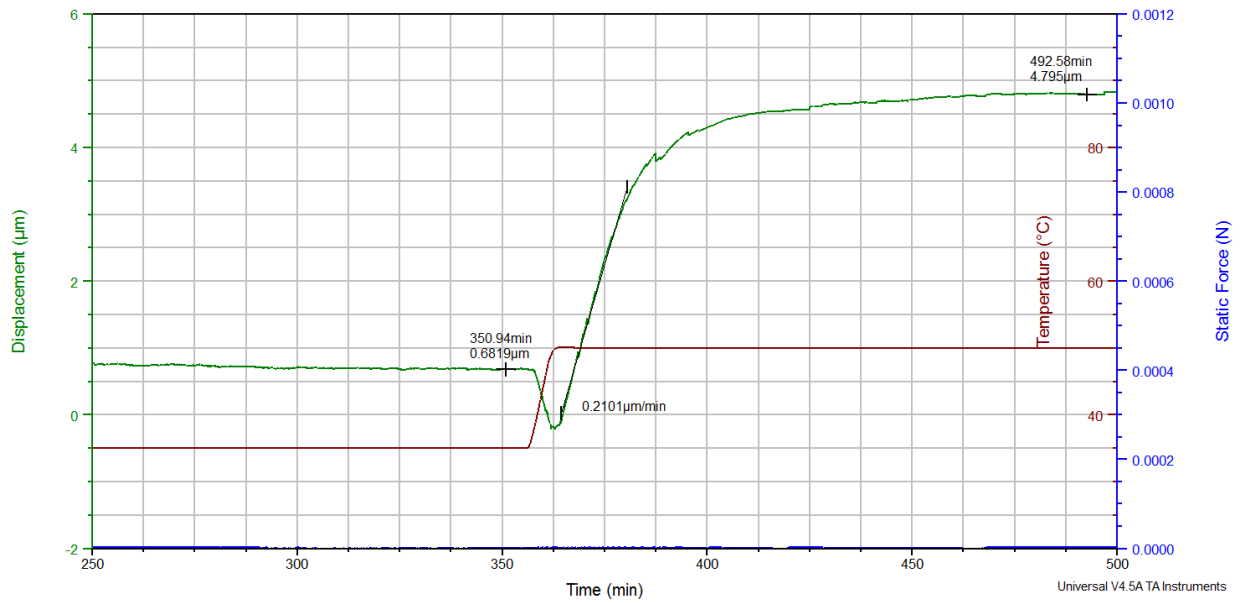
Figure 88: Stabilisation time of the displacement readout when the temperature was increased from 35 °C up to 50 °C.

A zoom of the graph showing the creep behaviour at 35 °C and the recovery time is shown in Figure 89.
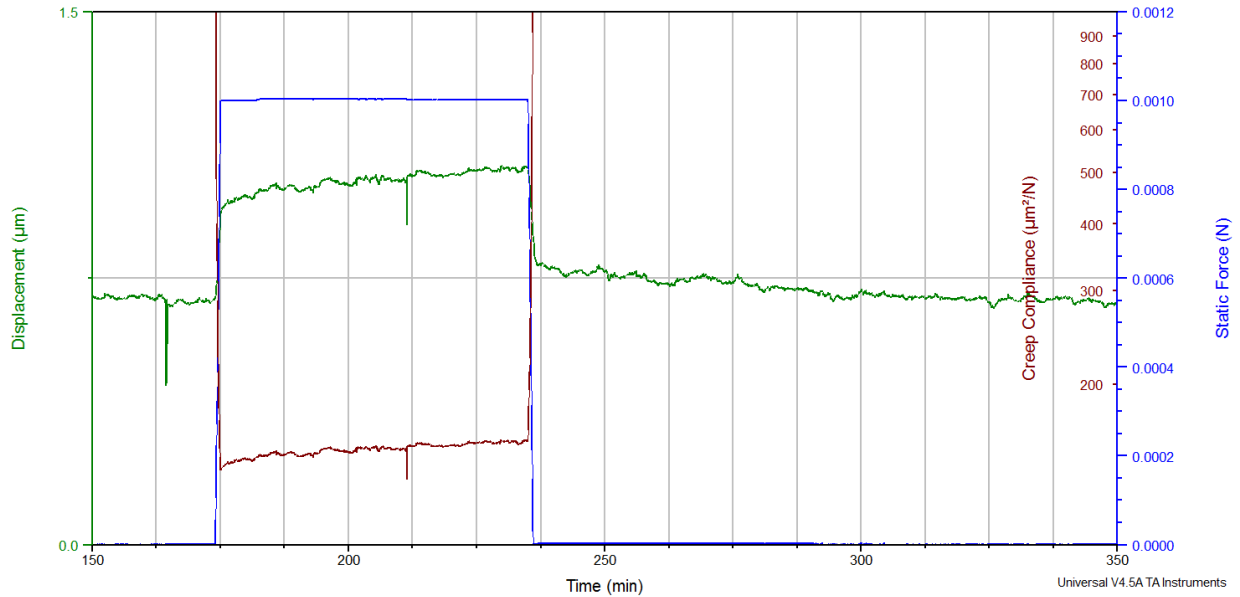
Figure 89: Creep behaviour of Al-1%Si at 35 °C.

For each of the three set-points of the test, the difference between the strain after 1 hour and the strain immediately before the load is applied was calculated, as well as the instantaneous elasticity (Figure 90). The instantaneous elasticity is a value of the "instantaneous" strain of the material immediately after the load is applied.

While the value of the instantaneous elasticity seems to be almost constant for the three temperatures, a linear increase in the strain after 1 hour is observed.
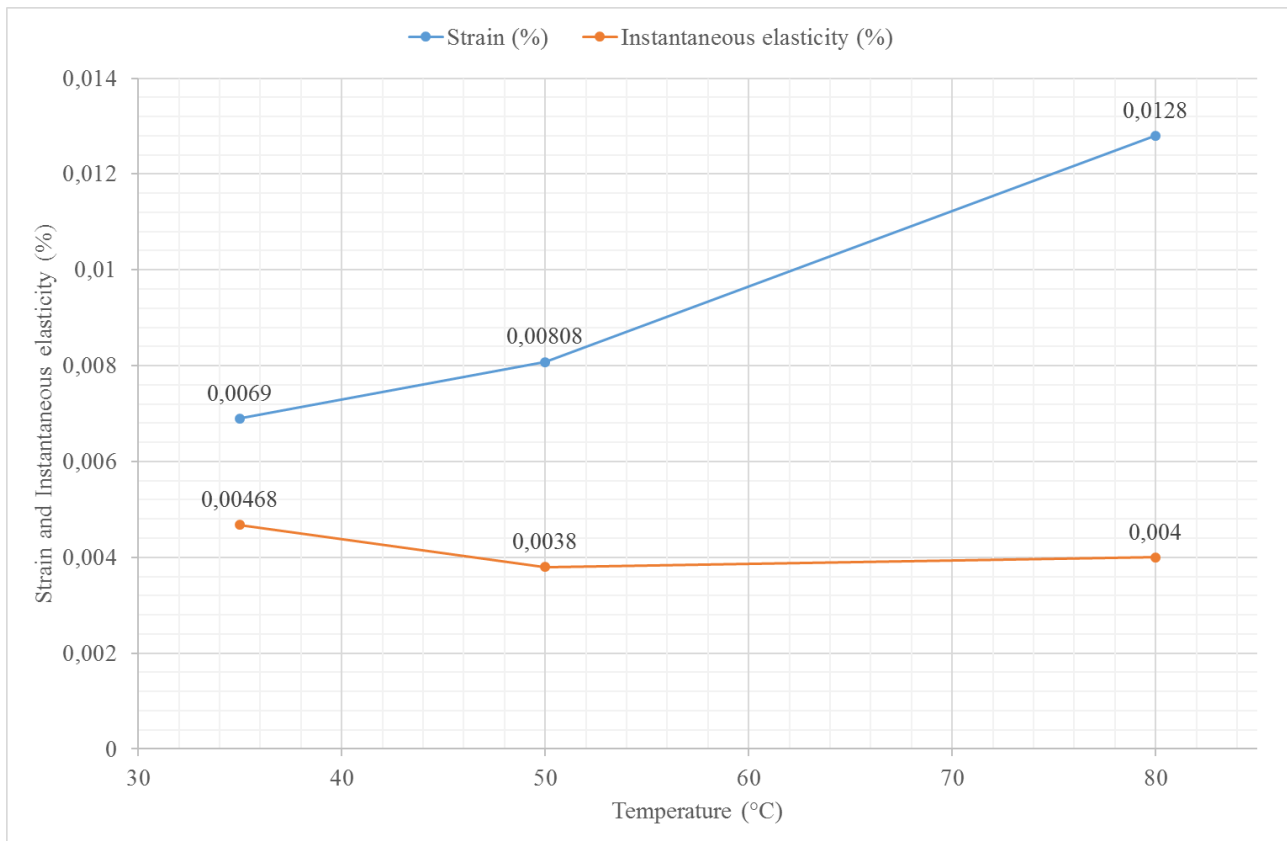
Figure 90: Strain and instantaneous elasticity for the three set-points of the creep test.

6.5.4. Strain rate sensitivity test

When a material is sensitive to the strain rate, the stress is dependent on it according to a power law with exponent *m*, as for the following equation, where *C* is a constant:

$$\sigma = C \cdot \dot{\varepsilon}^m$$

The strain-rate sensitivity test, or jump test, is used to determine the coefficient *m* of strain rate sensitivity.

At the beginning of the test, a displacement rate of 6 μm/min was applied. Then, once the derivative of the corresponding force readout was approaching zero (Figure 91), the displacement rate was doubled to 12 μm/min. Once again, when the derivative of the force readout came to zero, the displacement rate was reduced to 6 μm/min. This procedure has been repeated several times, continuously recording the load value.
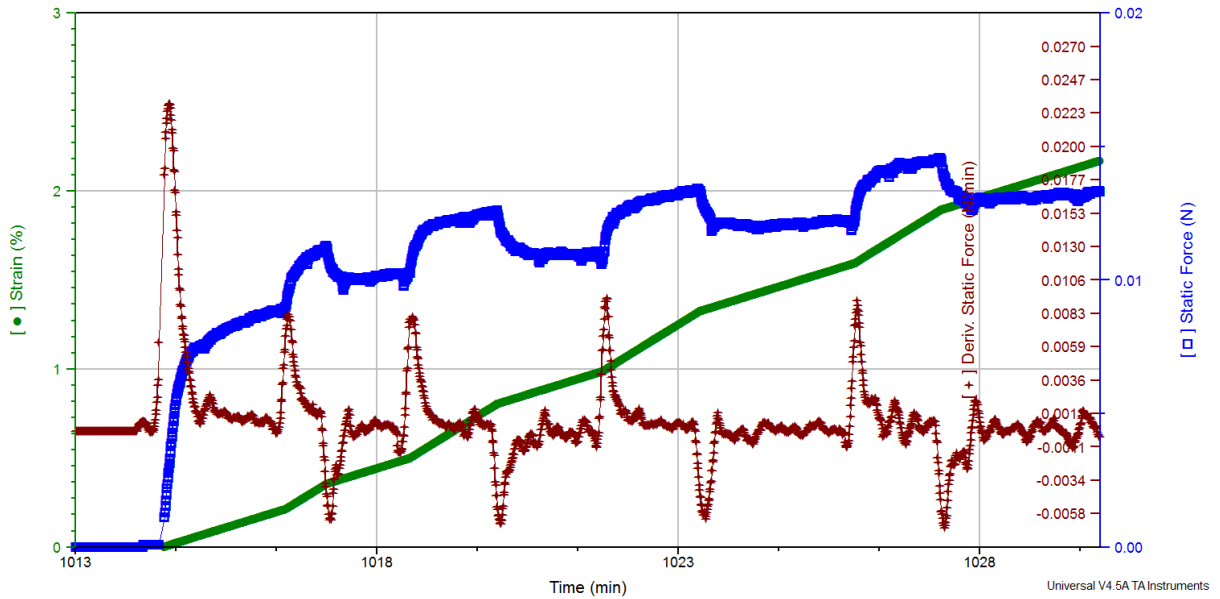
Figure 91: Strain rate sensitivity test parameters. When the derivative of the static force approached zero, the strain rate was changed.

The parameter *m* is calculated according to method 2 as defined in Edington *et al.* (1976):

$$m_2 = \frac{\log(\sigma_A/\sigma_C)}{\log(\dot{\varepsilon}_A/\dot{\varepsilon}_C)}$$

where A and C are the points of maximum load as shown in the Figure 92.

This method has the advantage that no complex data elaboration is required. The resulting value for *m* was 0.3. The details of the calculation are included in Table 2. By analysing the data according to the method 3, the one more accredited by Edington *et al.* (1976), lower values of *m* were obtained (0.12 to 0.18). This calculation, however, was considered to be more prone to errors.
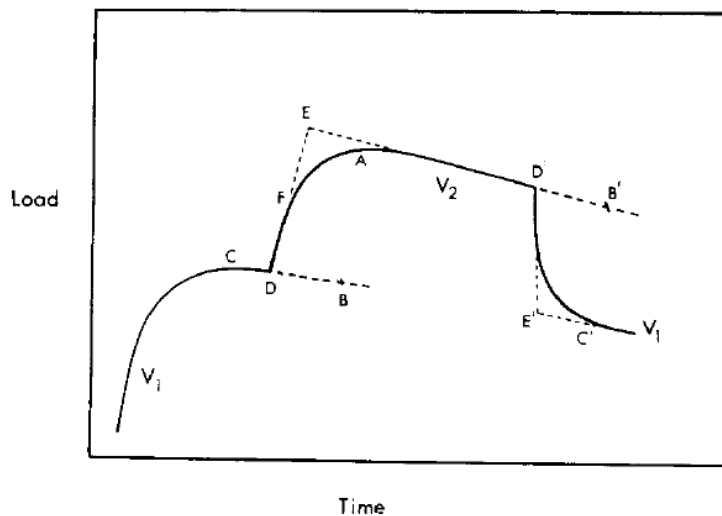
Figure 92: Schematic of load vs time curve for strain rate cycling in the jump test. Edington et al. *(1976).*

Table 2: Jump test results according Edington's method 2.

Jump test #	Plot point	Stress (MPa)	Strain rate (1/s)	Paramer *m*
1	A	13,5579	3,48E-05	0,30
	C	11,00131	1,75E-05	
2	A	14,9368	3,48E-05	0,23
	C	12,73019	1,75E-05	
3	A	16,03043	3,48E-05	0,24
	C	13,6002	1,75E-05	
4	A	17,49867	3,48E-05	0,21
	C	15,17016	1,75E-05	

Curves fitting the stress versus strain for the two different strain rates have been identified and the expressions reported in the Figure 93.
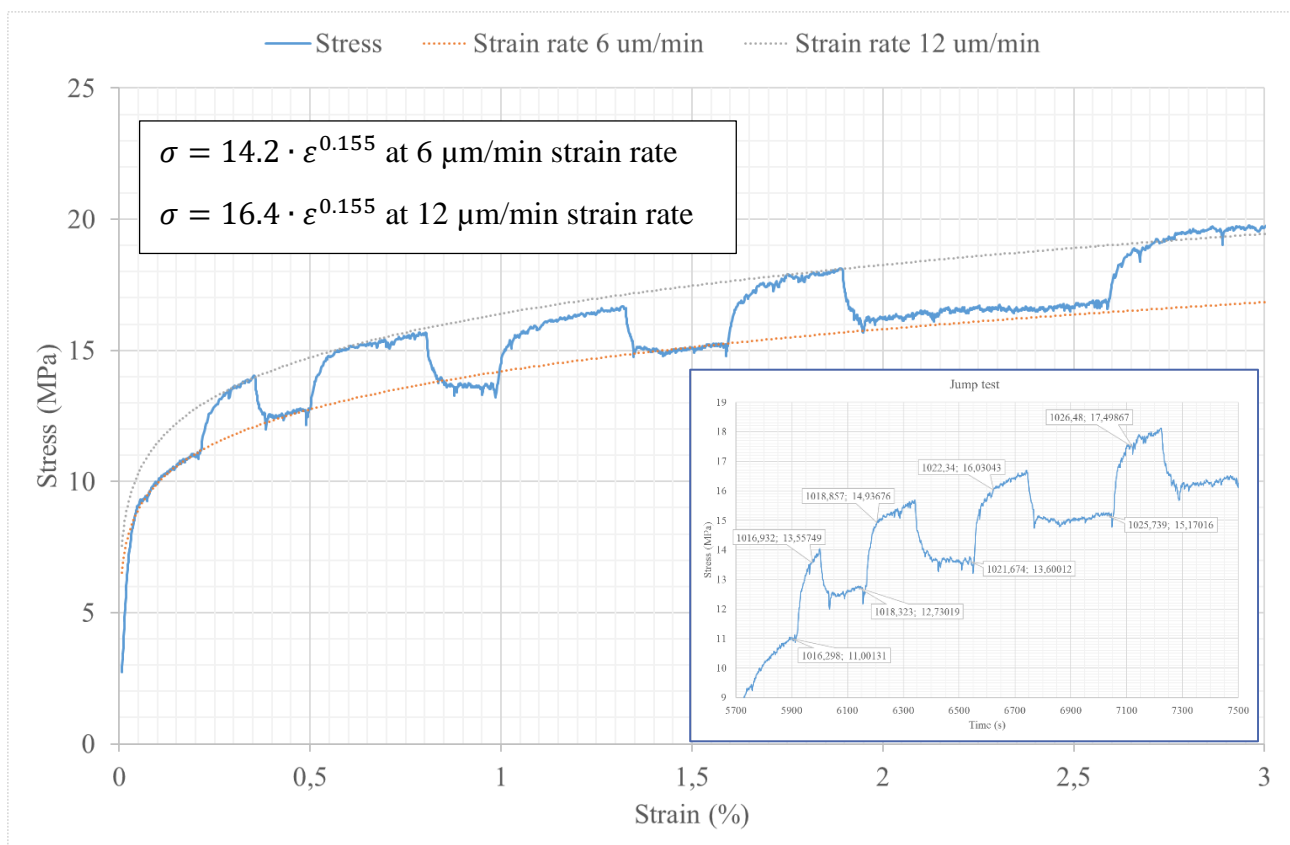
Figure 93: Results of the jump test.

6.5.5. Dynamic test

Viscoelastic materials respond with a stress which is non in-phase with the applied load, as shown in Figure 94.
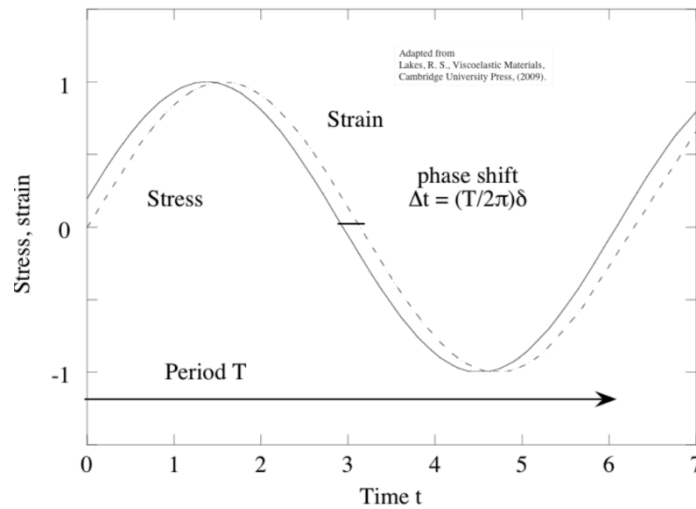
Figure 94: Dynamic response of viscoelastic materials.

The main output of the test is the value δ, a measure of the viscoelasticity of the material, for which:

$$\tan \delta = \frac{E''}{E'}$$

E' is the storage modulus and E'' is the loss modulus of the material (Basu *et al.* (2013)):

$$E' = \frac{L}{A}\left(\frac{F_0}{Z_0}\cos\delta\right)$$

$$E'' = \frac{L}{A}\left(\frac{F_0}{Z_0}\sin\delta\right)$$

where

- L is the instantaneous length
- A is the instantaneous cross-sectional area of the wire
- F_0 is the harmonic force
- Z_0 is the harmonic displacement.

Even if metals have generally a very low value of δ and its measure does not provide an added value to their mechanical characterisation, it was decided to verify the dynamic response of the material. As explained in Chapter 4, the E-sail tether may be subject to dynamic stresses due to the Coriolis force. For this reason, the dynamic test has been conducted.

The DMA provides a single data-point for each frequency selected. The data points are the result of seven loop repetitions. The results of the test are reported in Figure 95.

It can be immediately observed that the $\tan \delta$ at 50 Hz frequency is much lower than for all other frequencies observed. At ambient temperature its value is 0.016, while at 20 Hz it is 0.077. At temperature higher than 105 °C the $\tan \delta$ at 50 Hz is lower than zero and it can be therefore discarded.
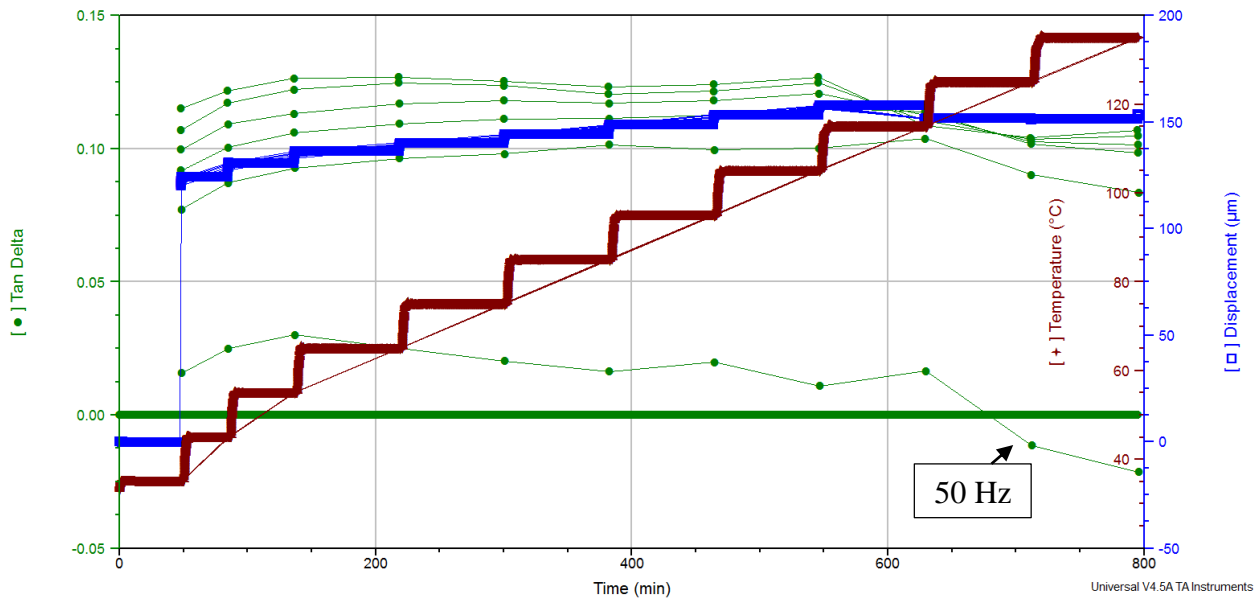
Figure 95: Dynamic test results.

The evolution of $\tan\delta$ as a function of temperature is reported in Figure 96.
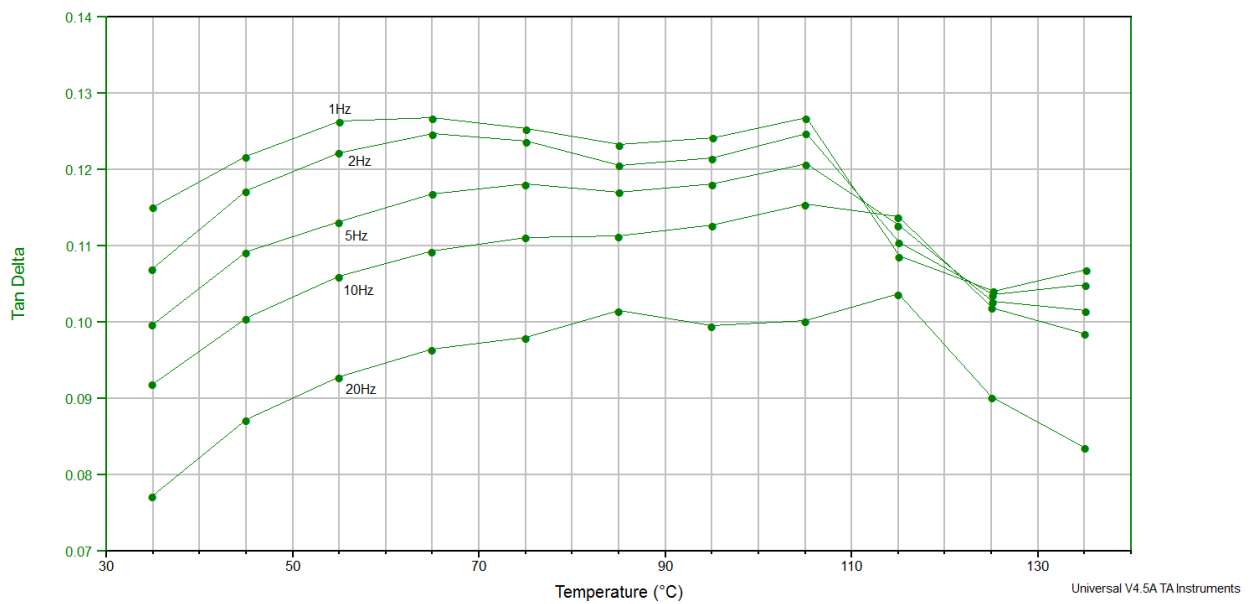
Figure 96: $\tan\delta$ as a function of temperature.

At a temperature of 35 °C we observed a decrease of the $\tan\delta$ with the frequency, while at 115 °C we observe an increase in $\tan\delta$ with the frequency up to 10 Hz (Figure 97). The decrease in $\tan\delta$ at 50 HZ is more due to a significant decrease in the loss modulus (decreased by 84%) than due to a decrease in the storage modulus (decreased of 11%).
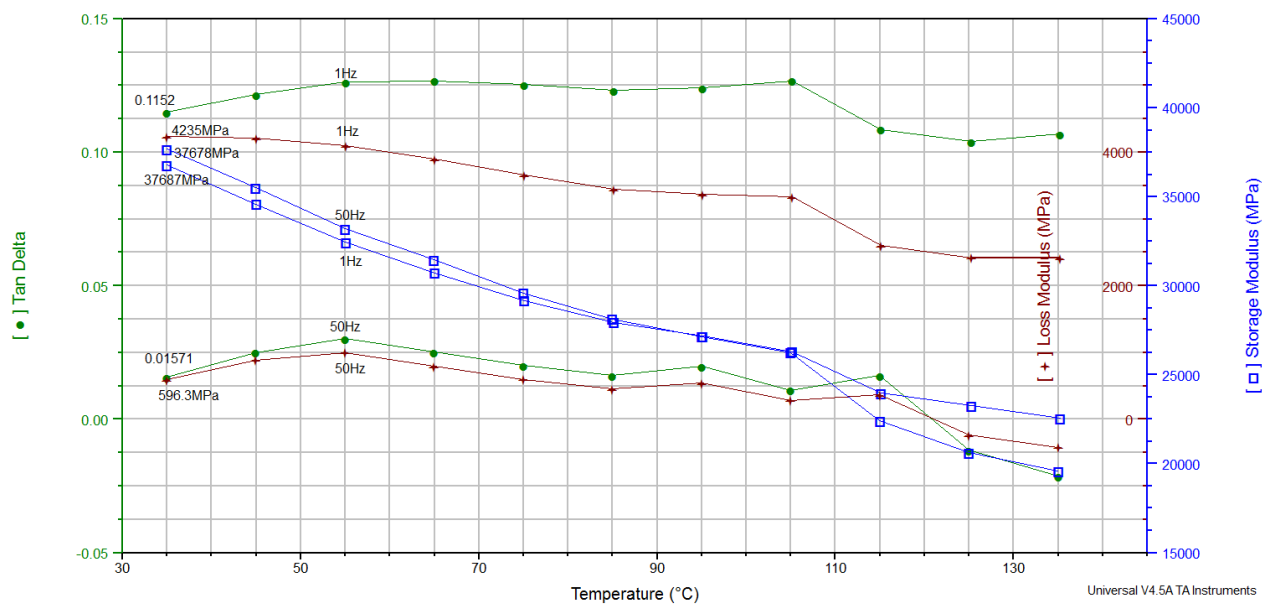
Figure 97: **tan δ**, *storage modulus and loss modulus as a function of temperature at 1 Hz and 50 Hz.*

As noticed in previous tests (e.g. the strain rate sensitivity test), the displacement readout suddenly changed with the increase of the temperature (Figure 98). This is mainly due to the termal expansion of the aluminium itself. However, other factors may contribute to this result, such as the effect of the temperature on the electronics of the DMA and the thermal expansion of the Kapton tape used to hold the wire in place at the DMA clamps. Since the strain is calculated as the ratio of the displacement versus the initial length, at temperatures higher than ambient, the total displacement measured at each set point (and for each frequency) is not only due to the applied load, but also due to the termal expansion of the material. This is reflected in the measured values of the storage modulus and loss modulus and, as a concequence, of $\tan \delta$.
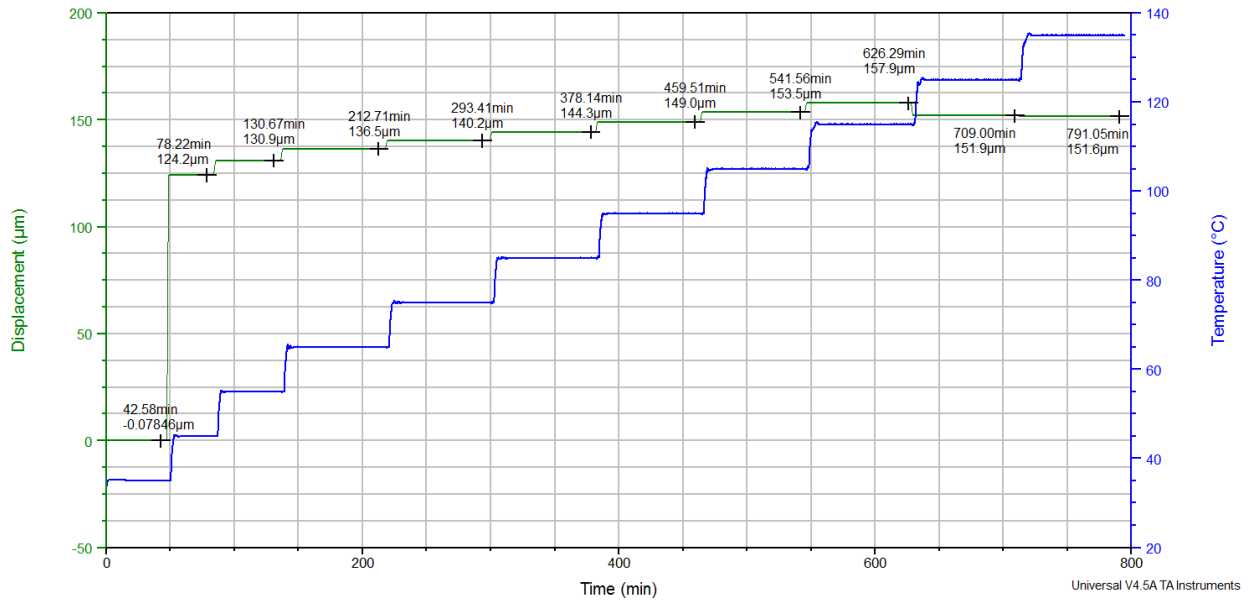
Figure 98: effect of the temperature on the displacement readout.

In this sense, it can be also noticed that the $\tan \delta$ increases up to 105 °C for frequencies less than 20 Hz, as the value of the displacement (Figure 99). At higher tempeatures, both $\tan \delta$ and the displacement decrease. At 50 Hz the behaviour is slightly different, as discussed below.

At 35 °C and for a frequency of 50 Hz the $\tan \delta$ measured was much lower than the one measured at 1 Hz (0.016 vs 0.12).
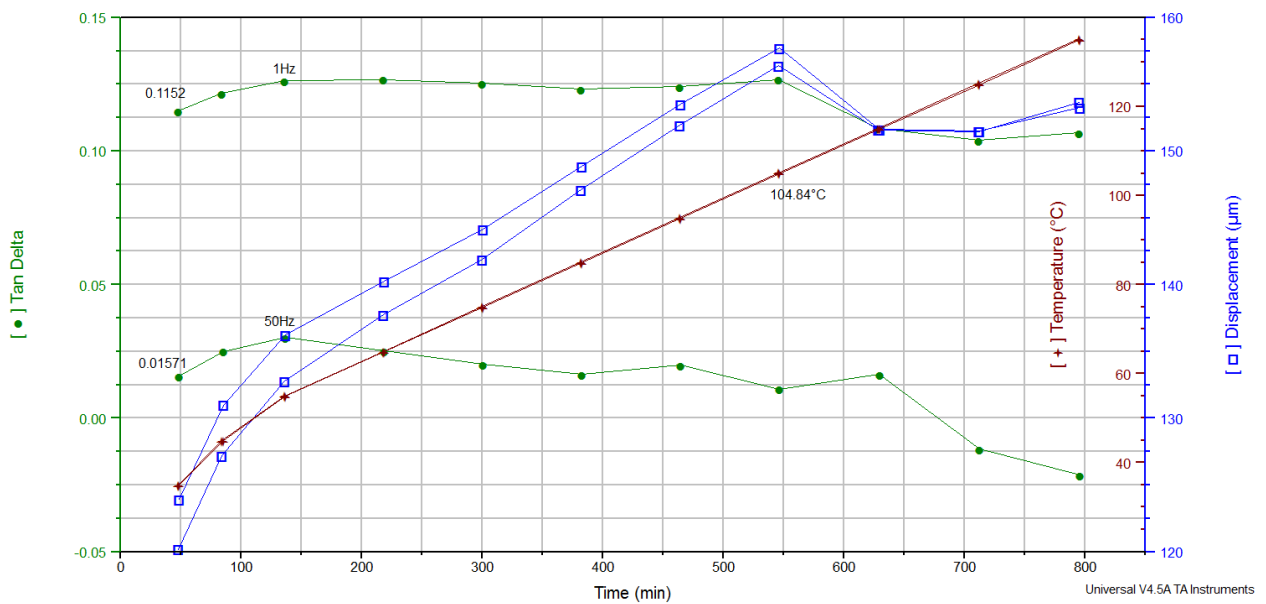
Figure 99: $\tan \delta$, displacement and temperature as a function of time at 1 Hz and 50 Hz.

6.6. EFFECT OF TESTING ON THE MICROSTRUCTURE (TEM IMAGES)

6.6.1.1. FIB/SEM images

The shape of the grains close to the fracture point of five samples subject to tensile tests at different temperatures (test 74, test 95, test 125, test 138 and no testing) has been observed with the FIB/SEM instrument. Images are included in Appendix C.

Figure 100 shows the cross section close to the fracture point for test 74. Since the grains/subcells have a higher length than the FIB cross-sectional area, it was not possible to measure the overall dimension of the grains/subcells. For each sample, only the width was measured and compared with the one of the untested tether.

Moreover, Si particles were identified in the material, presenting a homogeneous distribution in the volume. The particles were divided in two types: fine particles – having a dimeter of a few nm – and coarse particles – having a dimeter of tens of nm. This feature was observed in all cross sections.
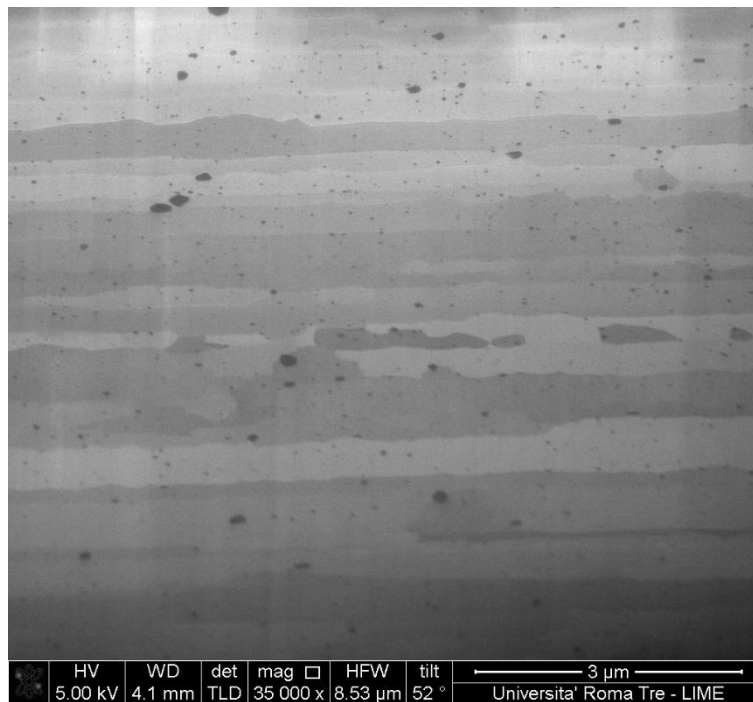
Figure 100: Cross section of sample subject to tensile test at 100 °C (Test 74) close to the fracture point.

The mean values of the thickness and the standard deviation for each sample are reported in Table 3. No significant difference between the high elongation tests and the low deformation ones has been identified.

Test #	Temperature of the test (°C)	Breaking load (mM)	Mean thickness of grain/subcells (nm)	Thickness St. dev. of grain/subcells (nm)
No testing	N/A	N/A	393	193
74	100	161	318	136
95	23	190	389	260
125	50	158	309	119
138	100	135	339	136

6.6.1.2.   TEM images

A TEM lamella of sample 138 after tensile test at 100 °C was taken close to the fracture section. The images were taken using 100 kV source with 700 nm spot in bright field. The contrast of the images was then improved using the software ITEM.

In Figure 101 we observe the grains oriented in the drawing direction. Dislocations are present in the grains, as it can be observed at a higher magnification in Figure 102.

1 µm

Figure 101: Grains oriented in the drawing direction in sample tested at 100 °C (test 138).
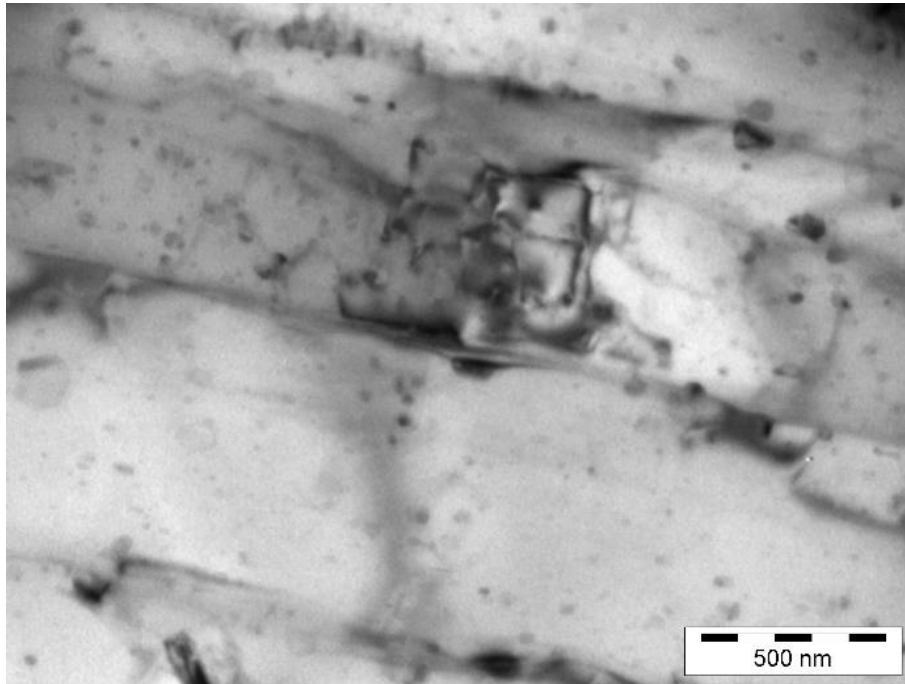
Figure 102: Cluster of dislocations in a single grain in sample tested at 100 °C (test 138).

In Figure 103 (a, b) we observe a detail of a precipitate with a parallelepiped shape. These could be Guinier-Preston zones, as described by Rosenbaum *et al.* (1958), Zhao *et al.* (2013), Ma *et al.* (2012), Ma *et al.* (2013) and Egorova *et al.* (2013) for Al-Si alloys. Lasagni *et al.* (2008) identified G-P zone in Al-Si even at low percentages of Si (1.7 %).

In Figure 103 (c, d) we observe crystallographic precipitates with higher molecular load than the grains. We also observe thin regions of higher contrast at the grain boundary, which could be precipitates. The precipitates may be either nickel or Si. Si inclusions along the grain boundaries are shown also in Lasagni *et al.* (2008). However, it was not possible to determine their nature using the Energy-dispersive X-ray spectroscopy (EDS) due to the low resolution of the instrument (about 20 nm).

In Figure 103 (e,f) we observe bands at the grain boundary. No reference could be found to these bands in the literature. However, they could be dislocation pile-ups and may be related to the relative motion between grains in the drawing direction.

a) TEM image containing Si precipitates	b) Detail of image a)
c) TEM image across grains/subcells boundary containing precipitates	d) Detail of image c)
e) TEM image across grains/subcells boundary containing bands	f) Detail of image e)
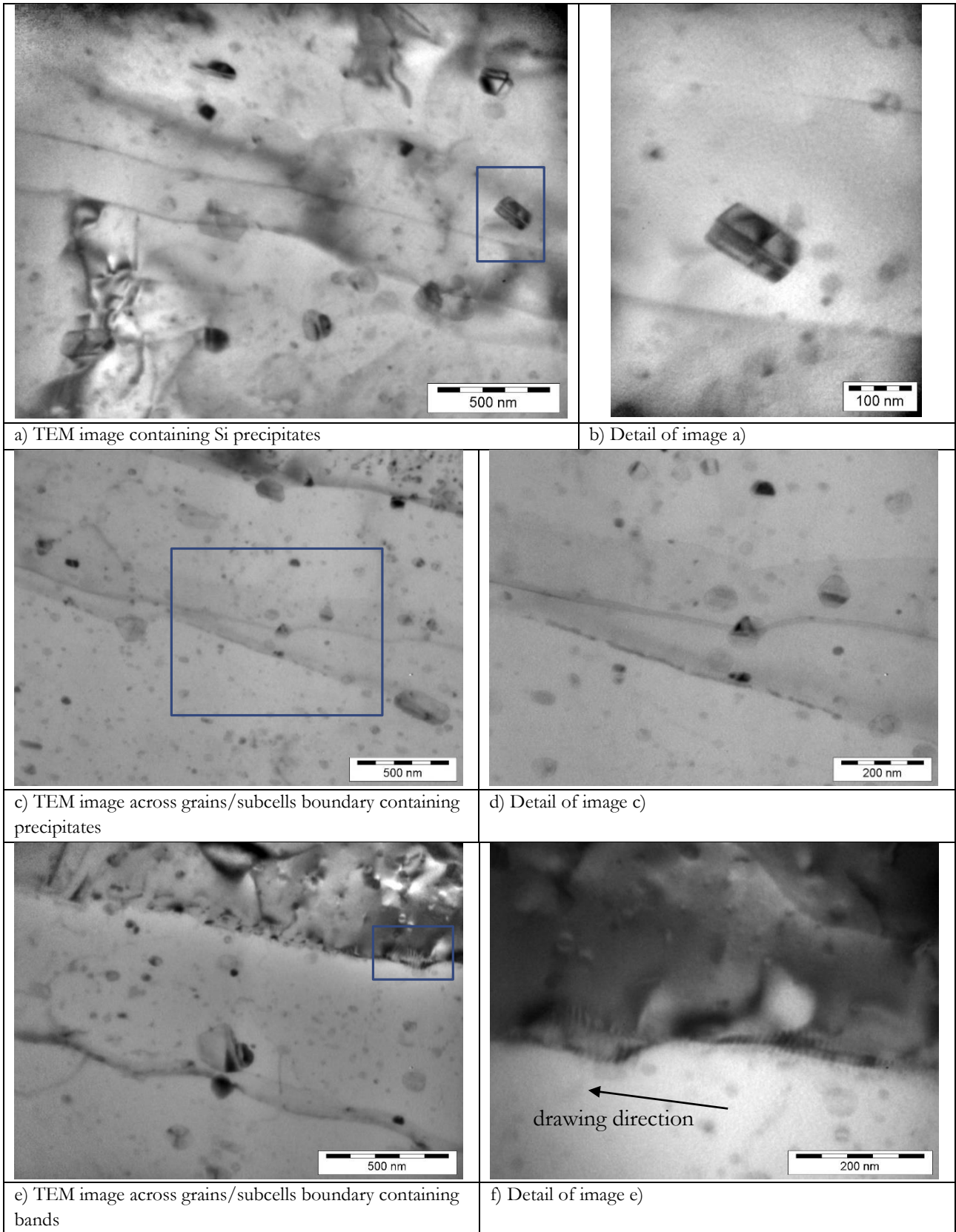
Figure 103: Details of TEM lamella of sample tested at 100 °C (test 138).

DDW/MBs have not been observed in this sample. However, it is believed that at a temperature of 100 °C, a complete recrystallization of the grain did not occur and that dislocations could have migrated to the cell/subgrain boundaries.

The crystalline structure of the grains has been also observed (Figure 104), showing little misalignment among the cell/subgrains. This observation confirming what has been observed for the sample "as provided" by the manufacturer (discussed in paragraph 5.4.1).
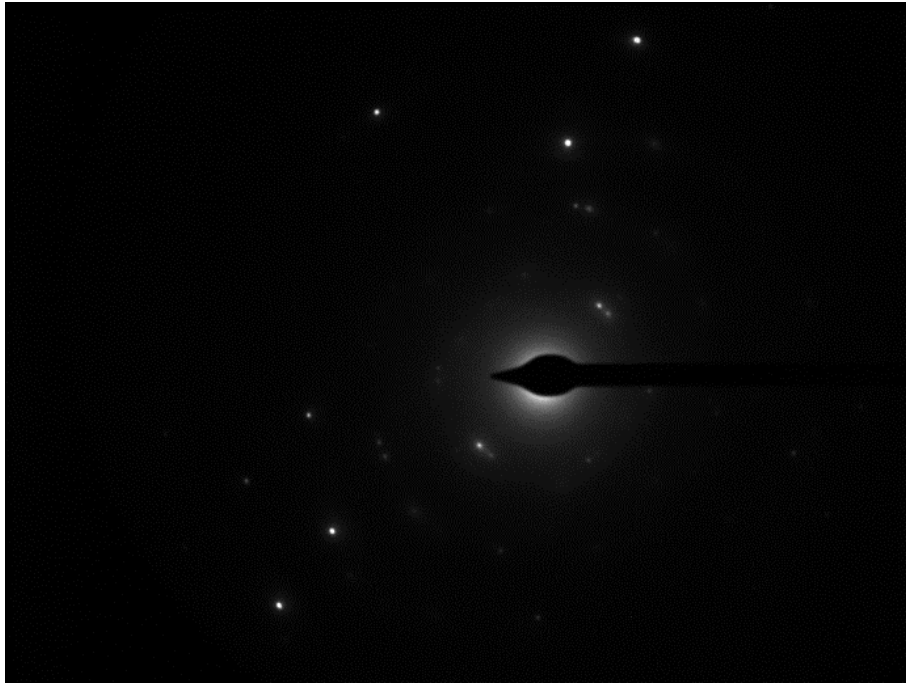
Figure 104: Crystallographic structure of the grains in sample tested at 100 °C (test 138).

7. Experimental activity: optical measurements of the tether's surface

7.1. Summary

This chapter presents the results of the optical measurements of the coating – ZnO, Al_2O_3, TiO_2, TiZnO –, in particular the absorbance and the emissivity. In the last part of the chapter, the results are discussed and the critical parameter α/ϵ is calculated.

Part of these results – namely those relative to the absorbance measurements – led to a publication (Hassan *et al.* (2017)). The simulation of the coating absorbance has been carried out by R. Li Voti (Sapienza University, Roma, Italy). The absorbance and emissivity measurements have been carried out by G.L. Leahu, G. Cesarini and R. Li Voti (Sapienza University, Roma, Italy). Additionally, 2D emissivity maps by the FTIR method have been carried out by J. Morikawa of the Tokyo Institute of Technology.

7.2. Absorbance

We measured the reflectance spectra R in the visible range for the flat samples (reported in Table 4). The reflectance spectra are obtained by using a standard spectrophotometric device. A 250 watt Xe lamp is used as optical source. The angle of incidence of light is 45° with respect to the sample surface, and the reflected light is collected specularly at 45° by an optical fibre connected to the Hamamatsu spectrum analyser. A polarising filter is also used to discriminate the two polarisations – the vertical (p) and the horizontal one (s). Finally, the spectrum of the sample is normalised to the spectrum of a reference Al mirror, according to a standard procedure for the reflectance measurements.

The measurements of the reflectance spectra have a double objective:

a) to verify the effective oxide thickness and/or oxide refractive index;
b) to estimate the absorbance spectra A=1-R as a complement of the reflectance R.

Figure 105 shows the normalised reflectance at 45° polarisation "s" for some oxide films on aluminium. The nominal thickness of the films is 100 nm. From the fitting procedure between the experiment (symbols) and the theoretical expectation (lines), it results that the ZnO film thickness is about 60 nm (Figure 105 a), the Al_2O_3 film thickness is about 70 nm (Figure 105 b), and the TiO_2 film thickness is about 115 nm (Figure 105 c). These values are in good agreement with the thicknesses measurements on the same samples (flat aluminium samples) using the FIB (Table 4).

Figure 105 d shows also the normalised reflectance for TiZnO oxide in both polarisations to be compared with the spectrum of the aluminium rough sample used before ALD. It should be noted that the reflectance for the Al sample is much lower than expected due to the strong scattering phenomenon that affects the short optical wavelengths. Moreover, the simulations in Figure 105 a and c are made without any effective medium approximation (EMA), just by applying a reduction of about 20% in the theoretical reflectance for the scattering.
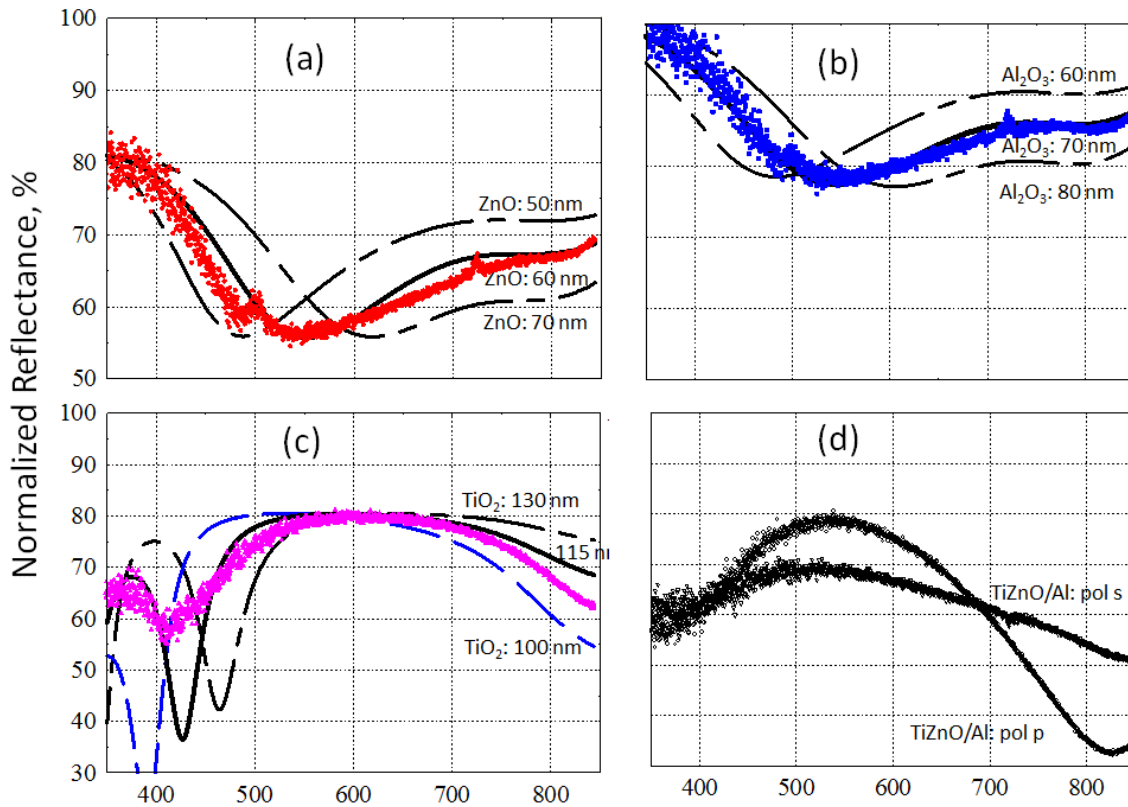
Figure 105: Normalised reflectance.

Table 4: Characteristics of the samples used for the optical measures.

	Sample		Thickness (nm)		
n.	**Substrate**	**Coating**	**Nominal**	**FIB-SEM**	**Reflectance**
10	Flat Al	TiO$_2$	100	102 (1)	115
11	Flat Al	ZnO	100	55 (7)	60
12	Flat Al	Ti-Zn mixed oxide	100	144 (3)	–
13	Flat Al	Al$_2$O$_3$	100	–	–

The absorbance spectra A are shown in Figure 106 for the four thin oxides. They are calculated as A=1-R again at 45° but by averaging the two polarisations. It is also possible to calculate the absorbance averaged over the solar spectrum in the range 350 nm – 850 nm, obtaining 0.1 for the Al$_2$O$_3$ film, 0.22 for the ZnO film, 0.18 for the TiO$_2$ film, and 0.23 for the TiZnO film, in agreement with the theoretical results reported in Figure 63.

It is worth noting that the optical scattering (not measured here) is neglected in the formula (Li Voti *et al.* (2009)). As a consequence, the absorbance in Figure 106 could be overestimated. In order to obtain

a direct measurement of the absorbance spectrum other techniques could be applied in the near future, such as photothermal deflection or photoacoustic spectroscopy (Li Voti *et al.* (2015)).
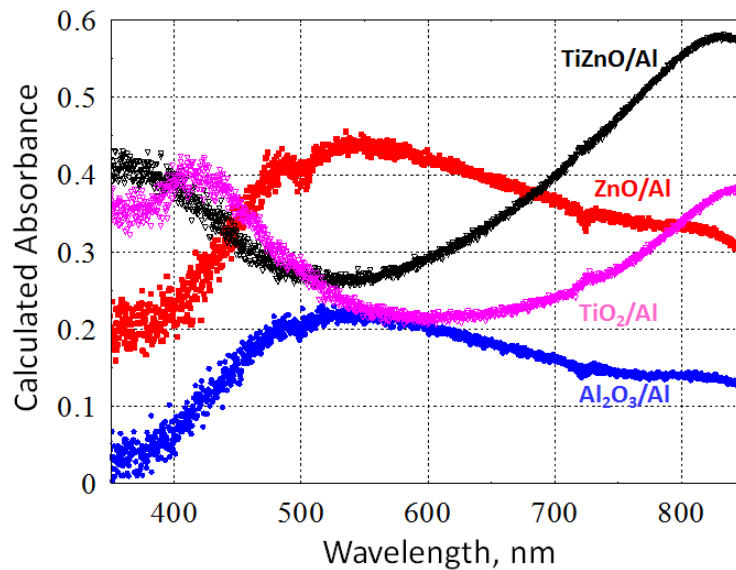
Figure 106: Calculated absorbance in the visible range.

7.3. EMISSIVITY

In this paragraph we describe the experimental setup to measure the emissivity of the samples (integrated in the range 2-12 μm) as a function of temperature in the range 30 °C – 110 °C. The sketch of the experimental setup is shown in Figure 107.

The copper body of the electrical heater is used for the sample temperature scan. The current temperature of the sample is measured by a copper-constantan thermocouple. The temperature scan of the sample is performed in a quasi-stationary regime, realised by changing linearly the sample temperature slowly with time, with a low speed of about 1 °C/min from 30 °C to 110 °C.

The infrared emittance from the sample surface is first modulated by a mechanical chopper at a fixed frequency and then collected by a germanium lens onto a HgCdZnTe photovoltaic IR detector with a high and rather flat sensitivity in the infrared range 2-12 μm. The germanium lens is placed at the distance 2F (F=50 mm is the focal lens) from both the sample and the detector, so to keep the image at the same size of the object.

The signal from detector is eventually sent to a lock-in amplifier, which amplifies only the signal at the same frequency of the mechanical chopper, filtering out the noise from the environment.
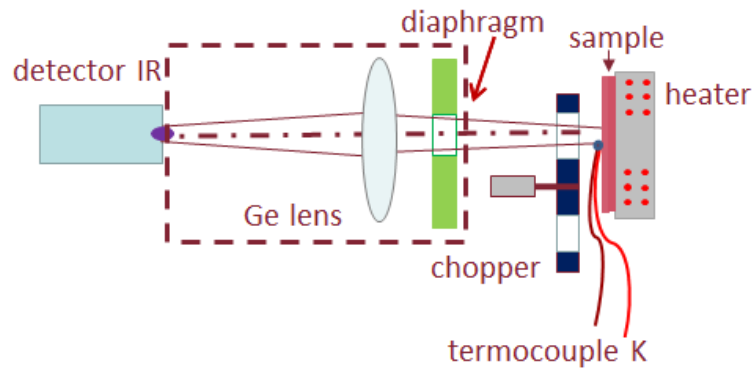
Figure 107: Emissivity test set-up.

We use such an infrared system to measure the emittance of the coated aluminium samples (ZnO/Al, Al2O3/Al, TiO2/Al, TiZnO/Al) as a function of temperature between 30 °C and 110 °C. In addition, as a reference, we measure also the emittance of a black body (a graphite flat sample of known high emissivity) as a function of temperature in the same range. The sample emissivity is finally obtained by the ratio between the sample emittance and the black body emittance at the same temperature (see Figure 108).
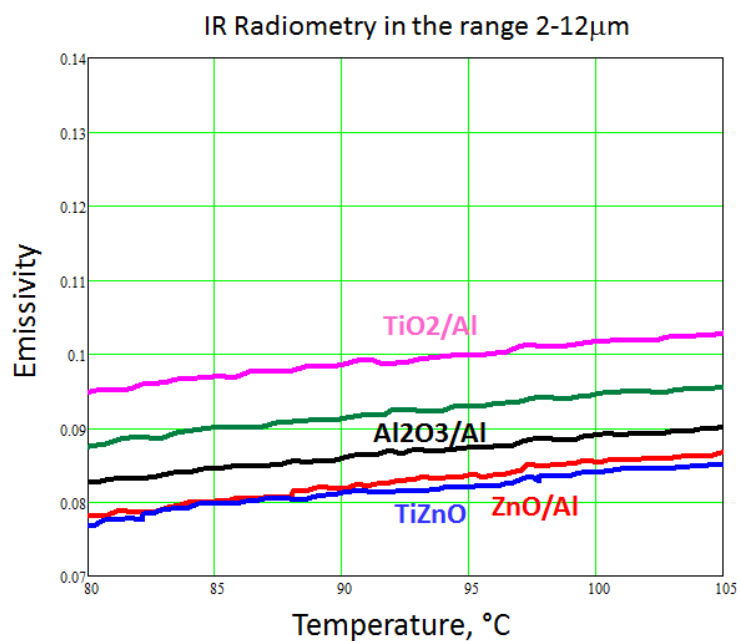
Figure 108: Sample emissivity in the narrow range 80 °C – 105 °C, where the data are less affected by noise. The green line refers to uncoated aluminium.

The increase of the sample emissivity as a function of temperature follows the theory of Hagen-Rubens (Seifter (2003)), according to which the emissivity grows linearly with temperature following the equation:

$$\varepsilon(T) = 0.0348 \cdot T \cdot \sqrt{r_{273°K}}$$

where $r_{273°K}$ is the resistivity at 273 °K.

We notice also that the slope of the curves is comparable to the one of bare aluminium. Therefore, it seems that the coating does not modify the slope of the curve, at least for the range of temperatures observed.

The parameters of the emissivity versus temperature fitted line are reported in Table 5.

Table 5: Intercept and slope parameters of the emissivity vs temperature fitted line.

Al203	Intercept (-)	0,055623
	Slope (1/ °C)	0,000268
TiO2	Intercept (-)	0,064754
	Slope (1/ °C)	0,000295
TiZnO	Intercept (-)	0,048979
	Slope (1/ °C)	0,00029
ZnO	Intercept (-)	0,047811
	Slope (1/ °C)	0,000313

By fitting the data and extrapolating the value at 25 °C we obtained the following values for the emissivity: 0.062 for Al_2O_3, 0.072 for TiO_2, 0.056 for TiZnO and 0.056 for ZnO.

In order to verify whether the roughness of the sample affected significantly the error in the measurement results, the emissivity at ambient temperature (290 K) has been also measured for the whole two-dimensional sample surface in the range 1-14 μm using a Fourier Transform Infrared Spectrometer (FTIR). The measurements have been performed by the Tokyo Institute of Technology.

The instrument provided the value of $B = \log(R)$, where R is the reflectance spectra. The emissivity was then calculated as $e = 1 - 10^B$. The results are shown in Figure 109.

a) TiO2

b) TiZnO

c) ZnO

d) Al2O3
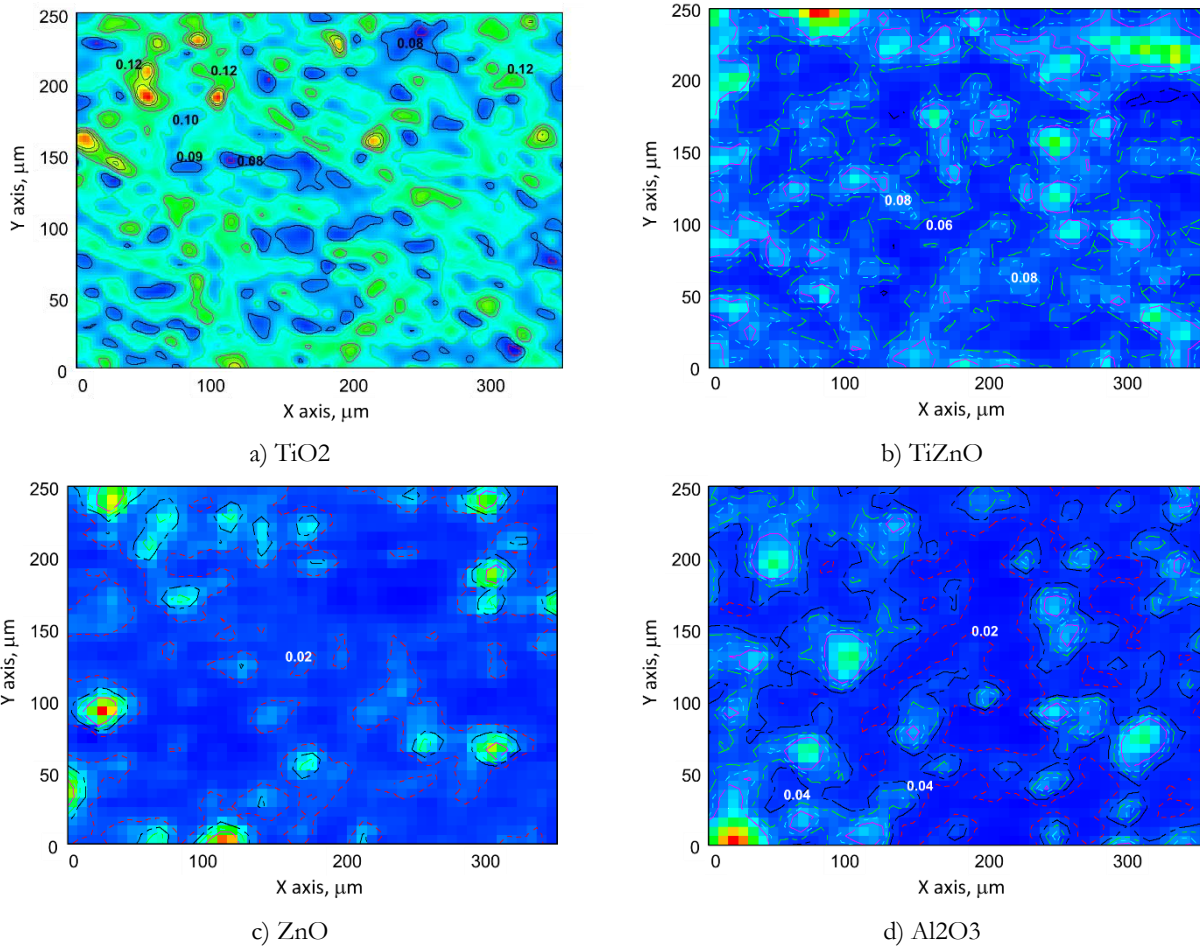
Figure 109: 2D plot of the emissivity measurement by the FTIR integrated in the range 1-12 µm (Tokyo Institute of Technology).

The standard deviations of the sample and the relative standard errors were:

- TiO_2 - standard deviation: 0.012; standard error: 0.00028
- ZnO - standard deviation: 0.038; standard error: 0.000892
- Al2O3 - standard deviation: 0.021; standard error: 0.000493
- TiZnO - standard deviation: 0.04; standard error: 0.000939.

The standard error was therefore very low compared to the mean values of emissivity, as it was expected. This confirmed that the roughness of the sample did not impact the emissivity measurement.

7.4. A/E RATIO

The measure of the emissivity of Al_2O_3 at ambient temperature was in line with the values obtained in the ESAIL FP7 project (Rauhala *et al.* (2013)), also taking into consideration that the values obtained in the ESAIL project presented a high variability. The linear dependence of the emissivity from the temperature, as foreseen by the theory of Hagen-Rubens, was also observed in Rauhala *et al.* (2013).

Based on the measurements of the absorbance and emissivity, and assuming a linear dependence of the emissivity on the temperature over a broader range of temperatures, the α/ε ratio has been estimated

for -40 °C, 0 °C, 25 °C, 50 °C and 100 °C. It was assumed that the absorbance did not significantly change in that range of temperature.

Table 6: Estimated a/ε ratio at different temperatures (-40 °C, 0 °C, 25 °C, 50 °C and 100 °C).

Coating type (100 nm thickness)	α (400-800 nm)	ε @ -40 °C	ε @ 0 °C	ε @ 25 °C	ε @ 50 °C	ε @ 100 °C	α/ε @ -40 °C	α/ε @ 0 °C	α/ε @ 25 °C	α/ε @ 50 °C	α/ε @ 100 °C
Al2O3	0,100	0,045	0,056	0,062	0,069	0,082	2,2	1,8	1,6	1,4	1,2
ZnO	0,220	0,035	0,048	0,056	0,063	0,079	6,2	4,6	4,0	3,5	2,8
TiO2	0,170	0,053	0,065	0,072	0,080	0,094	3,2	2,6	2,4	2,1	1,8
TiZnO	0,230	0,037	0,049	0,056	0,063	0,078	6,2	4,7	4,1	3,6	3,0

A bar chart showing the comparison between the α/ε ratio at different temperatures is reported in Figure 110.
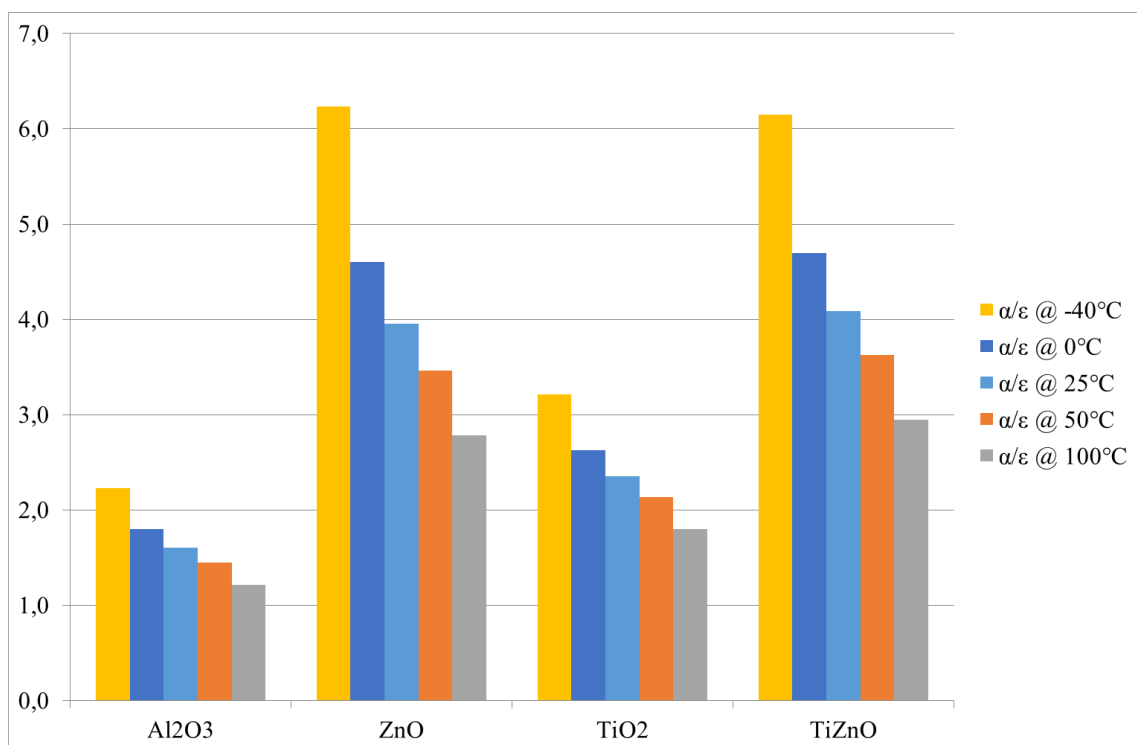
Figure 110: α/ε ratio at different temperatures.

8. DISCUSSION

Due to the fact that the tether diameter is in the order of micrometres, its mechanical properties may not be directly derived from the ones of bulk aluminium. This is because of scale effects, such as the dimension of the grains with respect to the tether's diameter. As stated by Engel *et al.* (2002), experimental research has shown that the flow stress decreases with increasing miniaturisation, since free surface grains show less hardening compared to the inner volume grains. This concept is clearly shown in Figure 111. On small scales the material cannot be considered as homogeneous continuum anymore. Similar considerations are reported in other literature as well (*e.g.* in Wang *et al.* (2009)).
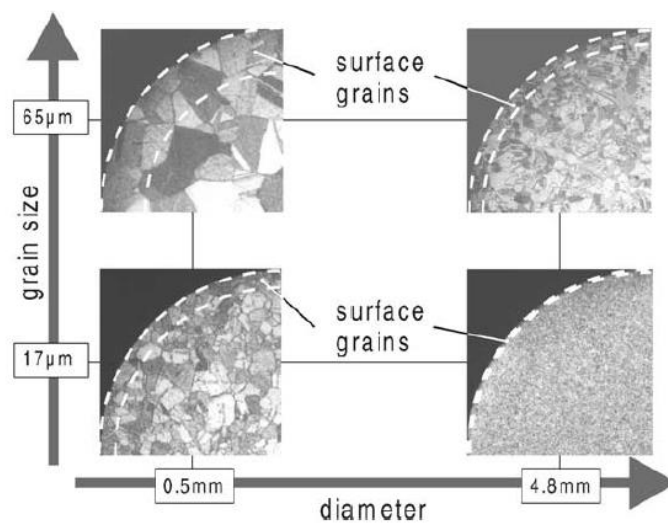
Figure 111: Share of surface grains. Engel et al. *(2002).*

In principle, we could expect that, as the structure of aluminium should not change over a broad range of temperatures, the strength should not change either. Nonetheless, creep may play a major role. From the plots shown in paragraph 4.3.2 (Liu *et al.* (2004)), the effect of the annealing temperatures higher than 150 °C on Al-1%Si properties is well documented. However, for our application it is interesting to study the mechanical behaviour at temperatures below 150 °C, also considering that these temperatures could be maintained in space for long periods of time. In order to fill this knowledge gap, several tests were performed using the DMA.

Other geometric factors also play a role (Liu *et al.* (2004)): a thin wire during annealing provides a higher heating speed compared to bulk aluminium. This factors "increase the sensitivity of structure transformation to the heating time, resulting in the non-uniformity of the microstructure in the different sections of the same specimen".

The results at ambient temperature of the tensile tests confirm the data of breaking strength and elongation to failure provided by the manufacturer, thus confirming that the test set-up was correct at ambient temperature. The values of elongation to failure have been further confirmed by the verification of the displacement measurement using the digital image correlation (DIC) method.

The values of breaking strength and elongation to failure at ambient temperature could be used to estimate the annealing temperature of the alloy by making reference to the graphs present in the literature (Liu *et al.* (1999)) and reported in paragraph 5.3.2. In light of this, an annealing temperature between 200 °C and 250 °C has been probably used. This would correspond to the minimum in the elongation to failure identified by Liu *et al.* (1999) at that temperature range.

Tests with similar techniques have been used to perform tensile and fatigue tests at ambient temperature by Danaher *et al.* (2011) on an Al-1%Si wire produced by the same manufacturer (*TANAKA Electronics*). The tests were carried out using the microforce testing system Tytron 250 by MTS Systems. The wires had a strength slightly less than 200 MPa and strain to failure of over 2%. The Young modulus measured was 71.7 GPa, while in our case it was in the order of 24 GPa.

This value is much lower than the nominal Young's modulus of aluminium (70 GPa) but it is close to its shear modulus (25 GPa). This could be related to a behaviour which is closer to the one of a single crystal (Liu *et al.* (2004)). The authors report that during tensile testing, the ultra-long grains play the role of a single crystal. This behaviour only occurred by single slipping in the preferable orientation grains, resulting in an elongation of 10–16%, lower than in bulk Al-1%Si alloy. However, this was observed for Al-1%Si alloy annealed at temperatures above 520 °C, which does not seem to be our case.

Even if the measure of the Young's modulus was not the main objective of this test campaign, especially considering the difficulties in the clamping of the sample, the value measured by the DIC method can be considered reliable. Still, there is a considerable difference with respect to the nominal value of aluminium. This can be eventually explained considering that in Danaher *et al.* (2011) the diameter of the wire used was 63 μm (almost double than the one used in this work). Moreover, Danaher *et al.* (2011) do not clarify whether nickel was also present in the alloy. Finally, a different annealing temperature, which is unknown for both materials, could have led to different mechanical properties (see Takagi *et al.* (2016) in the case of Au bonding wires, as well as considerations made in paragraph 5.4.1 on Al-1%Si). At that temperature, as explained by Liu *et al.* (1999), there are two mechanisms that lead to the elongation reduction: silicon precipitation and coarsening on one side and excessive grain growth on the other.

Kim *et al.* (2007) explained that, with the recent evolutions in material science going towards miniaturisation of parts, the specimen size scaling becomes a critical parameter, together with the grain size effect. The Hall-Petch equation, describing the effect of the gran size, is not sufficient to describe the contribution of the geometry to the flow stress. In practice, the strength of specimens containing only a small number of grains across the cross section decreases with the ratio *n* between the wire diameter and the grain diameter. In that paper a generalisation of the Hall-Petch equation was proposed, including the feature size effect. Kim *et al.* (2007) identified the value of n = 3 as the threshold below which the flow stress will mostly depend upon the texture or the local orientation of the grains. An example of such concept is shown in Figure 112.
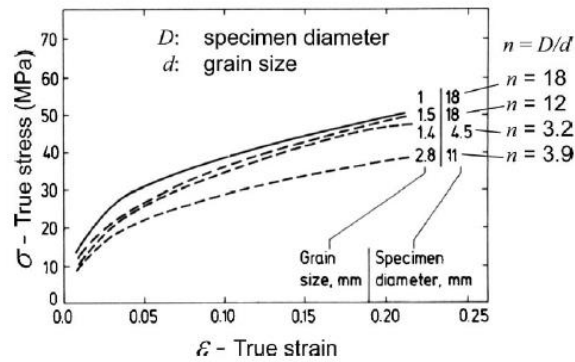
Figure 112: Stress-strain curves of 99.999% aluminium for various n values. Kim et al. *(2007)*

Assuming that the grain dimension is the same among the specimens studied in our work and the one observed in the work of Danaher *et al.* (2011), the parameter *n* would be double in our case – 32 µm diameter – compared to the other case – 63.3 µm dimeter. Danaher *et al.* (2011) measured an average grain diameter of 1.1 µm. This would lead to a value *n* of 57.5, which could be considered too high to provide flow stresses resembling a monocrystal. However, it must be noted that the SAED analysis performed in our work to obtain diffraction patterns of the Al-1%Si samples showed little differences among the grain orientations, leading to the conclusion that in our case subcells were probably observed instead of grains. Therefore, a Young's modulus lower than the one of bulk aluminium cannot be excluded, even if the anisotropy of aluminium is low.

In general, the geometry of the wire affects the reproducibility of results. Liu *et al.* (2004) showed that there is a higher variability in the measurement of the elongation to failure in the wires with respect to the bulk material. This is because the higher is the ratio of gauge length to diameter, the greater the possibility of non-uniformity in the specimen. This could partially explain the elevated scatter in the results of the elongation to failure, observed in particular at temperatures higher than 50 °C. Moreover, since the annealing temperature was probably close to the recrystallization temperature of Al-1%Si, there is high variability in the microstructure and therefore in the mechanical properties. In fact, Liu *et al.* (1999) identify 200 °C annealing temperature as the threshold below which recovery and recrystallization predominate. Above that value, on the contrary, silicon precipitation and coarsening predominate.

Similarly, Takagi *et al.* (2016) observed that, for Au bonding wires annealed at 200 °C, the test results provided a high scatter in both Young's modulus and yield strength ("by cross-sectional observation it was found that the difference in the degree of recrystallization, which was produced by annealing at a temperature very close to the recrystallization temperature for Au, gave rise to the scatter in the data").
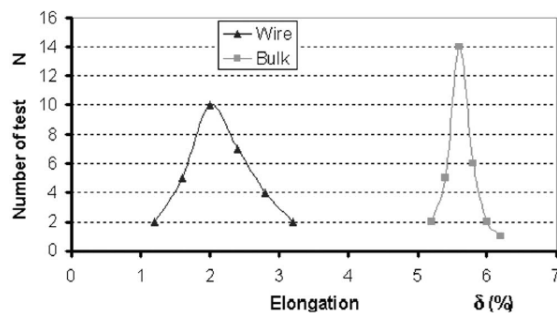
Figure 113: Distribution of the testing elongation data from 30 samples annealed at 275 °C for 10 h. Liu et al. (2004).

Concerning the mechanical properties of the wire at higher temperatures, it is difficult to compare the results of tensile tests obtained in this work with experiments reported in the literature. Deyhim *et al.* (1996) reported a fatigue resistance for Al-Si wires (25 μm diameter, 1-4% elongation to failure, 15-17 gmf tensile strength) slightly dependent on the temperature at 75 °C. However, little information is present in the literature on this topic.

The fact that the FIB/SEM images obtained close to the fracture points of the tether do not show a significant effect on the width of the grains/subcells also confirm the fact that strong elongation did not occur at necking, even at 100 °C, as discussed in paragraph 6.6.

At temperatures below ambient temperature, the elongation to failure decreases. This is expected due to the embrittlement of aluminium at low temperatures.

The objective of the load/unload test was to verify the behaviour of the material at low stress and low stress rate. The stress/strain curve presents a hysteresis loop, which was unexpected since it is typical of viscoelastic materials. The loop represents the energy lost in the load/unload process. Once again, the Young's modulus measured was in the order of 27 GPa. There are some doubts on the results of such test. The sliding of the sample in the clamp is not considered a source of error in this case, since the displacement returned to zero after the load was removed. Instead, what could explain such result is the presence of the silicon adhesive of the Kapton at one side of the support. The silicon adhesive could have carried the load instead of the tether sample in this case.

The strain rate measured during the creep test was very low, in the order of 10^{-9} s^{-1} for temperatures up to 80 °C. This low value could be explained by the low value of stress applied during the creep test (1.3 MPa). Studies on Al-Si creep reports values of strain rates above 10^{-7} s^{-1} for creep tests at 20 MPa for Al-7%Si (Jin *et al.* (2015)). Determining the creep rate is not trivial since the total strain measured is the sum of the elastic strain, the thermal strain and the creep strain (Jin *et al.* (2015)). The elastic strain is function of the applied stress and the Young's modulus at the testing temperature. The thermal strain is function of the material thermal expansion. In order to calculate the termal expansion as function of the temperature, preliminar tests such as the dilatometry tests should be conducted. Another study that would deserve to be conducted in the future concerns the creep tests at different stress levels, and different temperatures, with the objective of assessing the linearity of the response. The creep test is a crucial test for the material since the E-sail tether is supposed to be always under tension among the entire lifetime of the satellite.

The strain rate sensitivity test provided a value for the exponent m ranging from 0.12 to 0.3 at 110 °C. A value m between 0.3 and 0.5 is considered to be the threshold for the onset of a superplastic behaviour in the material (Edington *et al.* (1976)). A superplastic material is a material capable to resist to necking and/or to delay the final failure after the onset of the necking. A superplastic material at failure should then present an extended necking region with reduced diameter with respect to the initial value. The sample elongation can be estimated based on the neck cross-sectional area and on the parameter m (Edington *et al.* (1976)). In our case, however, we did not observe a significant thinning of the wire after failure. Therefore, we cannot state that the material behaved superplastically. It is believed that a value m closer to 0.12 should be probably considered. Similar values of the strain rate sensitivity coefficient have been found for fine-grained Au wires (Chew *et al.* (2008)) and (Kawasaki *et al.* (2007)). Studies on strain rate sensitivity of Ai-Si alloys have been carried out by Jiang *et al.* (2007). The authors discuss the effect of microstructure on strain rate sensitivity of Al- 11%Si alloy and identify a superplastic behaviour in some cases. Superplastic behaviour has been identified even for the Al-Si eutectic at strain rates range $10^{-4} - 10^{-3}$ s^{-1}, but no reference has been found for hypoeutectic Al-Si, which in our case.

Concerning the dynamic tests, the value of $\tan \delta$ measured was comparable with the one of polymers (Basu *et al.* (2013)), thus raising some doubts on these unexpected results. One possible source of error, in addition to the sliding of the sample in the support, could be the effect of temperature on the set-up. Since the strain is calculated as the ratio of the displacement versus the initial length, at temperatures higher than ambient temperature, the total displacement measured at each set point (and for each frequency) is not only due to the applied load, but also due to the termal expansion of the material. This is reflected in the measured values of the storage modulus and loss modulus and, as a concequence, of $\tan \delta$. In this sense, thermal strain should be considered, as also previously discussed for the creep test.

An alternative method for measuring the tensile strength and Young's modulus of these wires has been recently published by Basu *et al.* (2014). The method, named continuous dynamic analysis (CDA), is based on the use of extremely small harmonic force modulation applied throughout the tensile test. The resulting strain is independent from the applied quasi-static strain and it is much smaller in magnitude, thus remaining in the linear viscoelastic regime, even for polymers. This method is promising since it overcomes the DMA instrument limitation when performing tests at very small strains. The results for gold, tungsten and copper microwires, reported in Figure 114, show that the dynamic modulus is comparable with the one of the bulk material. The $\tan \delta$ was not reported by the authors since it was considered not to be relevant for metals. However, such method could not, for the moment, provide information at different temperatures. It is not excluded that a CDA instrument could be provided with a temperature stabilised chamber as the DMA in the future.
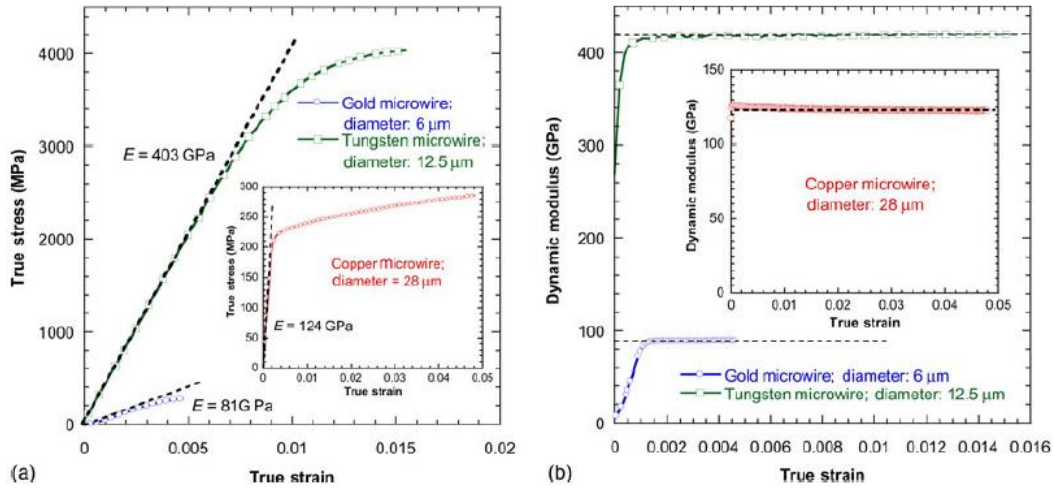
Figure 114: (a) Quasi-static tensile stress-strain response of tungsten and gold microwires. The response of copper microwire is shown in the inset as it deformed to larger strains compared with other microwires. (b) CDA during the tensile tests shown in (a). Basu et al. *(2013).*

Since the shape factor is a crucial feature for microwires, together with the grain dimension, if aluminium is to be confirmed as the E-sail tether material in the future, it could be necessary to perform a broader experimental activity to assess the impact of annealing temperatures on the tensile strength and strain rate sensitivity at different temperatures.

Moreover, further studies could be conducted on the strength of the bonding points of the heytether. In case of failure of the base wire, in fact, the bonding points would have a structural function, even if there would not be a single point of failure. Moreover, there seems to be room for further research on the adhesion of the coating on the substrate, especially at the bonding points.

Concerning the results of the optical measurements for the coating produced in the frame of this study, our research complements what has been done in the ESAIL FP7 project by Rauhala *et al.* (2013), even if using different methodologies. Not only the emissivity of three other coatings (TiO$_2$, ZnO and TiZnO), apart from Al$_2$O$_3$, has been measured, but also the absorbance. This test campaign allowed calculating the α/ε ratio, a fundamental parameter to estimate the equilibrium temperature of the tether in space.

It was demonstrated that all the three new coatings under test contribute to increase the equilibrium temperature of the tether with respect to Al$_2$O$_3$. It was also observed that the ALD coatings were able to cover in a uniform manner the tether's surface, which presented some roughness due to the drawing process.

As previously discussed, the equilibrium temperature of the tether in space is linearly dependent from the parameter $\sqrt[4]{\alpha/\varepsilon}$. This temperature factor has been also computed at different temperatures, assuming a linear dependence of the emissivity from the temperature, and it is shown in Figure 115. Compared to Al$_2$O$_3$, TiO$_2$ increases the temperature of the wire of about 10%, while ZnO and TiZnO by more than 20%.

128
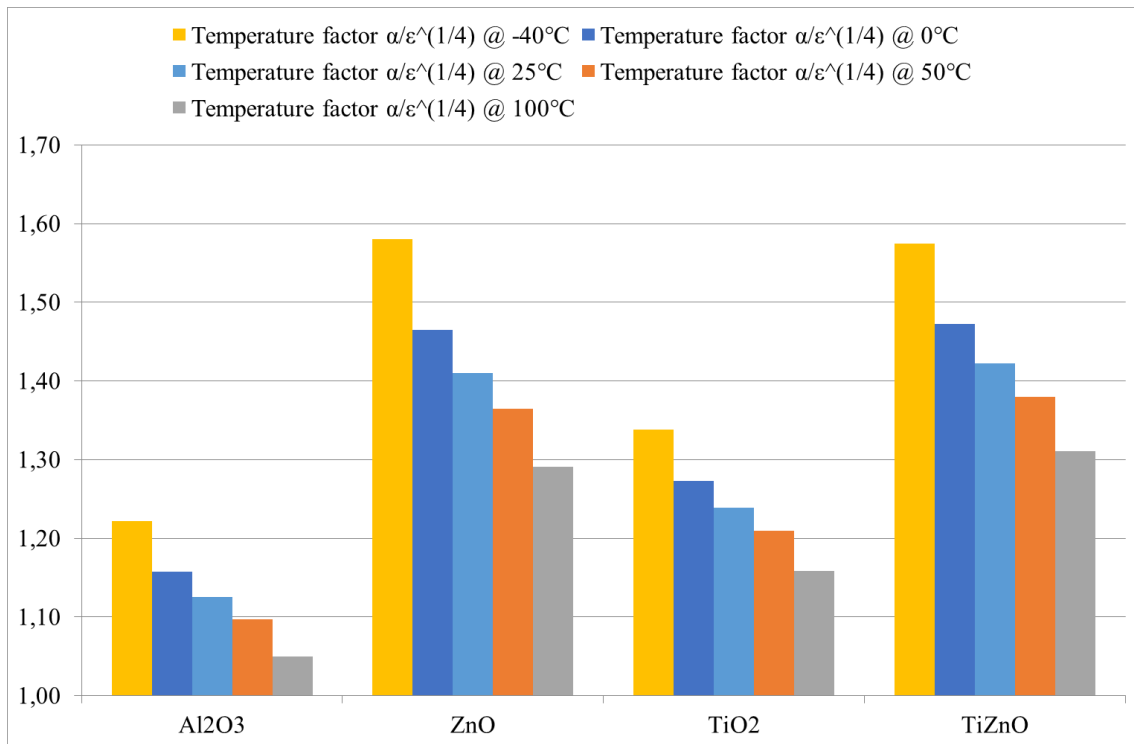
Figure 115: Temperature factor $\sqrt[4]{\alpha/\varepsilon}$ at different temperatures.

However, since the emissivity is a function of the equilibrium temperature itself, solving the thermal equilibrium is not trivial. To this scope, it is necessary to solve the thermal equilibrium equation numerically.

A direct impact of these results on the development of the technology is to give the possibility to system engineers to optimise the thrust estimation of the E-sail at different distances from the Sun. Based on this distance and on the selected coating, in fact, one can derive the equilibrium temperature of the tether and its maximum strength. This methodology – linking mechanical and optical properties – could be used to further improve the E-sail material. For instance, the ratio between wire diameter and grain dimension could be increased to provide higher strength.

Furthermore, this stream of research should continue with the aim of finding the optimal coating depending on the material selected (operating temperature) and the type of mission to be performed (distance from the Sun). This would be a major challenge when thinking to a mission close to the Sun. Developing a thin coating, with thickness in the order of nanometres, which is capable of absorbing little power radiated from the Sun in the optical range and of maximising its emittance in the infrared range, presents several criticalities, for instance related to scale effects, as already discussed in this work.

Finally, this research could be complemented by detailed studies on the electrical resistivity of the tether and the impact of the creep on such property.

9. CONCLUSIONS

In this work, the mechanical properties of the E-sail tether material – Al-1%Si – have been studied in order to determine its sensitivity to temperature variations. Such information should be considered a prerequisite for the identification of coatings modifying the equilibrium temperature of the tether in space. This can be obtained thanks to the modification of the optical properties of the surface of the tether – namely the absorbance/emissivity (α/ε) ratio.

First, the state of the art of the E-sail technology has been described in details. The concept, the underpinning physics theory and the E-sail system have been discussed. Then, the current E-sail projects have been listed. There is a considerable and increasing interest in this technology: currently, both the European Space Agency and the National Aeronautics and Space Administration are funding studies on E-sail. Several CubeSat mission are also under development to prove the concept in space.

In the following part, an extensive analysis of the tether material requirements has been carried out, focusing mainly on the tensile strength requirements and on the optical requirements for the tether's surface. To this purpose, also the coating requirements have been discussed. Tether and coating material options were also analysed.

The mechanical test campaign, carried out both at high temperature and below ambient temperature, allowed to have a detailed view of the trend of breaking load with temperature. The breaking load decreases at a rate of about 0.5 mN/ °C. Such information can be used to estimate the performance of the E-sail technology at different temperatures, since its thrust may be linked to the tensile strength, as discussed in chapter 4.

While the data obtained for the breaking load provided good reliability and reproducibility, the data related to the elongation to failure presented a higher variability. Possible sources of error have been extensively discussed and the Digital Image Correlation (DIC) method has been used to confirm the measurement of the displacement at ambient temperature. The viscoelastic properties that were observed for the Al-1%Si material, mainly through the creep test and strain rate sensitivity test, have been also discussed.

The microstructure of the Al-1%Si material has been observed with the Transmission Electron Microscope (TEM) both for the material as provided by the manufacturer and after a tensile test to failure at high temperature (100 °C). It was noticed that the crystallographic direction of the grains was quite similar among the grains, leading to the conclusion that in some cases the grains were subcells instead. While the material as provided presented dense dislocation walls (DDWs), the specimen after testing at 100 °C did not present the same feature. This could be due to migration of dislocations to the grain boundaries.

Four coatings have been produced – Al_2O_3, TiO_2, ZnO and TiZnO – and their morphology and optical properties have been studied. The optical measurements provided the α/ε parameter, crucial to estimate the equilibrium temperature in space. Moreover, the α/ε ratio itself is dependent on the temperature, since the emissivity is a function of the temperature according to the theory of Hagen-Rubens. This implies that the estimation of the equilibrium temperature of the tether in space is not trivial. This could be the object of further studies.

All coatings seem to increase the operating temperature and the highest values of α/ε ratio were obtained for ZnO e TiZnO. For these reasons, such coatings are believed to improve the thermal condition of the tether for space missions to the outer solar system, where temperatures are lower.

To conclude, this work permitted to identify the correlations between material microstructure, production process and mechanical properties, and provided a thorough discussion based on the evidence collected. Some of the results, namely the breaking load at different temperatures and the absorption/emissivity parameters for the different coatings produced, were not available in the literature for the materials under study. This methodological approach was originally applied in the frame of this study and will be need for the future development of the E-sail tether.

In the future, a more precise instrument, such as the continuous dynamic analysis (CDA) system, described in Basu *et al.* (2014), could be eventually used to measure the yield strength. Such value would provide an important input to the design of the E-sail structure.

Wires with improved strength over a wider range of temperatures could be also selected in the future. For instance, carbon nanotube wires would be good candidates, as they provide a theoretical strength ten times higher than aluminium. A methodological approach similar to the one used in this study would then be needed to link the structural, optical and even electrical properties of the tether.

LIST OF PUBLICATIONS

P. Janhunen, P. Toivanen, J. Envall, S. Merikallio, G. Montesanti, J. Gonzalez del Amo, U. Kvell, M. Noorma, S. Lätt, "Overview of electric solar wind sail applications", Proceedings of the Estonian Academy of Sciences, 2014, 63, 2S, pp. 267-278.

M. Hassan, L. Borgese, G. Montesanti, E. Bemporad, G. Cesarini, R. Li Voti, L.E. Depero, "Atomic layer deposition of semiconductor oxides on electric sail tethers", Thin Solid Films, Vol. 621 (2017), pp. 195-201.

BIBLIOGRAPHY

A.M. Abd El-Khalek, "The variation of work-hardening characteristics of Al–1 wt% Si and Al–1 wt% Si–0.1 wt% Zr–0.1 wt% Ti alloys", Physica B 315, **2002**, pp. 7-12.

A.M. Abd El-Khalek, "Steady state creep and creep recovery behaviours of pre-aging Al–Si alloys", Materials Science and Engineering A 500, **2009**, pp. 176-181.

P.A. Agyakwa, M.R. Corfield, L. Yang, J.F. Li, V.M.F. Marques, C.M. Johnson, "Microstructural evolution of ultrasonically bonded high purity Al wire during extended range thermal cycling", Microelectronics Reliability 51, **2011**, pp. 406-415.

P.A. Agyakwa, L. Yang, E. Arjmand, P. Evans, M.R. Corfield, C.M. Johnson, "Damage Evolution in Al Wire Bonds Subjected to a Junction Temperature Fluctuation of 30 K", Journal of Electronic Materials, Vol. 45, Issue 7, **2016**, pp. 3659-3672.

I. Alessandri, M. Zucca, M. Ferroni, E. Bontempi, L. Depero, "Growing ZnO nanocrystals on polystyrene nanospheres by extra-low-temperature atomic layer deposition, "Crystal Growth and Design", 9, **2009**, pp. 1258-1259.

R.J. Amodeo, N.M. Ghoniem, "A review of Experimental Observations and Theoretical Models of Dislocation Cells and Subgrains", Res Mechanica, 23, **1988**, pp. 137-160.

V.S. Ananthan, T. Leffers, N. Hansen, "Cell and band structures in cold rolled polycrystalline copper", Materials Science and Technology, Vol. 7, **1991**, pp. 1069-1075.

M. Ashby, "Materials Selection in Mechanical Design", Butterworth-Heinemann, **2010** (4th edition).

S. Basu, J.L. Hay, J.E. Swindeman, W.C. Oliver, "Continuous dynamic analysis: evolution of elastic properties with strain", Materials Research Society Communications, 4, **2014**, pp. 25-29.

B. Bay, N. Hansen, D. Kuhlmann-Wilsdorf, "Deformation Structures in Lightly Rolled Pure Aluminium", Materials Science and Engineering, A 113, **1989**, pp. 385-397.

BBC.com, "Japan tests innovative magnetic tether for slowing space junk", consulted in April **2016**, available at http://www.bbc.com/news/world-asia-38265676.

M. H. N. Beshai, G. H. Deaf, A. M. Abd El Khalek, G. Graiss, M. A. Kenawy, "Effect of Superimposed Low Frequency Oscillations on the Static Creep Behaviour of Al-1 wt% Si and A-wt% Si-0.1 wt% Zr-0.1 wt% Ti Alloys", Physica status solidi (a), 161, **1997**, pp. 65-74.

J. Bielen, J. Gommans, F. Theunis, "Prediction of high cycle fatigue in aluminum bond wires: A physics of failure approach combining experiment and multi-physics simulations", 7th. Int. Conf. on Thermal, Mechanical and Multiphysics Simulation and Experiments in Micro-Electronics and Micro-Systems, EuroSimE, **2006**, pp. 1-7.

L. Borgese, E. Bontempi, L.E. Depero, P. Colombi, I. Alessandri, "Tailoring phase and composition at the nanoscale: atomic layer deposition of Zn-Ti-O thin films", CrystEngComm, 13, **2011**, pp. 6621-6624.

E.J. Bosze, A. Alawar, O. Bertschger, Yun-I. Tsai, S.R. Nutt, "High-temperature strength and storage modulus in unidirectional hybrid composites", Composites Science and Technology, 66, **2006**, pp. 1963-1969.

C.D. Breach, "What is the future of bonding wire? Will copper entirely replace gold?", Gold Bulletin, Volume 43 No 3, **2010**, pp. 150-168.

X. Chen, Q. Lv, X. Yi, "Smart window coating based on nanostructured VO2 thin film", Optik - International Journal for Light and Electron Optics, Volume 123, Issue 13, **2012**, pp. 1187-1189.

X. Chen, "Low Work-Function Thermionic Emission and Orbital-Motion-Limited Ion Collection at Bare-Tether Cathodic Contact", Phd thesis at Universidad Politécnica de Madrid, Escuela Técnica Superior de Ingenieros Aeronáuticos, July **2015**.

Y. Chen, A.H. Clausen, O.S. Hopperstad, M. Langseth, "Stress–strain behaviour of aluminium alloys at a wide range of strain rates", International Journal of Solids and Structures 46, **2009**, pp. 3825-3835.

Y.H. Chew, C.C. Wong, F. Wulff, F.C. Lim, H.M. Goh, "Strain rate sensitivity and Hall–Petch behavior of ultrafine-grained gold wires", Thin Solid Films 516, **2008**, pp. 5376-5380.

E.W. Cooke, W.L. Long, "Anodic Coatings for Temperature Control in Space Vehicles, U.S. Wright Air Development Div. Technical Report 60-773, **1961**, pp. 281-297.

M.L. Cosmo, E.C. Lorenzini, "Tethers in Space Handbook", Smithsonian Astrophysical Observatory, **1997**.

R. Cumberland, W.B. Barvose Carter, A.F. Gross, "Tunable variable emissivity materials and methods for controlling the temperature of spacecraft using tunable variable emissivity materials", US Patent 7691284, filed 29/8/**2006**.

L. Curtis, J. Vaughn, K. Welzyn, J. Carroll, "Development of the flight tether for ProSEDS", AIP Conference Proceedings 608, 385, **2002**.

F.D. Danaher, J.J. Williams, D.R.P. Singh, L. Jiang, N. Chawla, "Tensile and Fatigue Behavior of Al-1Si Wire Used in Wire Bonding", Journal of Electronic Materials, Vol. 40, No. 6, **2011**.

J. R. Devore, "Refractive Indices of Rutile and Sphalerite", Journal of the Optical Society of America, 41, **1951**, pp. 416-419.

A. Deyhim, B. Yost, M. Lii, C. Li, "Characterization of the Fatigue Properties of Bonding Wires", **1996** Electronic Components and Technology Conference, pp. 836-841.

J.W. Diggle, T.C. Downie, C.W. Goulding, "Anodic oxide films on aluminum", Chemical Reviews, 69 (3), **1969**, pp. 365-405.

M. Djurdjevic, S. Manasijevic, Z. Odanovic, N. Dolic, "Calculation of Liquidus Temperature for Aluminum and Magnesium Alloys Applying Method of Equivalency", Advances in Materials Science and Engineering, October **2013**, pp. 1-8.

S. Edalatpour, M. Francoeur, "Size effect on the emissivity of thin films", Journal of Quantitative Spectroscopy & Radiative Transfer, 118, **2013**, pp. 75-85.

J.V. Edington, K.N. Melton, C.P. Cutler, "Superplasticity", Progress in Materials Science, Vol. 21, No. 2, **1976**, pp. 61-158.

L.M. Egorova, B.N. Korchunov, V.N. Osipov, V.A. Bershtein, S.P. Nikanorov, "Kinetics of Silicon Precipitation in a Directionally Crystallized Binary Aluminum–Silicon Alloy", Physics of the Solid State, Vol. 55, No. 12, **2013**, pp. 2549-2553.

U. Engel, R. Eckstein, "Microforming – from basic research to its realization", Journal of Materials Processing Technology, 125-126, **2002**, pp. 35-44.

J. Envall, P. Janhunen, P. Toivanen, M. Pajusalu, E. Ilbis, J. Kalde, M. Averin, H. Kuuste, K. Laizans, V. Allik, T. Rauhala, H. Seppänen, S. Kiprich, J. Ukkonen, E. Haeggström, T. Kalvas, O. Tarvainen, J. Kauppinen, A. Nuottajärvi, H. Koivisto, "E-sail test payload of the ESTCube-1 nanosatellite, Proceedings of the Estonian Academy of Sciences, 63, 2S, **2014**, pp. 210-221.

eoPortalDirectory, "Aalto-1: The Finnish Student Nanosatellite", consulted in April **2017**, available at https://directory.eoportal.org/web/eoportal/satellite-missions/a/aalto-1.

D. Fan, Q. Li, Y. Xuan, H. Tan, J. Fang, "Temperature-dependent infrared properties of Ca doped $(La,Sr)MnO_3$ compositions with potential thermal control application", Applied Thermal Engineering 51, **2013**, pp. 255-261.

A.C. Fischer, H. Gradin, S. Schröder, S. Braun, G. Stemme, W. van der Wijngaart, F. Niklaus, "Wire-bonder-assisted integration of non-bondable SMA wires into MEMS substrates", Journal of Micromechanics and Microengineering, Volume 22, Number 5, **2012**, pp. 2-19.

R.T. Fitzsimmons, C.E. Miller, "Brittle cracks induced in AlSi wire by the ultrasonic bonding tool", 41st Electronic Components and Technology Conference (Proceedings), **1991**.

U. Geibler, M. Schneider-Ramelow, H. Reichl, "Hardening and Softening in AlSi1 Bond Contacts During Ultrasonic Wire Bonding", IEEE Transactions on Components and Packaging Technologies, Vol. 32, Issue 4, **2009**, pp. 794-799.

A.P. Gerlich, L. Yue, P.F. Mendez, H. Zhang, "Plastic deformation of nanocrystalline aluminum at high temperatures and strain rate", Acta Materialia 58, **2010**, , pp. 2176-2185.

D.G. Gilmore (editor), "Spacecraft Thermal Control Handbook, Volume I: Fundamental Technologies", The Aerospace Corporation, **2002** (second edition).

K.A. Gittemeier, C.W. Hawk, M.M. Finckenor, E. Watts, "Space Environmental Effects on Coated Tether Materials", 41st AIAA/ASME/SAE/ASEE Joint Propulsion Conference, July **2005**.

G. Harman, J. Albers, "The Ultrasonic Welding Mechanism as Applied to Aluminum-and Gold-Wire Bonding in Microelectronics", IEEE Transactions on Parts, Hybrids, and Packaging, Vol. 13, Issue 4, **1977**, pp. 406-412.

M. Hassan, L. Borgese, G. Montesanti, E. Bemporad, G. Cesarini, R. Li Voti, L.E. Depero, "Atomic layer deposition of semiconductor oxides on electric sail tethers", Thin Solid Films, Vol. 621, **2017**, pp. 195-201.

J.E. Hatch, "Aluminum Properties and Physical Metallurgy", ASM International, **1984**.

S. Hazra, L. Borgese, S. Federici, E. Bontempi, M. Ferrari, V. Ferrari, J. Plaisier, X. Santarelli, G. Zerauschek, A. Lausi, "Electrical resistivity of Ti-Zn mixed oxide thin films deposited by atomic layer deposition", Thin Solid Films, 520, **2012**, pp. 5151-5154.

R. Hoyt, R. Forward, "Alternate interconnection hoytether failure resistant multiline tether", US Patent 6286788, filed 8/9/**2000**.

R. Hoyt, N. Voronka, T. Newton, I. Barnes, J. Shepherd, S.S. Frank, J. Slostad, B. Jaroux, R. Twiggs, "Early Results of the Multi-Application Survivable Tether (MAST) Space Tether Experiment", 21st Annual AIAA/USU Conference on Small Satellites, **2007**.

S. Hyun, T.K.Hooghan, W.L. Brown, R.P. Vinci, "Linear viscoelasticity in aluminum thin films", Applied Physics Letters 87, 061902, **2005**.

T. Ikeda, S. Kawamoto, "Multiple Bare Tethers for Electrodynamic Tether Propulsion", 30th International Electric Propulsion Conference, Florence, Italy, September 17 – 20, **2007**.

A. Inoue, "Amorphous, nanoquasicrystalline and nanocrystalline alloys in Al-based systems", Progress in Materials Science 43, **1998**, pp. 365-520.

P. Janhunen, "Electric Sail for Spacecraft Propulsion", Journal of Propulsion and Power, Vol. 20, No. 4, **2004**, pp. 763-764.

P. Janhunen, A. Sandroos, "Simulation study of solar wind push on a charged wire: basis of solar wind electric sail propulsion", Annales Geophysicae, 25, **2007**, pp. 755-767.

P. Janhunen, "On the feasibility of a negative polarity electric sail", Annales Geophysicae, 27, **2009**, pp. 1439-1447.

P. Janhunen, "Electrostatic Plasma Brake for Deorbiting a Satellite", Journal of Propulsion and Power, Vol. 26, No. 2, **2010**, pp. 370-372.

P. Janhunen, P. K. Toivanen, J. Polkko, S. Merikallio, P. Salminen, E. Haeggström, H. Seppänen, R. Kurppa, J. Ukkonen, S. Kiprich, G. Thornell, H. Kratz, L. Richter, O. Krömer, R. Rosta, M. Noorma, J. Envall, S. Lätt, G. Mengali, A. A. Quarta, H. Koivisto, O. Tarvainen, T. Kalvas, J. Kauppinen, A. Nuottajärvi, A. Obraztsov "Electric solar wind sail: toward test missions", Review of Scientific Instruments, 81, 111301, **2010**.

P. Janhunen, A. A. Quarta, G. Mengali, "Electric solar wind sail mass budget model", Geoscientific Instrumentation, Methods and Data Systems, 2, **2013**, pp. 85-95.

P. Janhunen, P. Toivanen, J. Envall, S. Merikallio, G. Montesanti, J. Gonzalez del Amo, U. Kvell, M. Noorma, S. Lätt, "Overview of electric solar wind sail applications", Proceedings of the Estonian Academy of Sciences, 63, 2S, **2014**, pp. 267-278.

P. Janhunen, P. Toivanen, "Safety criteria for flying E-sail through solar eclipse", Acta Astronautica, Vol. 114, **2015**, pp. 1-5.

Y. Jia, K. Peng, X. Gong, Z. Zhang, "Creep and recovery of polypropylene/carbon nanotube composites", International Journal of Plasticity, Volume 27, Issue 8, **2011**, pp. 1239-1251.

J. Jiang, A. Ma, N. Saito, A. Watazu, P. Lin, Y. Nishida, "Effect of microstructures on superplasticity of Al-11%Si alloy", Transactions of Nonferrous Metals Society of China, 17, **2007**, pp. 509-513.

S.H. Jin, J.U. Jong, "Assessment of Thermal Cycling Creep Lifetime of Al-Si Alloys" International Journal of Mechanics and Applications, 5(2), **2015**, pp. 41-47.

C.L. Johnson, J.L.C. Ballance, K.J. Welzyn, J.A. Vaughn, E. Lorenzini, P.S. Schuler, "Electrodynamic Tether" US Patent 7188074, filed 17/10/**2003**.

D. Juul Jensen, Å. Kvick, E.M. Lauridsen, U. Lienert, L. Margulies, S.F. Nielsen, H.F. Poulsen, "Plastic deformation and recrystallization studied by the 3D x-ray microscope", Materials Research Society symposia proceedings, Vol. 590, **2000**, pp. 227-240.

K. Kashihara, M. Cho, S. Kawamoto, "Ground Experiments and Computer Simulations of Interaction Between Bare Tether and Plasma", IEEE Transactions on Plasma Science, Vol. 36, No. 5, **2008**, pp. 2324-2335.

M. Kawasaki, T.G. Langdon, "Principles of superplasticity in ultrafine-grained materials", Journal of Materials Science, 42, **2007**, pp. 1782-1796.

O. Khurshid, P. Janhunen, M. Buhl, A. Visala, J. Praks, M. Hallikainen, "Attitude dynamics analysis of Aalto-1 satellite during de-orbiting experiment with Plasma Brake", 63rd International Astronautical Congress, Naples, Italy, Oct 1-5 **2012**.

G. Kim, J. Ni, M. Koç, "Modeling of the Size Effects on the Behavior of Metals in Microscale Deformation Processes", Transactions of the ASME, Vol. 129, **2007**, pp. 470-476.

H. Kim, D. Cho, E. Jeong, W. Kim, S. Lim, "Microstructure Evolution of Al-1% Si Bonding Wire for Microelectronic Reliability", Electronic Materials Letters, Vol. 5, No. 3, **2009**, pp. 99-103.

J. Kim, G. Sauti, R.J. Cano, R.A. Wincheski, J.G. Ratcliffe, M. Czabaj, N.W. Gardner, E.J. Siochi, "Assessment of carbon nanotube yarns as reinforcement for composite overwrapped pressure vessels", Composites Part A: Applied Science and Manufacturing, Vol. 84, **2016**, pp. 256-265.

K.S. Kim, J.Y. Song, E.K. Chung, J.K. Park, S.H. Hong, "Relationship between mechanical properties and microstructure of ultra-fine gold bonding wires", Mechanics of Materials 38, **2006**, pp. 119–127.

Y. Kim, D. Kang, S. Hong, Y. Kim, C. Kang, S. Choi, "Influence of variation in the silicon content on the silicon precipitation in the Al–Si binary system", Journal of Thermal Analysis and Calorimetry, 128, **2017**, pp. 107-113.

N. Kiomarsipour, R.S. Razavi, K. Ghanib, "Improvement of spacecraft white thermal control coatings using the new synthesized Zn-MCM-41 pigment", Dyes and Pigments, Volume 96, Issue 2, **2013**, pp. 403-406.

Knowles Capacitors, "Wire Bond / Ball Shear Application Note", available in **April 2017** at http://www.knowlescapacitors.com/File%20Library/Dilabs/English/GlobalNavigation/Quality/Wire bonding_Application_Notes.pdf.

H. Koivisto, T. Kalvas and P. Janhunen, "Tether space environment requirements", Deliverable D23.1 of the ESAIL FP7 project, **2011**.

J.E. Krzanowski, N. Murdeshwar, "Deformation and bonding processes in aluminum ultrasonic wire wedge bonding", Journal of Electronic Materials, Vol. 19, Issue 9, **1990**, pp. 919-928.

H. Kuuste, T. Eenmäe, V. Allik, A. Agu, R. Vendt, I. Ansko, K. Laizans, I. Sünter, S. Lätt, M. Noorma, "Imaging system for nanosatellite proximity operations", Proceedings of the Estonian Academy of Sciences, 63, 2S, **2014**, pp. 250-257.

T.G. Langdon, "Grain boundary sliding revisited: Developments in sliding over four decades", Journal of Materials Science, 41, **2006**, pp. 597-609.

T.G. Langdon, "Twenty-five years of ultrafine-grained materials: Achieving exceptional properties through grain refinement", Acta Materialia, Volume 61, Issue 19, **2013**, pp. 7035-7059.

F. Lasagni, B. Mingler, M. Dumont, H.P. Degischer, "Precipitation kinetics of Si in aluminium alloys", Materials Science and Engineering A 480, **2008**, pp. 383-391.

J.H. Lau (editor), "Chip on Board - Technologies for Multichip Modules", Van Nostrand Reinhold, New York, **1994**.

S. Lätt, A. Slavinskis, E. Ilbis, U. Kvell, K. Voormansik, E. Kulu, M. Pajusalu, H. Kuuste, I. Sünter, T. Eenmäe, K. Laizāns, K. Zālite, R. Vendt, J. Piepenbrock, I. Ansko, A. Leitu, A. Vahter, A. Agu, E. Eilonen, E. Soolo, H. Ehrpais, H. Lillmaa, I. Mahhonin, J. Mõttus, J. Viru, J. Kalde, J. Šubitidze, J. Mucenieks, J. Sate, J. Kütt, J. Polevskis, J. Laks, K. Kivistik, K.-L. Kusmin, K.-G. Kruus, K. Tarbe, K. Tuude, K. Kalniņa, L. Joost, M. Lõoke, M. Järve, M. Vellak, M. Neerot, M. Valgur, M. Pelakauskas, M. Averin, M. Mikkor, M. Veske, O. Schlere, P. Liias, P. Laes, R. Rantsus, R. Soosaar, R. Reinumägi, R. Valner, S. Kurvits, S.-E. Mändmaa, T. Ilves, T. Peet, T. Ani, T. Tilk, T.H.C. Tamm, T. Scheffler, T. Vahter, T. Uiboupin, V. Evard, A. Sisask, L. Kimmel, O. Krömer, R. Rosta, P. Janhunen, J. Envall, P. Toivanen, T. Rauhala, H. Seppänen, J. Ukkonen, E. Hæggström, R. Kurppa, T. Kalvas, O. Tarvainen, J. Kauppinen, A. Nuottajärvi, H. Koivisto, S. Kiprich, A. Obraztsov, V. Allik, A. Reinart and M. Noorma, "ESTCube-1 nanosatellite for electric solar wind sail in-orbit technology demonstration", Proceedings of the Estonian Academy of Sciences, 63, 2S, **2014**, pp. 200-209.

G. Lefranc, B. Weiss, C. Klos, J. Dick, G. Khatibi, H. Berg, "Aluminum bond-wire properties after 1 billion mechanical cycles", Microelectronics Reliability, 43, **2003**, pp. 1833-1838.

M. Legros, D.S. Gianola, K.J. Hemker, "In situ TEM observations of fast grain-boundary motion in stressed nanocrystalline aluminum films", Acta Materialia 56, **2008**, pp. 3380-3393.

J. Lennhoff, G. Harris, J. Vaughn, D. Edwards, J. Zwiener, "Electrically conductive space-durable polymeric films for spacecraft thermal and charge control", High Performance Polymers, 11, **1999**, pp. 101-111.

C.T. Liu, C.L. White, J.A. Horton, "Effect of boron on grain-boundaries in Ni3Al", Acta metallurgica, Vol. 33 No 2, **1985**, pp. 213-229.

H. Liu, N. Fank, C. Acosta, "Mechanical and Corrosion Properties of Aluminum Wires for Ultrasonic Bonding", The International Journal of Microcircuits and Electronic Packaging, Volume 22, Number 2, Second Quarter **1999**, pp. 121-126.

Y. Liu, W. K. Jones, "Microstructure and Mechanical Properties of Annealed Al-1%Si Bonding Wire", Journal of Electronic Materials, Vol. 33, No. 9, **2004**, pp. 929-934.

R. Li Voti, G.L. Leahu, S. Gaetani, C. Sibilia, V. Violante, E. Castagna, M. Bertolotti "Light scattering from a rough metal surface: theory and experiment", Journal of the Optical Society of America B, Vol. 26, Issue 8, **2009**, pp. 1585-1593.

R. Li Voti, "Optimization of transparent metal structures by genetic algorithms", Romanian Reports in Physics, 64, **2012**, pp. 446-466.

R. Li Voti, M.C. Larciprete, G.L. Leahu, C. Sibilia, M. Bertolotti, "Optimization of thermochromic VO2 based structures with tunable thermal emissivity" Journal of Applied Physics, 112 (3), 034305, **2012**.

R. Li Voti, G.Leahu, M.C. Larciprete, C. Sibilia, M. Bertolotti, I. Nefedov, I.V. Anoshkin, "Photoacoustic Characterization of Randomly Oriented Silver Nanowire Films", International Journal of Thermophysics, Vol. 36, Issue 5-6, **2015**, pp. 1342-1348

P. Ma, C. Zou, H. Wang, J. Jie, Y. Jia, B. Fu, Z. Wie, "Microstructure evolution and precipitation of SiC particle reinforced Al–20Si composite solidified under high pressures", Materials Letters 79, **2012**, pp. 232-234.

P. Ma, C.M. Zou, H.W. Wang, S. Scudino, K.K. Song, M. Samadi Khoshkhoo, Z.J. Wei, U. Kühn, J. Eckert, "Structure of GP zones in Al–Si matrix composites solidified under high pressure", Materials Letters 109, **2013**, pp. 1-4.

V. Maier, K. Durst, J. Mueller, B. Backes, H.W. Höppel, M. Göken, "Nanoindentation strain-rate jump tests for determining the local strain-rate sensitivity in nanocrystalline Ni and ultrafine-grained Al", Journal of Materials Research, Volume 26, Issue 11, **2011**, pp. 1421-1430.

E.E. Martinez-Flores, J. Negrete, G. Torres-Villaseñor, "Relationship between loss-modulus and homologous temperature in superplastic alloys", Journal of Thermal Analysis and Calorimetry, 97, **2009**, pp. 891-894.

H. Masuda, H. Tobe, E. Sato, Y. Sugino, S. Ukai, "Two-dimensional grain boundary sliding and mantle dislocation accommodation in ODS ferritic steel" Acta Materialia 120, **2016**, pp. 205-215.

B. McCandless, F.M. Kustas, L.S. Marshall, W.B. Lytle, N.P. Hansen, "Design Concept for a Reusable/Propellantless MXER Tether Space Transportation System", Spacecraft Propulsion Joint Meeting, 5-8 Dec. **2005**.

K.N. Melton, J.W. Edington, "Superplasticity in Extruded Zn-40wt.-%Al and Zn-50wt.-% Al Alloys", Metal Science Journal, 7:1, **1973**, pp. 172-175.

K.P. Menard, "Dynamic Mechanical Analysis: A Practical Introduction", CRC Press, **2008** (second edition).

G. Mengali, A.A. Quarta, "Non-Keplerian orbits for electric sails", Celestial Mechanics and Dynamical Astronomy, Volume 105, Issue 1, **2009**, pp. 179-195.

M.A. Meyers, A. Mishra, D.J. Benson, "Mechanical properties of nanocrystalline materials", Progress in Materials Science 51, **2006**, pp. 427-556.

A.V. Nagasekhar, T. Rajkumar, D. Stephan, Y. Tick-Hon, R.K. Guduru, "Microstructure and mechanical properties of pure gold processed by equal channel angular pressing", Materials Science and Engineering A 524, **2009**, pp. 204-207.

NASA, "Technology Roadmaps – TA 2: In-Space Propulsion Technologies", July **2015**.

Nasa.gov, "NASA Begins Testing of Revolutionary E-Sail Technology", 11/4/**2016**, available at https://www.nasa.gov/centers/marshall/news/news/releases/2016/nasa-begins-testing-of-revolutionary-e-sail-technology.html.

Nextbigfuture.com, "NASA NIAC E-sail Phase 2 Heliopause Electrostatic Rapid Transit System", 8/9/**2016**, available at http://www.nextbigfuture.com/2016/09/nasa-niac-e-sail-phase-2-heliopause.html.

S.P. Nikanorov, M.P. Volkov, V.N. Gurin, Yu.A. Burenkov, L.I. Derkachenko, B.K. Kardashev, L.L. Regel, W.R. Wilcox, "Structural and mechanical properties of Al–Si alloys obtained by fast cooling of a levitated melt", Materials Science and Engineering A 390, **2005**, pp. 63-69.

K.E. Paul, C. Zhu, J.C. Love, G.M. Whitesides, "Fabrication of mid-infrared frequency-selective surfaces by soft lithography", Applied Optics, Vol. 40, No. 25, **2001**, pp. 4557-4661.

Phys.org, "Japan launching 'space junk' collector", 9/12/**2016**, available at https://phys.org/news/2016-12-japan-space-junk-collector.html.

J. Polkko, "Auxiliary Tether Report", Deliverable D24.1 of the ESAIL FP7 project, **2012**.

A.A. Quarta, G. Mengali, "Electric sail mission analysis for outer solar system exploration", Journal of Guidance Control and Dynamics, No. 33, **2010**, pp. 740-755.

R. Raj, M.F. Ashby, "On Grain Boundary Sliding and Diffusional Creep", Metallurgical Transactions, Volume 2, **1971**, pp. 1113-1127.

T. Rauhala, G. Maconi, T. Kalvas, "Tether coating report", Deliverable D22.1 of the ESAIL FP7 project, **2013**.

H.S. Rosenbaum, D. Turnbull, "On the precipitation of silicon out of a supersaturated aluminium-silicon solid solution", Acta metallurgica, Vol. 6, **1958**, pp. 653-659.

N. Saini, D.K. Dwivedi, P.K. Jain, H. Singh, "Surface Modification of Cast Al-17%Si Alloys using Friction Stir Processing", Procedia Engineering 100, **2015**, pp. 1522-1531.

J.R. Sanmartín, R.D. Estes, "The orbital-motion-limited regime of cylindrical Langmuir probes", Physics of Plasmas, Vol. 6, N. 1, **1999**, pp. 395-405.

K. Sasaki, N. Ohno, "Fatigue life evaluation of aluminium bonding wire in silicone gel under random vibration testing", Microelectronics Reliability, Volume 53, Issues 9–11, **2013**, pp. 1766-1770.

M. Sebastiani, F. Massimi, G. Merlati, E. Bemporad, "Residual micro-stress distributions in heat-pressed ceramic on zirconia and porcelain-fused to metal systems: Analysis by FIB–DIC ring-core method and correlation with fracture toughness", Dental Materials, Volume 31, Issue 11, **2015**, pp. 1396-1405.

A. Seifter, "About the Meaning of the Hagen-Rubens Relation to Radiation Thermometry", Proceedings, XVII IMEKO World Congress, Dubrovnik, Croatia, June 22-27 **2003**.

H. Seppänen, "Tether factory (1 km) requirements", Deliverable D21.2 of the ESAIL FP7 project, **2013**.

H. Seppänen, T. Rauhala, S. Kiprich, J. Ukkonen, M. Simonsson, R. Kurppa, P. Janhunen, E. Hæggström, "One kilometer (1 km) electric solar wind sail tether produced automatically", Review of Scientific Instruments, Vol. 84, Issue 9, 095102, **2013**.

A. Slavinskis, M. Pajusalu, H. Kuuste, E. Ilbis, T. Eenmäe, I. Sünter, K. Laizans, H. Ehrpais, P. Liias, E. Kulu, J. Viru, J. Kalde, U. Kvell, J. Kütt, K. Zalite, K. Kahn, S. Lätt, J. Envall, P. Toivanen, J. Polkko, P. Janhunen, R. Rosta, T. Kalvas, R. Vendt, V. Allik, M. Noorma, "ESTCube-1 In-Orbit Experience and Lessons Learned", Aerospace and Electronic Systems Magazine, Volume 30, Number 8, **2015**, pp. 12-22.

K. Sorensen, "Conceptual Design and Analysis of an MXER Tether Boost Station", 37th Joint Propulsion Conference and Exhibit, February **2001**.

K. Sorensen, "Momentum eXchange Electrodynamic Reboost (MXER) Tether Technology Assessment Group Final Report", presented at NASA on July 24, **2003**.

Spaceflight Now, "Japanese cargo carrier set for launch Friday", 8/12/**2016**, available at https://spaceflightnow.com/2016/12/08/japanese-cargo-carrier-set-for-launch-friday/.

R.G. Sturmfels, "Design of space tethers formeteoroid and orbital debris impact survivability", 39th Aerospace Sciences Meeting &Exhibit, 8-11 Jan **2000**.

A. Takagi, T. Kato, S. Miyake, S. Inoue, T. Namazu, "Effect of Vacuum Annealing on Tensile Mechanical Characteristics of Au Bonding Wires", Sensors and Materials, Vol. 28, No. 2, **2016**, pp. 163-171.

S. Takeuchi, A.S. Argon, "Steady-state creep of alloys due to viscous motion of dislocations", Acta Metallurgica, Vol 24, **1976**, pp. 883-889.

TANAKA, "Material Safety Data Sheet Aluminium Bonding Wire (TABN)", 10 January **2015**, available at http://www.topline.tv/PDFfiles/MSDS_Tanaka_TABN.pdf.

M. Tehrani, M. Safdari, A.Y. Boroujeni, Z. Razavi, S.W. Case, K. Dahmen, H. Garmestani, M.S. Al-Haik, "Hybrid carbon fiber/carbon nanotube composites for structural damping applications", Nanotechnology 24, no. 15, 155704, **2013**.

A. Todoran, M. Mantel, A. Bés, C. Vachey, A. Lacoste, "Control of particle flux and energy on substrate in an inverted cylindrical magnetron for plasma PVD", Plasma Sources Science and Technology, 23 – 6, 065039, **2014**.

P. Toivanen, P. Janhunen, "Electric Sailing under Observed Solar Wind Conditions", Astrophysics and Space Sciences Transactions, 5, **2009**, pp. 61-69.

P. Toivanen, P. Janhunen, "Spin Plane Control and Thrust Vectoring of Electric Solar Wind Sail by Tether Potential Modulation", Journal of Propulsion and Power, 29, **2013**, pp. 178-185.

P. Toivanen, P. Janhunen, "Electric Solar Wind Sail: Deployment, Long-Term Dynamics, and Control Hardware Requirements", Chapter in Advances in Solar Sailing, Springer Praxis Books, **2014**, pp. 977-987.

P. Toivanen, P. Janhunen, "Thrust vectoring of an electric solar wind sail with a realistic sail shape", *Preprint submitted to Acta Astronautica* – March **2017**.

J. Van Laak, "Kapton Wire Concerns for Aerospace Vehicles", First NASA Workshop on Wiring for Space Applications, **1994**, pp. 11-17.

P. van Mourik, Th.H. de Keijser, E.J. Mittemeijer, "Kinetics of precipitation and of relaxation of precipitation-induced stresses in aluminium-silicon alloys", Scripta Metallurgica Vol. 21, **1987**, pp. 381-385.

J.A. Vaughn, P. Schuler, "Conductive Tether Coating for Electrodynamic Tethers", 11th Advanced Space Propulsion meeting, **2000**.

J. Vincent, "Structural Bimaterials", Princeton University Press, **2012** (third edition).

C. Wang, B. Guo, D. Shan, L. Sun, "Effects of specimen size on flow stress of micro rod specimen", Transactions of Nonferrous Metals Society of China, 19, **2009**, pp. 511-515.

L. Wang, T. Xin, D. Kong, X. Shu, Y. Chen, H. Zhou, J. Teng, Z. Zhang, J. Zou, X. Han, "In situ observation of stress induced grain boundary migration in nanocrystalline gold", Scripta Materialia 134 **2017**, pp. 95-99.

J. Wehrs, G. Mohanty, G. Guillonneau, A.A. Taylor, X. Maeder, D. Frey, L. Philippe, S. Mischler, J.M. Wheeler, J. Michler, "Comparison of In Situ Micromechanical Strain-Rate Sensitivity Measurement Techniques", The Journal of the Minerals, Metals & Materials Society 67(8), **2015**, pp. 1684-1693.

K.X. Wei, W. Wei, F. Wang, Q.B. Du, I.V. Alexandrov, J. Hu, "Microstructure, mechanical properties and electrical conductivity of industrial Cu–0.5%Cr alloy processed by severe plastic deformation", Materials Science and Engineering A 528, **2011**, pp. 1478-1484.

Q. Wei, S. Cheng, K.T. Ramesh, E. Ma, "Effect of nanocrystalline and ultrafine grain sizes on the strain rate sensitivity and activation volume: fcc versus bcc metals", Materials Science and Engineering A 381 **2004**, pp. 71-79.

C. Wen, I. Mudawar, "Modeling the effects of surface roughness on the emissivity of aluminum alloys", International Journal of Heat and Mass Transfer 49, **2006**, pp. 4279-4289.

B. M. Wiegmann, "Heliopause Electrostatic Rapid Transit System (HERTS)", 51st AIAA/SAE/ASEE Joint Propulsion Conference, AIAA Propulsion and Energy Forum, **2015**.

J.D. Williams, J.R. Sanmartín, L.P. Rand, "Low Work-Function Coating for an Entirely Propellantless Bare Electrodynamic Tether", IEEE Transactions on Plasma Science, Vol. 40, Issue 5, **2012**, pp. 1441-1445.

G. Winther, D. Juul Jensen, N. Hansen, "Dense dislocation walls and microbands aligned with slip planes – theoretical considerations". Acta materalia, Vol. 45, No. 12, **1997**, pp. 5059-5068.

Z. Yang, N. Sakaguchi, S. Watanabe, M. Kawai, "Dislocation Loop Formation and Growth under *In Situ* Laser and/or Electron Irradiation", Nature Scientific Reports 1, **2011**.

V.Y. Zenou, A. Kiv, D. Fuks, V. Ezerski, N. Moiseenko, "The microscopic mechanism of silicon precipitation in Al/Si system", Materials Science and Engineering A 435–436, **2006**, pp. 556-563.

Q. Zhao, B. Holmedal, "The effect of silicon on the strengthening and work hardening of aluminum at room temperature", Materials Science & Engineering A 563, **2013**, pp. 147-151.

S. Zhu, J. Yao, L. Sweet, M. Easton, J. Taylor, P. Robinson, N. Parson, "Influences of Nickel and Vanadium Impurities on Microstructure of Aluminum Alloys", The Journal of the Minerals, Metals & Materials Society, Vol. 65, No. 5, **2013**, pp. 584–592.

V.S. Zolotorevsky, N.I. Belov, "Casting Aluminum Alloys", Elsevier, Amsterdam, The Netherlands, **2007**.

J. Zrnik, S.V. Dobatkin, I. Mamuzič, "Processing of metals by severe plastic deformation (SPD) – structure and mechanical properties", Respondmetalurgija 47, 3, **2008**, pp. 211-216.

R.M. Zubrin, D.G. Andrews, "Magnetic sails and interplanetary travel", Journal of Spacecraft and Rockets, 28, **1991,** pp. 197-203.
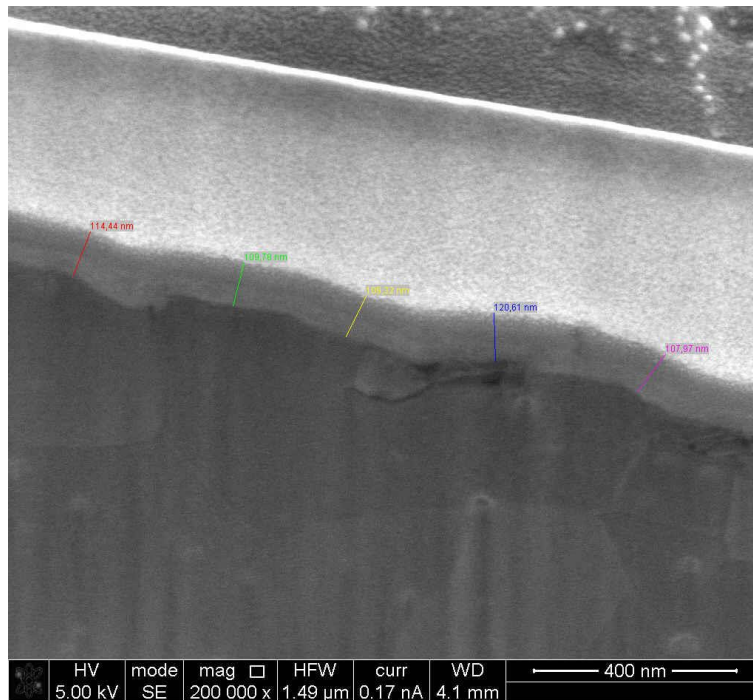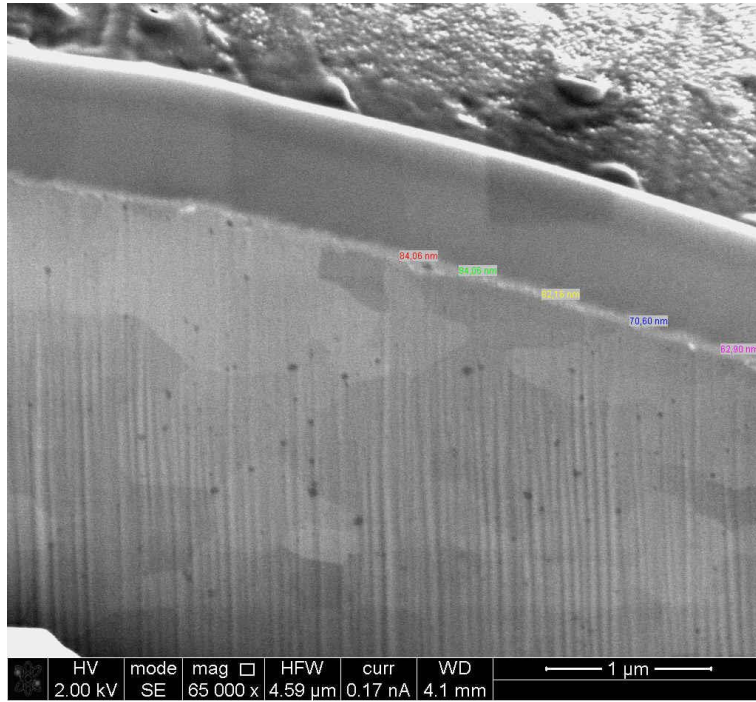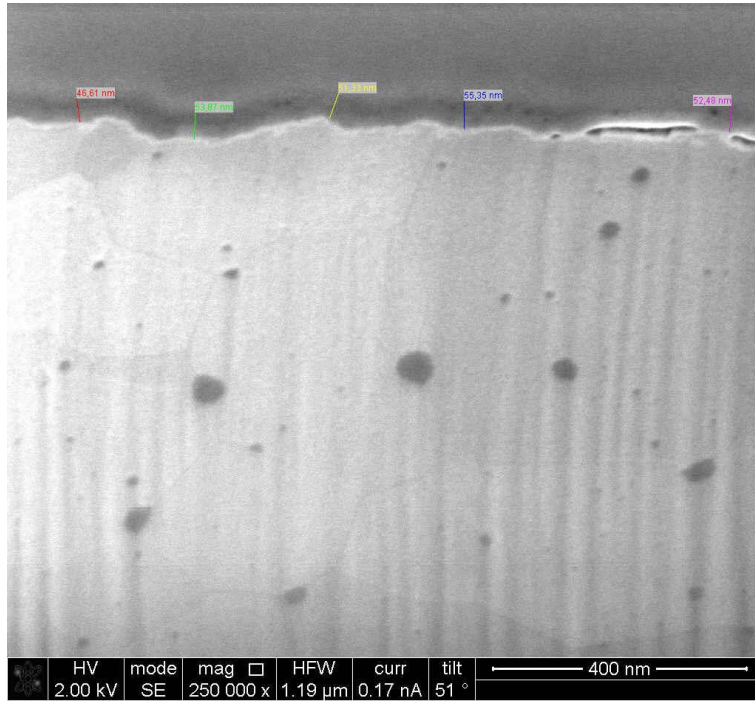
Micrographs of FIB-milled specimen, 100 nm nominal thickness. Particular of the coating, TiO2 coating, 100 nm nominal thickness
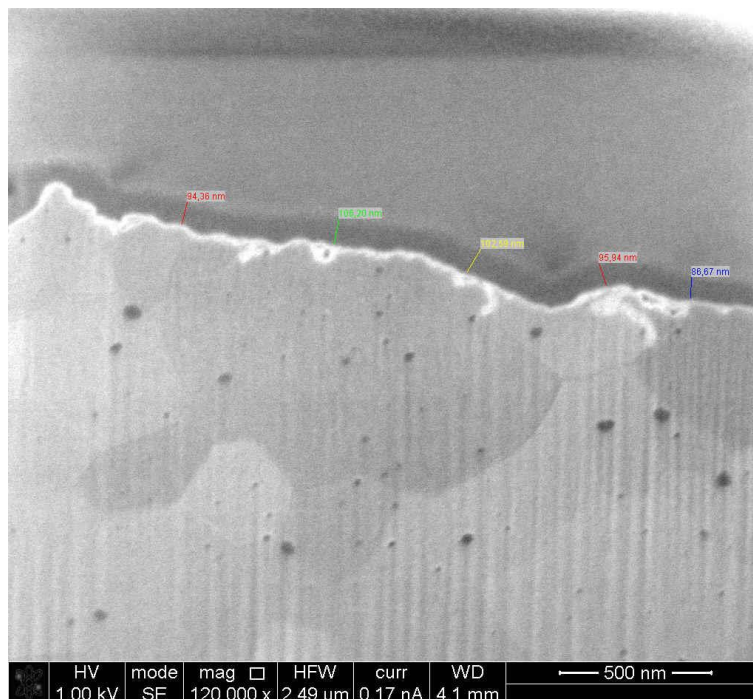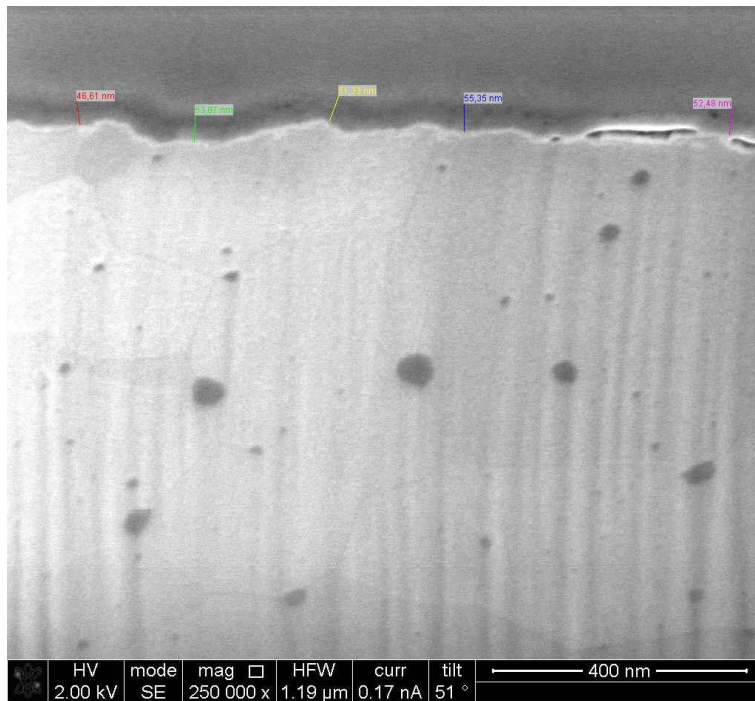

Micrographs of FIB-milled specimen, 100 nm nominal thickness. Particular of the coating, TiZnO coating, 100 nm nominal thickness
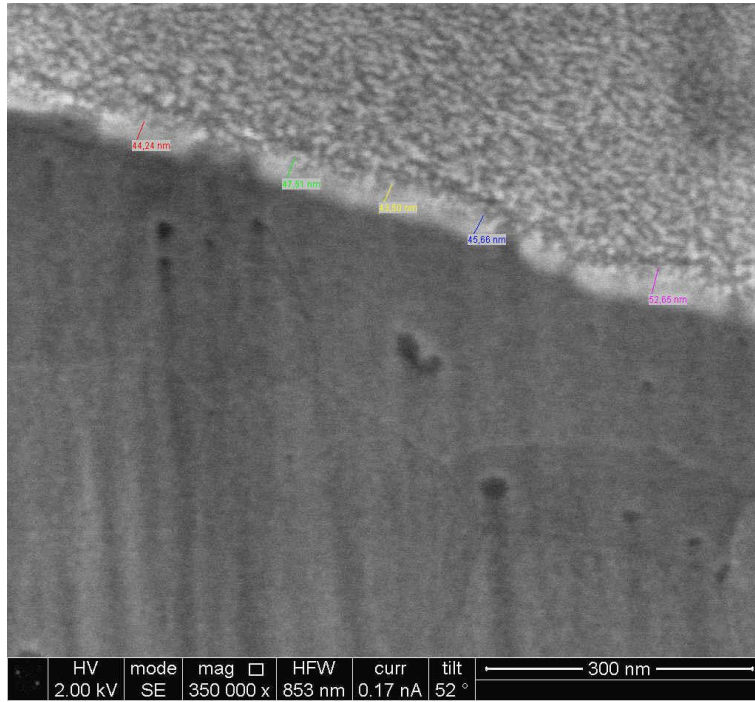
Micrographs of FIB-milled specimen, 100 nm nominal thickness. Particular of the coating, ZnO coating, 100 nm nominal thickness
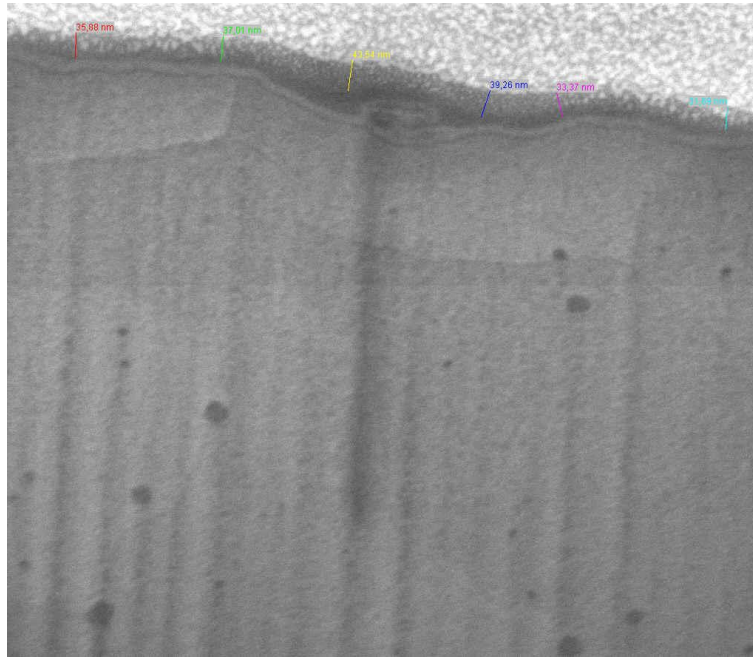
Micrographs of FIB-milled specimen, 50 nm nominal thickness. Particular of the coating, TiO2 coating, 50 nm nominal thickness
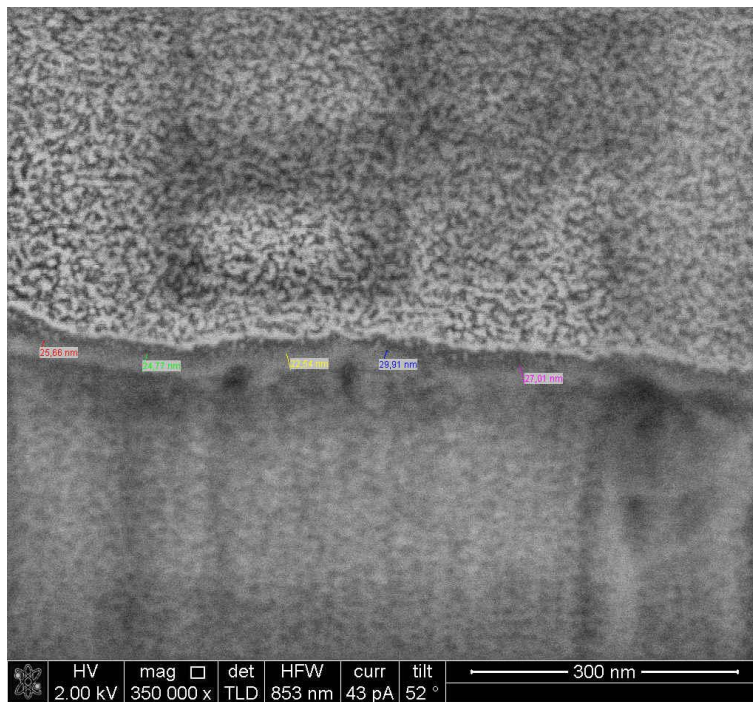

Micrographs of FIB-milled specimen, 50 nm nominal thickness. Particular of the coating, TiZnO coating, 50 nm nominal thickness
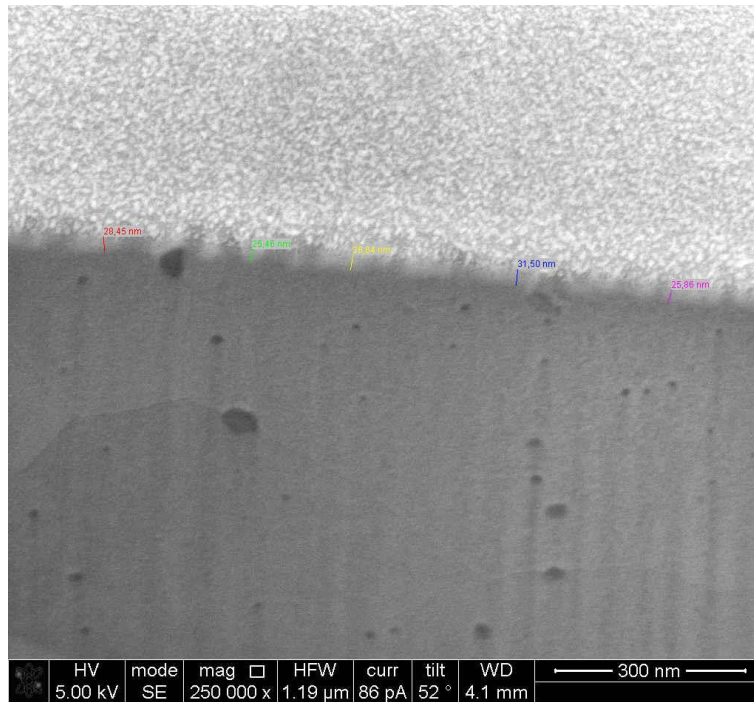
Micrographs of FIB-milled specimen, 50 nm nominal thickness. Particular of the coating, ZnO coating, 50 nm nominal thickness

Micrographs of FIB-milled specimen, 25 nm nominal thickness. Particular of the coating, TiO2 coating, 25 nm nominal thickness

Micrographs of FIB-milled specimen, 25 nm nominal thickness. Particular of the coating, TiZnO coating, 25 nm nominal thickness

Micrographs of FIB-milled specimen, 25 nm nominal thickness. Particular of the coating, ZnO coating, 25 nm nominal thickness
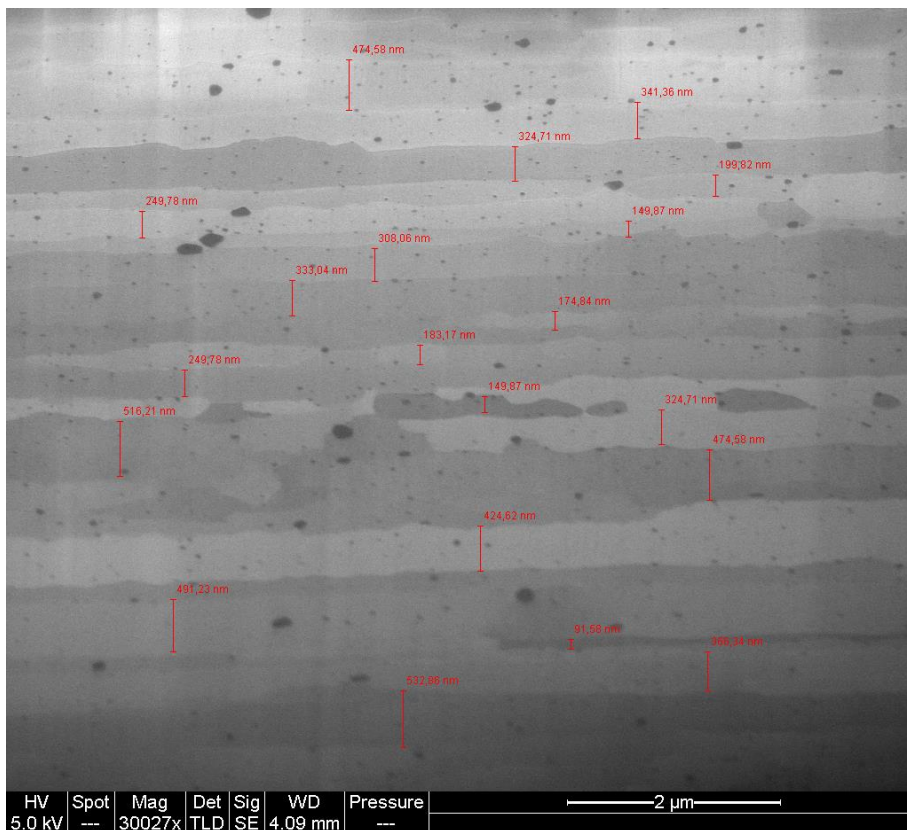
APPENDIX B – TENSILE TEST DATA

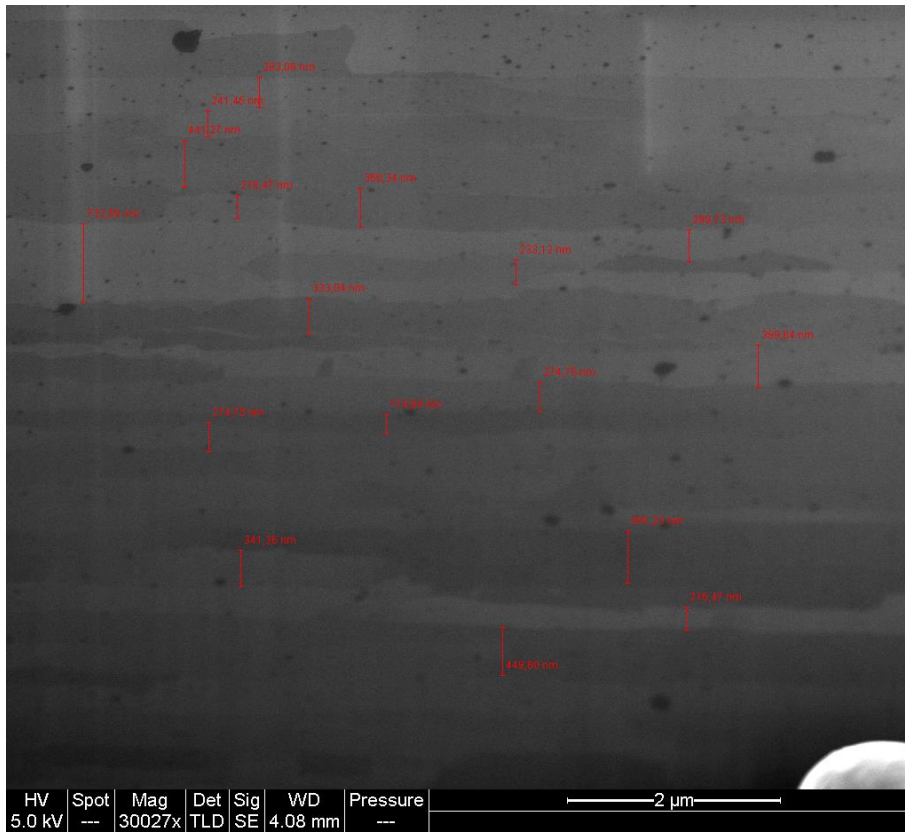| Test #	Temp. (°C)	Support type	Preload (mN)	Force rate (N/min)	Max load (mN)	Max eng. stress (Mpa)	Max true stress (Mpa)	Max true strain (%)
U33	-40	Rigid	10	0.03	199	247	247	0,8
U30	-40	Rigid	10	0.03	204	253	253	1,0
U32	-20	Rigid	10	0.03	205	255	255	5,1
U28	-20	Rigid	10	0.03	184	230	230	1,9
U31	0	Rigid	10	0.03	197	245	245	5,7
92	23	Graphite	10	0.03	183	228	227	4.0
95	23	Graphite	10	0.03	190	236	237	5.2
112	24	Graphite	10	0.02	178	221	221	6.4
27	27	Graphite	50	0.06	178	221	221	5.9
28	27	Graphite	50	0.06	186	231	231	4.9
32	27	Graphite	50	0.06	188	234	234	7.4
106	40	Graphite	10	0.02	160	199	200	7.7
117	40	Graphite	10	0.02	165	205	205	4.4
100	40	Graphite	10	0.03	178	221	222	5.5
67	40	no graphite	50	0.03	182	226	226	7.1
69	40	no graphite	50	0.03	169	210	210	6.9
125	50	Graphite	10	0.02	158	196	254	14.6
61	50	Graphite	50	0.03	172	214	213	11.6
66	50	Graphite	50	0.03	171	213	212	6.0
43	60	Graphite	50	0.03	175	218	215	20.5
70	60	no graphite	50	0.03	163	203	202	6.8
44	70	Graphite	50	0.03	167	208	200	15.1
72	70	no graphite	50	0.03	163	203	202	10.5
63	80	no graphite	50	0.03	162	201	202	25.56
73	80	no graphite	50	0.03	150	187	187	7.928
35	100	Graphite	50	0.03	155	193		
74	100	no graphite	50	0.03	161	200		
138	100	Graphite	10	0.02	135	168		
155	110	no graphite	10	0.02	140	174	278	23.1
157	110	no graphite	10	0.02	152	189	307	22.3
164	110	no graphite	10	0.02	129	160	283	32.7
159	150	no graphite	10	0.02	130	162		
162	150	no graphite	10	0.02	130	162		
163	150	no graphite	10	0.02	127	158		
167	250	no graphite	10	0.02	73	91		
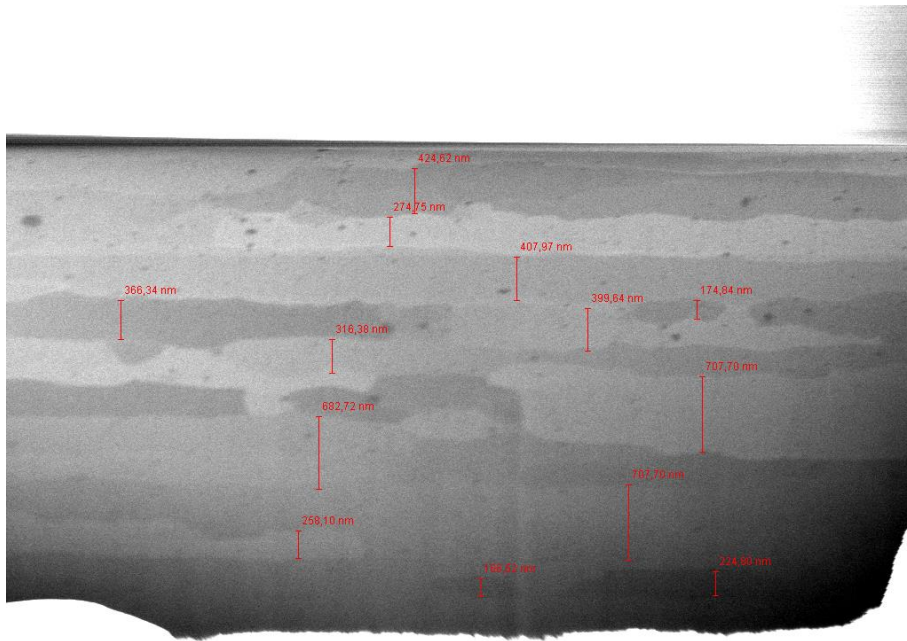
Sample "as received" by the manufacturer

Test 74

Test 95

Test 125

Test 138